# Improved Understanding of Processes Relevant for Artificial Photosynthesis: Studies on the Distance Dependence of Electron Transfer, Charge-Separated States and the Photosynthetic Z-Scheme

Inauguraldissertation

zur Erlangung der Würde eines Doktors der Philosophie

vorgelegt der Philosophisch-Naturwissenschaftlichen Fakultät

der Universität Basel

von

## Svenja Neumann

aus Deutschland

Basel, 2019

Genehmigt von der Philosophisch-Naturwissenschaftlichen Fakultät auf Antrag von

Fakultätsverantwortlicher und Dissertationsleiter: Prof. Dr. Oliver S. Wenger

Korreferent: Prof. Dr. Gerald J. Meyer

Basel, den 15.10.2019

_____

Prof. Dr. Martin Spiess, Dekan

We keep moving forward, opening new doors... because we're curious and curiosity keeps leading us down new paths.

*Walt Disney*

Meinen Eltern

# Acknowledgements

First of all, I would like to thank my supervisor **Prof. Oliver S. Wenger** for accepting me as his graduate student and for giving me the opportunity to work on such interesting projects. It was a pleasure to work with you and I highly appreciated your support and guidance over the last years and the great working atmosphere you are creating. You always had an open door if help was needed, which is one of the things I am most grateful for. You also encouraged me to have a healthy work-life balance and even supported me during the Basler Frauenlauf, the longest distance I ever ran and will ever run. I will never forget your face when I threw the water bottle back at you.

Special thanks are given to **Prof. Gerald J. Meyer** for kindly agreeing to co-examine this thesis.

I want to sincerely thank **Prof. Christof Sparr** for chairing my examination.

I also would like to thank the team from the **Swiss Nanoscience Institute** for all the nice conferences and the funding, as well as the **SNI PhD School** for the organized events.

I kindly thank **Sylvie Mittelheisser** for measuring elemental analysis and **Dr. Heinz Nadig** and **Dr. Michael Pfeffer** for measuring high-resolution mass spectra.

Many thanks are given to **Markus Hauri**, **Oliver Ilg**, the **NMR-Team** and the entire **Werkstatt-Team** for keeping the department and the daily lab-work run as smoothly as possible. For help concerning organizational and administrative matters, I thank **Brigitte Howald**, **Beatrice Erismann** and **Marina Mambelli Johnson**.

Special thanks are given to **Martin**, **Chris**, **Christoph** and **Mirj** for proof-reading my thesis and also for all the helpful discussions. I also would like to thank **Christoph** for our joint project and the successful cooperation.

Furthermore, I would like to thank the present and past members of the **AK Wenger** for the terrific working atmosphere and all the fun I had during my PhD thesis. Thank you **Patrick**, **Julia**, **Hauke**, **Chris**, **Christoph**, **Luci, Andrea** and **Mirj** for the great company during conferences.

Many thanks go to my 'original' lab 302, namely **Michael**, **Julia**, **Andrea** and **Hauke**, for the incredible lab spirit and our scientific and non-scientific discussions.

Thank you **Andrea** for our swimming (and running) dates and all the new card games you introduced me to.

Thank you **Michael** for your great sense of humor. I laughed a lot with you and it was always fun working next to you.

Thank you **Julia** for our time in the lab, but even more for the time outside the lab. It

was fun making a fool out of me during our T-Bow sessions, I enjoyed shopping with you or having a nice drink and talk about whatever came into our minds.

I also would like to thank **Tobi** for all the jokes in the lab and for disposing the waste and equipment refills. You made my last month in the lab a lot easier. Additionally, I always valued your input on my synthetic problems.

A big thanks also goes to **Mirj**, who organized most of our social group events and contributes a lot to our incredible working atmosphere. Furthermore, I very much enjoyed our holiday trips together.

Thank you **Patrick** for being the 'Lord of the Card Games'! The breaks would not have been the same otherwise. I also had a great time with you in London.

Thank you **Christoph** for being such a great office buddy. You were always happy to answer my questions and I learned a lot from you. One thing left to say: Ente, Ente, Ente, Ente...

The last year of my PhD thesis was the hardest and I want to thank my crisis management team **Tobi**, **Mirj**, **Christoph** and **Marianne** for their support. Thank you **Tobi** for listening to my problems. Thank you **Mirj** for giving me a hug when I needed one. Thank you **Christoph** for trying to cheer me up. Thank you **Marianne** for being around when I needed you, even when you were writing your own PhD thesis.

I also would like to thank **Marianne** and **Fabian** for the great game nights and the delicious food at their place. I always enjoy spending time with you.

Zum Schluss möchte ich mich noch von Herzen bei den Menschen bedanken, ohne die ich es nicht bis zur Promotion geschafft hätte. Danke **Kunal**, dass du mich durch die gesamte Studienzeit in Göttingen begleitet hast. Ohne deine Freundschaft hätte ich es vermutlich nicht über das erste Semester hinaus geschafft. Selbst heute kann ich immer noch auf deine Unterstützung bauen und bin sehr dankbar dafür. Der größte Dank gilt meinen Eltern. **Mama** und **Papa**, ihr habt mich bei jeder meiner Entscheidungen immer vollauf unterstützt. Als ich zu Studienbeginn überfordert war, seid ihr jeden Dienstagabend nach der Arbeit nach Göttingen gefahren, um mich zu trösten. Als ich für meine Promotion nach Basel gezogen bin, habt ihr mir beim Organisieren und Einrichten geholfen. Ihr wart und seid mein Anker und ich bin stolz eure Tochter zu sein.

# Abstract

Due to the growing world population and the enormous progress in technology over the last decades, there is an increasing demand on energy. To date, the worlds energy needs are mainly covered by the combustion of fossil fuels like natural gas, oil or coal. However, besides the limited availability in the future, combustion of fossil fuels is harmful to human health and the released gases contribute to global warming. An alternative and more sustainable energy source would be the sun since the solar energy that reaches the surface of the earth can already cover the worlds energy demands, but efficient solar energy conversion and storage is a challenge. Natural photosynthesis offers a blueprint for such processes. In this thesis, fundamental processes relevant for artificial photosynthesis are investigated to gain better understanding of and to improve future artificial systems.

Electron transfer over large distances is one of the major processes involved in photosynthesis. In the first project of this thesis (Chapter 3), the distance dependence of electron-transfer rates in donor-photosensitizer-acceptor triads, with either a low (*ca.* 1.2 eV in TAA-ph$_n$-Ru-ph$_n$-NDI) or a high (*ca.* 2.0 eV in TPA-ph$_n$-Ir-ph$_n$-AQ) driving force for thermal charge recombination, was studied. Symmetrical addition of phenyl spacers allowed the elongation of the donor-acceptor distances in the given triads (n =1,2). Earlier investigations in the WENGER group, on a comparable molecular triad with a driving force of *ca.* 1.6 eV, revealed an increase of the electron-transfer rate with increasing donor-acceptor distance. This was the first unambiguous experimental proof for a counterintuitive phenomenon that was predicted more than 20 years ago. To increase the understanding of this counterintuitive phenomenon, a systematic investigation regarding the influence of the driving force for thermal charge recombination was performed. The results of this project showed that highly exergonic electron-transfer reactions can exhibit fundamentally different distance dependences than the more commonly investigated weakly exergonic electron transfers. Elongation of the donor-acceptor distance in the set of triads with a low driving force resulted in a decrease of the electron-transfer rate. On the other hand, for the sets of triads with a high driving force, an increase of the transfer rate was observed upon elongation. These observations are in agreement with the MARCUS theory of electron transfer. For low driving forces of *ca.* 1.2 eV, electron transfer proceeds in an activationless manner in the shorter triad, whereas the electron-transfer step takes place in the normal regime of the MARCUS model in the longer compound. Thus, a decrease of the electron-transfer rate with increasing donor-acceptor distance results. At high driving forces of *ca.* 2.0 eV, thermal charge recombination in the shorter triad occurs in the inverted regime. With elongation of the system, activationless electron transfer can be observed. As a consequence, the electron-transfer rate for thermal charge

recombination in the triads with a high driving force increases with elongation of the donor-acceptor distance.

Charge-separated states (CSSs) are key intermediates in natural photosynthesis. Therefore, the second project in this thesis (Chapter 4) investigated the highly energetic CSSs of the iridium-based triads introduced in Chapter 3 in more detail. In particular, quantitative determinations of the quantum yields for CSS formation were performed to gain more insights into the factors that govern the CSS formation efficiency. Additionally, two-pulse laser experiments revealed the fate of the CSSs after absorption of a second photon. The CSS formation quantum yield reached *ca.* 80% when the formation proceeded *via* an MLCT transition. Admixture of an intraligand charge transfer (CT) transition, which is exclusively possible in the shorter triad, decreased the quantum yield significantly and gave rise to an unusual wavelength-dependence of the CSS quantum yield. One key finding of the investigations in this project is that light-induced charge recombination shows opposite behavior compared to thermal charge recombination in terms of their distance dependences. Thermal charge recombination in the longer triad was significantly more efficient than in the shorter one. However, light-induced charge recombination is much more efficient in the shorter triad.

In nature, the Z-scheme can be seen as the 'heart' of light-dependent natural photosynthesis and can be regarded as one of the most important processes in life. A detailed understanding of the Z-scheme is therefore highly desirable. However, molecular mimics of the Z-scheme are scarce. In the third project of this thesis (Chapter 5), a purely organic molecular mimic of the photosynthetic Z-scheme was designed. Like in nature, two photosystems are incorporated into the molecular design. Each photosystem is represented by a dyad (NMI-TPDB and PT-TAA) and the photosystems are linked with each other by a $p$-(di-$n$-hexyl)phenyl (hxy) spacer to afford a tetrad. To estimate if the approach of the tetrad was promising enough to pursue, reference dyads (NMI-TPDB, TPDB-PT and PT-TAA) were developed. While the successful synthesis of PT-TAA is still pending, the applicability of NMI-TPDB as one photosystem and the introduced linker between the two dyads were verified. NMI-TPDB formed a CSS after excitation with visible light whereas the hxy spacer minimized the possibility of a CT transition between the TPDB and PT units. A weak CT absorption band could be observed, but thermal charge recombination after excitation with visible light occurred rapidly and no CSS formation was detectable. Based on these results, further investigations of this all-organic tetrad approach seem to be very promising.

# Contents

# Abbreviations

| | |
|---|---|
| A | electron acceptor |
| $A_0$ | primary electron acceptor in photosystem I |
| $A_1$ | phylloquinone |
| ADP | adenosine diphosphate |
| anal. | analytical |
| ANI | 4-aminonaphthalene-1,8-dicarboximide |
| AQ | 9,10-anthraquinone |
| aq. | aqueous |
| ATP | adenosine triphosphate |
| Boc | *tert*-butoxycarbonyl |
| Bodipy | 4,4-difluoro-1,3,5,7-tetramethyl-2,6-diethyl-4-bora-3a,4a-diaza-*s*-indacene |
| B(pin) | (pinacolato)boron |
| bpy | 2,2'-bipyridine |
| Bu | butyl |
| C | catalyst |
| calcd. | calculated |
| CR | charge recombination |
| CSS | charge-separated state |
| CT | charge transfer |
| Cyt $b_6$f | cytochrome $b_6$f |
| D | electron donor |
| dba | dibenzylideneacetone |
| DCM | dichloromethane |
| DFT | density functional theory |
| DMF | *N,N*-dimethylformamide |
| DMSO | dimethylsulfoxide |
| DP | diphenyl |
| ESI | electrospray ionization |
| ET | electron transfer |
| Et | ethyl |
| $Et_2O$ | diethyl ether |
| EtOAc | ethyl acetate |
| eq. | equivalents |

| | |
|---|---|
| FD | ferredoxin |
| FeS | iron-sulfer cluster |
| FNR | ferredoxin nicotinamide adenine dinucleotide phosphate reductase |
| GS | ground-state |
| HOMO | highest occupied molecular orbital |
| HPLC | high-performance liquid chromatography |
| HRMS | high-resolution mass spectrometry |
| hxy | $p$-(di-$n$-hexyl)phenyl |
| IC | internal conversion |
| INT | intermediate |
| IR | infrared |
| ISC | intersystem crossing |
| LUMO | lowest unoccupied molecular orbital |
| M | molar, mol·L$^{-1}$ |
| Me | methyl |
| MLCT | metal-to-ligand charge transfer |
| $m/z$ | mass per charge |
| $n$ | normal |
| NADPH | reduced nicotinamide adenine dinucleotide phosphate |
| NDI / NI | naphthalene diimide |
| NHE | normal hydrogen electrode |
| NIR | near-infrared |
| NMI | naphthalene monoimide |
| NMR | nuclear magnetic resonance |
| OEC | oxygen evolving complex |
| OMe | methoxy |
| $p$ | para |
| PC | plastocyanin |
| ph / P | phenyl |
| Pheo | pheophytin |
| PI | pyromellitimide |
| PPh$_3$ | triphenylphosphine |
| ppm | parts per million |
| ppy | 2-phenylpyridine |
| PQ | plastoquinone |
| PQH$_2$ | plastoquinol |
| PS | photosystem |

| | |
|---|---|
| PT | pyrene-4,5,9,10-tetraone |
| P680 | pigment that absorbs 680 nm light in photosystem II |
| P700 | pigment that absorbs 700 nm light in photosystem I |
| $Q_A$ | primary plastoquinone electron acceptor |
| $Q_B$ | secondary plastoquinone electron acceptor |
| quant. | quantitative |
| RC | reaction center |
| ref | reference |
| rt | room temperature |
| S | singlet |
| sA | strong electron acceptor |
| sat. | saturated |
| SCE | saturated calomel electrode |
| sD | strong electron donor |
| $S$-Phos | 2-dicyclohexylphosphino-2',6'-dimethoxybiphenyl |
| T | triplet |
| TAA | triarylamine |
| TAPD | tetraalkylphenyldiamine |
| $TBAPF_6$ | tetrabutylammonium hexafluorophosphate |
| TCSPC | time-correlated single photon counting |
| TD | time-dependent |
| TFA | trifluoroacetic acid |
| th | thiophene |
| THF | tetrahydrofuran |
| TMS | trimethylsilyl |
| TMSCl | chlorotrimethylsilane |
| TPA | triphenylamine |
| TPDB | tetraphenyl-diaminobenzol |
| Tyr | tyrosine |
| UV | ultraviolet |
| Vis | visible |
| wA | weak electon acceptor |
| wD | weak electron donor |

# 1 General Introduction and Motivation

Enormous progress in technology and a growing world population over recent decades have drastically increased the worlds energy demand. The amount of energy required in 2016, roughly 18 TW, is almost twice that of the year 1980 and is mainly covered by the combustion of the fossil fuels coal, oil and natural gas (*ca.* 81%, Figure 1.1).[1]
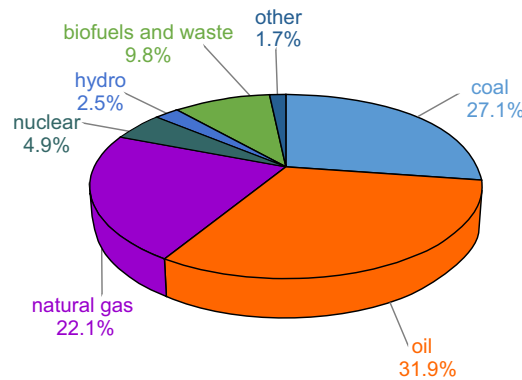
**Figure 1.1:** World total primary energy supply by fuels in 2016.[1]

However, to rely on fossil fuels has several drawbacks. Fossil fuels are a non-renewable energy source, *i.e.* the resources are limited. Even more critical are the consequences of the combustion of fossil fuels, since harmful gases and particles are released that threaten human health and contribute to global climate changes.[2, 3] A change to a renewable and less harmful source of energy is therefore of great importance. Ideally, this alternative energy source should be environmentally clean, abundant, economical, inexpensive and fairly distributed all over the world. The most attractive potential energy source that fulfills these requirements is the sun, which delivers about 120,000 TW of electromagnetic radiation to the earth's surface each year.[4, 5] To cover the annual energy demand of humankind, already 1.5 h of (direct) sunlight would be more than sufficient. However, the solar energy that reaches the surface of the earth cannot be directly exploited and needs to be converted and stored. In nature, photosynthesis provides a blueprint for these processes and the production of fuels, with the formation of dioxygen as a 'waste' product (Chapter 2.1). Thereby, the inexpensive and abundant raw materials water and carbon dioxide provide electrons, protons and carbon atoms that can be incorporated

into different types of fuels. A generalized artificial approach for the production of a fuel, which is based on natural photosynthesis, is illustrated in Scheme 1.1.[4]
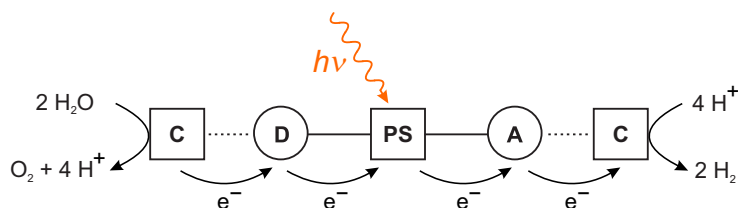


**Scheme 1.1:** Schematic representation of an artificial system capable of hydrogen production after photoexcitation. The system consists of a photosensitizer (PS) coupled with an electron donor (D) and an electron acceptor (A), which are in close contact to catalysts (C). The scheme is based on ref[4].

The system shown in Scheme 1.1 consists of three parts: (i) A catalytic system (C) that can oxidize an electron source, in this case water, (ii) a triad (D-PS-A) that is able to harvest light and convert the excitation energy into electrochemical energy, and (iii) a second catalytic system to form the fuel. Excitation of the photosensitizer (PS) leads to a charge separation in the triad ($D^{\cdot+}$-PS-$A^{\cdot-}$), which facilitates the oxidation of water, on the oxidized side of the triad, and the reduction of protons to generate molecular hydrogen, on the reduced side of the triad. The complete process relies on an efficient electron-transfer chain over large distances and a successful coupling of a one-photon process (photoinduced charge separation) with multi-electron processes (water oxidation and fuel production).[4, 5] The given example nicely demonstrates the complexity of artificial (and natural) photosynthesis. Natural photosynthesis is highly regulated and additionally includes protective mechanisms to limit damage from excess light.[6, 7]

Due to the complexity of natural photosynthesis, it is important to gain an improved understanding of the different processes that are relevant in the context of artificial photosynthesis. In this thesis, three topics are discussed. As illustrated in Scheme 1.1, electron transfer over large distances is one of the major processes involved in photosynthesis. Chapter 3 therefore studies the distance dependence of electron-transfer rates in different molecular triads. As mentioned above, successful fuel production, and solar energy conversion and storage in general, also rely on an (efficient) formation of a charge-separated state, which is why Chapter 4 is dedicated to this process. In Chapter 5, an artificial system imitating the central part of light-induced natural photosynthesis is discussed, namely a molecular mimic of the photosynthetic Z-scheme. The Z-scheme, in which two photosystems work in series, can be seen as the 'heart' of light-dependent natural photosynthesis and an improved understanding is desirable. Here, electron transfer over large distances, the formation of a (highly energetic) charge-separated state, as well as multiple photon absorption are relevant.

In the following chapter, a short overview of natural photosynthesis is given, which emphasises the essential reaction steps. Additionally, the theoretical background about excited states and electron transfer are discussed. Following this, two-pulse laser experiments are introduced and selected studies are presented.

# 2 Theoretical Background

## 2.1 Natural Photosynthesis

Photosynthesis is nature's way to use the energy of sunlight to convert water and carbon dioxide, both low-energy raw materials, into $O_2$ and energy-rich organic molecules like carbohydrates, *i.e.* solar energy is stored in the form of chemical bonds. Without photosynthesis, life as we know it would not be possible since photosynthesis provides us with useful forms of energy and with atmospheric oxygen. In general, the process of photosynthesis can be divided into a light-dependent reaction and a so-called dark reaction (Scheme 2.1).[8] In the light-dependent reaction, water is oxidized and $O_2$ is released. Additionally, reduced nicotinamide adenine dinucleotide phoshate (NADPH), which represents the biological form of molecular hydrogen and acts as a hydrogen carrier, and adenosine triphosphate (ATP), which is a biological energy carrier, are generated.[9] Subsequently, NADPH and ATP are used in the dark reaction to form carbohydrates out of carbon dioxide.[10, 11]
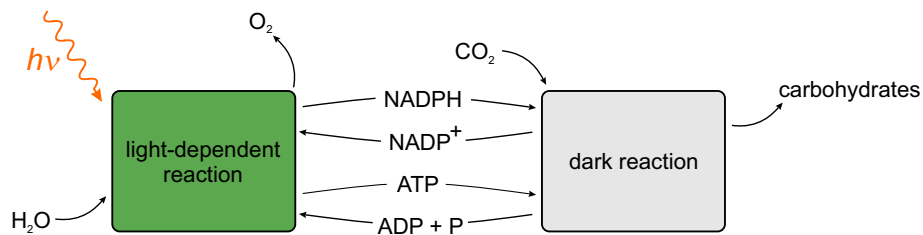


**Scheme 2.1:** Simplified representation of the overall natural photosynthesis.[8]

In nature, green plants, algae and cyanobacteria are able to perform photosythesis.[5] The light-dependent process relies on different protein complexes, named photosystem I and II (PS I, PS II), cytochrome $b_6f$ (Cyt $b_6f$) and ATP-synthase. These (redox) active sites are embedded in the thylakoid membrane of the chloroplasts, which separates the inner part (lumen) and the outer part (stroma) of the thylakoids (Scheme 2.2). In the course of light-induced photosynthesis, a transmembrane proton gradient is built up between stroma and lumen, which drives the synthesis of ATP.[7–9, 12]
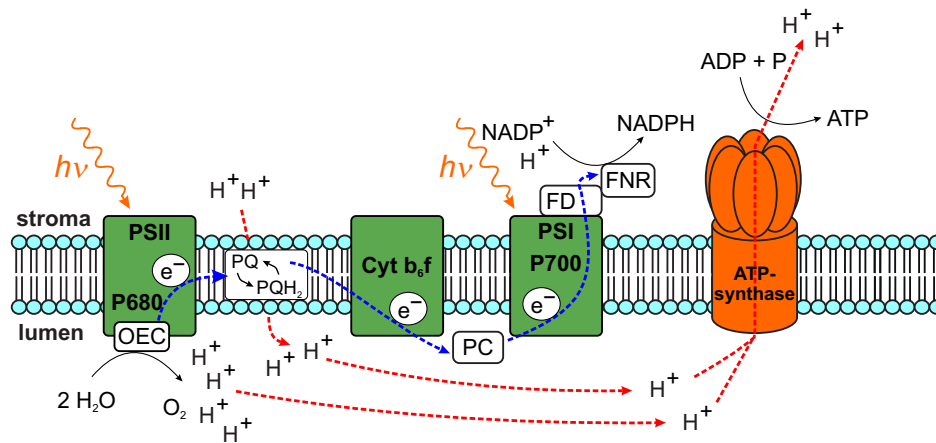
**Scheme 2.2:** Schematic representation of the thylakoid membrane, containing relevant intermembrane protein complexes for photosynthesis. The scheme is based on refs[8, 9]. The abbreviations are explained in the text.

As shown in Scheme 2.2, PS II and PS I work in series during photosynthesis. Both photosystems contain central chlorophyll dimers, called P680 in PS II and P700 in PS I, which can be excited by light.[9] This excitation can occur by direct absorption of a photon or by energy transfer from the light-harvesting antennas of the respective photosystem.[5, 7, 9] After photoexcitation, a reaction cascade takes place, which is known as the Z-scheme (Scheme 2.3).[9, 12, 13] Due to the reactions presented in the Z-scheme, water can be split into $O_2$ and protons and NADPH is formed.
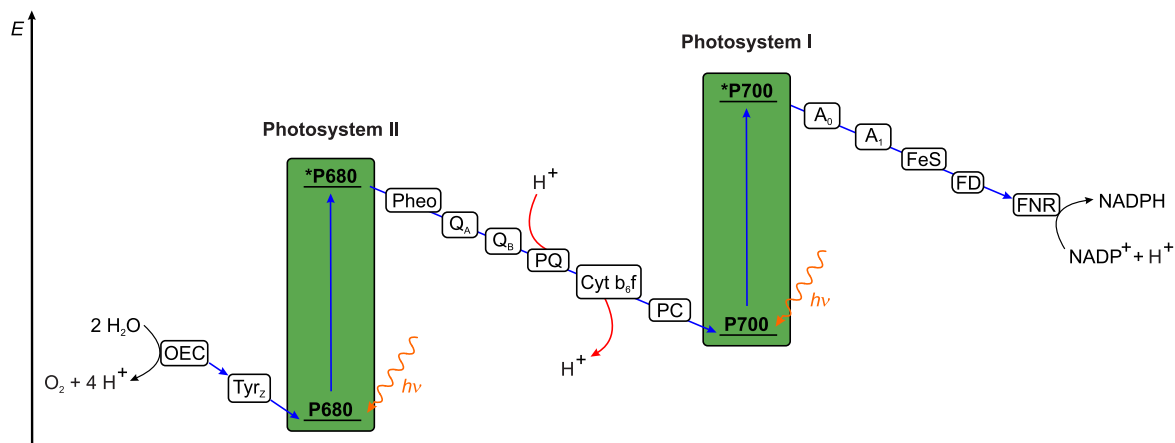


**Scheme 2.3:** Simplified Z-scheme of the light-dependent reaction steps in PS II and PS I. The scheme is based on refs[9, 12, 13]. The abbreviations are explained in the text.

As shown in Scheme 2.3, excitation of P680 results in an excited (singlet) state (P680*), which provides an electron for the reduction of a nearby pheophytin molecule (Pheo). This process generates the radical pair P680$^{\bullet+}$Pheo$^{\bullet-}$, which prevents direct charge recombination by a transfer of the reducing equivalent to a primary plastoquinone electron acceptor

$(Q_A)$.[7, 9] In general, the electron that was transferred to Pheo upon photoexcitation is transported to PS I *via* a stepwise electron-transport chain. The primary plastoquinone acceptor $Q_A$ is firmly bound to the protein structure of PS II and passes the electron on to the secondary plastoquinone electron acceptor $(Q_B)$.[14] Whereas $Q_A$ can only accept one reducing equivalent and does not undergo protonation, $Q_B$ needs to be reduced twice before it can diffuse away from its binding site in PS II into the membrane matrix. During the reduction process, $Q_B$ accepts two protons from the stroma side to form plastoquinol $(PQH_2$, Scheme 2.2). The free $Q_B$ binding site is then occupied by an oxidized plasto-quinol from the plastoquinone pool (PQ).[7, 9] The electron-transport chain continues *via* the Cyt $b_6f$ complex and plastocyanin (PC) until PS I is reached. The protons bound in $PQH_2$ are then released into the lumen, which generates a transmembrane proton gradient usable for ATP synthesis (see Scheme 2.2). In PS I, absorption of a photon leads to the formation of the excited (singlet) state (P700*), which transfers an electron to the primary electron acceptor in PS I $(A_0)$. As in PS II, the reducing equivalent is transported stepwise down a redox gradient. From $A_0$, the electron is passed on to phylloquinone $(A_1)$ and proceeds to the ferredoxin NADP reductase (FNR) *via* different iron-sulfur centers (FeS) and ferredoxin (FD). Finally, the reduction equivalent is used to synthesize the reduced hydrogen carrier NADPH.[9, 13]

As mentioned above, excitation of P680 leads to the formation of $P680^{\bullet+}$, which has a very oxidizing redox potential (1.2 V *vs.* NHE).[4] Due to its redox potential, $P680^{\bullet+}$ can drive the splitting of water in the oxygen evolving complex (OEC), which is incorporated in the protein structure of PS II.[14] A crystal structure of PS II with a resolution of 1.9 Å revealed that the active center of water oxidation is a $Mn_4CaO_5$ cluster, which has a cubane-like structure composed of three manganese, one calcium and four oxygen atoms.[15] The fourth manganese atom and the remaining oxygen atom are located outside the cubane-like structure. In the cluster, the oxygen atoms serve as oxo-bridges between the five metal atoms. Since the oxidizing side of the PS II and the OEC are not directly linked with each other, a nearby tyrosine $(Tyr_z)$ acts as an intermediate electron carrier, which reduces $P680^{\bullet+}$ and then extracts the electrons from the OEC.[9] However, water oxidation is a four electron process and therefore requires the successive absorption of four photons by PS II. With each photon absorption, an oxidized $Tyr_z$ $(Tyr_z^{\bullet})$ is generated, which then accepts an electron from the OEC. This stepwise electron transfer from the $Mn_4CaO_5$ cluster to $Tyr_z^{\bullet}$ was summarized in a so-called S-state cycle by KOK *et al.*.[16] Each S-state ($S_0$ to $S_4$, whereby $S_1$ to $S_4$ are oxidized states) represents a different oxidation state of the $Mn_4CaO_5$ cluster. The model from KOK was extended by DAU and HAUMANN, who reported a more detailed mechanism for water oxidation (Scheme 2.4).[17, 18]
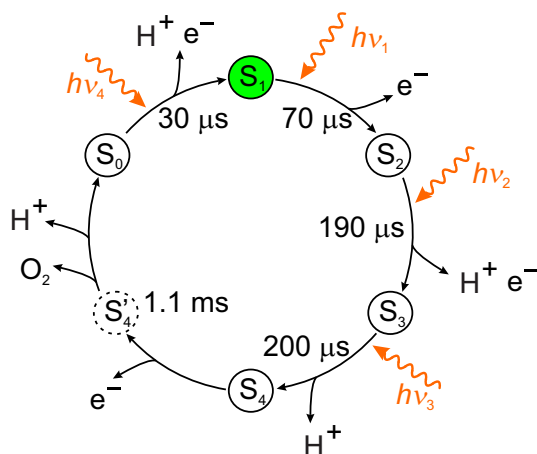
**Scheme 2.4:** Extended S-state cycle for water oxidation as proposed by DAU and HAU-MANN. The cycle starts with the dark-stable resting state $S_1$ (marked in green). Stepwise excitation leads to different oxidation states of the $Mn_4CaO_5$ cluster in the oxygen evolving complex. The half-lives of the S-state transitions are added.[17]

As pointed out in Scheme 2.4, the water oxidation cycle starts with the (long-term) dark-stable resting state $S_1$. The absorption of a first photon induces the release of an electron from the OEC. During the $S_2 \rightarrow S_3$ transition, which takes place after the absorption of a second photon, a proton and an electron are extracted. It is postulated that the proton is most likely removed from the OEC or its ligand environment. Within the third flash, $O_2$ is formed. Therefore, a proton is released to form the $S_4$ state. After the extraction of a further electron, the hypothetical intermediate $S_4'$ is generated, in which four electrons have been extracted from the $Mn_4CaO_5$ cluster. $O_2$ is released during the transition from the $S_4'$ state to the $S_0$ state. Additionally, a proton is extracted in the course of the $S_4' \rightarrow S_0$ transition. The absorption of the fourth photon leads to the transition to the $S_1$ state and therefore closes the cycle. The last absorption goes in hand with the release of a proton and an electron.

## 2.2 The Excited State

The formation of an excited state is a fundamental requirement to investigate the photo-physical and photochemical properties of a given system. The excited state (ES) can be generated from the ground-state (GS) by the uptake of a photon as illustrated in Scheme 2.5. In the frame of this thesis, photoinduced reactions rely on electronic transitions that require photons in the visible region of the electromagnetic spectrum.
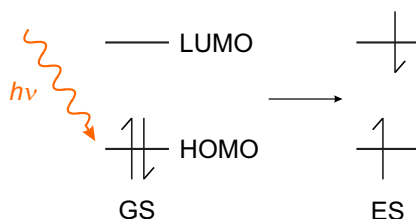


**Scheme 2.5:** Schematic depiction of the formation of an excited state (ES) after the uptake of a photon.

In the given example (Scheme 2.5), an electron of the highest occupied molecular orbital (HOMO) is promoted to the lowest unoccupied molecular orbital (LUMO) to form the excited state. However, the absorption of a photon with a sufficiently high energy can also lead to a population of a higher-energy electronic state. Various selection rules determine whether a transition is allowed.[19, 20] Forbidden transitions can occur, but their molar extinction coefficients will be significantly lower than for allowed transitions. Possible transition and deactivation pathways after photoexcitation are illustrated in a so-called JABLONSKI diagram (Figure 2.1).[21, 22]
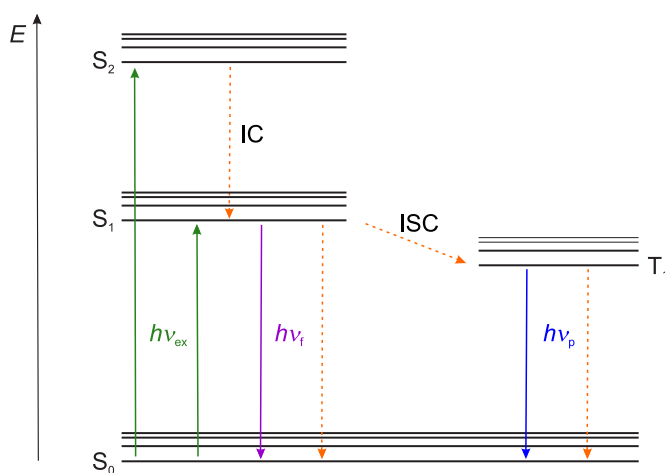


**Figure 2.1:** JABLONSKI diagram of molecular electronic states. Absorptions and radiative transitions (solid lines) and non-radiative transitions (dashed lines) are indicated. The transitions concerning excitation (ex) as well as fluorescence (f) and phosphorescence (p), internal conversion (IC) and intersystem crossing (ISC) are visualized. The diagram is based on refs[21, 22].

The transitions shown in the JABLONSKI diagram can be radiative (solid lines) or non-radiative (dashed lines). First, the promotion of an electron from the singlet ground-state of the system ($S_0$) to a higher excited singlet state ($S_1$, $S_2$) occurs after excitation with a photon. In a given multiplicity, non-radiative internal conversion (IC) to a lower-energy state (here $S_2 \rightarrow S_1$) can occur since the transition is spin-allowed. In contrast, direct excitation of the $S_0$ state to a triplet state (T) is not allowed since this transition is spin-forbidden.[23] However, the population of the lowest energy triplet state ($T_1$) is possible due to non-radiative intersystem crossing (ISC) from the corresponding singlet state ($S_1 \rightarrow T_1$). Although this transition is spin-forbidden, the introduction of heavy atoms will strongly increase its probability due to spin-orbit coupling.[24–27] Relevant heavy atoms in this thesis are ruthenium and iridium (see Chapters 3 and 4) and complexes containing these metals are known for their fast and productive ISC.[28, 29] For systems without heavy atoms, *e.g.* purely organic molecules (see Chapter 5), slow ISC rates can be expected. Deactivation of the excited state back to the ground-state can occur thermally (and non-radiatively) or by emission of a photon. However, significant luminescence is only observable from the lowest excited state of a given multiplicity ($S_1$, $T_1$), as stated by KASHA.[27] This implies that the excited state will undergo internal conversion until the lowest excited state is reached within a multiplicity. If the lowest accessible excited state is a singlet, the luminescence is called fluorescence and the transition is spin-allowed. In case of a triplet state, the transition to the ground-state is spin-forbidden and the emission is called phosphorescence. The fact that decay from the $T_1$ state to the $S_0$ state is forbidden leads to longer radiative excited state lifetimes of the triplet state.[28] A longer lifetime of an excited state facilitates interaction with another molecule before the deactivation to the ground-state occurs. Such an interaction can be either energy or electron transfer. In the context of this thesis, the relevant quenching mechanism is electron transfer and the possible mechanisms are illustrated in Scheme 2.6.[30]
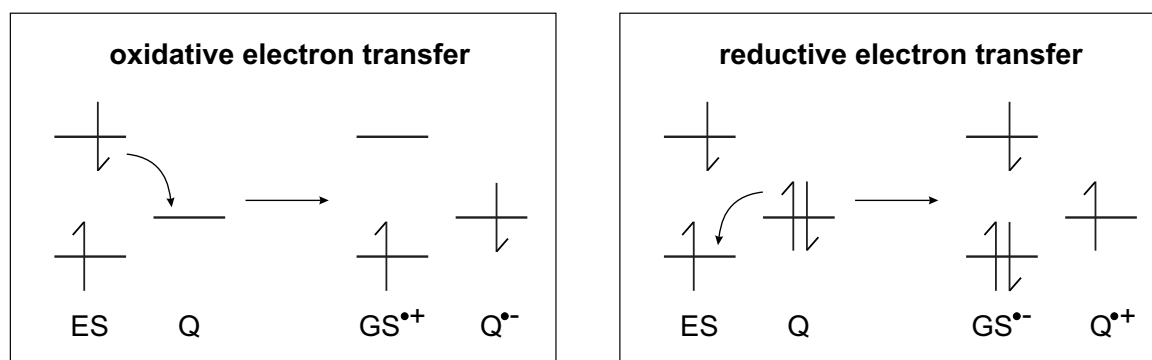


**Scheme 2.6:** Quenching of the excited state by oxidative electron transfer (left) and reductive electron transfer (right).[30]

In an oxidative electron transfer mechanism, the electron of the higher excited state orbital is transferred to an electron-poor quencher (Q), leading to an oxidized ground-state (GS$^{\cdot+}$) and a reduced quencher (Q$^{\cdot-}$) (Scheme 2.6, left part). The excited state acts as a reducing agent in this mechanism, whereas it functions as an oxidizing agent in the course of reductive electron transfer (Scheme 2.6, right part). Here, an electron of an electron-rich quencher is accepted by the low-energy hole left by the promoted electron, which oxidizes the quencher (Q$^{\cdot+}$). Electron transfer processes proceeding from the excited state of a photoactive system can enable reactions that would not be possible from the ground-state. This is attributable to a stronger oxidation and reduction potential of the excited state than in the ground-state as indicated in the LATIMER diagrams of the photosensitizers relevant to this thesis, Ru(bpy)$_3$$^{2+}$ and Ir(bpy)(dF-CF$_3$-ppy)$_2$$^+$ (Figure 2.2).[28, 31]
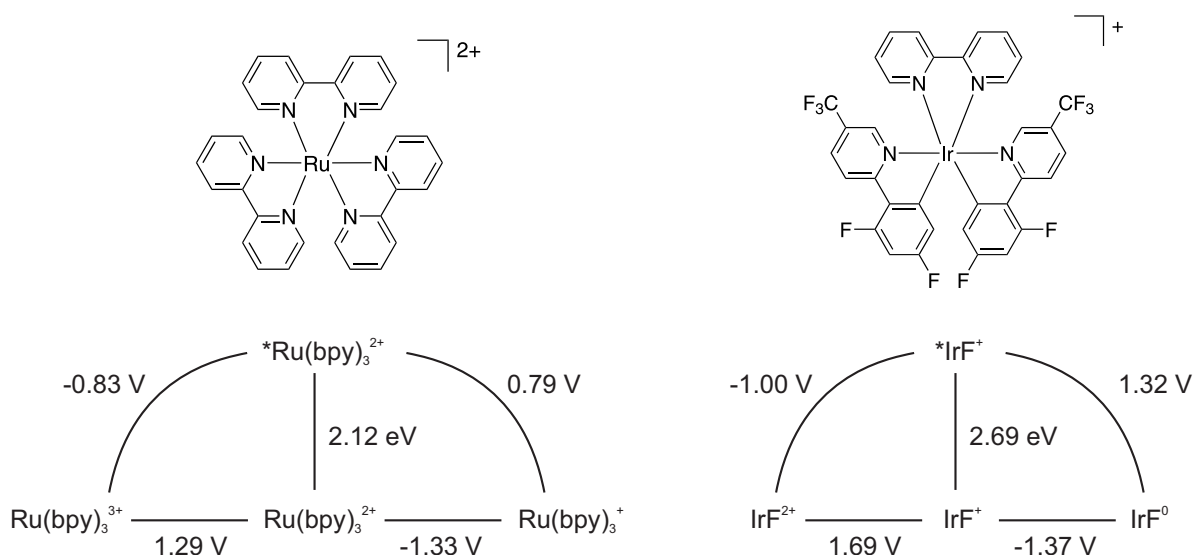


**Figure 2.2:** LATIMER diagrams of Ru(bpy)$_3$$^{2+}$ (left) and Ir(bpy)(dF-CF$_3$-ppy)$_2$$^+$ (right, the abbreviation IrF was used for clarity) photosensitizers. The stated redox potentials are given *vs.* SCE and in CH$_3$CN.[28, 31, 32]

In both photosensitizers, which have a d$^6$ low-spin configuration, electron transfer from the excited state proceeds *via* an $^3$MLCT state as visualized in Scheme 2.7.[28] In the ground-state of the complexes, the HOMO ($t_{2g}$) is metal-based, whereas the LUMO ($\pi^*$) belongs to the ligand. Photoexcitation induces a metal-to-ligand charge transfer (MLCT). The formed $^1$MLCT state undergoes intersystem crossing to yield an $^3$MLCT state, which participates in electron-transfer reactions.
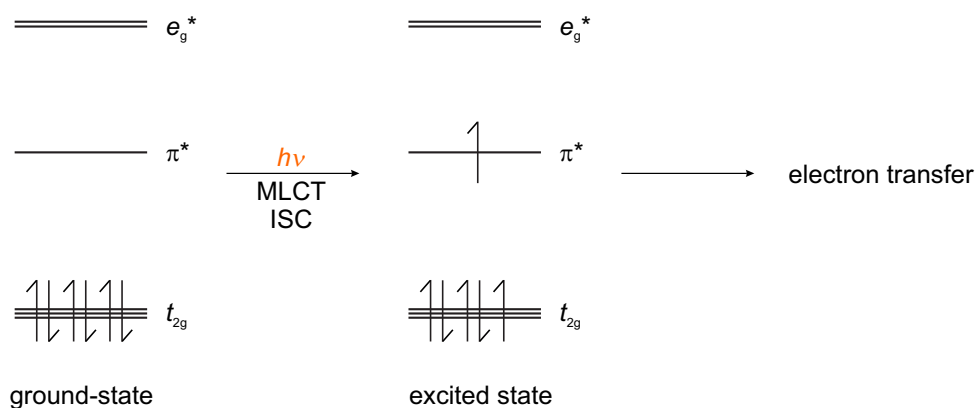
**Scheme 2.7:** Simplified representation of molecular orbitals of the octahedral $d^6$ low-spin $Ru(bpy)_3{}^{2+}$ complex, before and after photoexcitation.[28]

## 2.3 Electron-Transfer Reactions

Electron-transfer reactions can be divided into (i) outer-sphere electron transfer or (ii) inner-sphere electron transfer.[33] In case of an outer-sphere electron transfer between two redox centers, the reactants are not covalently linked and rely on the formation of a so-called close contact outer-sphere complex to enhance the weak electronic coupling between the electron donor (D) and the electron acceptor (A). It needs to be noted that the formation of such a complex and the subsequent electron transfer do not involve any bond cleavage or bond formation processes. However, in the course of an electron-transfer event, bond lengths and bond angles of the reactants in the complex need to be adapted. Additionally, reorganization of the solvent molecules surrounding the redox centers needs to take place. Both adjustments lead to an increase of the activation barrier for electron transfer and have therefore an influence on the electron-transfer rate ($k_{ET}$). A theoretical explanation on electron-transfer rates of outer-sphere self-exchange reactions was established by RUDOLPH A. MARCUS in the 1950s and is referred to as the classical MARCUS theory.[34–37] NOEL S. HUSH extended this theory to inner-sphere electron-transfer reactions.[38, 39] In the case of inner-sphere electron transfer, the two redox centers are covalently linked by a bridging ligand or atom, which facilitates the transfer of an electron. The MARCUS-HUSH theory is also known as the semi-classical MARCUS theory and describes the electron-transfer rate as stated in Equation 2.1.[40]

$$k_{ET} = \sqrt{\frac{\pi}{\hbar^2 \lambda k_B T}} \cdot H_{DA}{}^2 \cdot exp\left(-\frac{(\lambda + \Delta G_{ET}^0)^2}{4\lambda k_B T}\right) \tag{2.1}$$

According to Equation 2.1, three parameters determine the electron-transfer rate: (i) The reorganization energy ($\lambda$), (ii) the electronic coupling between the donor and the acceptor ($H_{DA}$) and (iii) the reaction free energy ($\Delta G_{ET}^0$). $\lambda$ and $\Delta G_{ET}^0$ are visualized in the potential energy surface picture for non-adiabatic electron transfer shown in Figure 2.3 (based on refs[41–43]). The potential energy surfaces respond to changes in the electronic coupling between the reactants. If there is no electronic coupling, the energy surfaces of the initial state (D-A) and the final state (D$^{\cdot+}$-A$^{\cdot-}$) intersect, but no electron transfer is possible. Electronic interaction in the D-A system leads to a splitting of the potential energy surfaces (solid lines in Figure 2.3). In case of a weak electronic coupling, the splitting is small (Figure 2.3, left part, inset) and the reaction from the ground-state to the charge-separated state can take place after the uptake of external energy to overcome the activation barrier (given by $\Delta G^{\ddagger}$) since the system needs to pass through the intersection surface. Thus, the D$^{\cdot+}$-A$^{\cdot-}$ state is formed non-adiabatically. However, the potential energy surface splitting is more pronounced for strong electronic couplings and leads to an upper and a lower potential energy surface (solid lines in Figure 2.3, right part). The

reaction will proceed along the lower potential energy surface and the product state is formed adiabatically. The reaction is therefore independent of the electronic coupling, which is why Equation 2.1 is only valid for non-adiabatic electron transfer. In the frame of this thesis, the electron-transfer reactions are treated as non-adiabatic.
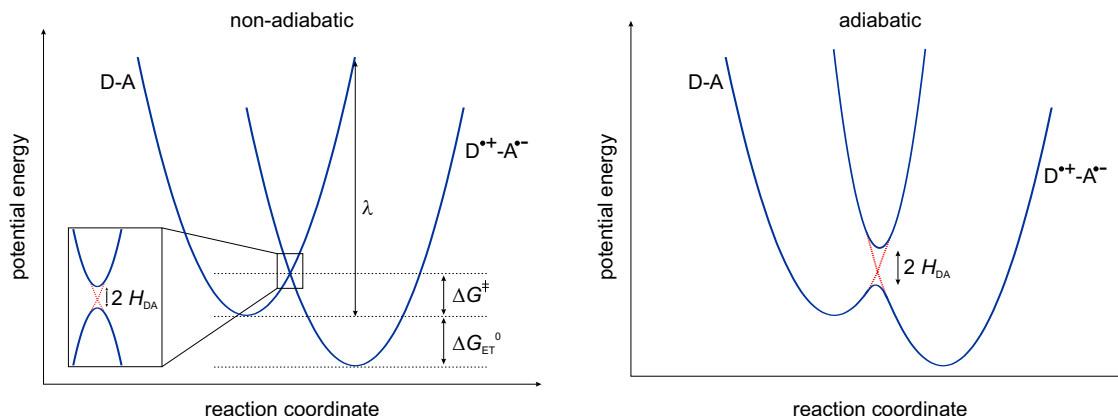


**Figure 2.3:** Schematic potential energy surfaces of non-adiabatic (left) and adiabatic (right) electron transfer in a donor-acceptor system with relevant parameters for the electron-transfer rate. The figures are based on refs[41–43].

## Reorganization Energy

As mentioned above, electron-transfer reactions are accompanied by reorganization processes to adjust to the geometrical changes in the course of an electron-transfer event.[33, 44] The energy involved in these processes is called reorganization energy. The overall reorganization energy ($\lambda$) can be divided into an inner-sphere ($\lambda_i$) and an outer-sphere ($\lambda_o$) reorganization energy (Equation 2.2), whereby $\lambda_o$ usually makes the dominant contribution for reactions in solution.

$$\lambda = \lambda_i + \lambda_o \tag{2.2}$$

$\lambda_i$ is often treated as a distance-independent parameter and refers to adjustments of the donor-acceptor molecule, *i.e.* bond lengths and bond angles. The reorganization of the chemical environment of the molecule, like solvent molecules, is reflected by $\lambda_o$, which is strongly dependent on distances and the solvent polarity (Equation 2.3).

$$\lambda_o = (\Delta e)^2 \cdot \left( \frac{1}{2r_D} + \frac{1}{2r_A} - \frac{1}{r_{DA}} \right) \cdot \left( \frac{1}{D_{op}} - \frac{1}{D_s} \right) \tag{2.3}$$

Equation 2.3 includes the charge transferred from the donor to the acceptor moiety ($\Delta e$) and the optical and static dielectric constants of the solvent ($D_{op}$ and $D_s$). $D_{op}$ can also

be described as the square of the refractive index of the solvent, *i.e.* $D_{op} = \eta^2$. The distance dependence is reflected by the radii of the (spherical) donor ($r_D$) and acceptor ($r_A$) units and the center-to-center separation distance between these moieties ($r_{DA}$). An example of the outer-sphere reorganization energy as a function of $r_{DA}$ is given in Figure 2.4 for CH$_3$CN as a solvent ($D_s = 35.7$, $\eta = 1.3341$) and with radii of the spherical donor and acceptor units of 4 Å.[44]
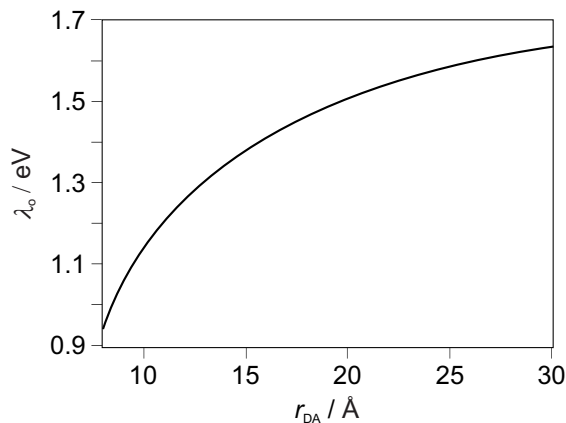


**Figure 2.4:** Distance dependence of the outer-sphere reorganization energy in CH$_3$CN ($D_s = 35.7$, $\eta = 1.3341$) with spherical donor and acceptor radii of 4 Å.[44]

## Electronic Coupling

Electronic coupling between the donor and the acceptor units ($H_{DA}$) displays the interaction between the distant redox partners. Electronic coupling is a necessary requirement for electron-transfer reactions and $H_{DA}$ defines the amount of splitting between the reactant and product potential energy surfaces (see above and Figure 2.3). Even at greater distances, $H_{DA}$ can be non-zero since covalent linkers or solvent molecules between the donor and acceptor units can mediate long-range electronic coupling, according to superexchange theory.[45] For non-adiabatic reactions, *i.e.* weak electronic coupling, $H_{DA}$ is determined by the electronic coupling between the reactants at contact distance ($H_{DA}{}^0$), the distance decay parameter ($\beta$), the donor-acceptor distance ($r_{DA}$) and the contact distance of donor and acceptor ($r_0$) (Equation 2.4).[44]

$$H_{DA}(r_{DA}) = H_{DA}^0 \cdot exp(-\beta(r_{DA} - r_0)) \tag{2.4}$$

It is clear from Equation 2.4 that $H_{DA}$ is a distance-dependent parameter and $\beta$ therefore determines how strong $H_{DA}$ depends on the distance. $H_{DA}$ usually deceases exponentially with increasing $r_{DA}$. Since the electron-transfer rate is proportional to $H_{DA}{}^2$ (Equation
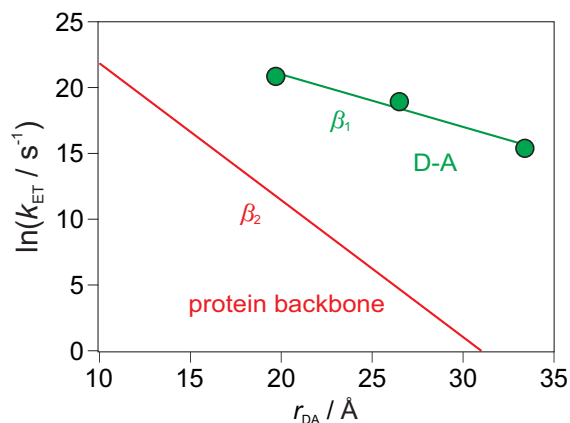
**Figure 2.5:** Distance dependence of the electron-transfer rate in a protein backbone (red) and a donor-acceptor system (green).[46, 47] The slopes correspond to the different distance decay parameters.

2.1), $k_{ET}$ must decrease as a consequence, if the donor-acceptor distance is increased (Figure 2.5).

# Reaction Free Energy

As shown in the potential energy surface picture of non-adiabatic electron transfer (Figure 2.3, left part), the reaction free energy ($\Delta G_{ET}^0$) is the difference in energy between the reactant and the product potential energy surface minima. The negative reaction free energy (-$\Delta G_{ET}^0$) is referred to as the driving force of an electron-transfer reaction. The dependence of the electron-transfer rate on the driving force is visualized in Figure 2.6. Based on MARCUS theory, three regions for electron transfer are accessible: (i) Normal regime, (ii) activationless electron transfer and (iii) inverted regime.[33, 40] In the normal regime (-$\Delta G_{ET}^0 < \lambda$), an activation barrier between the reactant and product potential energy surfaces needs to be overcome in the course of electron transfer. This barrier decreases if the driving force is increased, *i.e.* $k_{ET}$ increases with an increasing driving force. The increase of $k_{ET}$ is observable until the driving force equals the reorganization energy. Here, maximal $k_{ET}$ is reached and electron transfer proceeds activationlessly. A further increase of the driving force is followed by a decrease of $k_{ET}$ and entails the occurrence of an increasing activation barrier with increasing driving force. This region, where -$\Delta G_{ET}^0 > \lambda$, is called the inverted regime.
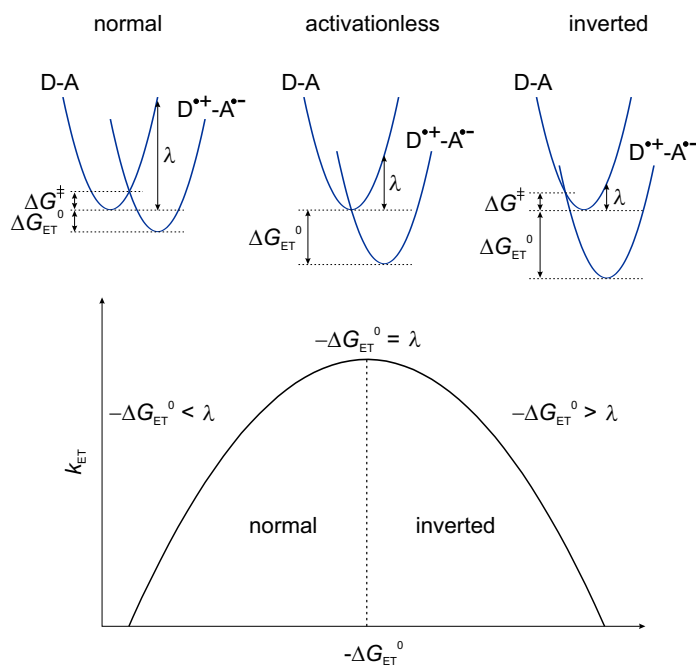
**Figure 2.6:** Simplified dependence of the electron-transfer rate on the driving force, including the different regions of the MARCUS theory of electron transfer. The figure is based on ref[40].

## 2.4 Two-Pulse Laser Experiments

At present, two-pulse laser experiments (either realized by traditional two-pulse laser flash photolysis or by pump-pump-probe spectroscopy) are becoming more important to initiate and study photochemical processes. The double excitation approach allows it to obtain more detailed information about processes and mechanisms than obtainable from single-pulse experiments.[48, 49] Excitation with two pulses can also lead to new chemical processes, unachievable by conventional excitation.[49, 50] This is mainly due to the fact that the exclusively formed excited states, like excited radical ions, show different reactivities than in the ground-state, *e.g.* higher redox abilities.[51] Additionally, high-energy excited states can be reached that are not accessible by one-photon excitation.[52, 53] The general working principle of two-pulse laser experiments is illustrated in Figure 2.7.[50, 54]
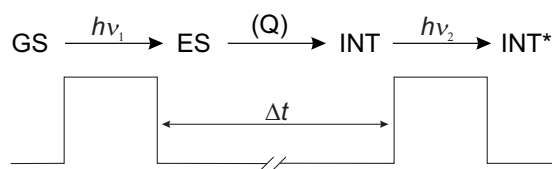


**Figure 2.7:** Schematic illustration of the two-pulse method based on refs[50, 54].

The ground-state (GS) is excited with a first laser pulse to produce the (reaction) intermediate (INT). The formation of the INT species, which can for example be a radical (ion) or the lowest triplet state of the GS species, occurs either directly over the locally excited state of GS (ES) or a quencher (Q) is added to get from ES to the INT species. Since the first laser pulse has a synthetic purpose, it can also be called the 'preparation pulse' or 'actinic pulse'. After a delay time ($\Delta t$), the second laser pulse is applied to study the photochemistry of the intermediate, as INT* is generated by that pulse (Figure 2.7). This pulse can also be called the 'investigation pulse'. Since the intermediate and the ground-state species usually show spectral differences, the excitation wavelength of the second pulse can be chosen selectively to ensure only excitation of the intermediate. The following parameters can be varied in the course of a two-pulse experiment: (i) The delay time, (ii) the laser wavelengths and their intensities, (iii) if necessary, a quencher can be added to convert the GS species into the desired intermediate. The optimization of the experimental conditions is crucial in two-pulse laser experiments. For example, in a multicomponent system, composed of a photosensitizer, a reversible electron donor and the methylviologen dication ($MV^{2+}$), successful light-driven two-charge accumulation on $MV^{2+}$ can only be achieved when a high concentration of the first charge-separated state (CSS) $MV^{\cdot+}$ is present before the second laser pulse is applied.[55] Additionally, the wavelength of the second pulse needed to be chosen in a way that no direct excitation of

$MV^{\cdot +}$ was possible since the electron transfer in the given charge accumulation process relied on quenching of the excited photosensitizer by the added electron donor.

Multiple-pulse experiments, whereby mainly two-pulse experiments are used, have three main applications: (i) They can be used to generate higher excited singlet and triplet states as well as excited radicals, which can then be investigated concerning excited state behavior and dynamics, subsequent reactions and lifetimes.[49, 50, 54, 56–58] (ii) Such experiments can also be used to achieve dissociation or fragmentation of highly excited species *via* bond cleavage or photoionization.[48, 59–65] In particular, photoionization is an interesting field of application since hydrated electrons can be generated, which are extremely strong reductants. One way to generate hydrated electrons is by excitation with two photons below 400 nm.[48, 61] Here, the preparation pulse produces a neutral or anionic radical which undergoes photoionization after the second pulse. In the case of the anionic radical, a quencher needed to be added. Optimization of the latter mechanism towards a sustainable production of hydrated electrons can be reached with green light while a ruthenium complex catalyst and a bioavailable sacrificial electron donor are used in the overall photoionization process.[62, 66] Recently, a water-soluble iridium catalyst was reported as a sustainable hydrated electron source after absorption of two visible photons, which is applicable for challenging lab-scale reductions.[63] (iii) Additionally, electron and energy transfer reactions in molecular donor-acceptor systems, like dyads, triads or tetrads, can be performed and investigated with two-pulse excitation.[52, 67–71] Within the frame of this thesis, two-pulse laser experiments are applied to molecular triads, hence a more detailed description of the application of two-pulse experiments is limited to selected examples of twofold light-induced electron transfer in donor-acceptor arrays.

Wasielewski *et al.* reported femtosecond two-pulse experiments for a molecular donor-acceptor dyad and a molecular donor-acceptor-acceptor triad (Figure 2.8), which were tested for their ability to function as molecular switches.[52] Both arrays contained a 4-aminonaphthalene-1,8-dicarboximide chromophore (ANI), which acted as an electron donor, and a naphthalenediimide (NI) acceptor, connected by a *p*-xylene bridge. In the case of the triad, an additional pyromellitimide (PI) acceptor was directly linked to the NI unit. In both compounds, the first laser flash at 416 nm directly excited the charge transfer transition of the ANI chromophore. Subsequent electron transfer from the excited ANI moiety to the NI acceptor produced an ion pair, whose fate was controlled by the second laser flash at 480 nm after a time delay of 3 ns (Figure 2.8). At 480 nm, selective excitation of the $NI^{\cdot -}$ species occurred. It was observed for the dyad that the second photon rapidly switched the formed state back to the locally excited state on ANI ($^{1*}$ANI-NI). However, the second pulse in the triad resulted in the CSS $ANI^{\cdot +}$-NI-$PI^{\cdot -}$ since the pulse provided the necessary energy to transfer the electron from the reduced NI unit to PI. This electron-

transfer step is significantly faster than the switching to the locally excited state on ANI. The two-pulse experiments of WASIELEWSKI *et al.* showed that it is possible to control the movement of electrons within the given arrays on a femtosecond time scale.
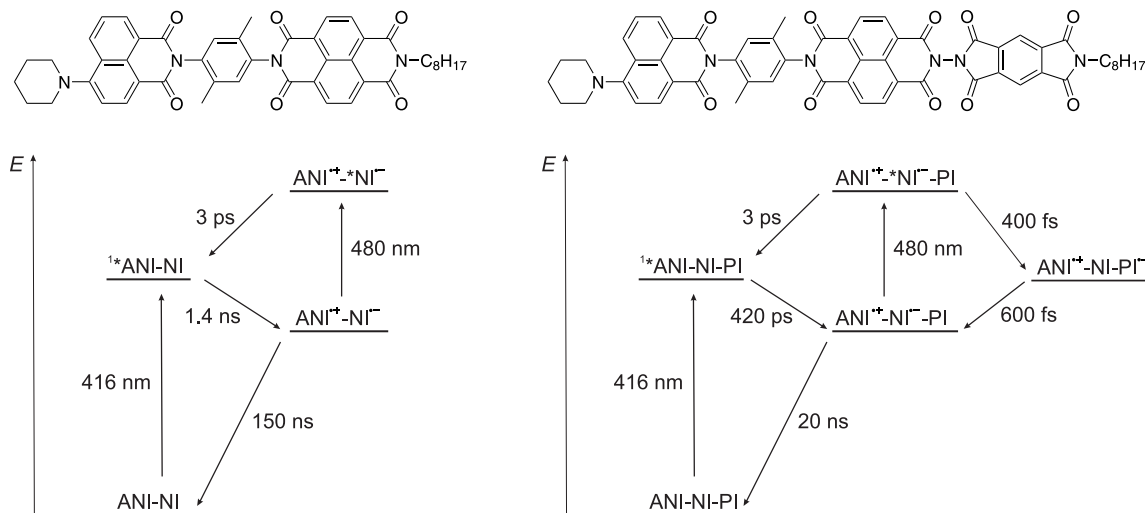


**Figure 2.8:** Left: Molecular structure of the ANI-NI dyad and schematic energy diagram showing the relevant excited states and CSSs after twofold photoexcitation. Right: Molecular structure of the ANI-NI-PI triad and schematic energy diagram showing the relevant excited states and CSSs after twofold photoexcitation. Schematic diagrams are adapted from ref[52].

A few years later, WASIELEWSKI *et al.* published an investigation on a molecular tetrad TMPD-6PMI-ZnP-PI (Figure 2.9) and its gating behavior.[67] The tetrad was comprised of two donor-acceptor pairs (TMPD-6PMI and ZnP-PI), covalently linked by a phenyl spacer.

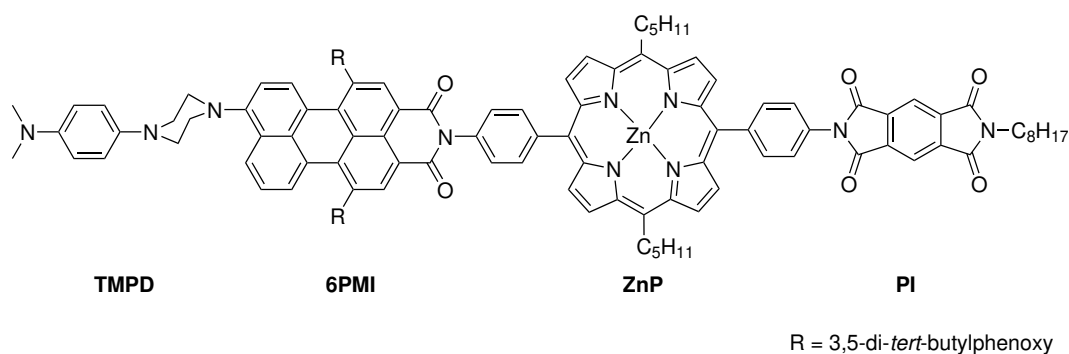

**Figure 2.9:** Molecular structure of TMPD-6PMI-ZnP-PI.

Each donor-acceptor pair could be selectively excited. Excitation of the 6PMI unit was performed at 540 nm and afforded the CSS TMPD$^{\cdot+}$-6PMI$^{\cdot-}$, which underwent rapid

thermal charge recombination ($\tau$ = 55 ps) back to the ground-state. The CSS ZnP$^{\bullet+}$-PI$^{\bullet-}$ was obtained after excitation of the ZnP unit at 420 nm and recombination to the ground-state occurred in 320 ps. One-pulse excitation of the tetrad therefore resulted in a so-called 'off' state. However, subsequent excitation with a second pulse to excite the second donor-acceptor pair formed a long-lived distal ion pair TMPD$^{\bullet+}$-6PMI-ZnP-PI$^{\bullet-}$, which represented the so-called 'on' state. The reversible formation of this long-lived CSS only occurred when two excitation pulses were applied to the tetrad (see also Chapter 5).

Wenger *et al.* used the two-pulse technique to explore the fundamentals important for charge accumulation.[68] In 2016, they reported a molecular pentad (Figure 2.10) which was able to form a long-lived electron accumulated state without the use of sacrifical reagents after (intense) visible light excitation, but such examples are scarce.[72] In such a compound, undesired reaction channels are opened after the absorption of a second photon, which can inhibit successful charge accumulation. To gain more insights into those undesired processes, Wenger *et al.* used a molecular triad (Figure 2.10), which is structurally similar to the pentad, to trigger and study these processes in isolation since the triad cannot undergo charge accumulation. The triad is comprised of a triarylamine (TAA) electron donor, a ruthenium photosensitizer and an anthraquinone (AQ) electron acceptor.
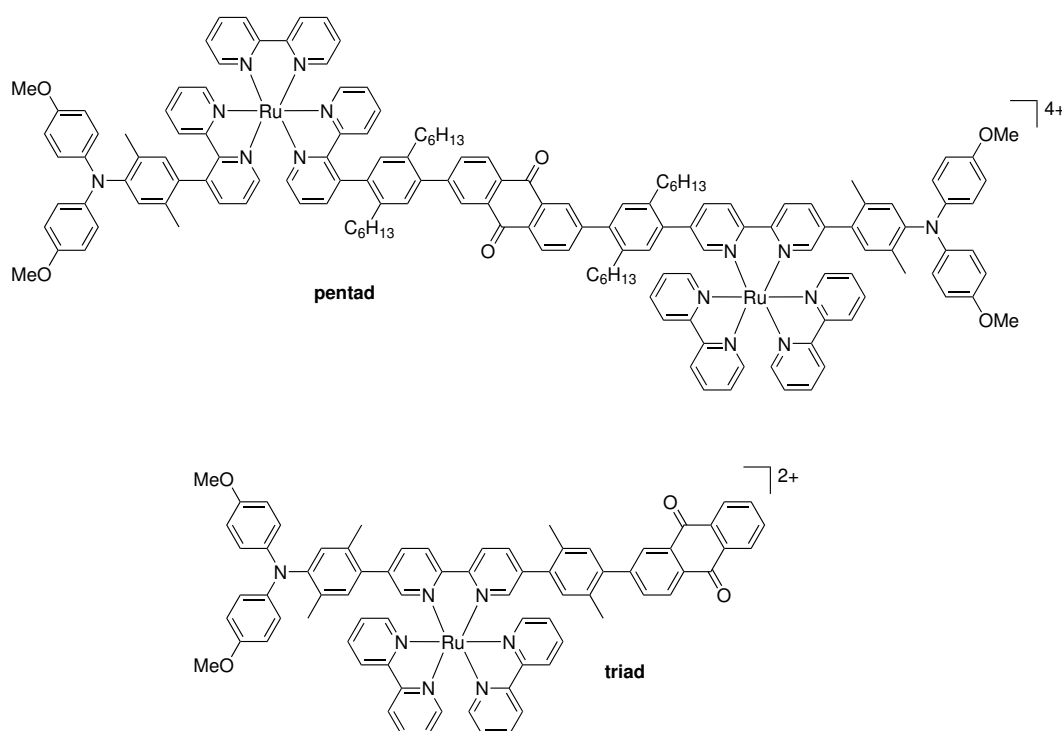


**Figure 2.10:** Molecular structure of the pentad that undergoes charge accumulation and the triad that was used to investigate the fundamentals of light-induced charge accumulation.

The preparation pulse at 532 nm served to produce the CSS of the triad, composed of an oxidized TAA ($TAA^{\cdot+}$) unit and a reduced AQ ($AQ^{\cdot-}$) moiety. Formation of this state was possible due to an intramolecular electron-transfer process. With the second pulse, selective excitation of the $AQ^{\cdot-}$ moiety at 580 nm or selective excitation of the $TAA^{\cdot+}$ unit at 810 nm was performed after a time delay of 400 ns. In both cases, rapid reverse electron transfer to the ground-state of the triad was induced by the second pulse. This means that the excitation of the radical ion species caused a light-induced charge recombination between $AQ^{\cdot-}$ and $TAA^{\cdot+}$. Here, two-pulse experiments gave direct evidence for a process that can hamper light-induced charge accumulation. A similar observation was also reported by WASIELEWSKI et al. in the context of molecular switches as stated above.

The importance of the structural design of molecular systems for two-pulse laser experiments manifests in a recently reported study by AUKAULOO et al..[69] With the molecular dyad $H_2P$-$Ru_{cat}$ (Figure 2.11), charge accumulation in presence of a reversible electron acceptor was intended, as well as investigations of the mechanism of charge transfer and the elemental steps leading towards charge accumulation. The dyad consists of a porphyrine photosensitizer and a ruthenium-based catalyst. $MV^{2+}$ was used as an electron acceptor.



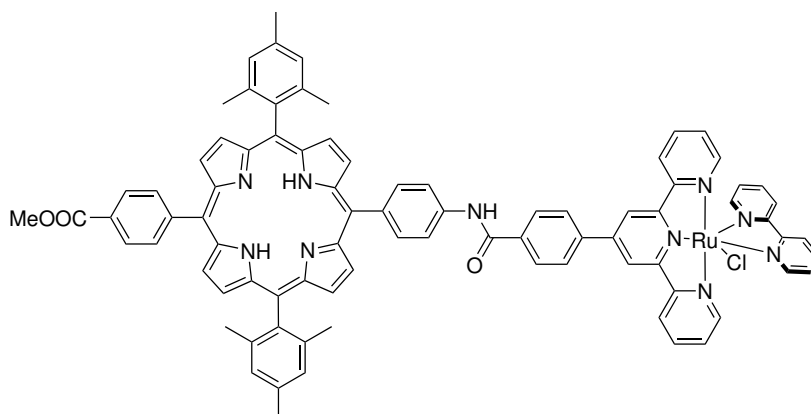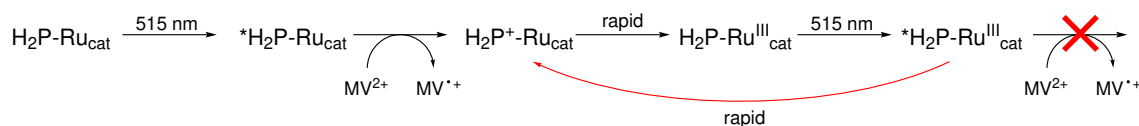**Figure 2.11:** Molecular structure of $H_2P$-$Ru_{cat}$.

However, no charge accumulation was observed after twofold excitation of $H_2P$-$Ru_{cat}$ with visible light. The proposed reaction behavior is summarized in Scheme 2.8.



**Scheme 2.8:** Proposed reaction behavior of $H_2P$-$Ru_{cat}$ upon twofold excitation. Mechanism adapted from ref[69].

With the first pulse, the porphyrin chromophore was excited and the excited state was then quenched by $MV^{2+}$ to yield $MV^{\cdot+}$ and $H_2P^+$-$Ru_{cat}$. However, $H_2P^+$-$Ru_{cat}$ was not the final intermediate of the preparation pulse since it undergoes rapid intramolecular charge transfer to form $H_2P$-$Ru^{III}_{cat}$. Application of the second pulse on the final intermediate $H_2P$-$Ru^{III}_{cat}$ did not result in desired charge accumulation since the excited state *$H_2P$-$Ru^{III}_{cat}$ performed a rapid intramoleclar electron transfer, instead of intermolecular quenching with $MV^{2+}$, to yield $H_2P^+$-$Ru_{cat}$, which then converted to the final intermediate of the first pulse $H_2P$-$Ru^{III}_{cat}$. AUKAULOO *et al.* explained their observation with a rapid reverse electron transfer upon secondary excitation, combined with a low driving force of the forward photodriven electron-transfer reaction. Those results underline the importance of an appropriate molecular design for two-pulse experiments. In particular, it needs to be considered that the driving force for forward electron transfer after secondary excitation is high enough for the anticipated reaction to occur. Additionally, stabilization of the charge transfer states could help to avoid reverse electron transfer.

In summary, two-pulse laser experiments are a powerful tool to gain more knowledge about highly excited states and processes relevant for artificial photosynthesis and solar energy conversion. However, an appropriate molecular design and the choice of the experimental parameters are crucial to obtain meaningful results. It needs to be noted that radical anions as intermediates, which are produced by the preparation pulse, can also be formed *via* pulse radiolysis[51, 73, 74] or (electro)chemically.[51, 75, 76] Here, the 'second' pulse still serves to investigate the fate of the intermediate upon secondary excitation.

# 3 Influence of the Driving Force on the Distance Dependences of Electron-Transfer Rates

Finding alternatives for fossil fuels is of key importance to cover current and future energy demands since the resources are known to be limited and the combustion of fossil fuels has a negative impact on the climate.[3] In comparison, the sun would be a 'greener' and more sustainable energy source. However, to ensure efficient solar energy conversion and storage, distinct knowledge about the distance dependence of electron-transfer rates is desirable since long-range electron transfer plays a crucial role in photosynthesis.[77–79] An increase of the distance between two reactants is normally followed by a decrease of the electron-transfer rate.[46, 47, 80–83] However, a regime in which the rate constants for electron transfer increase with increasing distance was predicted in two early theory papers by SUTIN and TACHIYA and can be understood in the framework of MARCUS theory (see also Chapter 2.3).[84, 85] To illustrate and explain this matter, so-called MARCUS parabolas for different donor-acceptor distances ($r_{DA}$) are schematically shown in Figure 3.1 (left part).
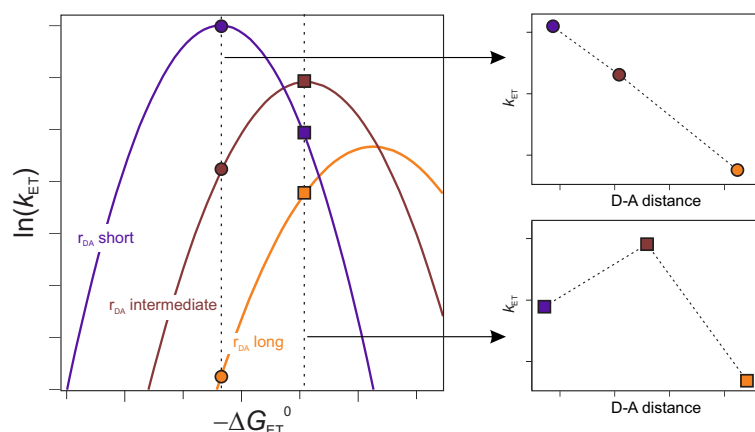


**Figure 3.1:** Left: Schematic driving force dependence of the electron-transfer rate for different donor-acceptor distances with a high driving force (squares) and a low driving force (circles). Right: Schematic distance dependence of $k_{ET}$ with a low driving force (upper graph) and a high driving force (lower graph).

In general, MARCUS parabolas exhibit a Gaussian dependence of electron-transfer rates ($k_{ET}$) on driving forces ($-\Delta G_{ET}^0$), which are negative reaction free energies, for constant donor-acceptor distances.[33] Each parabola shows a maximal $k_{ET}$ when $-\Delta G_{ET}^0$ equals the reorganization energy ($\lambda$). Here, electron transfer is activationless. When $-\Delta G_{ET}^0 < \lambda$, an increase of $k_{ET}$ with increasing driving force can be observed in the so-called normal regime. However, $k_{ET}$ decreases with increasing driving force when $-\Delta G_{ET}^0 > \lambda$, and this is known as the so-called inverted regime.[86–88] An increase of $r_{DA}$ results in a shift of the parabolas to the bottom right of Figure 3.1. Besides $\Delta G_{ET}^0$, $k_{ET}$ is dependent on the reorganization energy ($\lambda$) and the electronic coupling between donor and acceptor ($H_{DA}$).[33, 89] $H_{DA}$ usually decreases exponentially when $r_{DA}$ increases, which leads to an exponentially decrease of $k_{ET}$ in the tunneling regime.[46, 80, 90, 91] This shifts the parabolas down. The shift to the right can be explained by an increase of the (outer-sphere) reorganization energy. An increase of $r_{DA}$ causes more isolated point charges, which result in an increase of $\lambda$.[92] Since a maximal $k_{ET}$ is reached when $-\Delta G_{ET}^0 = \lambda$, the parabolas shift to higher driving forces and therefore to the right. Thus, the combination of an increasing $\lambda$ and a decreasing $H_{DA}$ with increasing $r_{DA}$ results in the shifts shown in Figure 3.1.

In a given donor-photosensitizer-acceptor triad, the driving force can be seen as essentially constant if $r_{DA}$ is increased (vertical dotted lines in Figure 3.1). Depending on the driving force of the triad, different behaviors can occur as indicated in the parabola picture. Low driving forces are in agreement with the usually observed constant decrease of $k_{ET}$ with increasing donor-acceptor distance (Figure 3.1, upper right). However, it is indicated for high driving forces that $k_{ET}$ increases before a decrease can be observed (lower right in Figure 3.1). This predicted counterintuitive behavior was experimentally observed for the first time by WENGER et al. in 2016 in covalently linked donor-photosensitizer-acceptor triads.[93, 94] The first of their triads that displayed the counterintuitive behavior is shown in Figure 3.2. After a first elongation of the donor-acceptor distance, an increase in $k_{ET}$ for thermal charge recombination was observed. Further increase of $r_{DA}$ resulted in a decrease of $k_{ET}$. The observations were explained by a changeover from inverted to barrierless electron transfer, after the first elongation step, to normal electron transfer after the second elongation of the donor-acceptor distance.
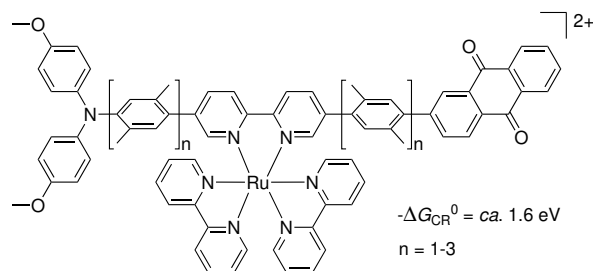
**Figure 3.2:** Molecular structure and driving force of the first donor-photosensitizer-acceptor triad that showed counterintuitive behavior after a first elongation step.

To increase the understanding of this counterintuitive phenomenon, systematic investigations regarding the influence of the driving force on the distance dependence of electron-transfer rates were performed in the project presented in this chapter. Therefore, two sets of molecular triads were designed in which the donor-acceptor distances could be increased by symmetrical addition of *p*-xylene spacers (Figure 3.3). The triads have either a significantly lower driving force for thermal charge recombination (*ca.* 1.2 eV in TAA-ph$_n$-Ru-ph$_n$-NDI) or a higher driving force (*ca.* 2.0 eV in TPA-ph$_n$-Ir-ph$_n$-AQ), compared to a reported triad by WENGER *et al.* with a driving force of roughly 1.6 eV (Figure 3.2).[93] It is intended to observe the usually expected decrease of the electron-transfer rate when going to a significantly lower driving force. The set of triads with even higher driving forces should show similar behavior as reported by WENGER *et al.* since electron transfer is expected to occur in the inverted region for the shortest triad.
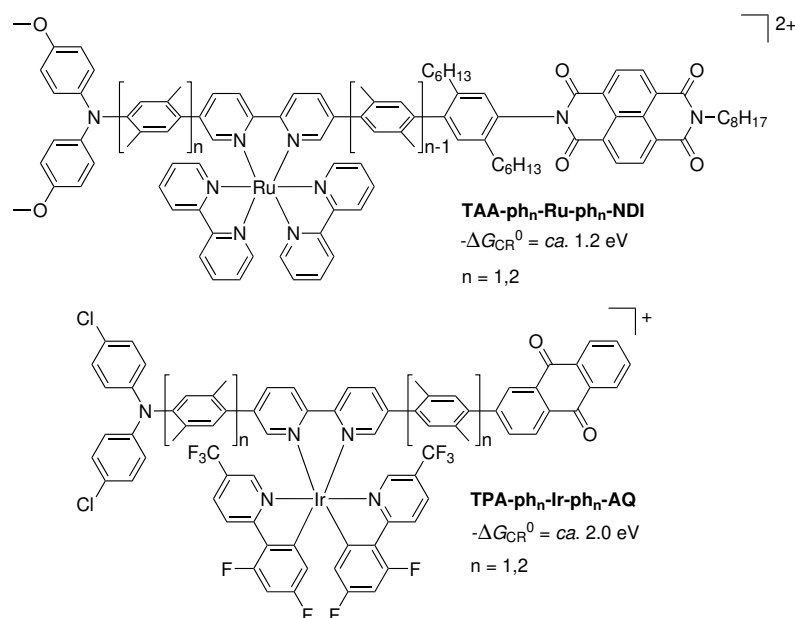


**Figure 3.3:** Molecular structures of the investigated triads TAA-ph$_n$-Ru-ph$_n$-NDI and TPA-ph$_n$-Ir-ph$_n$-AQ in this chapter. Driving forces for thermal charge recombination are added.

The studies on the triads in Figure 3.3 confirm the view that highly exergonic electron-transfer reactions can exhibit fundamentally different distance dependences than the more commonly investigated weakly exergonic electron transfers. In TAA-ph$_n$-Ru-ph$_n$-NDI, the electron-transfer rate for thermal charge recombination decreases with increasing donor-acceptor distance. However, the electron-transfer rate in TPA-ph$_n$-Ir-ph$_n$-AQ increases with increasing donor-acceptor distance. This is attributable to a changeover from the inverted regime to activationless electron transfer, for the triad with a high driving force (TPA-ph$_n$-Ir-ph$_n$-AQ), or to a changeover from activationless electron transfer to the normal region of the MARCUS model in case of the triad with a low driving force (TAA-ph$_n$-Ru-ph$_n$-NDI).

The results of the project that is presented in this chapter were published in Inorganic Chemistry[95] during these PhD studies. Additional calculations concerning the energy diagrams in the supporting information can be found in the Appendix.

- Neumann, S.; Wenger, O. S. Fundamentally Different Distance Dependences of Electron-Transfer Rates for Low and High Driving Forces. *Inorg. Chem.* **2019**, *58*, 855-860.

## Author Contribution

Svenja Neumann contributed to the molecular design, carried out synthesis and performed and analyzed all measurements. She contributed equally to data interpretation and the preparation of the main manuscript and the supporting information.

Oliver S. Wenger drafted the main concept of the project and contributed equally to the systems design, data interpretation and the preparation of the main manuscript and the supporting information.

Paper reprinted with permission from Neumann, S.; Wenger, O. S. Fundamentally Different Distance Dependences of Electron-Transfer Rates for Low and High Driving Forces. *Inorg. Chem.* **2019**, *58*, 855-860. Copyright (2019) American Chemical Society.

# Fundamentally Different Distance Dependences of Electron-Transfer Rates for Low and High Driving Forces

Svenja Neumann and Oliver S. Wenger*

Department of Chemistry, University of Basel, St. Johanns-Ring 19, 4056 Basel, Switzerland

Ⓢ *Supporting Information*

**ABSTRACT:** The distance dependences of electron-transfer rates ($k_{ET}$) in three homologous series of donor−bridge−acceptor compounds with reaction free energies ($\Delta G_{ET}^0$) of ca. −1.2, −1.6, and −2.0 eV for thermal charge recombination after initial photoinduced charge separation were studied by transient absorption spectroscopy. In the series with low driving force, the distance dependence is normal and $k_{ET}$ decreases upon donor−acceptor distance ($r_{DA}$) elongation. In the two series with higher driving forces, $k_{ET}$ increases with increasing distance over a certain range. This counterintuitive behavior can be explained by a weakly distance-dependent electronic donor−acceptor coupling ($H_{DA}$) in combination with an increasing reorganization energy ($\lambda$). Our study shows that highly exergonic electron transfers can have distance dependences that differ drastically from those of the more commonly investigated weakly exergonic reactions.
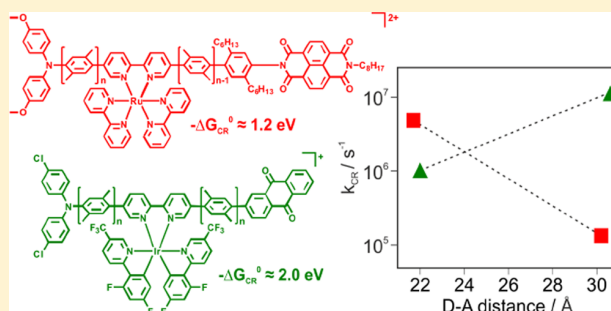
## INTRODUCTION

Numerous prior studies investigated the distance dependence of electron-transfer rates ($k_{ET}$) and the role of the intervening medium between the donor and the acceptor.[1] Rigid rod-like donor−bridge−acceptor compounds,[2−13] properly folded proteins, or DNA equipped with suitable photosensitizers are particularly useful for investigations in which the donor−acceptor distance ($r_{DA}$) must be kept constant on the timescale of an electron-transfer event.[1,14−17] Saturated hydrocarbon bridges or protein backbone typically enable long-range electron transfer via tunneling,[18,19] whereas conjugated bridges or DNA can give rise to hopping.[20−27] Though the distance dependences of $k_{ET}$ are markedly different for these two mechanisms, both usually lead to a decrease of $k_{ET}$ with increasing distance. Experimental studies that reported on an increase of $k_{ET}$ at greater $r_{DA}$ are extremely rare.[28−30] To complement such distance-dependence studies, other investigations focused on the dependence of $k_{ET}$ on reaction free energy ($\Delta G_{ET}^0$),[31−35] and the dependence of $k_{ET}$ on $\Delta G_{ET}^0$ at fixed $r_{DA}$ is now reasonably well understood. However, we are unaware of prior systematic studies of the distance dependence of $k_{ET}$ as a function of $\Delta G_{ET}^0$. Against the background of our recent finding that $k_{ET}$ can increase with increasing distance in donor−photosensitizer−acceptor triads,[36,37] and given the theoretical prediction of such counterintuitive effects,[38,39] we explored the distance dependence of $k_{ET}$ in the three series of triads shown in Scheme 1. These triads contain either a relatively strong triarylamine (TAA) donor with methoxy substituents or a weaker triphenylamine (TPA) donor with chloro substituents. As acceptors, a naphthalene diimide (NDI) unit or an anthraquinone (AQ) moiety was employed.

Excitation of the metal photosensitizers in these compounds induces rapid (≤10 ns) charge separation leading to a radical pair state that subsequently undergoes thermal charge recombination between reduced acceptor and oxidized donor. The driving force for that recombination process ($−\Delta G_{CR}^0$) varies from ca. 1.2 eV (TAA-ph$_n$-Ru-ph$_n$-NDI series) to ca. 1.6 eV (TAA-ph$_n$-Ru-ph$_n$-AQ) and ca. 2.0 eV (TPA-ph$_n$-Ir-ph$_n$-AQ). The key finding is that for the triads with $−\Delta G_{CR}^0 \approx 1.2$ eV, the distance dependence of the electron-transfer rate for charge recombination ($k_{CR}$) is normal (i.e., $k_{CR}$ decreases with increasing distance), whereas in the two other triad series, $k_{CR}$ increases with increasing donor−acceptor separation. This shows that highly exergonic electron transfers can have distance dependences that differ fundamentally from those of the more frequently investigated weakly exergonic reactions.
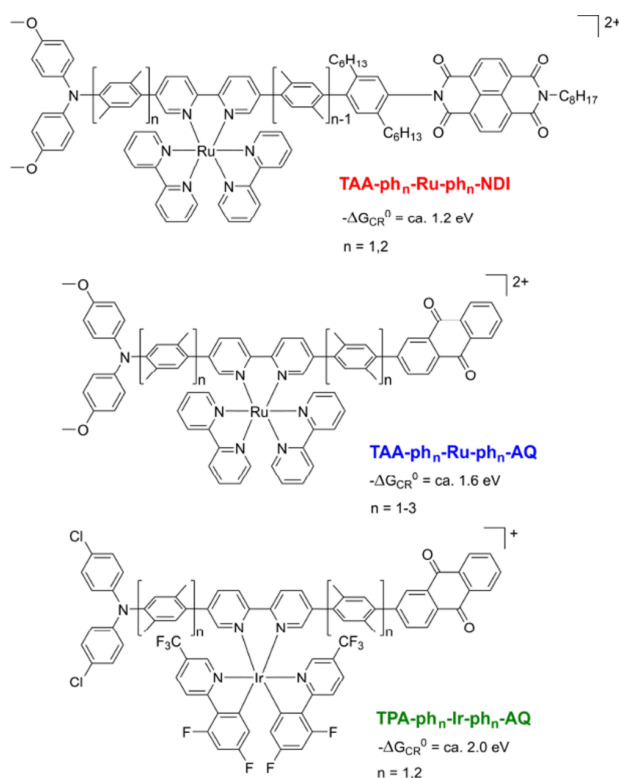
## RESULTS AND DISCUSSION

The molecular triads were synthesized and characterized as described in the Supporting Information. Cyclic voltammetry was used to determine the redox potentials of the individual components of all triads (Supporting Information, page S35), leading to the $−\Delta G_{CR}^0$ values in Scheme 1. When exciting a 20 μM CH$_3$CN solution of TAA-ph$_1$-Ru-ph$_1$-NDI at 532 nm with laser pulses of ∼10 ns duration, the transient absorption spectrum recorded immediately afterward (Figure 1a) shows the spectroscopic signatures of the anticipated charge-separated state, as confirmed by the chemical oxidation and reduction UV−vis difference spectra for TAA$^+$ (Figure 1b) and

**Scheme 1. Structures of Molecular Triads and Driving Forces for Charge Recombination ($-\Delta G_{CR}^0$) between Oxidized Donors and Reduced Acceptors**

TAA-ph$_n$-Ru-ph$_n$-NDI

$-\Delta G_{CR}^0$ = ca. 1.2 eV

n = 1,2

TAA-ph$_n$-Ru-ph$_n$-AQ

$-\Delta G_{CR}^0$ = ca. 1.6 eV

n = 1-3

TPA-ph$_n$-Ir-ph$_n$-AQ

$-\Delta G_{CR}^0$ = ca. 2.0 eV

n = 1,2



**Figure 1.** (a) Transient UV−vis absorption spectrum of 20 $\mu$M TAA-ph$_1$-Ru-ph$_1$-NDI in de-aerated CH$_3$CN at 20 °C. The sample was excited at 532 nm with laser pulses of ca. 10 ns duration, detection occurred by integration over a period of 200 ns immediately afterward. (b) UV−vis difference spectrum resulting from chemical oxidation of the TAA unit in TAA-ph$_1$-Ru-ph$_1$-NDI with Cu(ClO$_4$)$_2$ in CH$_3$CN. (c) UV−vis difference spectrum resulting from chemical one-electron reduction of the NDI unit in TAA-ph$_1$-Ru-ph$_1$-NDI with sodium in tetrahydrofuran. (d) Temporal evolution of the transient absorption signals for TAA-ph$_1$-Ru-ph$_1$-NDI ($n$ = 1) and TAA-ph$_2$-Ru-ph$_2$-NDI ($n$ = 2) monitoring the NDI$^-$ band at 475 nm. (e) Analogous to (d) but monitoring the TAA$^+$ band at 770 nm.

NDI$^-$ (Figure 1c). After selective excitation of the Ru(II) sensitizer at 532 nm, $^3$MLCT-quenching by NDI followed by subsequent electron transfer from TAA to Ru(III) is mainly responsible for the rapid ($\leq$10 ns) formation of the observable TAA$^+$/NDI$^-$ photoproduct (Supporting Information, page S41). This is also the case for the longer congener TAA-ph$_2$-Ru-ph$_2$-NDI (Supporting Information, page S41). Consequently, when monitoring the temporal evolution of the TAA$^+$ and NDI$^-$ signals at the relevant wavelengths (Figure 1d/e and Supporting Information, page S46), one observes instant decays because of thermal charge recombination via intramolecular electron transfer (Supporting Information, page S47). On the basis of kinetic measurements at 475, 607, and 770 nm, rate constants ($k_{CR}$) of $(4.8 \pm 0.5) \times 10^6$ s$^{-1}$ and $(1.3 \pm 0.1) \times 10^5$ s$^{-1}$ were determined for TAA-ph$_1$-Ru-ph$_1$-NDI and TAA-ph$_2$-Ru-ph$_2$-NDI in de-aerated CH$_3$CN at 20 °C (Table 1). Thus, a decrease of $k_{CR}$ is observed when elongating $r_{DA}$ from 21.7 to 30.2 Å (red squares in Figure 2), as commonly expected. $r_{DA}$ corresponds to the centroid-to-centroid distances between donors and acceptors of our triads.

However, the new TAA-ph$_n$-Ru-ph$_n$-NDI data are in clear contrast to the results previously obtained for the TAA-ph$_n$-Ru-ph$_n$-AQ series of triads (Scheme 1, middle), in which the elongation from $n$ = 1 to $n$ = 2 caused an increase of $k_{CR}$ by roughly a factor of 8 (blue circles in Figure 2).[36,37] In this triad series where AQ instead of NDI is the terminal acceptor, $-\Delta G_{CR}^0$ is considerably higher (ca. 1.6 eV, Scheme 1), and an activation barrier ($\Delta G_{CR}^\ddagger$) of ca. 43 meV made electron transfer in the compound with $n$ = 1 relatively slow, whereas in the triad with $n$ = 2, it was activationless. Given the relatively strongly exergonic nature of charge recombination in that
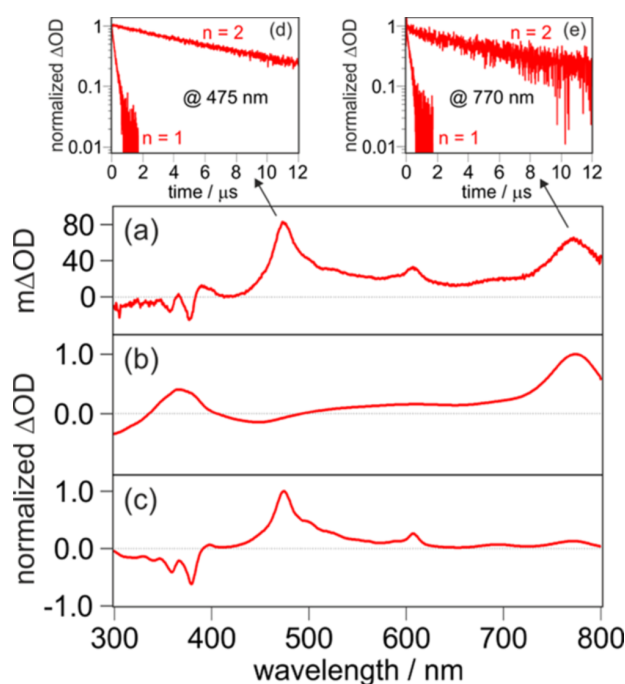
series and the expected increase of the (outer-sphere) reorganization energy ($\lambda$) with increasing distance,[40,41] these observations were attributed to a changeover from the inverted regime ($-\Delta G_{CR}^0 > \lambda$ for $n$ = 1) to the activationless point ($-\Delta G_{CR}^0 = \lambda$ for $n$ = 2).[36,37] This raised the question whether in a compound series with even more negative $\Delta G_{CR}^0$, an even stronger increase of $k_{CR}$ with increasing distance could become observable because the reaction could be more deeply inverted in the shortest compound. This question can now be addressed with the TPA-ph$_n$-Ir-ph$_n$-AQ series for which $\Delta G_{CR}^0$ = ca. $-2.0$ eV (Scheme 1 bottom, Supporting Information, page S38).

The envisioned formation of a charge-separated state storing 2.0 eV necessitated the use of a cyclometalated Ir(III) sensitizer with a photoactive $^3$MLCT state at higher energy than that of Ru(bpy)$_3^{2+}$. In combination with a chloro-substituted TPA donor and an AQ acceptor, a highly energetic charge-separated state comprising TPA$^+$ and AQ$^-$ is indeed formed within 10 ns in both TPA-ph$_1$-Ir-ph$_1$-AQ and TPA-ph$_2$-Ir-ph$_2$-AQ after excitation at 450/420 nm (Supporting Information, page S43). When monitoring the transient absorption decays at the wavelengths diagnostic for TPA$^+$ and AQ$^-$ (Supporting Information, page S46), this radical ion pair is found to collapse with rate constants of $(1.0 \pm 0.1) \times 10^6$ s$^{-1}$ in the compound with $n$ = 1 and $(1.2 \pm 0.1) \times 10^7$ s$^{-1}$ in the triad with $n$ = 2 (Table 1). Evidently, electron transfer accelerates with increasing distance (green triangles in Figure

**Table 1. Electron-Transfer Parameters for the Four New Triads: Donor–Acceptor Distance ($r_{DA}$), Rate Constant for Thermal Charge Recombination ($k_{CR}$), (Negative) Reaction Free Energy ($\Delta G^0_{CR}$), Activation Free Energy ($\Delta G^{\ddagger}_{CR}$), Reorganization Energy ($\lambda$), and Electronic Donor–Acceptor Coupling ($H_{DA}$)**

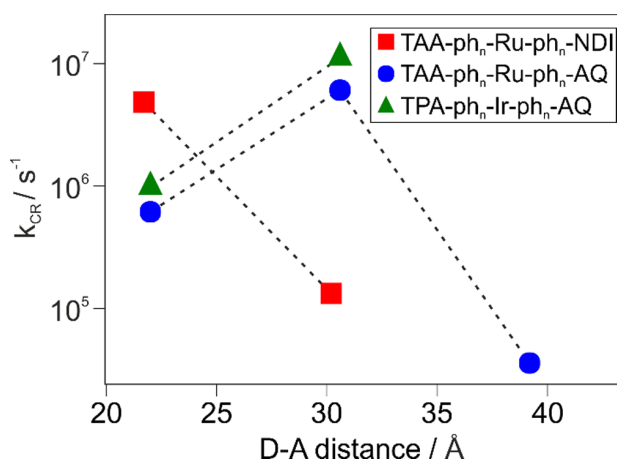| compound | $r_{DA}$/Å | $k_{CR}$/s$^{-1}$ | $-\Delta G^0_{CR}$/eV | $\Delta G^{\ddagger}_{cr}$/meV | $\lambda$/eV | $H_{DA}$/cm$^{-1}$ |
|---|---|---|---|---|---|---|
| TAA-ph$_1$-Ru-ph$_1$-NDI | 21.7 | $(4.8 \pm 0.5) \times 10^6$ | $1.27 \pm 0.05$ | 0 | $1.27 \pm 0.05$ | $0.13 \pm 0.02$ |
| TAA-ph$_2$-Ru-ph$_2$-NDI | 30.2 | $(1.3 \pm 0.1) \times 10^5$ | $1.23 \pm 0.05$ | $47 \pm 6$ | $1.82 \pm 0.35$ | $0.09 \pm 0.02$ |
| TPA-ph$_1$-Ir-ph$_1$-AQ | 22.0 | $(1.0 \pm 0.1) \times 10^6$ | $1.99 \pm 0.05$ | $69 \pm 5$ | $1.37 \pm 0.36$ | $0.35 \pm 0.06$ |
| TPA-ph$_2$-Ir-ph$_2$-AQ | 30.6 | $(1.2 \pm 0.1) \times 10^7$ | $1.96 \pm 0.05$ | 0 | $1.96 \pm 0.05$ | $0.22 \pm 0.04$ |



**Figure 2.** Distance dependence of $k_{CR}$ in the three triad series from Scheme 1.

2), contrasting the behavior found for the TAA-ph$_n$-Ru-ph$_n$-NDI series (red squares in Figure 2) but in line with the TAA-ph$_n$-Ru-ph$_n$-AQ triads (blue circles in Figure 2). In the TPA-ph$_n$-Ir-ph$_n$-AQ series where charge recombination is more exergonic ($\Delta G^0_{CR} = -2.0$ eV), $k_{CR}$ increases by a factor of 12 between $n = 1$ and $n = 2$, compared to a factor of 8 for the TAA-ph$_n$-Ru-ph$_n$-AQ triads ($\Delta G^0_{CR} = -1.6$ eV). Thus, the anticipated enhancement of the rate acceleration upon further increase of the driving force ($-\Delta G^0_{CR}$) is indeed observable but it is modest. By measuring the charge recombination kinetics as a function of temperature (Supporting Information, page S49), an activation energy of 69 meV is found for TPA-ph$_1$-Ir-ph$_1$-AQ, whereas the charge recombination turns out to be activationless in TPA-ph$_2$-Ir-ph$_2$-AQ (Table 1, Supporting Information, page S49). Thus, in TPA-ph$_1$-Ir-ph$_1$-AQ, electron transfer occurs in the more deeply inverted regime than in the previously investigated TAA-ph$_1$-Ru-ph$_1$-AQ triad ($\Delta G^{\ddagger}_{CR} = 43$ meV),[36,37] as anticipated. The driving force is essentially temperature independent in the relevant regime (Supporting Information, page S39).

It is insightful to compare all relevant electron-transfer parameters in the two extreme cases of the newly investigated TAA-ph$_n$-Ru-ph$_n$-NDI and TPA-ph$_n$-Ir-ph$_n$-AQ systems (Table 1). On the basis of the experimentally determined activation energies, reorganization energies ($\lambda$) can be estimated (Supporting Information, page S51), and they are found to increase from 1.3–1.4 eV in the systems with $n = 1$ to 1.8–2.0 eV in the triads with $n = 2$ (Table 1). The dielectric continuum model based on spherical donors and acceptors with radii of 4 Å predicts an increase in $\lambda$ of ca. 0.3 eV for CH$_3$CN solvent,[36,37,40–43] but the experimentally observed effect is larger (0.5–0.6 eV). However, it has been noted earlier that dielectric continuum models tend to underestimate the

increase of the distance-dependent outer-sphere reorganization energy ($\lambda_0$),[41] and such models cannot be expected to give an accurate quantitative description of our triads. All our compounds include a cationic photosensitizer, and the reorganization of counteranions in the course of intramolecular electron transfer is likely to play a non-negligible role, yet is not included in such models. Moreover, the experimental uncertainties in $\lambda$ are up to nearly 0.4 eV (Table 1) for reasons discussed in the Supporting Information on page S51. The key point from this analysis of reorganization energies is that $\lambda_0$ shows the qualitatively expected increase upon distance elongation, but simple models are unable to provide a quantitative description of the observable effect, and large experimental uncertainties make application of more sophisticated models not worthwhile. The prior use of a model taking electron–vibrational coupling[44] into account did not lead to a significant improvement.[37]

The temperature-dependent measurements of $k_{CR}$ furthermore give access to estimates of the electronic donor–acceptor couplings ($H_{DA}$, Supporting Information, page S52), and we find values on the order of 0.1–0.4 cm$^{-1}$ (Table 1). Depending on donor–acceptor distances and the type of molecular bridge, values in the range of $10^2$ to $10^{-1}$ cm$^{-1}$ are not uncommon.[45–47] The decrease in $H_{DA}$ upon distance elongation from $n = 1$ to $n = 2$ is relatively modest and would translate to distance decay constants ($\beta$) of ca. 0.1 Å$^{-1}$, which is considerably lower than what is typically expected for oligo-$p$-phenylene bridges ($\beta = 0.4–0.8$ Å$^{-1}$).[28,47–50] However, $\beta$ is not a bridge-specific parameter but instead depends on the entire combination of donor, bridge, and acceptor.[51–53] Moreover, our estimate for $\beta$ can only be based on two data points, and it is possible that there are nonexponential contributions to the distance-dependent electronic coupling.[54] Evidently, our bridges all contain a bipyridine ligand and as such do not constitute a homologous series of identical elements, which is a key assumption of many models treating the distance dependence of $k_{ET}$.[55,56] As noted earlier,[57] the distance decay constants below 0.2 Å$^{-1}$ are likely to be an indication of a more complex situation, which may involve conformational variability and which could signal the onset of multistep hopping rather than tunneling. On the other hand, our earlier investigations of oligo-$p$-xylenes demonstrated that the electronic structure of this particular bridge type is significantly less length dependent than that of oligo-$p$-phenylenes,[48,49,58] making a distance-dependent changeover from tunneling to hopping, as reported previously for unsubstituted $p$-phenylene bridges,[28] less likely in our systems.

Using the parameters in Table 1, Marcus parabola showing $k_{CR}$ as a function of reaction free energy ($\Delta G^0_{CR}$) at fixed $r_{DA}$ can be calculated (Figure 3). Upon distance elongation, the parabolas undergo the expected bottom rightward shift because of the decrease of $H_{DA}$ and the increase of $\lambda$ with increasing distance (Table 1).[42] The driving force is essentially
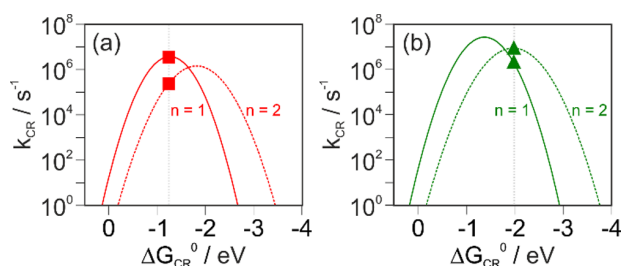
**Figure 3.** Plots of $k_{CR}$ vs $\Delta G_{CR}^0$ based on the parameters from Table 1. (a) TAA-ph$_n$-Ru-ph$_n$-NDI systems with $n = 1$ (solid red) and $n = 2$ (dotted red). (b) TPA-ph$_n$-Ir-ph$_n$-AQ systems with $n = 1$ (solid green) and $n = 2$ (dotted green). The dotted vertical lines mark the relevant driving forces for charge recombination.

constant in a given series of our triads, and this is represented by dotted vertical lines in Figure 3. In the TAA-ph$_n$-Ru-ph$_n$-NDI series where $\Delta G_{CR}^0$ is relatively low ($-1.2$ eV), this nicely visualizes the changeover from activationless electron transfer in the compound with $n = 1$ (red square at the top of the solid red parabola, Figure 3a) to electron transfer in the normal regime (red square in the left half of the dotted red parabola, Figure 3a) in the triad with $n = 2$. By contrast, in the TPA-ph$_n$-Ir-ph$_n$-AQ series, charge recombination in the compound with $n = 1$ occurs in the inverted regime (green triangle in the right half of the solid green parabola of Figure 3b), whereas in the compound with $n = 2$, it takes place at the activationless point (green triangle at the top of the dotted green parabola of Figure 3b).

## CONCLUSIONS

In summary, our study shows that electron-transfer rates can either increase or decrease with increasing donor−acceptor distance, in clear contrast to the common belief that reaction rates always get slower when the distance between individual reactants increases.[43] This counterintuitive behavior is readily understandable in the framework of Marcus theory, as pointed out in two early theory papers,[38,39] yet this does not seem to be nearly as widely known as the inverted driving force effect. The present study is the first systematic investigation of the distance dependence of $k_{ET}$ as a function of driving force, geared at testing these early theoretical predictions. The key finding is that highly exergonic electron-transfer reactions can indeed exhibit fundamentally different distance dependences than the more commonly studied weakly exergonic reactions.

The semiclassical Marcus model used herein (and in the early theoretical prediction)[38] provides an adequate qualitative description, but there is evidence from our investigations that an accurate quantitative description will require more sophisticated models.[36] Specifically, the model used herein yields relatively large increases of the outer-sphere reorganization energy paired with rather shallow distance dependences of $H_{DA}$. The combination of these two effects might point at a systematic error made when using the simple Marcus model.

The qualitative picture has now become fairly clear from the investigation of the seven triads presented herein, and the simple Marcus model is very valuable to understand the little-known effect of increasing reaction rates with increasing distance. Just like the much better known inverted driving force effect,[46,59] the phenomenon predicted by Sutin and Tachiya,[38,39] and then first observed in an unambiguous manner by us,[36] might have important implications for solar

energy conversion.[42] In particular, the competition between photoinduced charge separation and (undesired) thermal charge recombination reactions in solar energy conversion devices could crucially depend on the different distance dependences of weakly and more strongly exergonic electron-transfer reactions.

## ASSOCIATED CONTENT

### ⓢ Supporting Information
The Supporting Information is available free of charge on the ACS Publications website at DOI: 10.1021/acs.inorgchem.8b02973.

> Synthetic protocols and characterization data, description of equipment and methods, supplementary electrochemical and spectroscopic data, and thermochemical discussion (PDF)

## AUTHOR INFORMATION

**Corresponding Author**
*E-mail: oliver.wenger@unibas.ch.
**ORCID** ⓘD
Oliver S. Wenger: 0000-0002-0739-0553
**Notes**
The authors declare no competing financial interest.

## ACKNOWLEDGMENTS

## REFERENCES

(1) Edwards, P. P.; Gray, H. B.; Lodge, M. T. J.; Williams, R. J. P. Electron Transfer and Electronic Conduction through an Intervening Medium. *Angew. Chem., Int. Ed.* **2008**, *47*, 6758−6765.

(2) Meylemans, H. A.; Hewitt, J. T.; Abdelhaq, M.; Vallett, P. J.; Damrauer, N. H. Exploiting Conformational Dynamics to Facilitate Formation and Trapping of Electron-Transfer Photoproducts in Metal Complexes. *J. Am. Chem. Soc.* **2010**, *132*, 11464−11466.

(3) Johansson, P. G.; Kopecky, A.; Galoppini, E.; Meyer, G. J. Distance Dependent Electron Transfer at TiO$_2$ Interfaces Sensitized with Phenylene Ethynylene Bridged Ru$^{II}$-Isothiocyanate Compounds. *J. Am. Chem. Soc.* **2013**, *135*, 8331−8341.

(4) Majewski, M. B.; de Tacconi, N. R.; MacDonnell, F. M.; Wolf, M. O. Long-Lived, Directional Photoinduced Charge Separation in Ru$^{II}$ Complexes Bearing Laminate Polypyridyl Ligands. *Chem.—Eur. J.* **2013**, *19*, 8331−8341.

(5) Sukegawa, J.; Schubert, C.; Zhu, X.; Tsuji, H.; Guldi, D. M.; Nakamura, E. Electron Transfer Through Rigid Organic Molecular Wires Enhanced by Electronic and Electron-Vibration Coupling. *Nat. Chem.* **2014**, *6*, 899−905.

(6) Lee, S.-H.; Chan, C. T.-L.; Wong, K. M.-C.; Lam, W. H.; Kwok, W.-M.; Yam, V. W.-W. Design and Synthesis of Bipyridine Platinum(II) Bisalkynyl Fullerene Donor-Chromophore-Acceptor Triads with Ultrafast Charge Separation. *J. Am. Chem. Soc.* **2014**, *136*, 10041−10052.

(7) Klein, J. H.; Schmidt, D.; Steiner, U. E.; Lambert, C. Complete Monitoring of Coherent and Incoherent Spin Flip Domains in the Recombination of Charge-Separated States of Donor-Iridium Complex-Acceptor Triads. *J. Am. Chem. Soc.* **2015**, *137*, 11011−11021.

(8) Hu, K.; Blair, A. D.; Piechota, E. J.; Schauer, P. A.; Sampaio, R. N.; Parlane, F. G. L.; Meyer, G. J.; Berlinguette, C. P. Kinetic Pathway

for Interfacial Electron Transfer from a Semiconductor to a Molecule. *Nat. Chem.* **2016**, *8*, 853−859.

(9) Favereau, L.; Makhal, A.; Pellegrin, Y.; Blart, E.; Petersson, J.; Göransson, E.; Hammarström, L.; Odobel, F. A Molecular Tetrad That Generates a High-Energy Charge-Separated State by Mimicking the Photosynthetic Z-Scheme. *J. Am. Chem. Soc.* **2016**, *138*, 3752−3760.

(10) Delor, M.; Archer, S. A.; Keane, T.; Meijer, A. J. H. M.; Sazanovich, I. V.; Greetham, G. M.; Towrie, M.; Weinstein, J. A. Directing the Path of Light-Induced Electron Transfer at a Molecular Fork using Vibrational Excitation. *Nat. Chem.* **2017**, *9*, 1099−1104.

(11) Schroot, R.; Schlotthauer, T.; Dietzek, B.; Jäger, M.; Schubert, U. S. Extending Long-Lived Charge Separation Between Donor and Acceptor Blocks in Novel Copolymer Architectures Featuring a Sensitizer Core. *Chem.—Eur. J.* **2017**, *23*, 16484−16490.

(12) Arrigo, A.; Santoro, A.; Puntoriero, F.; Lainé, P. P.; Campagna, S. Photoinduced Electron Transfer in Donor-Bridge-Acceptor Assemblies: The Case of Os(II)-bis(terpyridine)-(bi)pyridinium Dyads. *Coord. Chem. Rev.* **2015**, *304−305*, 109−116.

(13) Bao, D.; Upadhyayula, S.; Larsen, J. M.; Xia, B.; Georgieva, B.; Nuñez, V.; Espinoza, E. M.; Hartman, J. D.; Wurch, M.; Chang, A.; Lin, C.-K.; Larkin, J.; Vasquez, K.; Beran, G. J. O.; Vullev, V. I. Dipole-Mediated Rectification of Intramolecular Photoinduced Charge Separation and Charge Recombination. *J. Am. Chem. Soc.* **2014**, *136*, 12966−12973.

(14) Giese, B.; Amaudrut, J.; Köhler, A.-K.; Spormann, M.; Wessely, S. Direct Observation of Hole Transfer Through DNA by Hopping Between Adenine Bases and by Tunnelling. *Nature* **2001**, *412*, 318−320.

(15) Genereux, J. C.; Barton, J. K. Mechanisms for DNA Charge Transport. *Chem. Rev.* **2010**, *110*, 1642−1662.

(16) Minnihan, E. C.; Nocera, D. G.; Stubbe, J. Reversible, Long-Range Radical Transfer in E. coli Class Ia Ribonucleotide Reductase. *Acc. Chem. Res.* **2013**, *46*, 2524−2535.

(17) Renaud, N.; Harris, M. A.; Singh, A. P. N.; Berlin, Y. A.; Ratner, M. A.; Wasielewski, M. R.; Lewis, F. D.; Grozema, F. C. Deep-Hole Transfer Leads to Ultrafast Charge Migration in DNA Hairpins. *Nat. Chem.* **2016**, *8*, 1015−1021.

(18) Wiberg, J.; Guo, L.; Pettersson, K.; Nilsson, D.; Ljungdahl, T.; Mårtensson, J.; Albinsson, B. Charge Recombination versus Charge Separation in Donor−Bridge−Acceptor Systems. *J. Am. Chem. Soc.* **2007**, *129*, 155−163.

(19) Benniston, A. C.; Harriman, A. Charge on the Move: How Electron-Transfer Dynamics Depend on Molecular Conformation. *Chem. Soc. Rev.* **2006**, *35*, 169−179.

(20) Davis, W. B.; Svec, W. A.; Ratner, M. A.; Wasielewski, M. R. Molecular-Wire Behaviour in *p*-Phenylenevinylene Oligomers. *Nature* **1998**, *396*, 60−63.

(21) Vail, S. A.; Krawczuk, P. J.; Guldi, D. M.; Palkar, A.; Echegoyen, L.; Tomé, J. P. C.; Fazio, M. A.; Schuster, D. I. Energy and Electron Transfer in Polyacetylene-Linked Zinc-Porphyrin-[60]Fullerene Molecular Wires. *Chem.—Eur. J.* **2005**, *11*, 3375−3388.

(22) Welter, S.; Lafolet, F.; Cecchetto, E.; Vergeer, F.; De Cola, L. Energy Transfer by a Hopping Mechanism in Dinuclear Ir^III/Ru^II Complexes: A Molecular Wire? *ChemPhysChem* **2005**, *6*, 2417−2427.

(23) Montes, V. A.; Pérez-Bolívar, C.; Agarwal, N.; Shinar, J.; Anzenbacher, P. Molecular-Wire Behavior of OLED Materials: Exciton Dynamics in Multichromophoric Alq_3-Oligofluorene-Pt(II) Porphyrin Triads. *J. Am. Chem. Soc.* **2006**, *128*, 12436−12438.

(24) Barlow, S.; Risko, C.; Chung, S.-J.; Tucker, N. M.; Coropceanu, V.; Jones, S. C.; Levi, Z.; Brédas, J.-L.; Marder, S. R. Intervalence Transitions in the Mixed-Valence Monocations of Bis(triarylamines) Linked with Vinylene and Phenylene−Vinylene Bridges. *J. Am. Chem. Soc.* **2005**, *127*, 16900−16911.

(25) Lloveras, V.; Vidal-Gancedo, J.; Figueira-Duarte, T. M.; Nierengarten, J.-F.; Novoa, J. J.; Mota, F.; Ventosa, N.; Rovira, C.; Veciana, J. Tunneling versus Hopping in Mixed-Valence Oligo-*p*-phenylenevinylene Polychlorinated Bis(triphenylmethyl) Radical Anions. *J. Am. Chem. Soc.* **2011**, *133*, 5818−5833.

(26) O'Hanlon, D. C.; Cohen, B. W.; Moravec, D. B.; Dallinger, R. F.; Hopkins, M. D. Electronic, Redox, and Photophysical Consequences of Metal-for-Carbon Substitution in Oligo-Phenylene-Ethynylenes. *J. Am. Chem. Soc.* **2014**, *136*, 3127−3136.

(27) Vela, S.; Bauroth, S.; Atienza, C.; Molina-Ontoria, A.; Guldi, D. M.; Martín, N. Determining the Attenuation Factor in Molecular Wires Featuring Covalent and Noncovalent Tectons. *Angew. Chem., Int. Ed.* **2016**, *55*, 15076−15080.

(28) Weiss, E. A.; Ahrens, M. J.; Sinks, L. E.; Gusev, A. V.; Ratner, M. A.; Wasielewski, M. R. Making a Molecular Wire: Charge and Spin Transport through *para*-Phenylene Oligomers. *J. Am. Chem. Soc.* **2004**, *126*, 5577−5584.

(29) Stangel, C.; Schubert, C.; Kuhri, S.; Rotas, G.; Margraf, J. T.; Regulska, E.; Clark, T.; Torres, T.; Tagmatarchis, N.; Coutsolelos, A. G.; Guldi, D. M. Tuning the Reorganization Energy of Electron Transfer in Supramolecular Ensembles - Metalloporphyrin, Oligophenylenevinylenes, and Fullerene - and the Impact on Electron Transfer Kinetics. *Nanoscale* **2015**, *7*, 2597−2608.

(30) Luo, Y.; Barthelmes, K.; Wächtler, M.; Winter, A.; Schubert, U. S.; Dietzek, B. Increased Charge Separation Rates with Increasing Donor-Acceptor Distance in Molecular Triads: The Effect of Solvent Polarity. *J. Phys. Chem. C* **2017**, *121*, 9220−9229.

(31) Waskasi, M. M.; Kodis, G.; Moore, A. L.; Moore, T. A.; Gust, D.; Matyushov, D. V. Marcus Bell-Shaped Electron Transfer Kinetics Observed in an Arrhenius Plot. *J. Am. Chem. Soc.* **2016**, *138*, 9251−9257.

(32) Rosspeintner, A.; Angulo, G.; Vauthey, E. Bimolecular Photoinduced Electron Transfer Beyond the Diffusion Limit: The Rehm-Weller Experiment Revisited with Femtosecond Time Resolution. *J. Am. Chem. Soc.* **2014**, *136*, 2026−2032.

(33) Suneesh, C. V.; Balan, B.; Ozawa, H.; Nakamura, Y.; Katayama, T.; Muramatsu, M.; Nagasawa, Y.; Miyasaka, H.; Sakai, K. Mechanistic Studies of Photoinduced Intramolecular and Intermolecular Electron Transfer Processes in RuPt-centred Photo-Hydrogen-Evolving Molecular Devices. *Phys. Chem. Chem. Phys.* **2014**, *16*, 1607−1616.

(34) Lim, G. N.; Obondi, C. O.; D'Souza, F. A High-Energy Charge-Separated State of 1.70 eV from a High-Potential Donor-Acceptor Dyad: A Catalyst for Energy-Demanding Photochemical Reactions. *Angew. Chem., Int. Ed.* **2016**, *55*, 11517−11521.

(35) Higashino, T.; Yamada, T.; Yamamoto, M.; Furube, A.; Tkachenko, N. V.; Miura, T.; Kobori, Y.; Jono, R.; Yamashita, K.; Imahori, H. Remarkable Dependence of the Final Charge Separation Efficiency on the Donor-Acceptor Interaction in Photoinduced Electron Transfer. *Angew. Chem., Int. Ed.* **2015**, *55*, 629−633.

(36) Kuss-Petermann, M.; Wenger, O. S. Increasing Electron-Transfer Rates with Increasing Donor-Acceptor Distance. *Angew. Chem., Int. Ed.* **2015**, *55*, 815−819.

(37) Kuss-Petermann, M.; Wenger, O. S. Electron Transfer Rate Maxima at Large Donor-Acceptor Distances. *J. Am. Chem. Soc.* **2016**, *138*, 1349−1358.

(38) Brunschwig, B. S.; Ehrenson, S.; Sutin, N. The Distance Dependence of Electron Transfer Reactions: Rate Maxima and Rapid Rates at Large Reactant Separations. *J. Am. Chem. Soc.* **1984**, *106*, 6858−6859.

(39) Tachiya, M.; Murata, S. New Explanation for the Lack of the Inverted Region in Charge Separation Reactions. *J. Phys. Chem.* **1992**, *96*, 8441−8444.

(40) Marcus, R. A.; Sutin, N. Electron Transfers in Chemistry and Biology. *Biochim. Biophys. Acta* **1985**, *811*, 265−322.

(41) Isied, S. S.; Vassilian, A.; Wishart, J. F.; Creutz, C.; Schwarz, H. A.; Sutin, N. The Distance Dependence of Intramolecular Electron-Transfer Rates: Importance of the Nuclear Factor. *J. Am. Chem. Soc.* **1988**, *110*, 635−637.

(42) Kuss-Petermann, M.; Wenger, O. S. Unusual Distance Dependences of Electron Transfer Rates. *Phys. Chem. Chem. Phys.* **2016**, *18*, 18657−18664.

(43) Kuss-Petermann, M.; Wenger, O. S. Reaction Rate Maxima at Large Distances between Reactants. *Chimia* **2016**, *70*, 177−181.

(44) Barbara, P. F.; Meyer, T. J.; Ratner, M. A. Contemporary Issues in Electron Transfer Research. *J. Phys. Chem.* **1996**, *100*, 13148−13168.

(45) Kirk, M. L.; Shultz, D. A.; Depperman, E. C.; Brannen, C. L. Donor−Acceptor Biradicals as Ground State Analogues of Photoinduced Charge Separated States. *J. Am. Chem. Soc.* **2007**, *129*, 1937−1943.

(46) Fox, L. S.; Kozik, M.; Winkler, J. R.; Gray, H. B. Gaussian Free-Energy Dependence of Electron-Transfer Rates in Iridium Complexes. *Science* **1990**, *247*, 1069−1071.

(47) Weiss, E. A.; Tauber, M. J.; Kelley, R. F.; Ahrens, M. J.; Ratner, M. A.; Wasielewski, M. R. Conformationally Gated Switching between Superexchange and Hopping within Oligo-*p*-phenylene-based Molecular Wires. *J. Am. Chem. Soc.* **2005**, *127*, 11842−11850.

(48) Hanss, D.; Wenger, O. S. Electron Tunneling through Oligo-*p*-xylene Bridges. *Inorg. Chem.* **2008**, *47*, 9081−9084.

(49) Hanss, D.; Wenger, O. S. Tunneling Barrier Effects on Photoinduced Charge Transfer through Covalent Rigid Rod-Like Bridges. *Inorg. Chem.* **2009**, *48*, 671−680.

(50) Indelli, M. T.; Chiorboli, C.; Flamigni, L.; De Cola, L.; Scandola, F. Photoinduced Electron Transfer across Oligo-*p*-phenylene Bridges. Distance and Conformational Effects in Ru(II)−Rh(III) Dyads. *Inorg. Chem.* **2007**, *46*, 5630−5641.

(51) Natali, M.; Campagna, S.; Scandola, F. Photoinduced Electron Transfer across Molecular Bridges: Electron- and Hole-Transfer Superexchange Pathways. *Chem. Soc. Rev.* **2014**, *43*, 4005−4018.

(52) Eng, M. P.; Albinsson, B. The Dependence of the Electronic Coupling on Energy Gap and Bridge Conformation - Towards Prediction of the Distance Dependence of Electron Transfer Reactions. *Chem. Phys.* **2009**, *357*, 132−139.

(53) Lewis, F. D.; Liu, J.; Weigel, W.; Rettig, W.; Kurnikov, I. V.; Beratan, D. N. Donor-Bridge-Acceptor Energetics Determine the Distance Dependence of Electron Tunneling in DNA. *Proc. Natl. Acad. Sci. U.S.A.* **2002**, *99*, 12536−12541.

(54) Eng, M. P.; Albinsson, B. Non-Exponential Distance Dependence of Bridge-Mediated Electronic Coupling. *Angew. Chem., Int. Ed.* **2006**, *45*, 5626−5629.

(55) McConnell, H. M. Intramolecular Charge Transfer In Aromatic Free Radicals. *J. Chem. Phys.* **1961**, *35*, 508−515.

(56) Wenger, O. S. How Donor−Bridge−Acceptor Energetics Influence Electron Tunneling Dynamics and Their Distance Dependences. *Acc. Chem. Res.* **2011**, *44*, 25−35.

(57) Berlin, Y. A.; Grozema, F. C.; Siebbeles, L. D. A.; Ratner, M. A. Charge Transfer in Donor-Bridge-Acceptor Systems: Static Disorder, Dynamic Fluctuations, and Complex Kinetics. *J. Phys. Chem. C* **2008**, *112*, 10988−11000.

(58) Hanss, D.; Walther, M. E.; Wenger, O. S. Importance of Covalence, Conformational Effects and Tunneling-barrier Heights for Long-range Electron Transfer: Insights from Dyads with Oligo-*p*-phenylene, Oligo-*p*-xylene and Oligo-*p*-dimethoxybenzene Bridges. *Coord. Chem. Rev.* **2010**, *254*, 2584−2592.

(59) Closs, G. L.; Miller, J. R. Intramolecular Long-Distance Electron Transfer in Organic Molecules. *Science* **1988**, *240*, 440−447.

# Fundamentally Different Distance Dependences of Electron Transfer Rates for Low and High Driving-Forces

Svenja Neumann and Oliver S. Wenger*

*Department of Chemistry, University of Basel, St. Johanns-Ring 19, 4056 Basel, Switzerland*

Table of contents

Synthesis and product characterization data for triads TAA-ph$_1$-Ru-ph$_1$-NDI and TAA-ph$_2$-Ru-ph$_2$-NDI

The syntheses and characterization data of compounds **1-4** [1-3] and **6-16** [2-7] have been reported previously, but full experimental details for all synthetic steps are given in the following protocols. Compound **5** is commercially available.
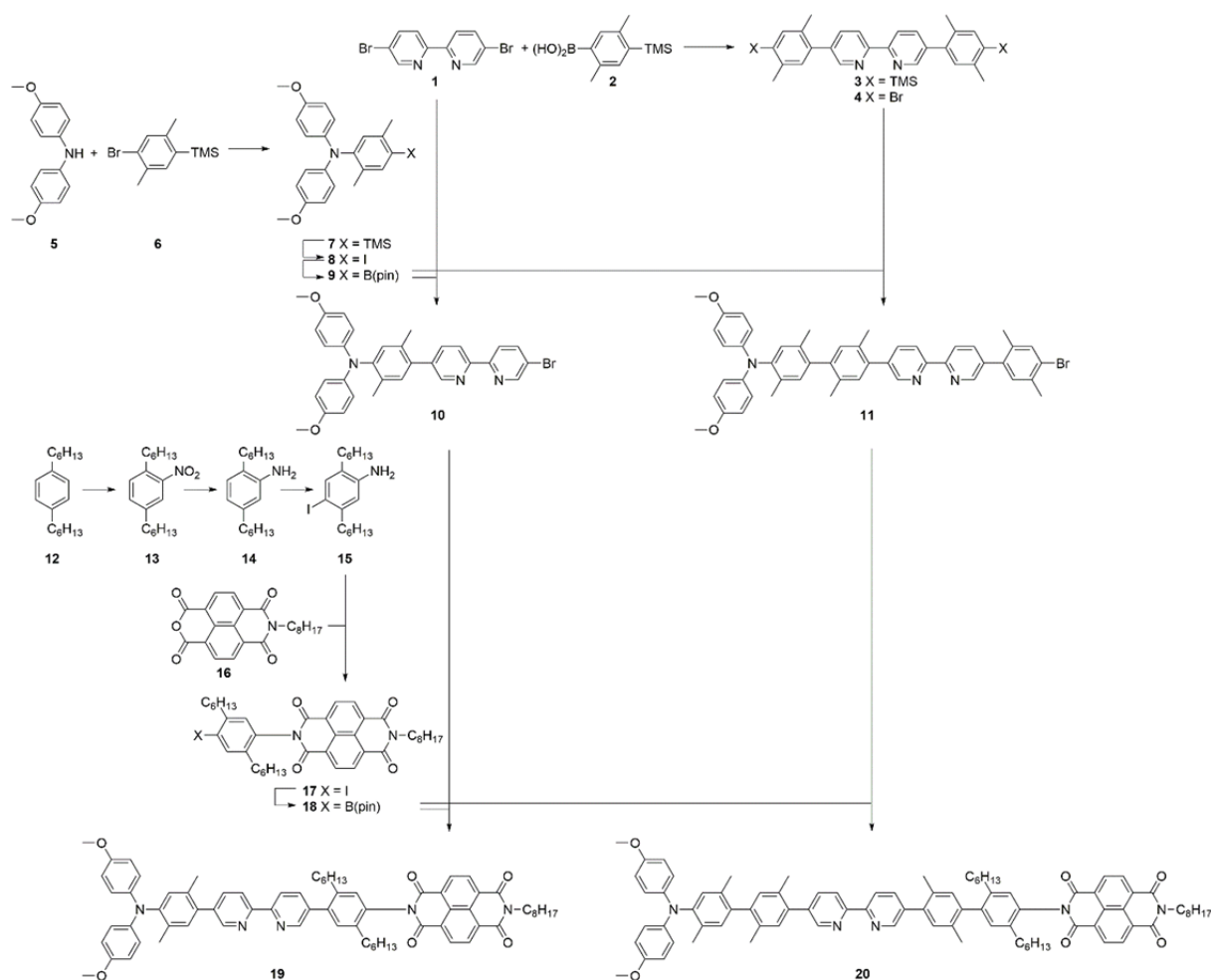


**Scheme S1.** Synthesis of the key ligands for triad **TAA-ph$_1$-Ru-ph$_1$-NDI** and triad **TAA-ph$_2$-Ru-ph$_2$-NDI**.
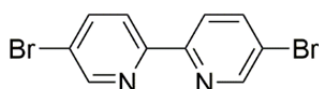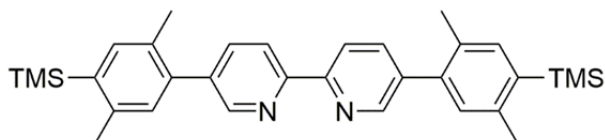


Compound **1**. The following procedure was adapted from literature.[1] 5-Bromo-2-iodopyridine (10.0 g, 35.2 mmol, 1.00 eq.) was dissolved in dry *m*-xylene (60 mL) and

hexa(*n*-butyl)distannane (8.90 mL, 17.6 mmol, 0.50 eq.) was added under $N_2$. After degassing the reaction mixture for 1 h, Pd(PPh$_3$)$_4$ (814 mg, 0.70 mmol, 0.02 eq.) was suspended and the mixture was degassed further for 15 min. The mixture reacted at reflux for 66 h, and then the black precipitate was filtered off. After removal of the solvent under reduced pressure, the product was purified by gradient chromatography on a silica gel column with *n*-pentane to DCM as an eluent. The pure product was obtained as a beige solid (3.00 g, 9.55 mmol, 54%). ^{1}H NMR (400 MHz, CDCl$_3$): δ [ppm] = 8.70 (dd, *J* = 2.3, 0.6 Hz, 2 H), 8.28 (dd, *J* = 8.5, 0.6 Hz, 2 H), 7.93 (dd, *J* = 8.5, 2.4 Hz, 2 H).
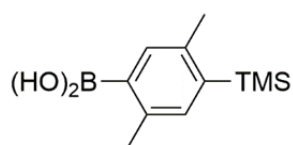


Compound **2**. (4-Bromo-*p*-xylene)trimethylsilane **6** (see below for synthesis of this compound[2]) (8.54 g, 33.2 mmol, 1.00 eq.) was dissolved in dry THF (100 mL) and the solution was cooled to −78 °C under $N_2$. *n*-BuLi (2.5 M in hexane, 16.0 mL, 40.0 mmol, 1.20 eq.) was slowly added and the mixture was stirred for 1.5 h at −78 °C. Afterwards, trimethylborate (3.77 mL, 33.2 mmol, 1.00 eq.) was slowly added while cooling to −78 °C was maintained. The reaction mixture was warmed up to room temperature and stirred for 18 h. Aqueous HCl solution (2 M, 100 mL) was added to the reaction mixture and the phases were separated. The aqueous phase was extracted with DCM (4 × 50 mL). The combined organic phases were washed with brine (50 mL) and dried over anhydrous $Na_2SO_4$. The solvents were removed under reduced pressure and the residue was recrystallized from *n*-hexane. The product was obtained as a white solid (3.82 g, 17.2 mmol, 52%). ^{1}H NMR (400 MHz, CDCl$_3$): δ [ppm] = 7.94 (s, 1 H), 7.36 (s, 1 H), 2.76 (s, 3 H), 2.50 (s, 3 H), 0.36 (s, 9 H).
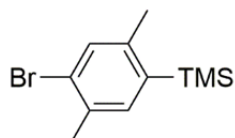


Compound **3**. The following procedure was adapted from literature.[3] A mixture of compound **1** (587 mg, 1.87 mmol, 1.00 eq.), compound **2** (1.00 g, 4.50 mmol, 2.40 eq.) and $Na_2CO_3$ (1.19 g, 11.2 mmol, 6.00 eq.) was suspended in a mixture of THF (30 mL) and water (10 mL)

under $N_2$. The mixture was degassed for 30 min and Pd(PPh$_3$)$_4$ (216 mg, 0.19 mmol, 0.10 eq.) was added. The mixture was further degassed for 15 min and then stirred at 85°C for 1 d. After cooling to room temperature, the phases were separated and the aqueous phase was extracted with DCM (3 × 30 mL). The combined organic phases were dried over anhydrous $Na_2SO_4$ and the solvents were removed under reduced pressure. After purification of the product by chromatography on a silica gel column with DCM to 7:1 (v:v) $n$-pentane/EtOAc as an eluent, a yellow solid was obtained (550 mg, 1.08 mmol, 58%). $^1$H NMR (400 MHz, CDCl$_3$): δ [ppm] = 8.72 (d, $J$ = 1.6 Hz, 2 H), 8.52 (d, $J$ = 8.1 Hz, 2 H), 7.84 (dd, $J$ = 8.1, 2.2 Hz, 2 H), 7.42 (s, 2 H), 7.13 (s, 2 H), 2.51 (s, 6 H), 2.33 (s, 6 H), 0.39 (s, 18 H).
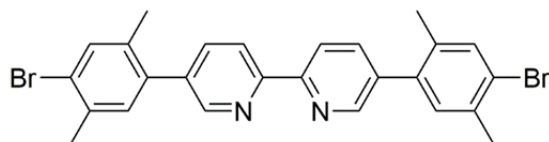


Compound **4**. The following procedure was adapted from literature.[3] Compound **3** (150 mg, 0.29 mmol, 1.00 eq.) and NaOAc (48.3 mg, 0.59 mmol, 2.03 eq.) were suspended in dry THF (10 mL) under $N_2$. The mixture was cooled to 0 °C and protected from light. Bromine (0.06 mL, 1.17 mmol, 4.03 eq.) in dry THF (3 mL) was added slowly. The reaction mixture was stirred at 0 °C for 10 min and was then allowed to reach room temperature while stirring for another 2.5 h. Then, NEt$_3$ (0.33 mL, 2.37 mmol, 8.17 eq.) and aqueous saturated $Na_2S_2O_3$ solution were added and the phases were separated. The aqueous phase was extracted with DCM (3 × 30 mL) and the combined organic phases were dried over anhydrous $Na_2SO_4$. After removing the solvents under reduced pressure, the product was purified by chromatography on a silica gel column with 7:1 (v:v) $n$-pentane/EtOAc as an eluent. The pure product was obtained as a white solid (139 mg, 0.27 mmol, 93%). $^1$H NMR (400 MHz, CDCl$_3$): δ [ppm] = 8.66 (d, $J$ = 1.6 Hz, 2 H), 8.52 (d, $J$ = 8.2 Hz, 2 H), 7.81 (dd, $J$ = 8.1, 2.2 Hz, 2 H), 7.51 (s, 2 H), 7.15 (s, 2 H), 2.42 (s, 6 H), 2.27 (s, 6 H).

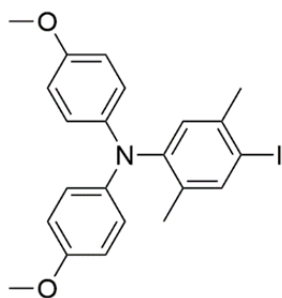

Compound **6**. The following procedure was adapted from literature.[2] 2,5-Dibromo-$p$-xylene (20.0 g, 75.8 mmol, 1.00 eq.) was dissolved in dry THF (150 mL) and cooled to −78 °C under

N$_2$. *n*-BuLi (2.5 M in hexane, 36.4 mL, 91.0 mmol, 1.20 eq.) was slowly added and the mixture was stirred for 30 min at −78 °C. Chlorotrimethylsilane (12 mL, 94.6 mmol, 1.25 eq.) was slowly added while cooling to −78 °C was maintained. The reaction mixture was warmed to room temperature and stirred for 18 h. Water (150 mL) was added and the phases were separated. The aqueous phase was extracted with DCM (3 × 100 mL) and the combined organic phases were dried over anhydrous Na$_2$SO$_4$. After removal of the solvents under reduced pressure, the product was purified by chromatography on a silica gel column with *n*-pentane as an eluent. The pure product was obtained as a colorless oil (18.2 g, 70.6 mmol, 93%). $^1$H NMR (400 MHz, CDCl$_3$): δ [ppm] = 7.34 (s, 1 H), 7.26 (s, 1 H), 2.39 (s, 3 H), 2.36 (s, 3 H), 0.31 (s, 9 H).
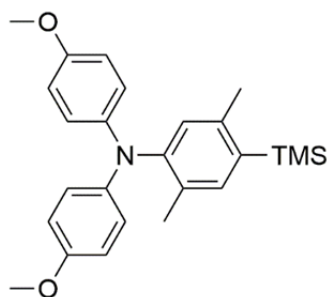


Compound **7**. Following a previously published protocol,[3] a mixture of 4,4′-dimethoxydiphenylamine **5** (1.15 g, 5.02 mmol, 1.00 eq.), compound **6** (1.41 g, 5.48 mmol, 1.10 eq.), Pd(dba)$_2$ (148 mg, 0.26 mmol, 0.05 eq.), tri-*tert*-butylphosphonium tetrafluoroborate (73.0 mg, 0.25 mmol, 0.05 eq.) and potassium *tert*-butoxide (1.68 g, 15.0 mmol, 3.00 eq.) was suspended in dry and degassed toluene (25 mL) under N$_2$. The mixture was reacted at 90 °C for 18.5 h, cooled to room temperature and diluted with water (100 mL). The mixture was extracted with DCM (3 × 200 mL) and the combined organic phases were dried over anhydrous Na$_2$SO$_4$. After removal of the solvents under reduced pressure, the product was purified by chromatography on a silica gel column with 5:1 (v:v) *n*-pentane/EtOAc as an eluent. The pure product was obtained as a yellow solid (1.94 g, 4.78 mmol, 95%). $^1$H NMR (400 MHz, CDCl$_3$): δ [ppm] = 7.22 (s, 1 H), 6.89−6.84 (m, 4 H), 6.80 (s, 1 H), 6.78−6,74 (m, 4 H), 3.77 (s, 6 H), 2.31 (s, 3 H), 1.95 (s, 3 H), 0.31 (s, 9 H).
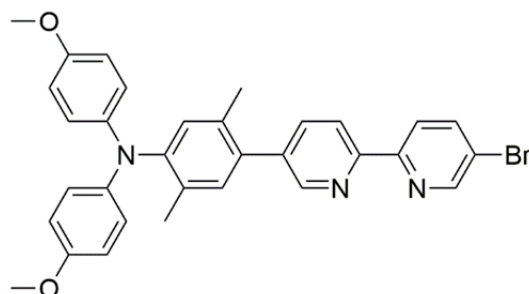
Compound **8**. The following procedure was adapted from literature.[3] Compound **7** (1.68 g, 4.14 mmol, 1.00 eq.) was dissolved in dry DCM (30 mL) and cooled to −78 °C under $N_2$. Iodine monochloride (0.42 mL, 8.25 mmol, 2.00 eq.) in dry DCM (10 mL) was added dropwise and the reaction mixture was stirred for 10 min before saturated aqueous $Na_2S_2O_3$ solution was added. The mixture was allowed to reach room temperature and extracted with DCM (3 × 100 mL). The combined organic phases were dried over anhydrous $Na_2SO_4$ and the solvent was removed under reduced pressure. After purification of the product by chromatography on a silica gel column with 1:1 (v:v) *n*-pentane/DCM as an eluent, a beige solid was obtained (1.76 g, 3.83 mmol, 93%). $^1$H NMR (400 MHz, CDCl$_3$): δ [ppm] = 7.62 (s, 1 H), 6.90 (s, 1 H), 6.87−6.81 (m, 4 H), 6.78−6.73 (m, 4 H), 3.77 (s, 6 H), 2.29 (s, 3 H), 1.91 (s, 3 H).
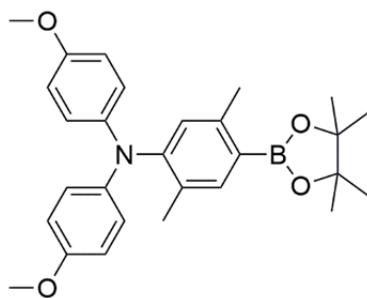


Compound **9**. The following procedure was adapted from literature.[3] A mixture of compound **8** (1.76 g, 3.83 mmol, 1.00 eq.), bis(pinacolato)diboron (1.46 g, 5.75 mmol, 1.50 eq.) and KOAc (1.50 g, 15.3 mmol, 4.00 eq.) in DMSO (20 mL) was degassed for 30 min under $N_2$. Pd(PPh$_3$)$_2$Cl$_2$ (133 mg, 0.19 mmol, 0.05 eq.) was added and the mixture was degassed further for 15 min and then stirred at 90 °C for 21 h. After cooling to room temperature, saturated aqueous NH$_4$Cl solution and water (60 mL) were added. The mixture was extracted with Et$_2$O (3 × 100 mL) and the combined organic phases were dried over anhydrous $Na_2SO_4$. After removal of the solvent under reduced pressure, the product was purified by chromatography on a silica gel column with 9:1 (v:v) *n*-pentane/Et$_2$O as an eluent. The pure product was

obtained as a white solid (1.60 g, 3.48 mmol, 91%). $^1$H NMR (400 MHz, CDCl$_3$): δ [ppm] = 7.58 (s, 1 H), 6.87−6.82 (m, 4 H), 6.81 (s, 1 H), 6.77−6.72 (m, 4 H), 3.77 (s, 6 H), 2.40 (s, 3 H), 1.93 (s, 3 H), 1.34 (s, 12 H).



Compound **10**. The following procedure was adapted from literature.[4] Compound **9** (300 mg, 0.65 mmol, 1.00 eq.), compound **1** (307 mg, 0.98 mmol, 1.51 eq.) and Na$_2$CO$_3$ (207 mg, 1.95 mmol, 3.00 eq.) were suspended in a mixture of THF (10 mL) and water (2 mL) and degassed for 20 min. Pd(PPh$_3$)$_4$ (46.0 mg, 0.04 mmol, 0.06 eq.) was added, the mixture was degassed further for 15 min and then stirred at 85 °C under N$_2$ for 1 d. Once the mixture had cooled to nearly room temperature, it was diluted with water and extracted with DCM (3 × 20 mL). The combined organic phases were dried over anhydrous Na$_2$SO$_4$ and the solvents were removed under reduced pressure. The product was purified by chromatography on silica gel columns. First, a gradient chromatography was performed with 4:1 (v:v) *n*-pentane/DCM + 2% MeOH to 2:1 (v:v) *n*-pentane/DCM + 2% MeOH as an eluent. Further purification was possible with a column with 7:1 (v:v) *n*-pentane/EtOAc as an eluent. The product was obtained as a yellow solid (157 mg, 0.28 mmol, 43%). $^1$H NMR (400 MHz, CDCl$_3$): δ [ppm] = 8.74 (dd, *J* = 2.3, 0.6 Hz, 1 H), 8.68 (dd, *J* = 2.2, 0.7 Hz, 1 H), 8.41 (dd, *J* = 8.2, 0.7 Hz, 1 H), 8.35 (dd, *J* = 8.5, 0.6 Hz, 1 H), 7.96 (dd, *J* = 8.5, 2.4 Hz, 1 H), 7.81 (dd, *J* = 8.2, 2.3 Hz, 1 H), 7.09 (s, 1 H), 6.98 (s, 1 H), 6.95−6.89 (m, 4 H), 6.84−6.76 (m, 4 H), 3.79 (s, 6 H), 2.21 (s, 3 H), 2.01 (s, 3 H).
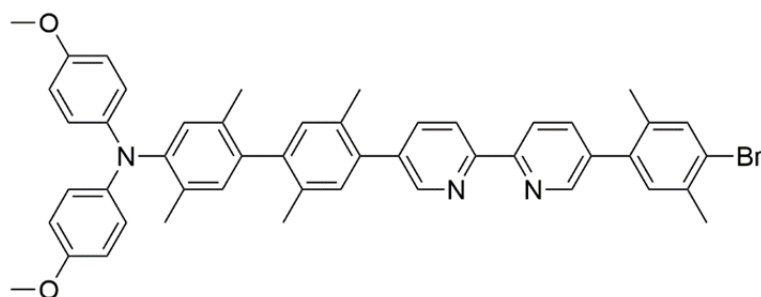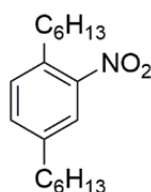
Compound **11**. Following a previously published protocol,[3] compound **9** (82.7 mg, 0.18 mmol, 1.00 eq.), compound **4** (139 mg, 0.27 mmol, 1.50 eq.) and $Na_2CO_3$ (57.2 mg, 0.54 mmol, 3.00 eq.) were suspended in a mixture of THF (5 mL) and water (1 mL). The mixture was degassed for 15 min and $Pd(PPh_3)_4$ (10.4 mg, 0.009 mmol, 0.05 eq.) was added. After further degassing for 15 min the mixture was reaction at 85 °C for 21 h. After cooling to room temperature, the phases were separated and the aqueous phase was extracted with DCM (3 × 15 mL). The combined organic phases were dried over anhydrous $Na_2SO_4$ and the solvents were removed under reduced pressure. The crude product was purified by chromatography on a silica gel column with 5:1 (v:v) *n*-pentane/$Et_2O$ + 2% $NEt_3$ as an eluent. The product was obtained as a white solid (50.4 mg, 0.07 mmol, 36%). $^1H$ NMR (400 MHz, CDCl$_3$): δ [ppm] = 8.76 (dd, *J* = 2.2, 0.8 Hz, 1 H), 8.66 (dd, *J* = 2.3, 0.8 Hz, 1 H), 8.51 (ddd, *J* = 8.2, 1.7, 0.8 Hz, 2 H), 7.89 (dd, *J* = 8.1, 2.3 Hz, 1 H), 7.79 (dd, *J* = 8.2, 2.3 Hz, 1 H), 7.51 (s, 1 H), 7.20 (s, 1 H), 7.16 (s, 1 H), 7.13 (s, 1 H), 6.98 (s, 1 H), 6.97 (s, 1 H), 6.96−6.90 (m, 4 H), 6.82−6.78 (m, 4 H), 3.79 (s, 6 H), 2.43 (s, 3 H), 2.34 (s, 3 H), 2.28 (s, 3 H), 2.15 (s, 3 H), 2.02 (s, 3 H), 2.01 (s, 3 H).
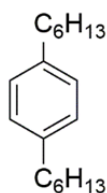


Compound **12**. This procedure followed a previously published protocol.[5] Dry $Et_2O$ (50 mL) was added to magnesium turnings (4.86 g, 200 mmol, 2.50 eq.) and 1-bromohexane (~3 mL from 28 mL, 200 mmol, 2.50 eq.) was added to start the Grignard reaction under $N_2$. Once the reaction had been initiated, the remaining portion of 1-bromohexane (25 mL) was added dropwise while keeping the reaction mixture at slight reflux. After complete addition, the mixture was heated to reflux for 5 h and then was allowed to reach room temperature. Inert conditions were applied to a second flask and 1,4-dichlorobenzene (11.76 g, 80.0 mmol, 1.00 eq.), $NiCl_2(dppp)$ (dppp = 1,3-bis(diphenylphosphino)propane) (81.3 mg, 0.15 mmol, $1.86 \cdot 10^3$ eq.) and dry $Et_2O$ (30 mL) were added to the second flask. This mixture was cooled to 0 °C and then the Grignard reagent from the first flask was added to the second flask over a dropping funnel under protection from air. After complete addition, the green solution was heated to reflux under $N_2$ for 15.5 h. After cooling to 0 °C, water (40 mL) and aqueous HCl solution (1 M, 120 mL) were added slowly. The organic phase was separated and the aqueous

layer was extracted with Et$_2$O (3 × 50 mL). The combined organic phases were washed with water (50 mL) and brine (50 mL) and dried over anhydrous Na$_2$SO$_4$. After removing the solvent under reduced pressure, the product was purified by chromatography on a silica gel column with *n*-pentane as an eluent. The pure product was obtained as a colorless oil (17.6 g, 71.4 mmol, 89%). $^1$H NMR (400 MHz, CDCl$_3$): δ [ppm] = 7.10 (s, 4 H), 2.63−2.54 (m, 4 H), 1.66−1.55 (m, 4 H), 1.43−1.26 (m, 12 H), 0.97−0.86 (m, 6 H).
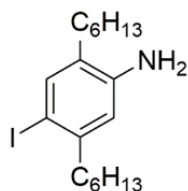


Compound **13**. This procedure followed a previously published protocol.[6] A mixture of sulfuric acid (95%, 54 mL) and acetic acid (36 mL) was cooled between −5 and −10 °C by direct addition of dry ice before 1,4-di-*n*-hexylbenzene **12** (17.6 g, 71.4 mmol, 1.00 eq.) was added under N$_2$. During the addition of **12**, the temperature was kept below 0 °C. After complete addition, a mixture of sulfuric acid (95%, 36 mL) and nitric acid (65%, 5.5 mL, 77.7 mmol, 1.08 eq.) previously cooled to −5 to −10 °C was added at 0 °C, and then the mixture was reacted for 10 min at −10 °C. The mixture was poured on an ice/water mixture (350 mL) and Et$_2$O (100 mL) was added. The organic phase was separated and the aqueous phase was extracted with Et$_2$O (3 × 100 mL). The combined organic phases were washed with brine (3 × 150 mL) and dried over anhydrous Na$_2$SO$_4$. After removal of the solvent under reduced pressure, the product was purified by chromatography on a silica gel column with *n*-pentane as an eluent. The pure product was obtained as a yellow oil (11.7 g, 40.1 mmol, 56%). $^1$H NMR (400 MHz, CDCl$_3$): δ [ppm] = 7.67 (d, *J* = 1.7 Hz, 1 H), 7.30 (dd, *J* = 7.9, 1.8 Hz, 1 H), 7.22 (d, *J* = 7.9 Hz, 1 H), 2.86−2.79 (m, 2 H), 2.67−2.60 (m, 2 H), 1.67−1.56 (m, 4 H), 1.41−1.24 (m, 12 H), 0.92−0.84 (m, 6 H).
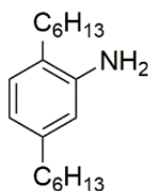
Compound **14**. This procedure followed a previously published protocol.[6] Compound **13** (11.5 g, 39.5 mmol, 1.00 eq.) and iron powder (8.96 g, 160 mmol, 4.05 eq.) were suspended in ethanol (50%, 400 mL) and concentrated aqueous HCl solution (12 M, 6.50 mL, 80.2 mmol, 2.03 eq.) was added. The reaction mixture was heated at 90 °C for 21 h, then cooled to room temperature and an aqueous KOH solution (4.50 g, 80.2 mmol, 2.03 eq.) was added. The resulting mixture was filtered over silica and washed with ethanol (4 × 50 mL). The filtrates were combined and the solvents were removed under reduced pressure. The residue was re-dissolved in DCM and dried over anhydrous $Na_2SO_4$. The solvent was removed under reduced pressure and the product was purified by chromatography on a silica gel column with 20:1 (v:v) *n*-pentane/EtOAc as an eluent. The product was obtained as a brown oil (6.34 g, 24.2 mmol, 61%). ^{1}H NMR (400 MHz, $CDCl_3$): δ [ppm] = 6.94 (d, $J = 7.6$ Hz, 1 H), 6.56 (dd, $J = 7.6$, 1.7 Hz, 1 H), 6.51 (d, $J = 1.6$ Hz, 1 H), 3.56 (broad s, 2 H), 2.54−2.36 (m, 4 H), 1.67−1.49 (m, 4 H), 1.44−1.22 (m, 12 H), 0.97−0.81 (m, 6 H).



Compound **15**. This procedure followed a previously published protocol.[6] A solution of compound **14** (1.44 g, 5.51 mmol, 1.00 eq.) in DMSO (30 mL) was stirred for 5 min at room temperature and then *N*-iodosuccinimide (1.24 g, 5.51 mmol, 1.00 eq.) was added. The reaction mixture was stirred at room temperature for 23 h and then water (60 mL) and $Et_2O$ (60 mL) were added. The organic phase was separated and the aqueous phase was extracted with $Et_2O$ (3 × 60 mL). The combined organic phases were dried over anhydrous $Na_2SO_4$. The solvent was removed under reduced pressure and the product was purified by chromatography on a silica gel column with 20:1 (v:v) *n*-pentane/EtOAc as an eluent. The product was obtained as a red oil (1.83 g, 4.72 mmol, 86%). ^{1}H NMR (400 MHz, $CDCl_3$): δ [ppm] = 7.40 (s, 1 H), 6.55 (s, 1 H), 3.57 (broad s, 2 H), 2.60−2.51 (m, 2 H), 2.42−2.35 (m, 2 H), 1.62−1.49 (m, 4 H), 1.43−1.24 (m, 12 H), 0.95−0.85 (m, 6 H).
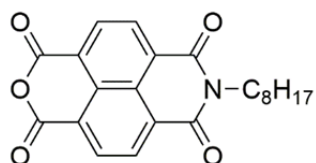
Compound **16**. The following procedure was adapted from literature.[7] 1,4,5,8-Naphthalenetetracarboxylic dianhydride (2.00 g, 7.46 mmol, 1.00 eq.) was suspended in a mixture of degassed water (20 mL) and degassed *n*-propanol (20 mL) under $N_2$. The mixture was protected from light and *n*-octylamine (6.00 mL, 36.3 mmol, 4.87 eq.) was added. The mixture was stirred for 10 min and then heated to 50 °C for 22 h. After cooling to room temperature, the reaction mixture was acidified with aqueous HCl solution (2 M) to pH 1 and stirred for 1 h. The resulting precipitate was filtered off and stirred in boiling acetic acid (18 M, 200 mL) for 2 h. After cooling to room temperature, the solution was diluted with DCM (400 mL) and extracted with water (400 mL). The organic phase was separated and dried over anhydrous $Na_2SO_4$. The solvent was removed under reduced pressure and the product was purified by chromatography on a silica gel column with 30:1 (v:v) DCM/acetone as an eluent. The product was obtained as a beige solid (1.57 g, 4.14 mmol, 55%). [1]H (400 MHz, $CDCl_3$): δ [ppm] = 8.81 (s, 4 H), 4.22−4.17 (m, 2 H), 1.46−1.23 (m, 12 H), 0.90−0.84 (m, 3 H).
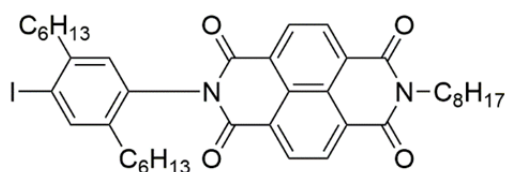


Compound **17**. A mixture of compound **15** (1.64 g, 4.23 mmol, 1.00 eq.) and compound **16** (1.77 g, 4.66 mmol, 1.10 eq.) in dry DMF (30 mL) was heated to reflux under $N_2$ for 22 h. After cooling to room temperature, water (75 mL) was added and the reaction mixture was extracted with DCM (4 × 100 mL). The combined organic phases were dried over anhydrous $Na_2SO_4$ and the solvents were removed under reduced pressure. After purification of the product by chromatography on a silica gel column with DCM as an eluent, a brown oil was obtained (2.19 g, 2.93 mmol, 69%). ^{1}H NMR (400 MHz, $CDCl_3$): δ [ppm] = 8.80 (s, 4 H), 7.88 (s, 1 H), 7.02 (s, 1 H), 4.26−4.16 (m, 2 H), 2.75−2.60 (m, 2 H), 2.43−2.29 (m, 2 H), 1.81−1.06 (m, 28 H), 0.91−0.84 (m, 6 H), 0.73−0.68 (m, 3 H). ESI-HRMS (*m/z*): calcd. for $C_{40}H_{49}N_2O_4I^-$: 748.2742; found: 748.2751.
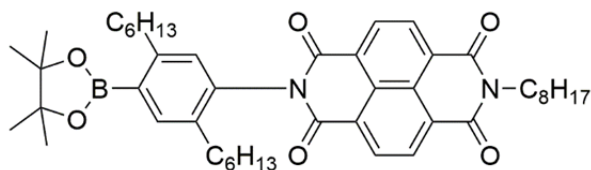
Compound **18**. A mixture of compound **17** (415 mg, 0.55 mmol, 1.00 eq.), bis(pinacolato)-diboron (211 mg, 0.83 mmol, 1.51 eq.) and KOAc (216 mg, 2.20 mmol, 4.00 eq.) in DMSO (12 mL) was degassed for 30 min. $Pd(PPh_3)_2Cl_2$ (38.6 mg, 0.055 mmol, 0.10 eq.) was added and the mixture was degassed further for 15 min and then heated to 100 °C under $N_2$ for 6.5 d. The mixture was diluted with water (25 mL), extracted with $Et_2O$ (4 × 40 mL) and the combined organic phases were dried over anhydrous $Na_2SO_4$. After removal of the solvent under reduced pressure, the product was purified by chromatography on a silica gel column with DCM as an eluent. The pure product was obtained as a brown solid (161 mg, 0.22 mmol, 40%). $^1H$ NMR (400 MHz, $CDCl_3$): δ [ppm] = 8.80 (s, 4 H), 7.84 (s, 1 H), 7.00 (s, 1 H), 4.24−4.18 (m, 2 H), 2.94−2.85 (m, 2 H), 2.42−2.35 (m, 2 H), 1.81−1.70 (m, 2 H), 1.63−1.08 (m, 38 H), 0.91−0.84 (m, 6 H), 0.71-0.65 (m, 3 H). ESI-HRMS (*m/z*): calcd. for $C_{46}H_{61}N_2O_6B^-$: 748.4636; found: 748.4630. Anal. calcd. for $C_{46}H_{61}N_2O_6B$: C, 73.78; H, 8.21; N, 3.74; found: C, 73.78; H, 7.99; N, 3.75.
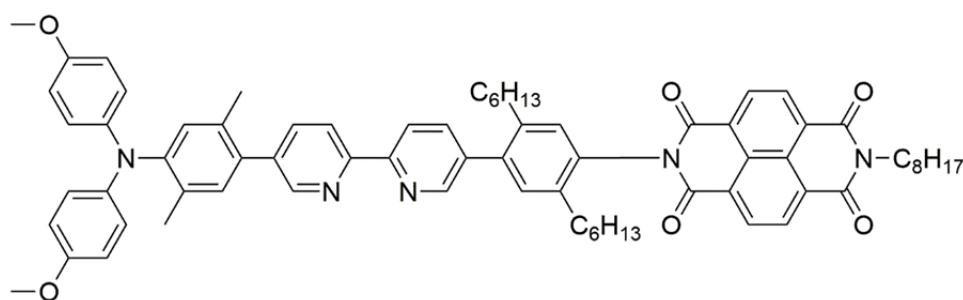


Ligand **19**. Compound **18** (161 mg, 0.22 mmol, 1.20 eq.), compound **10** (104 mg, 0.18 mmol, 1.00 eq.) and $Na_2CO_3$ (60.0 mg, 0.57 mmol, 3.15 eq.) were dissolved in a mixture of THF (8 mL) and water (2 mL) under $N_2$. The solution was degassed for 15 min, $Pd(PPh_3)_4$ (10.4 mg, 0.01 mmol, 0.05 eq.) was added and the mixture was degassed further for 10 min. The mixture was reacted at 85 °C for 66 h and then cooled to room temperature. Water was added and the mixture was extracted with DCM (3 × 25 mL). The combined organic phases were dried over anhydrous $Na_2SO_4$ and the solvents were removed under reduced pressure. After purification of the crude product by chromatography on a silica gel column with 4:1

(v:v) *n*-pentane/Et₂O as an eluent, a green solid was obtained (53.0 mg, 0.048 mmol, 27%). $^{1}$H NMR (400 MHz, CDCl₃): δ [ppm] = 8.87−8.82 (m, 4 H), 8.77 (dd, $J$ = 2.2, 0.8 Hz, 1 H), 8.74 (dd, $J$ = 2.2, 0.9 Hz, 1 H), 8.55−8.49 (m, 2 H), 7.90 (dd, $J$ = 8.1, 2.3 Hz, 1 H), 7.86 (dd, $J$ = 8.2, 2.3 Hz, 1 H), 7.34 (s, 1 H), 7.18 (s, 1 H), 7.14 (s, 1 H), 6.99 (s, 1 H), 6.96−6.91 (m, 4 H), 6.84−6.78 (m, 4 H), 4.28−4.17 (m, 2 H), 3.80 (s, 6 H), 2.68−2.58 (m, 2 H), 2.50−2.40 (m, 2 H), 2.24 (s, 3 H), 2.03 (s, 3 H), 1.84−1.68 (m, 2 H), 1.61−1.09 (m, 26 H), 0.91−0.84 (m, 3 H), 0.82−0.76 (m, 3 H), 0.73−0.64 (m, 3 H).
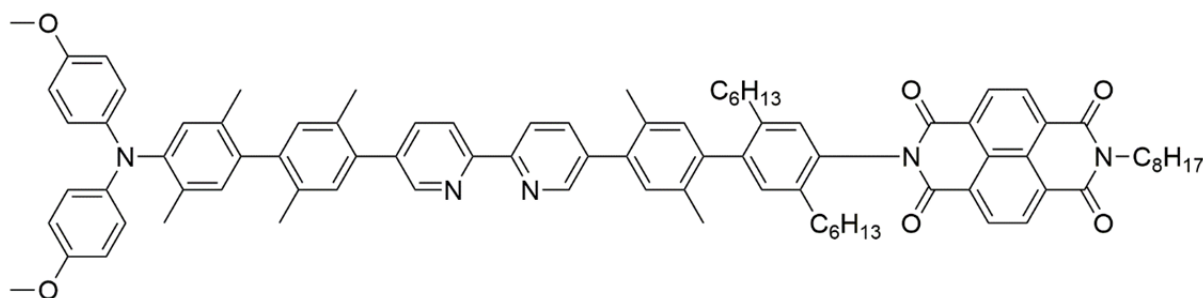


Ligand **20**. Compound **18** (58.5 mg, 0.08 mmol, 1.20 eq.), compound **11** (50.4 mg, 0.07 mmol, 1.00 eq.) and Na₂CO₃ (20.8 mg, 0.20 mmol, 3.02 eq.) were dissolved in a mixture of THF (2.5 mL) and water (0.5 mL) under N₂. The solution was degassed for 8 min, Pd(PPh₃)₄ (6.00 mg, 0.005 mmol, 0.08 eq.) was added and the mixture was degassed further for 6 min. The mixture was reacted at 85 °C for 67 h under N₂ and then cooled to room temperature. Water (5 mL) was added and the mixture was extracted with DCM (3 × 10 mL). The combined organic phases were dried over anhydrous Na₂SO₄ and the solvent was removed under reduced pressure. After purification of the crude product by chromatography on a silica gel column with 2:1 (v:v) *n*-pentane/Et₂O + 5% NEt₃ as an eluent, a greenish solid was obtained (52.0 mg, 0.04 mmol, 61%). $^{1}$H NMR (400 MHz, CDCl₃): δ [ppm] = 8.86−8.80 (m, 4 H), 8.77 (ddd, $J$ = 5.8, 2.2, 0.9 Hz, 2 H), 8.52 (ddd, $J$ = 8.1, 2.6, 0.8 Hz, 2 H), 7.90−7.87 (m, 2 H), 7.24 (s, 1 H), 7.22−7.20 (m, 3 H), 7.14 (s, 1 H), 7.12 (s, 1 H), 6.98 (s, 1 H), 6.96 (s, 1 H), 6.94−6.90 (m, 4 H), 6.81−6.76 (m, 4 H), 4.26−4.18 (m, 2 H), 3.78 (s, 6 H), 2.52−2.39 (m, 4 H), 2.36 (s, 3 H), 2.34 (s, 3 H), 2.18 (s, 3 H), 2.14 (s, 3 H), 2.01 (s, 3 H), 2.00 (s, 3 H), 1.81−1.72 (m, 2 H), 1.59−1.11 (m, 24 H), 0.92−0.84 (m, 5 H), 0.83−0.78 (m, 3 H), 0.74−0.68 (m, 3 H).
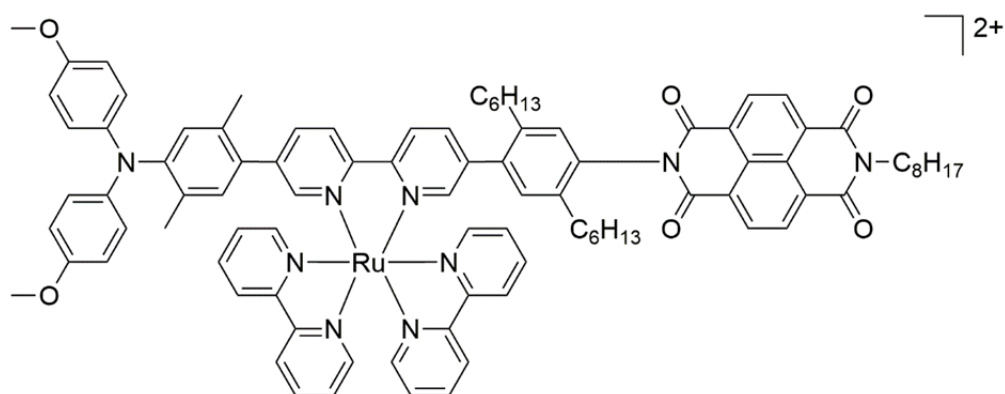
**TAA-ph₁-Ru-ph₁-NDI**. Ligand **19** (53.0 mg, 0.048 mmol, 1.00 eq.) and [Ru(bpy)₂]Cl₂ · 2H₂O (27.0 mg, 0.052 mmol, 1.09 eq.) in a mixture of ethanol (12 mL) and CHCl₃ (4 mL) were stirred at 90 °C under N₂ for 22 h. The solvents were removed under reduced pressure and the crude product was purified by chromatography on a silica gel column with acetone to 9:1 (v:v) acetone/water to 9:1 (v:v) acetone/water + 1% sat. aq. KNO₃ solution as eluents. Saturated aqueous KPF₆ solution was added to the chromatography fractions containing the desired Ru(II) complex, and the acetone was removed under reduced pressure. The aqueous residue was extracted with DCM, and the combined organic phases were washed with water afterwards. Removal of the solvent under reduced pressure yielded the product as a red solid (73.0 mg, 0.04 mmol, 84%). $^1$H NMR (400 MHz, CDCl₃): δ [ppm] = 8.82−8.76 (m, 4 H), 8.65−8.60 (m, 2 H), 8.53−8.42 (m, 4 H), 8.08−7.85 (m, 8 H), 7.77−7.72 (m, 3 H), 7.62 (d, $J$ = 1.9 Hz, 1 H), 7.59−7.51 (m, 2 H), 7.47−7.39 (m, 2 H), 7.27 (s, 1 H), 7.06 (s, 1 H), 6.99 (s, 1 H), 6.83−6.78 (m, 5 H), 6.75−6.70 (m, 4 H), 4.25−4.16 (m, 2 H), 3.73 (s, 6 H), 2.42−2.33 (m, 2 H), 2.29−2.20 (m, 1 H), 2.15−2.05 (m, 1 H), 1.89 (s, 3 H), 1.76 (s, 3 H), 1.53−0.95 (m, 28 H), 0.91−0.84 (m, 3 H), 0.79−0.73 (m, 3 H), 0.66−0.60 (m, 3 H). IR ν [cm$^{-1}$]: 2924 (w, br), 2853 (w, br), 1707 (w), 1666 (m), 1581 (w), 1502 (m), 1464 (m), 1446 (m), 1339 (m), 1238 (s), 1032 (w), 832 (s), 764 (s), 730 (m), 556 (s). ESI-HRMS (*m/z*): calcd. for C₉₂H₉₃N₉O₆Ru$^{2+}$: 760.8153; found: 760.8164. Anal. calcd. for C₉₂H₉₃N₉O₆RuP₂F₁₂: C, 60.99; H, 5.17; N, 6.96; found: C, 61.23; H, 5.51; N, 6.55.
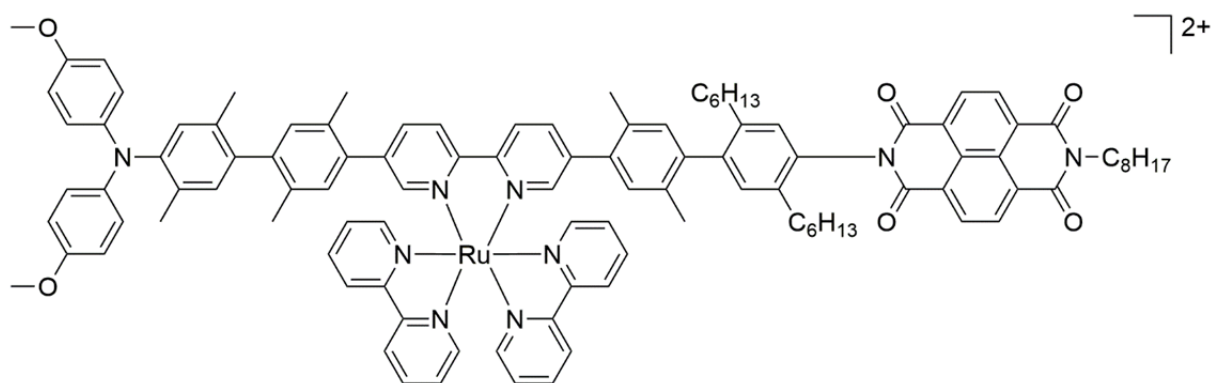
**TAA-ph₂-Ru-ph₂-NDI**. Ligand **20** (48.3 mg, 0.037 mmol, 1.00 eq.) and [Ru(bpy)₂]Cl₂ · 2H₂O (20.8 mg, 0.04 mmol, 1.09 eq.) in a mixture of ethanol (12 mL) and CHCl₃ (4 mL) were stirred at 90 °C under N₂ for 90 h. The solvents were removed under reduced pressure and the crude product was purified by chromatography on a silica gel column with acetone to 9:1 (v:v) acetone/water to 9:1 (v:v) acetone/water + 1% sat. aq. KNO₃ solution as eluents. Saturated aqueous KPF₆ solution was added to the chromatography fractions containing the desired Ru(II) complex, and the acetone was removed under reduced pressure. The residue was extracted with DCM (3 × 30 mL) and the combined organic phases were washed with water (30 mL). Removal of the solvent under reduced pressure yielded the product as a red solid (60.0 mg, 0.033 mmol, 90%). $^1$H NMR (400 MHz, CD₃CN): δ [ppm] = 8.76−8.70 (m, 4 H), 8.64 (dd, $J$ = 8.6, 2.9 Hz, 2 H), 8.56−8.49 (m, 4 H), 8.19−8.14 (m, 2 H), 8.13−8.08 (m, 2 H), 8.07−8.01 (m, 2 H), 7.97−7.94 (m, 2 H), 7.82−7.79 (m, 2 H), 7.74−7.71 (m, 2 H), 7.52−7.48 (m, 2 H), 7.42−7.37 (m, 2 H), 7.26 (s, 1 H), 7.15 (d, $J$ = 3.8 Hz, 1 H), 7.12−7.09 (m, 3 H), 7.01 (s, 1 H), 6.95 (s, 1 H), 6.91 (s, 1 H), 6.86−6.81 (m, 8 H), 4.17−4.12 (m, 2 H), 3.75 (s, 6 H), 2.50−2.39 (m, 3 H), 2.34−2.25 (m, 1 H), 2.10 (s, 3 H), 2.05 (s, 3 H), 2.04−1.99 (m, 6 H), 1.99 (s, 3 H), 1.91 (s, 3 H), 1.77−1.69 (m, 2 H), 1.51−1.06 (m, 26 H), 0.91−0.86 (m, 3 H), 0.78−0.72 (m, 3 H), 0.69−0.64 (m, 3 H). ESI-HRMS (*m/z*): calcd. for C₁₀₈H₁₀₉N₉O₆Ru²⁺: 864.8769; found: 864.8781. Anal. calcd. for C₁₀₈H₁₀₉N₉O₆RuP₂F₁₂ · 1.5H₂O: C, 63.37; H, 5.52; N, 6.16; found: C, 63.39; H, 5.81; N, 5.94.

Synthesis and product characterization data for [Ir(dF-CF$_3$-ppy)$_2$Cl]$_2$

The syntheses and characterization data of compounds **23** and **24** [8] have been reported previously. Nevertheless, full synthetic details are given below. Compounds **21** and **22** are commercially available.
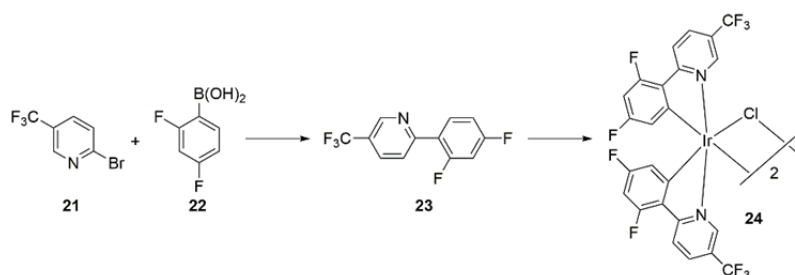


**Scheme S2.** Synthesis of **[Ir(dF-CF$_3$-ppy)$_2$Cl]$_2$ (24)**.
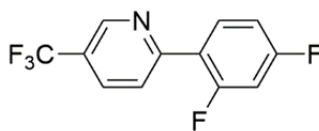


Compound **23**. The following procedure was adapted from a previously published protocol.[8] A flask with 2-bromo-5-(trifluoromethyl)pyridine **21** (3.39 g, 15.0 mmol, 1.00 eq.), (2,4-difluorophenyl) boronic acid **22** (2.84 g, 18.0 mmol, 1.20 eq.), Pd(OAc)$_2$ (101 mg, 0.45 mmol, 0.03 eq.), PPh$_3$ (236 mg, 0.90 mmol, 0.06 eq.) and K$_2$CO$_3$ (6.22 g, 45.0 mmol, 3.00 eq.) was evacuated and backfilled with N$_2$ three times. Toluene (20 mL), water (20 mL) and ethanol (4 mL) were added, and the reaction mixture was heated to reflux for 23 h under N$_2$. Once the mixture had cooled to room temperature, water was added (50 mL) and the phases were separated. The aqueous phase was extracted with Et$_2$O (3 × 20 mL) and the combined organic phases were washed with brine (3 × 30 mL) and dried over anhydrous Na$_2$SO$_4$. After removal of the solvent under reduced pressure, the product was purified by chromatography on a silica gel column with $n$-pentane to 7:1 (v:v) $n$-pentane/EtOAc as an eluent. The pure product was obtained as a white solid (2.95 g, 11.4 mmol, 76%). $^1$H NMR (400 MHz, CDCl$_3$): δ [ppm] = 8.96 (s, 1 H), 8.31−8.06 (m, 1 H), 8.01−7.97 (m, 1 H), 7.93−7.89 (m, 1 H), 7.08−7.02 (m, 1 H), 6.99−6.91 (m, 1 H).
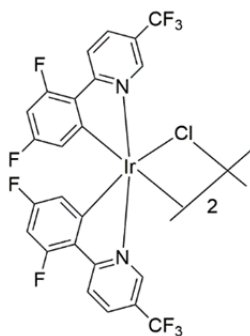
Precursor complex **24** (**[Ir(dF-CF₃-ppy)₂Cl]₂**). Following a previous published protocol,[8] compound **23** (1.02 g, 3.94 mmol, 2.05 eq.) and IrCl₃ · H₂O (608 mg, 1.92 mmol, 1.00 eq.) were dissolved in a mixture of water (7.5 mL) and 2-ethoxyethanol (15 mL) under N₂. The mixture was degassed for 30 min and then stirred at 120 °C for 23 h. Subsequently, it was cooled to room temperature and the resulting precipitate was collected and washed with water (3 × 20 mL). The crude product was obtained as a yellow solid (997 mg, 0.67 mmol, 35%).
¹H NMR (400 MHz, CDCl₃): δ [ppm] = 9.51 (d, *J* = 1.6 Hz, 3 H), 8.46 (dd, *J* = 8.8, 3.0 Hz, 4 H), 8.05 (dd, *J* = 8.7, 2.0 Hz, 4 H), 6.47–6.39 (m, 5 H), 5.07 (dd, *J* = 8.8, 2.3 Hz, 4 H).

Synthesis and product characterization data for triads TPA-ph$_1$-Ir-ph$_1$-AQ and TPA-ph$_2$-Ir-ph$_2$-AQ

The syntheses and characterization data of compounds **27** [9] and **33-35** [3] have been reported previously. Complete synthetic details and characterization data are given in the following. Compounds **25, 26** and **32** are commercially available.



**Scheme S3.** Synthesis of the key ligands for triad **TPA-ph$_1$-Ir-ph$_1$-AQ** and triad **TPA-ph$_2$-Ir-ph$_2$-AQ**.



Compound **27**. The following procedure was adapted from literature.[9] To a mixture of 4-chloroaniline **25** (2.56 g, 20.1 mmol, 1.00 eq.), 1-bromo-4-chlorobenzene **26** (9.56 g, 49.9 mmol, 2.48 eq.), PPh$_3$ (52.0 mg, 0.20 mmol, 0.01 eq.), Cs$_2$CO$_3$ (19.5 g, 59.8 mmol, 2.98 eq.) and Pd(PPh$_3$)$_2$Cl$_2$ (70.0 mg, 0.01 mmol, 0.005 eq.), dry *m*-xylene (160 mL) was
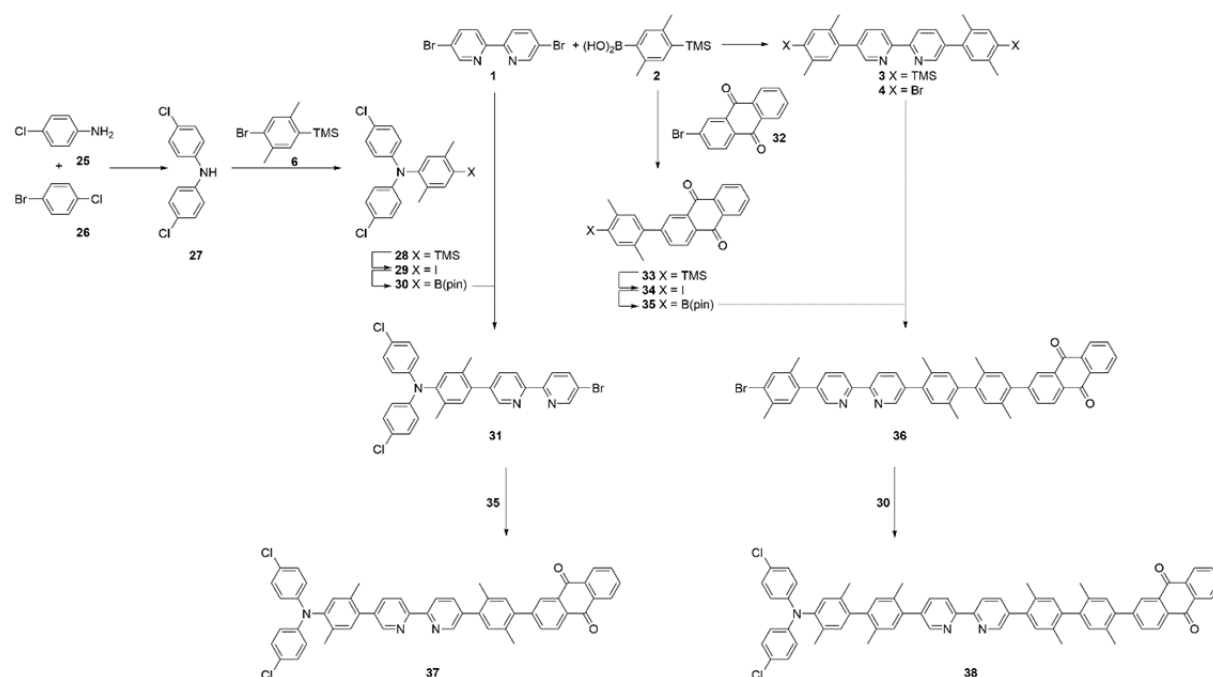
S18

added under $N_2$. After stirring at 155 °C for 19.5 h, the mixture was cooled to near room temperature before water (150 mL) was added. The aqueous phase was extracted with $Et_2O$ (3 × 200 mL) and the combined organic phases were dried over anhydrous $Na_2SO_4$. After removal of the solvents under reduced pressure, the product was purified by chromatography on a silica gel column with 4:1 (v:v) *n*-pentane/$Et_2O$ as an eluent. The pure product was obtained as a brown solid (3.55 g, 14.9 mmol, 74%). $^1$H NMR (400 MHz, $CDCl_3$): δ [ppm] = 7.25−7.20 (m, 4 H), 6.99−6.93 (m, 4 H), 5.65 (broad s, 1 H).
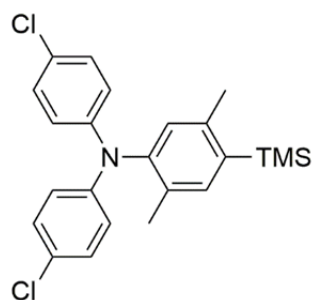


Compound **28**. A mixture of compound **27** (1.22 g, 5.12 mmol, 1.00 eq.), compound **6** (1.45 g, 5.64 mmol, 1.10 eq.), $Pd(dba)_2$ (147 mg, 0.26 mmol, 0.05 eq.), tri-*tert*-butylphosphonium tetrafluoroborate (74.3 mg, 0.26 mmol, 0.05 eq.) and potassium *tert*-butoxide (1.72 g, 15.3 mmol, 3.00 eq.) was suspended in dry toluene (25 mL) under $N_2$. The reaction mixture was degassed for 10 min and then stirred at 90 °C for 16 h. After cooling to room temperature, water (100 mL) was added. The mixture was extracted with DCM (3 × 100 mL) and the combined organic phases were dried over anhydrous $Na_2SO_4$. After removal of the solvents under reduced pressure, the product was purified by chromatography on a silica gel column with *n*-pentane as an eluent. The pure product was obtained as a white solid (1.20 g, 2.90 mmol, 57%). $^1$H NMR (400 MHz, $CDCl_3$): δ [ppm] = 7.27 (s, 1 H), 7.18–7.13 (m, 4 H), 6.90–6.85 (m, 4 H), 6.82 (s, 1 H), 2.34 (s, 3 H), 1.95 (s, 3 H), 0.33 (s, 9 H).
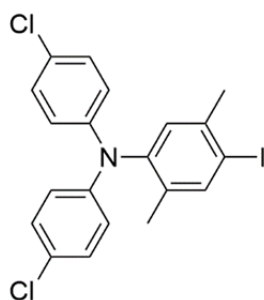
Compound **29**. Compound **28** (1.04 g, 2.51 mmol, 1.00 eq.) was dissolved in dry DCM (20 mL) and cooled to −78 °C under $N_2$. Iodine monochloride (0.26 mL, 5.10 mmol, 2.03 eq.) in dry DCM (10 mL) was added dropwise and the reaction mixture was stirred for 10 min before saturated aqueous $Na_2S_2O_3$ solution was added. The mixture was warmed to room temperature and extracted with DCM (3 × 100 mL). The combined organic phases were dried over anhydrous $Na_2SO_4$, and the solvent was removed under reduced pressure. After purification of the product by chromatography on a silica gel column with *n*-pentane as an eluent, a white solid was obtained (1.11 g, 2.37 mmol, 94%). ^{1}H NMR (400 MHz, $CDCl_3$): δ [ppm] = 7.69 (s, 1 H), 7.20–7.13 (m, 4 H), 6.92 (s, 1 H), 6.88–6.82 (m, 4 H), 2.32 (s, 3 H), 1.91 (s, 3 H).
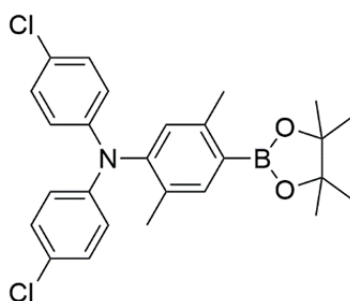


Compound **30**. A mixture of compound **29** (0.98 g, 2.09 mmol, 1.00 eq.), bis(pinacolato)diboron (797 mg, 3.14 mmol, 1.50 eq.), KOAc (820 mg, 8.36 mmol, 4.00 eq.) and $Pd(PPh_3)_2Cl_2$ (73.3 mg, 0.10 mmol, 0.05 eq.) in DMSO (18 mL) was degassed for 10 min under $N_2$. The mixture was stirred at 90 °C for 22 h and then cooled to room temperature before saturated aqueous $NH_4Cl$ solution (20 mL) and water (60 mL) were added. The mixture was extracted with DCM (3 × 100 mL) and the combined organic phases were dried over anhydrous $Na_2SO_4$. After removal of the solvents under reduced pressure, the product was purified by chromatography on a silica gel column with 10:1 (v:v) *n*-pentane/$Et_2O$ as an eluent. The pure product was obtained as a white solid (861 mg, 1.84 mmol, 88%). ^{1}H NMR

(400 MHz, CDCl$_3$): δ [ppm] = 7.63 (s, 1 H), 7.16–7.12 (m, 4 H), 6.88–6.83 (m, 5 H), 2.43 (s, 3 H), 1.94 (s, 3 H), 1.35 (s, 12 H).
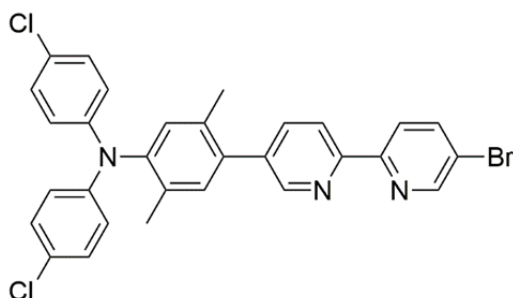


Compound **31**. Compound **30** (250 mg, 0.53 mmol, 1.00 eq.), compound **1** (250 mg, 0.80 mmol, 1.51 eq.) and Na$_2$CO$_3$ (169 mg, 1.59 mmol, 3.00 eq.) were dissolved in a mixture of THF (10 mL) and water (2 mL) and degassed for 20 min. Pd(PPh$_3$)$_4$ (30.6 mg, 0.03 mmol, 0.05 eq.) was added and the mixture was degassed further for 10 min and then stirred at 85 °C under N$_2$ for 15 h. Once the reaction mixture had nearly reached room temperature, water (10 mL) was added, and then it was extracted with DCM (3 × 20 mL). The combined organic phases were dried over anhydrous Na$_2$SO$_4$ and the solvents were removed under reduced pressure. The product was purified by chromatography on two silica gel columns. First, a chromatography with 4:1 (v:v) *n*-pentane/DCM + 2% MeOH as an eluent was performed. Further purification was possible on a second column using 7:1 (v:v) *n*-pentane/EtOAc as an eluent. The product was obtained as a yellow solid (65.0 mg, 0.11 mmol, 21%). $^1$H NMR (400 MHz, CDCl$_3$): δ [ppm] = 8.76 (d, *J* = 2.1 Hz, 1 H), 8.69 (d, *J* = 1.7 Hz, 1 H), 8.47 (d, *J* = 8.2 Hz, 1 H), 8.42 (d, *J* = 8.2 Hz, 1 H), 7.99 (dd, *J* = 8.5, 2.3 Hz, 1 H), 7.87 (d, *J* = 7.7 Hz, 1 H), 7.22–7.17 (m, 4 H), 7.14 (s, 1 H), 7.01 (s, 1 H), 6.96–6.90 (m, 4 H), 2.23 (s, 3 H), 2.01 (s, 3 H).
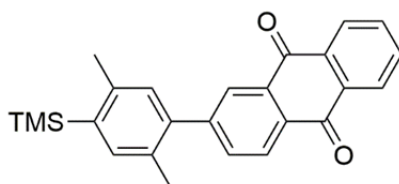


Compound **33**. Following a previously published protocol,[3] 2-bromoanthracene-9,10-dione **32** (4.31 g, 15.0 mmol, 1.00 eq.), compound **2** (4.00 g, 18.0 mmol, 1.20 eq.), Na$_2$CO$_3$ (4.77 g, 45.0 mmol, 3.00 eq.) and Pd(PPh$_3$)$_4$ (873 mg, 0.76 mmol, 0.05 eq.) were dissolved in a mixture of THF (60 mL) and water (15 mL) under N$_2$. This mixture was degassed for 15 min, stirred at 85 °C for 20 h and then cooled to room temperature. Water (10 mL) was added and

the product was extracted with DCM (3 × 30 mL). The combined organic phases were dried over anhydrous Na$_2$SO$_4$ and the solvents were removed under reduced pressure. After purification of the product by chromatography on a silica gel column with neat DCM to 2/1 (v:v) *n*-pentane/DCM as an eluent, a yellow solid was obtained (4.37 g, 11.4 mmol, 76%). ^{1}H NMR (400 MHz, CDCl$_3$): δ [ppm] = 8.36–8.29 (m, 4 H), 7.83–7.76 (m, 3 H), 7.42 (s, 1 H), 7.12 (s, 1 H), 2.50 (s, 3 H), 2.32 (s, 3 H), 0.39 (s, 9 H).
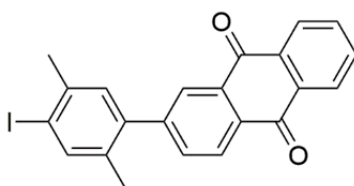


Compound **34**. The following procedure was adapted from literature.[3] At room temperature, compound **33** (4.19 g, 10.9 mmol, 1.00 eq.) was dissolved in dry DCM (45 mL) and iodine monochloride (0.84 mL, 16.4 mmol, 1.50 eq.) in dry DCM (11 mL) was added slowly under N$_2$. After stirring for 1 h, saturated aqueous Na$_2$S$_2$O$_3$ solution (40 mL) was added and the aqueous phase was extracted with DCM (3 × 100 mL). The combined organic phases were dried over anhydrous Na$_2$SO$_4$ and the solvent was removed under reduced pressure. The crude product was purified by chromatography on a silica gel column with 1:1 (v:v) *n*-pentane/DCM to DCM as an eluent. The pure product was obtained as a yellow solid (2.78 g, 6.34 mmol, 58%). ^{1}H NMR (400 MHz, CDCl$_3$): δ [ppm] = 8.38–8.31 (m, 3 H), 8.25 (d, *J* = 1.6 Hz, 1 H), 7.85–7.81 (m, 2 H), 7.79 (s, 1 H), 7.73 (dd, *J* = 8.0, 1.8 Hz, 1 H), 7.14 (s, 1 H), 2.45 (s, 3 H), 2.23 (s, 3 H).
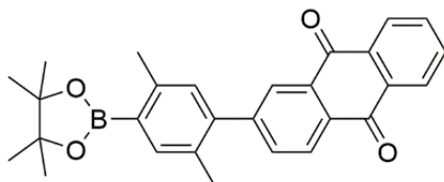


Compound **35**. Following a previously published protocol,[3] a mixture of compound **34** (2.78 g, 6.34 mmol, 1.00 eq.), bis(pinacolato)diboron (2.41 g, 9.51 mmol, 1.50 eq.), KOAc (2.49 g, 25.4 mmol, 4.00 eq.) and Pd(PPh$_3$)$_2$Cl$_2$ (225 mg, 0.32 mmol, 0.05 eq.) in DMSO (40 mL) was degassed for 15 min under N$_2$. The mixture was stirred at 90 °C for 14 h and then cooled to room temperature. Subsequently, water (130 mL) and saturated aqueous NH$_4$Cl

solution (26 mL) were added. The mixture was extracted with Et$_2$O (3 × 100 mL) and the combined organic phases were dried over anhydrous Na$_2$SO$_4$. After removal of the solvent under reduced pressure, the product was purified by chromatography on a silica gel column with 4:1 (v:v) *n*-pentane/Et$_2$O as an eluent. The pure product was obtained as a yellow solid (2.02 g, 4.61 mmol, 73%). $^1$H NMR (400 MHz, CDCl$_3$): δ [ppm] = 8.38–8.32 (m, 3 H), 8.28 (d, $J$ = 1.6 Hz, 1 H), 7.85–7.80 (m, 2 H), 7.76 (dd, $J$ = 8.0, 1.8 Hz, 1 H), 7.72 (s, 1 H), 7.11 (s, 1 H), 2.56 (s, 3 H), 2.28 (s, 3 H), 1.37 (s, 12 H).
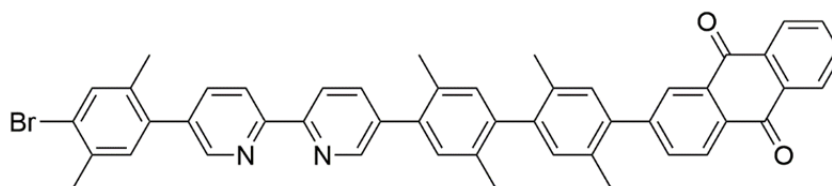


Compound **36**. Compound **35** (65.5 mg, 0.15 mmol, 1.00 eq.), compound **4** (156 mg, 0.30 mmol, 2.00 eq.) and Na$_2$CO$_3$ (47.8 mg, 0.45 mmol, 3.00 eq.) were dissolved in a mixture of THF (5 mL) and water (1 mL) and degassed for 15 min. Pd(PPh$_3$)$_4$ (9.20 mg, 0.008 mmol, 0.05 eq.) was added and the mixture was degassed further for 15 min and then stirred at 85 °C under N$_2$ for 23 h. Once the reaction mixture had nearly reached room temperature, water (15 mL) was added, and then it was extracted with DCM (2 × 20 mL), Et$_2$O (1 × 20 mL) and CHCl$_3$ (3 × 20 mL). The combined organic phases were dried over anhydrous Na$_2$SO$_4$ and the solvents were removed under reduced pressure. The product was purified by chromatography on two separate silica gel columns. First, a chromatography with 2:1 (v:v) *n*-pentane/Et$_2$O as an eluent was performed. Further purification was possible on a column with DCM + 2% MeOH as an eluent. The product was obtained as a yellow solid (61.1 mg, 0.08 mmol, 54%). $^1$H NMR (400 MHz, CDCl$_3$): δ [ppm] = 8.79 (s, 1 H), 8.67 (s, 1 H), 8.55 (d, $J$ = 7.8 Hz, 2 H), 8.40 (d, $J$ = 8.0 Hz, 1 H), 8.38–8.34 (m, 3 H), 7.95–7.91 (m, 1 H), 7.88–7.80 (m, 4 H), 7.52 (s, 1 H), 7.23 (s, 2 H), 7.16 (s, 1 H), 7.14 (d, $J$ = 3.2 Hz, 2 H), 2.43 (s, 3 H), 2.36 (s, 3 H), 2.34 (s, 3 H), 2.28 (s, 3 H), 2.17 (s, 6 H).
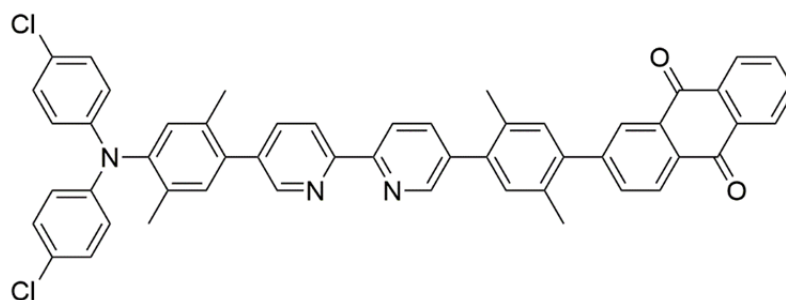
Ligand **37**. Compound **31** (119 mg, 0.35 mmol, 1.00 eq.), compound **35** (184 mg, 0.42 mmol, 1.20 eq.) and $Na_2CO_3$ (114 mg, 1.08 mmol, 3.09 eq.) were dissolved in a mixture of THF (5 mL) and water (1 mL) and degassed for 15 min. $Pd(PPh_3)_4$ (23.0 mg, 0.02 mmol, 0.06 eq.) was added, and the reaction mixture was degassed further for 15 min prior to stirring at 85 °C under $N_2$ for 42.5 h. Once the reaction mixture had nearly reached room temperature, water (10 mL) was added, and then it was extracted with DCM (3 × 20 mL). The combined organic phases were dried over anhydrous $Na_2SO_4$ and the solvents were removed under reduced pressure. The crude product was purified by chromatography on a silica gel column with 4:1 (v:v) *n*-pentane/EtOAc as an eluent. The pure product was obtained as a yellow solid (39.4 mg, 0.05 mmol, 14%). $^1$H NMR (400 MHz, CDCl$_3$): δ [ppm] = 8.76 (d, $J$ = 11.4 Hz, 2 H), 8.62–8.54 (m, 2 H), 8.41 (d, $J$ = 8.0 Hz, 1 H), 8.38–8.33 (m, 3 H), 7.91 (t, $J$ = 9.0 Hz, 2 H), 7.86–7.82 (m, 3 H), 7.28 (d, $J$ = 2.8 Hz, 2 H), 7.23–7.17 (m, 5 H), 7.02 (s, 1 H), 6.97–6.92 (m, 4 H), 2.38 (s, 3 H), 2.36 (s, 3 H), 2.26 (s, 3 H), 2.03 (s, 3 H).
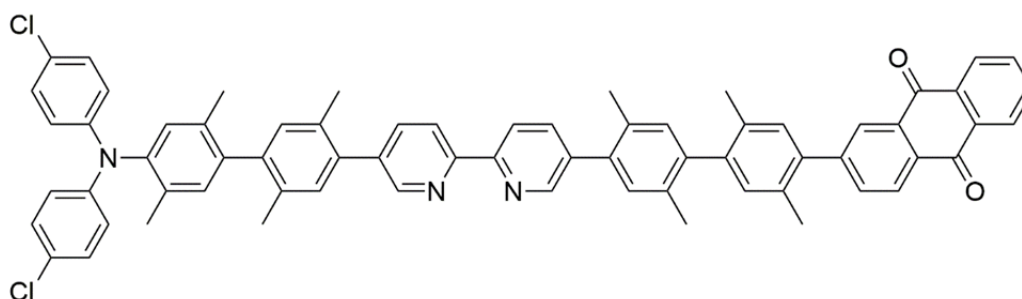


Ligand **38**. Compound **36** (61.1 mg, 0.08 mmol, 1.00 eq.), compound **30** (45.7 mg, 0.10 mmol, 1.20 eq.) and $Na_2CO_3$ (26.0 mg, 0.25 mmol, 3.02 eq.) in THF (5 mL) and water (1 mL) were degassed for 15 min. Then, $Pd(PPh_3)_4$ (5.10 mg, 0.004 mmol, 0.05 eq.) was added and the mixture was degassed further for 15 min. The reaction mixture was stirred at 85 °C under $N_2$ for 23 h and then cooled to room temperature. The mixture was diluted with water (15 mL) and extracted with DCM (3 × 10 mL). The combined organic phases were dried over anhydrous $Na_2SO_4$ and the solvents were removed under reduced pressure. The

product was purified by chromatography on a silica gel column with 4:1 (v:v) *n*-pentane/EtOAc as an eluent and was obtained as an orange solid (73.6 mg, 0.07 mmol, 90%). $^1$H NMR (400 MHz, CDCl$_3$): δ [ppm] = 8.80 (dd, *J* = 4.6, 1.9 Hz, 2 H), 8.58 (d, *J* = 8.1 Hz, 2 H), 8.40 (d, *J* = 8.0 Hz, 1 H), 8.38 (d, *J* = 1.7 Hz, 1 H), 8.37–8.33 (m, 2 H), 7.96–7.91 (m, 2 H), 7.86 (dd, *J* = 8.0, 1.8 Hz, 1 H), 7.84–7.80 (m, 2 H), 7.25 (s, 2 H), 7.23 (s, 1 H), 7.22–7.17 (m, 4 H), 7.16–7.13 (m, 3 H), 7.05 (s, 1 H), 7.00 (s, 1 H), 6.97–6.93 (m, 4 H), 2.39–2.32 (m, 9 H), 2.19 (s, 6 H), 2.16 (s, 3 H), 2.05 (s, 3 H), 2.02 (s, 3 H).
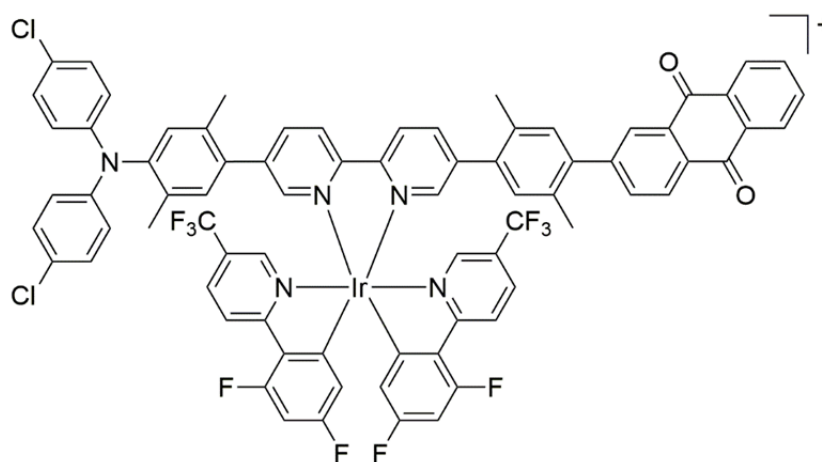


**TPA-ph$_1$-Ir-ph$_1$-AQ**. Similar complexation conditions as reported previously were used.[10] Ligand **37** (9.20 mg, 0.012 mmol, 2.70 eq.) and **[Ir(dF-CF$_3$-ppy)$_2$Cl]$_2$** precursor complex **24** (6.30 mg, 4.23 · 10$^{-3}$ mmol, 1.00 eq.) were suspended in ethylene glycol (2 mL) and stirred at 150 °C under N$_2$ for 22 h. After cooling to room temperature, water (20 mL) was added and the aqueous phase was extracted with DCM (3 × 10 mL). The combined organic phases were dried over anhydrous Na$_2$SO$_4$ and the solvents were removed under reduced pressure. The product was purified by chromatography on a silica gel column with acetone to 9:1 (v:v) acetone/water as eluents. To the chromatography fractions containing the desired complex, saturated aqueous KPF$_6$ solution was added and acetone was removed under reduced pressure. The aqueous residue was extracted with DCM (3 × 10 mL) and the combined organic phases were washed with water (10 mL) afterwards. After drying over anhydrous Na$_2$SO$_4$, the solvent was removed under reduced pressure. The resulting residue was then dissolved in a minimum of acetone, precipitated by adding an excess of *n*-pentane and filtered off. The product was obtained as a yellow solid (9.00 mg, 5.42 · 10$^{-3}$ mmol, 64%). $^1$H NMR (400 MHz, acetone-d$_6$): δ [ppm] = 9.07 (dd, *J* = 8.4, 5.5 Hz, 2 H), 8.68–8.62 (m, 2 H), 8.51 (ddd, *J* = 13.3, 8.4, 2.0 Hz, 2 H), 8.45 (d, *J* = 8.9 Hz, 2 H), 8.39–8.30 (m, 5 H), 8.24 (s, 2 H),

8.20 (d, $J$ = 1.7 Hz, 1 H), 8.00–7.96 (m, 2 H), 7.94 (dd, $J$ = 8.0, 1.8 Hz, 1 H), 7.34 (s, 1 H), 7.32–7.27 (m, 4 H), 7.25 (s, 2 H), 7.09 (s, 1 H), 6.96–6.91 (m, 4 H), 6.91–6.83 (m, 2 H), 6.07–6.01 (m, 2 H), 2.31 (s, 3 H), 2.17 (s, 3 H), 2.05 (s, 3 H), 2.00 (s, 3 H). ESI-HRMS ($m/z$): calcd. for $C_{76}H_{47}N_5O_2Cl_2F_{10}Ir^+$: 1514.2564; found: 1514.2569. Anal. Calcd. for $C_{76}H_{47}N_5O_2Cl_2IrPF_{16} \cdot H_2O$: C, 54.39; H, 2.94; N, 4.17; found: C, 54.29; H, 3.17; N, 4.30.
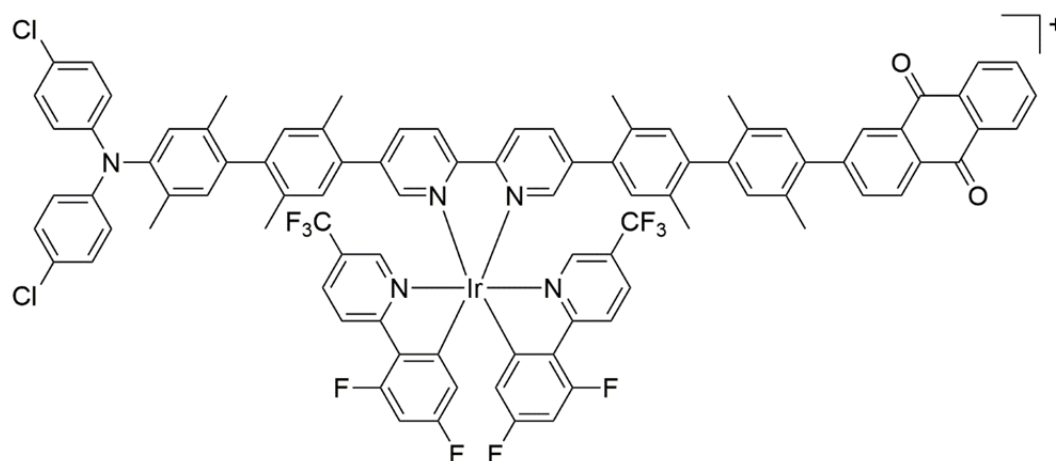


**TPA-ph₂-Ir-ph₂-AQ**. Similar complexation conditions as reported previously were used.[10] Ligand **38** (40.0 mg, 0.039 mmol, 2.20 eq.) and **[Ir(dF-CF₃-ppy)₂Cl]₂** precursor complex **24** (26.7 mg, 0.018 mmol, 1.00 eq.) were suspended in ethylene glycol (3 mL) and stirred at 150 °C under $N_2$. After 13 h, AgNO₃ (6.50 mg, 0.038 mmol, 2.10 eq.) was added and the mixture was stirred further for 22 h under protection from light. The mixture was allowed to reach room temperature, and then water (20 mL) was added and the aqueous phase was extracted with DCM (3 × 20 mL). The combined organic phases were washed with water (10 mL) and dried over anhydrous $Na_2SO_4$. After removal of the solvents under reduced pressure, the product was purified by chromatography on two silica gel columns. First, a chromatography with acetone to 9:1 (v:v) acetone/water as eluents was performed. To the chromatography fractions containing the desired complex, saturated aqueous KPF₆ solution was added and acetone was removed under reduced pressure. The aqueous residue was extracted with DCM (3 × 20 mL) and the combined organic phases were washed with water (10 mL) afterwards. After drying over anhydrous $Na_2SO_4$, the solvent was removed under reduced pressure. Further purification was possible with a column using 5:1 (v:v) DCM/acetone as an eluent. The resulting product was then dissolved in a minimum of acetone, precipitated by adding an excess of *n*-pentane and filtered off. The pure product was obtained as a yellow solid (27.5 mg, 14.7 · 10⁻³ mmol, 41%). ¹H NMR (400 MHz, CD₃OD):

δ [ppm] = 8.97–8.92 (m, 2 H), 8.65–8.59 (m, 2 H), 8.47–8.41 (m, 2 H), 8.41–8.30 (m, 5 H), 8.27 (d, $J$ = 1.7 Hz, 1 H), 8.16–8.12 (m, 2 H), 7.95–7.89 (m, 5 H), 7.27–7.17 (m, 7 H), 7.11 (s, 1 H), 7.09 (s, 1 H), 7.07 (d, $J$ = 3.5 Hz, 1 H), 7.01 (s, 2 H), 6.97–6.92 (m, 4 H), 6.87–6.78 (m, 2 H), 5.86 (dt, $J$ = 8.1, 2.2 Hz, 2 H), 2.31 (s, 3 H), 2.16–2.06 (m, 15 H), 2.01 (s, 3 H), 1.97 (d, $J$ = 4.6 Hz, 3 H). ESI-HRMS ($m/z$): calcd. for $C_{92}H_{63}N_5O_2Cl_2F_{10}Ir^+$: 1722.3819; found: 1722.3824. Anal. Calcd. for $C_{92}H_{63}N_5O_2Cl_2IrPF_{16} \cdot 3H_2O$: C, 57.47; H, 3.58; N, 3.93; found: C, 57.47; H, 3.62; N, 3.64.
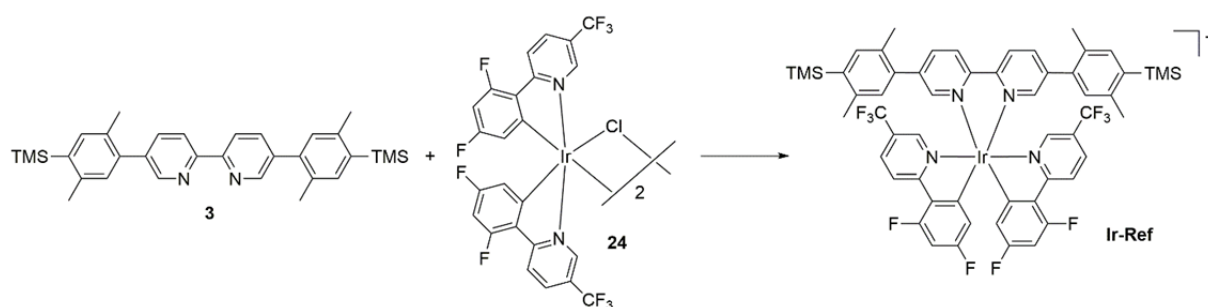
**Scheme S4**. Synthesis of **Ir-Ref**.
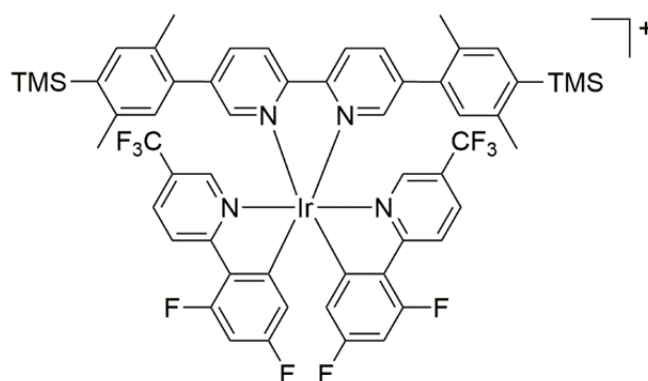


Compound **Ir-Ref**. Similar complexation conditions as reported previously were used.[10] Compound **3** (20.0 mg, 0.039 mmol, 2.21 eq.) and **[Ir(dF-CF₃-ppy)₂Cl]₂** precursor complex **24** (26.3 mg, 0.018 mmol, 1.00 eq.) were suspended in ethylene glycol (2 mL) and stirred at 150 °C under $N_2$ for 21.5 h. After cooling to room temperature, water (20 mL) was added and the aqueous phase was extracted with DCM (3 × 10 mL). The combined organic phases were dried over anhydrous $Na_2SO_4$ and the solvent was removed under reduced pressure. The product was purified by chromatography on a silica gel column with acetone to 9:1 (v:v) acetone/water as an eluent. To the chromatography fractions containing the desired complex, saturated aqueous $KPF_6$ solution was added and acetone was removed under reduced pressure. The aqueous residue was extracted with DCM (3 × 10 mL) and the combined organic phases were washed with water (10 mL) afterwards. After drying over anhydrous $Na_2SO_4$, the solvent was removed under reduced pressure. The resulting residue was then dissolved in a minimum of acetone, precipitated by adding an excess of *n*-pentane and filtered off. The product was obtained as a yellow solid (29.6 mg, 0.022 mmol, 61%). ¹H NMR (400 MHz, acetone-d₆): δ [ppm] = 9.01 (d, *J* = 8.1 Hz, 2 H), 8.63 (dd, *J* = 8.8, 2.6 Hz, 2 H), 8.46–8.40 (m,

4 H), 8.28 (d, $J$ = 1.6 Hz, 2 H), 8.20–8.16 (m, 2 H), 7.38 (s, 2 H), 7.01 (s, 2 H), 6.89–6.81 (m, 2 H), 6.00 (dd, $J$ = 8.4, 2.3 Hz, 2 H), 2.42 (s, 6 H), 2.07 (s, 6 H), 0.33 (s, 18 H). ESI-HRMS ($m/z$): calcd. for $C_{56}H_{50}N_4F_{10}Si_2Ir^+$: 1217.3040; found: 1217.3045. Anal. Calcd. for $C_{56}H_{50}N_4Si_2IrPF_{16} \cdot 0.5H_2O$: C, 49.05; H, 3.75; N, 4.09; found: C, 49.30; H, 4.15; N, 4.36.

## Equipment and methods

^{1}H NMR spectroscopy was performed on a Bruker Avance III instrument operating at 400 MHz frequency. The instrument was equipped with a direct observe 5-mm BBFO smart probe. Mass spectra were measured on a Bruker maxis 4G QTOF EDI spectrometer by Dr. Heinz Nadig in the Department of Chemistry at University of Basel. Elemental analyses were performed by Ms. Sylvie Mittelheisser on a Vario Micro Cube instrument in the Department of Chemistry at University of Basel.

For cyclic voltammetry, a Versastat3-200 potentiostat from Princeton Applied Research was used. A silver wire served as the counter electrode and a glassy carbon disk electrode was used as a working electrode. The reference electrode was an SCE and the measurements performed in $CH_3CN$ were made using 0.1 M $TBAPF_6$ as an electrolyte. For all measurements a potential scan rate of 0.1 V/s was applied. A Cary 5000 instrument from Varian was used for optical absorption spectroscopy. Chemical oxidation was achieved via UV-Vis titration of the investigated compound with copper(II) perchlorate as an oxidant in $CH_3CN$. Chemical reduction was performed in dry THF with sodium as a reductant. For spectro-electrochemical UV-Vis measurements, a Pt grid electrode in a quartz cuvette was used. SCE served as a reference electrode and a platinum wire was employed as a counter electrode. The electrodes were connected to the potentiostat mentioned above. Transient absorption spectra were measured on an LP920-KS instrument from Edinburgh Instruments. A Quantel Brilliant b laser with a frequency-doubled output was used for excitations at 532 nm for the **TAA-ph$_n$-Ru-ph$_n$-NDI** triads. Excitation of **TPA-ph$_1$-Ir-ph$_1$-AQ** occurred at 450 nm using an OPO from Opotek attached to the same laser system, and **TPA-ph$_2$-Ir-ph$_2$-AQ** was excited at 420 nm using the same laser/OPO combination. The laser pulse duration was ca. 10 ns. The pulse frequency was 10 Hz and the typical pulse energy for transient absorption studies was 15 mJ. For the detection of the transient absorption spectra, an iCCD camera from Andor was used. Kinetic studies with single-wavelength detection were made using a photomultiplier tube. Temperature changes were directly applied to the cuvette holder using a temperature controller from Edinburgh Instruments. De-aerated conditions using home-built quartz cuvettes were applied for all optical spectroscopic experiments. Oxygen was removed using the freeze-pump-thaw technique. For the emission measurements, a Fluorolog-322 instrument from Horiba Jobin-Yvon was used.

The optical absorption spectra of **TAA-ph$_1$-Ru-ph$_1$-NDI**, **TAA-ph$_2$-Ru-ph$_2$-NDI**, **TPA-ph$_1$-Ir-ph$_1$-AQ** and **TPA-ph$_2$-Ir-ph$_2$-AQ** were measured in CH$_3$CN at 20 °C and are shown in Figure S1 and Figure S2. The spectra of the Ru(bpy)$_3^{2+}$ photosensitizer reference complex and the **Ir-Ref** photosensitizer reference complex, as well as the free ligands **20** and **38**, are also included in these figures. Due to solubility reasons, ligand **20** was measured in DCM.
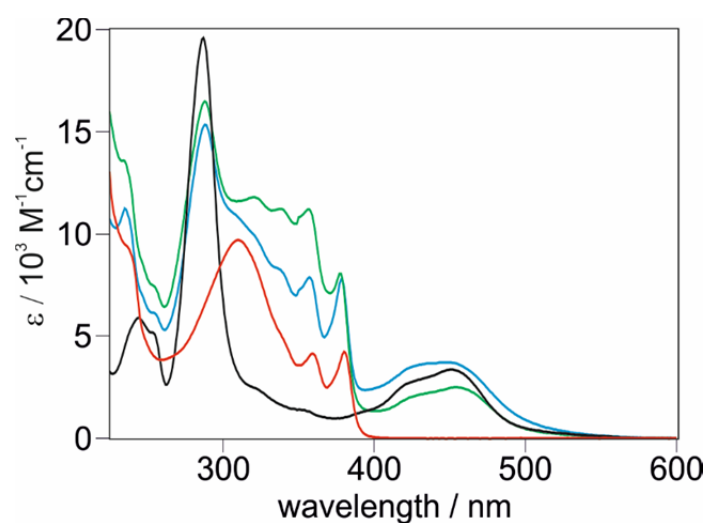


**Figure S1.** UV-Vis spectra of **TAA-ph$_1$-Ru-ph$_1$-NDI** (blue), **TAA-ph$_2$-Ru-ph$_2$-NDI** (green) and Ru(bpy)$_3^{2+}$ (black) in CH$_3$CN at 20 °C. Ligand **20** (red) was measured in DCM at 20 °C.

The spectra of the triads exhibit MLCT absorption bands at around 450 nm and $\pi$-$\pi^*$ absorption bands at 288 nm due to the Ru(bpy)$_3^{2+}$ sub-unit. TAA and NDI related absorptions manifest between 300 and 390 nm as the comparison of the absorption spectrum of the free ligand **20** (red trace) with the spectrum of Ru(bpy)$_3^{2+}$ (black trace) shows. The TAA unit has an absorption band at 310 nm whereas the bands at 340, 359 and 380 nm are caused by the NDI unit.
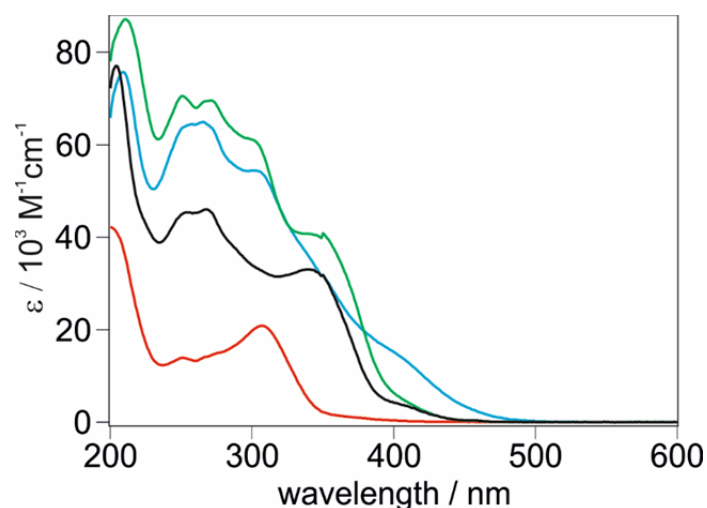
**Figure S2.** UV-Vis spectra of **TPA-ph$_1$-Ir-ph$_1$-AQ** (blue), **TPA-ph$_2$-Ir-ph$_2$-AQ** (green), **Ir-Ref** (black) and ligand **38** (red) in CH$_3$CN at 20 °C.

The optical absorption spectrum of **Ir-Ref** (Figure S2, black trace) exhibits a broad and relatively weak MLCT absorption in the spectral range between 390-440 nm. In comparison, the extinction coefficient for **TPA-ph$_1$-Ir-ph$_1$-AQ** at 400 nm (blue trace) is too high to be simply an MLCT absorption band. Thus, it seems that the **TPA-ph$_1$-Ir-ph$_1$-AQ** triad does not simply exhibit MLCT transitions in this spectral range, but instead there is also significant oscillator strength for optical charge transfer from the triphenylamine donor to the bipyridine ligand of the photosensitizer. Since the distance between the triphenylamine donor and the bipyridine ligand in **TPA-ph$_1$-Ir-ph$_1$-AQ** is significantly shorter than in **TPA-ph$_2$-Ir-ph$_2$-AQ**, the oscillator strength of that optical charge transfer is significantly higher for **TPA-ph$_1$-Ir-ph$_1$-AQ** (blue trace) than for **TPA-ph$_2$-Ir-ph$_2$-AQ** (green trace) between 380 and 480 nm.

As is evident from the main paper, our studies focus on the recombination rate of the final charge-separated states of our triads, and it is not particularly relevant whether these states are reached via excitation into an MLCT transitions or an optical charge transfer transition.

Electrochemistry and optical spectroscopy of Ir-Ref

Cyclic voltammograms of **Ir-Ref** were measured in dry $CH_3CN$ with 0.1 M TBAPF$_6$ (Figure S3). A glassy carbon disk was used as a working electrode and a silver wire served as the counter electrode. The scan rate was 0.1 V/s and the potentials are given against an SCE reference (Table S1).
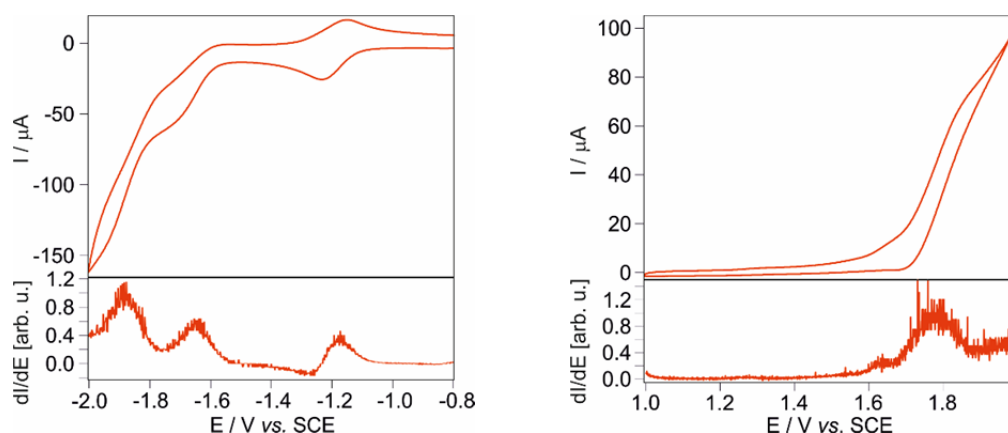


**Figure S3.** Cyclic voltammograms and first their derivatives for **Ir-Ref** in dry and de-aerated $CH_3CN$ *vs*. SCE. TBAPF$_6$ (0.1 M) was used as an electrolyte and a scan rate of 0.1 V/s was applied.

In cyclic voltammetry experiments performed with **Ir-Ref** metal-centered oxidation is observed at 1.78 V *vs*. SCE whereas reductive sweeps reveal consecutive reductions of the bipyridine and the dF-CF$_3$-ppy ligands. The redox potentials determined from this data (Table S1) are in good agreement with those reported earlier for closely related compounds.[10]

**Table S1.** Redox potentials (in Volts *vs*. SCE) extracted from Figure S3.

|  | **Ir-Ref** |
|---|---|
| $E^0$(dF-CF$_3$-ppy$^{-/2-}$) | -1.88 |
| $E^0$(dF-CF$_3$-ppy$^{-/2-}$) | -1.65 |
| $E^0$(bpy$^{0/-}$) | -1.19 |
| $E^0$(Ir$^{IV/III}$) | 1.78 |

The energy ($E_{00}$) of the lowest $^3$MLCT excited state of the Ir photosensitizer unit in the triads was estimated by determining the intersection between the onset of the absorption of **Ir-Ref** at 20 °C in dry $CH_3CN$ (red trace in Figure S4) and the onset of luminescence in dry MeTHF at 77 K (blue trace in Figure S4). This method yields an excited state energy of 2.61 eV.
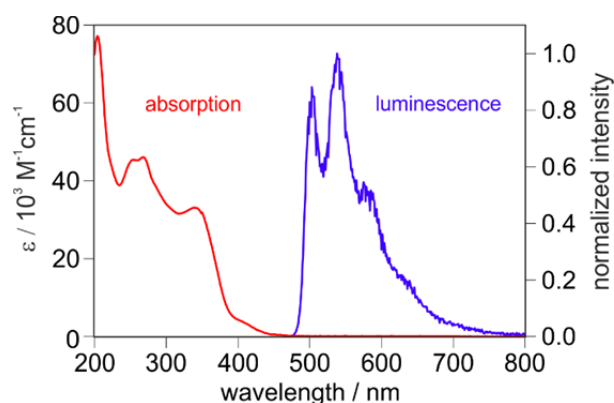


**Figure S4.** Absorption spectrum of **Ir-Ref** in dry $CH_3CN$ (red) at room temperature and luminescence of **Ir-Ref** in dry MeTHF at 77 K (blue). Excitation occurred at 450 nm.

Transient absorption of **Ir-Ref** was measured in dry $CH_3CN$ at 20 °C following excitation at 450 nm (Figure S5). An absorption maximum of the excited photosensitizer is detected at 560 nm. The bleach at 342 nm is caused by disappearance of the ground-state absorption band at that wavelength (Figure S4).
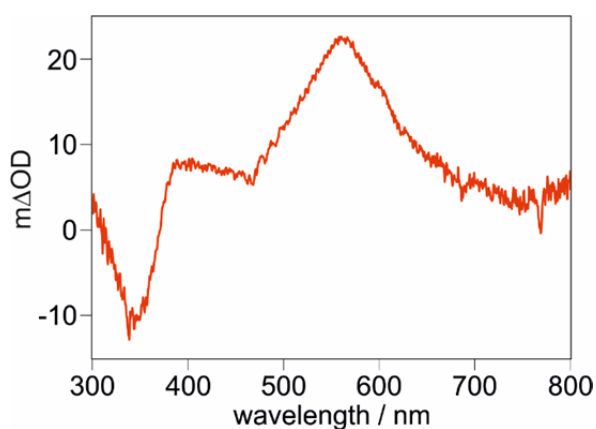


**Figure S5.** Transient absorption spectrum of **Ir-Ref** (20 μM in dry and de-aerated $CH_3CN$) following excitation at 450 nm with laser pulses of ca. 10 ns duration. The spectrum was recorded by time-averaging over a period of 200 ns immediately after excitation.

Cyclic voltammetry of the triads

Cyclic voltammograms of **TAA-ph$_1$-Ru-ph$_1$-NDI**, **TAA-ph$_2$-Ru-ph$_2$-NDI**, **TPA-ph$_1$-Ir-ph$_1$-AQ** and **TPA-ph$_2$-Ir-ph$_2$-AQ** were measured in CH$_3$CN with 0.1 M TBAPF$_6$ (Figure S6 and Figure S7). A glassy carbon disk was used as a working electrode and a silver wire served as the counter electrode. The scan rate was 0.1 V/s and the potentials are given against an SCE reference (Tables S2 and S3).
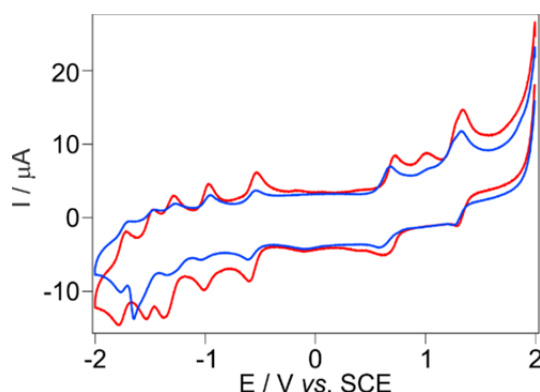


**Figure S6.** Cyclic voltammograms of **TAA-ph$_1$-Ru-ph$_1$-NDI** (red) and **TAA-ph$_2$-Ru-ph$_2$-NDI** (blue) in de-aerated CH$_3$CN. TBAPF$_6$ (0.1 M) was used as an electrolyte and a scan rate of 0.1 V/s was applied.

Oxidative cyclic voltammetry of **TAA-ph$_1$-Ru-ph$_1$-NDI** (Figure S6, red trace) and **TAA-ph$_2$-Ru-ph$_2$-NDI** (Figure S6, blue trace) is dominated by the one-electron oxidation of the TAA donor at 0.64-0.69 V *vs*. SCE and oxidation of Ru$^{II}$ to Ru$^{III}$ at ca. 1.3 V *vs*. SCE. One- and two-electron reduction of the NDI acceptor occurs more readily than reduction of the bipyridine ligands. For the latter, three separate reduction waves can be observed due to individual one-electron ligand reductions. The redox potentials (Table S2) determined from Figure 6 are in good agreement with those reported previously for related compounds.[11,12,13]

**Table S2.** Redox potentials (in Volts *vs.* SCE) extracted from Figure S6.

|  | TAA-ph$_1$-Ru-ph$_1$-NDI | TAA-ph$_2$-Ru-ph$_2$-NDI |
|---|---|---|
| $E^0(bpy^{0/-})$ | -1.75 | -1.75 |
| $E^0(bpy^{0/-})$ | -1.51 | |
| $E^0(bpy^{0/-})$ | -1.33 | -1.30 |
| $E^0(NDI^{-/2-})$ | -0.99 | -1.00 |
| $E^0(NDI^{0/-})$ | -0.56 | -0.58 |
| $E^0(TAA^{+/0})$ | 0.69 | 0.64 |
| $E^0(Ru^{III/II})$ | 1.31 | 1.30 |
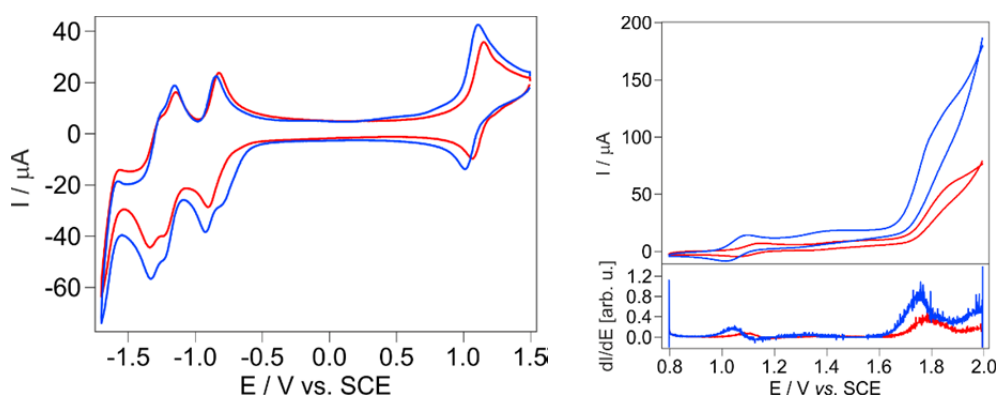


**Figure S7**: Cyclic voltammograms (and first their derivatives) for **TPA-ph$_1$-Ir-ph$_1$-AQ** (red) and **TPA-ph$_2$-Ir-ph$_2$-AQ** (blue) in dry and de-aerated CH$_3$CN. TBAPF$_6$ (0.1 M) was used as an electrolyte and a scan rate of 0.1 V/s was applied.

In oxidative cyclic voltammetry sweeps performed with **TPA-ph$_1$-Ir-ph$_1$-AQ** (Figure S7, red trace) and **TPA-ph$_2$-Ir-ph$_2$-AQ** (Figure S7, blue trace) the one-electron oxidations of the TPA donor unit and of the iridium unit are observed. In the reductive sweeps, a first (one-electron) reduction of the AQ acceptor is followed by the reduction of one of the bipyridine ligands. Subsequently, the second reduction of the AQ unit (to the quinone dianion) can be observed before the dF-CF$_3$-ppy ligands are finally each reduced by one electron.

**Table S3.** Redox potentials (in Volts *vs.* SCE) extracted from Figure S7.

| | TPA-ph$_1$-Ir-ph$_1$-AQ | TPA-ph$_2$-Ir-ph$_2$-AQ |
|---|---|---|
| $E^0$(dF-CF$_3$-ppy$^{-/2-}$) | -1.88 | -1.87 |
| $E^0$(dF-CF$_3$-ppy$^{-/2-}$) | -1.65 | -1.62 |
| $E^0$(AQ$^{-/2-}$) | -1.30 | -1.30 |
| $E^0$(bpy$^{0/-}$) | -1.19 | -1.19 |
| $E^0$(AQ$^{0/-}$) | -0.86 | -0.89 |
| $E^0$(TPA$^{+/0}$) | 1.11 | 1.06 |
| $E^0$(Ir$^{IV/III}$) | 1.78 | 1.75 |

Reaction free energies for thermal charge recombination in the triads

The reaction free energy ($\Delta G_{CR}{}^0$) for thermal charge recombination between oxidized donors (D$^+$) and reduced acceptors (A$^-$) in the individual triads **TAA-ph$_1$-Ru-ph$_1$-NDI**, **TAA-ph$_2$-Ru-ph$_2$-NDI**, **TPA-ph$_1$-Ir-ph$_1$-AQ** and **TPA-ph$_2$-Ir-ph$_2$-AQ** was estimated using equation S1 and the redox potentials reported in Tables S2 and S3.[14] $e$ is the elemental charge, $\varepsilon_0$ is the vacuum permittivity, and $\varepsilon_S$ is the dielectric constant of the solvent (35.9 for CH$_3$CN).[15] The center-to-center distance ($r_{DA}$) corresponds to the distance between the N-atom of the amine donor and the centroid of the acceptor unit. All $r_{DA}$ values are reported in Table 1 of the main paper.

$$\Delta G_{CR}{}^0 = e \cdot \left[ E^0\left(A^{0/-}\right) - E^0\left(D^{+/0}\right) \right] - \frac{e^2}{4\pi\varepsilon_0\varepsilon_S r_{DA}} \qquad \text{(eq S1)}$$

**Table S4.** Estimated reaction free energies ($\Delta G_{CR}{}^0$) for thermal charge recombination in the individual triads on the basis of the redox potentials in Tables S2 and S3.

| Cmpd | $\Delta G_{CR}{}^0$ [eV] |
|---|---|
| **TAA-ph$_1$-Ru-ph$_1$-NDI** | -1.27 |
| **TAA-ph$_2$-Ru-ph$_2$-NDI** | -1.23 |
| **TPA-ph$_1$-Ir-ph$_1$-AQ** | -1.99 |
| **TPA-ph$_2$-Ir-ph$_2$-AQ** | -1.96 |

Temperature-dependent cyclic voltammetry studies for triads TAA-ph$_1$-Ru-ph$_1$-NDI and TAA-ph$_2$-Ru-ph$_2$-NDI

Cyclic voltammograms of **TAA-ph$_1$-Ru-ph$_1$-NDI** and **TAA-ph$_2$-Ru-ph$_2$-NDI** were measured at several temperatures between 8.5 and 50 °C to assess whether there is any significant temperature dependence of the driving-force (-$\Delta G_{CR}^0$) for thermal charge recombination between photogenerated D$^+$ and A$^-$. The voltammograms were measured in CH$_3$CN with 0.1 M TBAPF$_6$ (Figures S8 and S9). A glassy carbon disk was used as a working electrode and a silver wire served as the counter electrode. The scan rate was 0.1 V/s and the potentials are reported against an SCE reference (Tables S5 and S6).
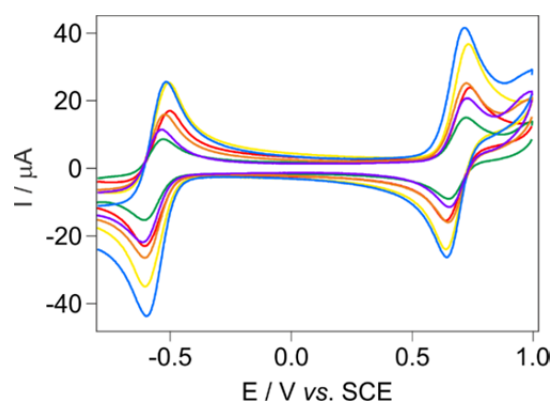


**Figure S8.** Cyclic voltammograms of **TAA-ph$_1$-Ru-ph$_1$-NDI** at 8.5 °C (red), 15 °C (yellow), 25 °C (green), 35 °C (orange), 43 °C (blue) and 50 °C (purple) in de-aerated CH$_3$CN. TBAPF$_6$ (0.1 M) was used as an electrolyte and a scan rate of 0.1 V/s was applied.

**Table S5.** Redox potentials (in Volts *vs.* SCE) of the **TAA-ph$_1$-Ru-ph$_1$-NDI** triad extracted from Figure S8 at various temperatures. The driving-force (-$\Delta G_{CR}^0$) for thermal electron transfer from NDI$^-$ to TAA$^+$ was estimated with equation S1 on the basis of the relevant potentials.

| T [°C] | E$^0$(NDI$^{0/-}$) | E$^0$(TAA$^{+/0}$) | -$\Delta G_{CR}^0$ [eV] |
|--------|--------|--------|--------|
| 8.5 | -0.55 | 0.69 | 1.26 |
| 15 | -0.56 | 0.69 | 1.27 |
| 25 | -0.57 | 0.69 | 1.28 |
| 35 | -0.56 | 0.69 | 1.27 |
| 43 | -0.56 | 0.68 | 1.26 |

| 50 | -0.58 | 0.69 | 1.29 |
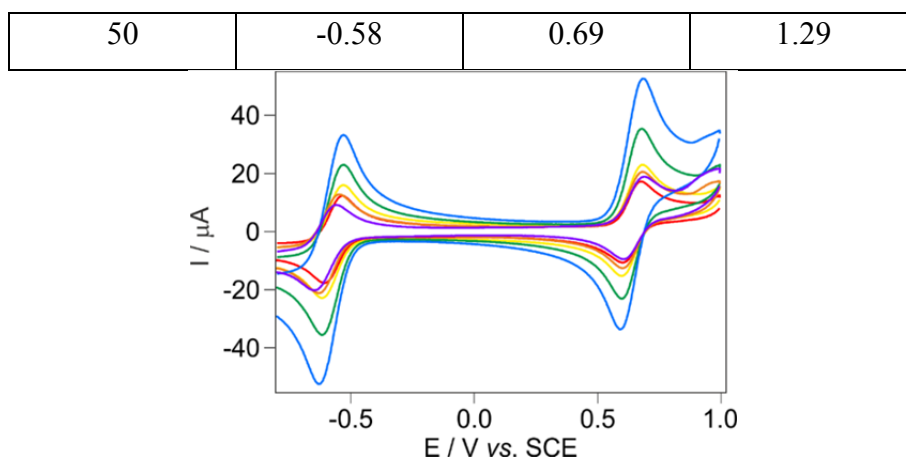


**Figure S9.** Cyclic voltammograms of **TAA-ph$_2$-Ru-ph$_2$-NDI** at 8.5 °C (red), 15 °C (yellow), 25 °C (green), 34 °C (orange), 43 °C (blue) and 55 °C (purple) in de-aerated CH$_3$CN. TBAPF$_6$ (0.1 M) was used as an electrolyte and a scan rate of 0.1 V/s was applied.

**Table S6.** Redox potentials for triad **TAA-ph$_2$-Ru-ph$_2$-NDI** (in Volts *vs.* SCE) extracted from Figure S9. The driving-force (-$\Delta G_{CR}^0$) for thermal electron transfer from NDI$^-$ to TAA$^+$ was estimated with equation S1 using the experimentally determined potentials.

| T [°C] | E$^0$(NDI$^{0/-}$) | E$^0$(TAA$^{+/0}$) | -$\Delta G_{CR}^0$ [eV] |
|---|---|---|---|
| 8.5 | -0.57 | 0.64 | 1.22 |
| 15 | -0.57 | 0.64 | 1.22 |
| 25 | -0.57 | 0.64 | 1.22 |
| 34 | -0.59 | 0.64 | 1.24 |
| 43 | -0.58 | 0.64 | 1.23 |
| 55 | -0.60 | 0.65 | 1.26 |

The experimental uncertainty associated with our cyclic voltammetry experiments is approximately ±0.05 V. Consequently, the driving-force for thermal charge recombination between oxidized donor and reduced acceptor can be regarded as temperature independent in both triads, at least in the range considered here. This finding is relevant for the temperature-dependent transient absorption studies reported below. We assume that this is also the case for the **TPA-ph$_1$-Ir-ph$_1$-AQ** and **TPA-ph$_2$-Ir-ph$_2$-AQ** triads.
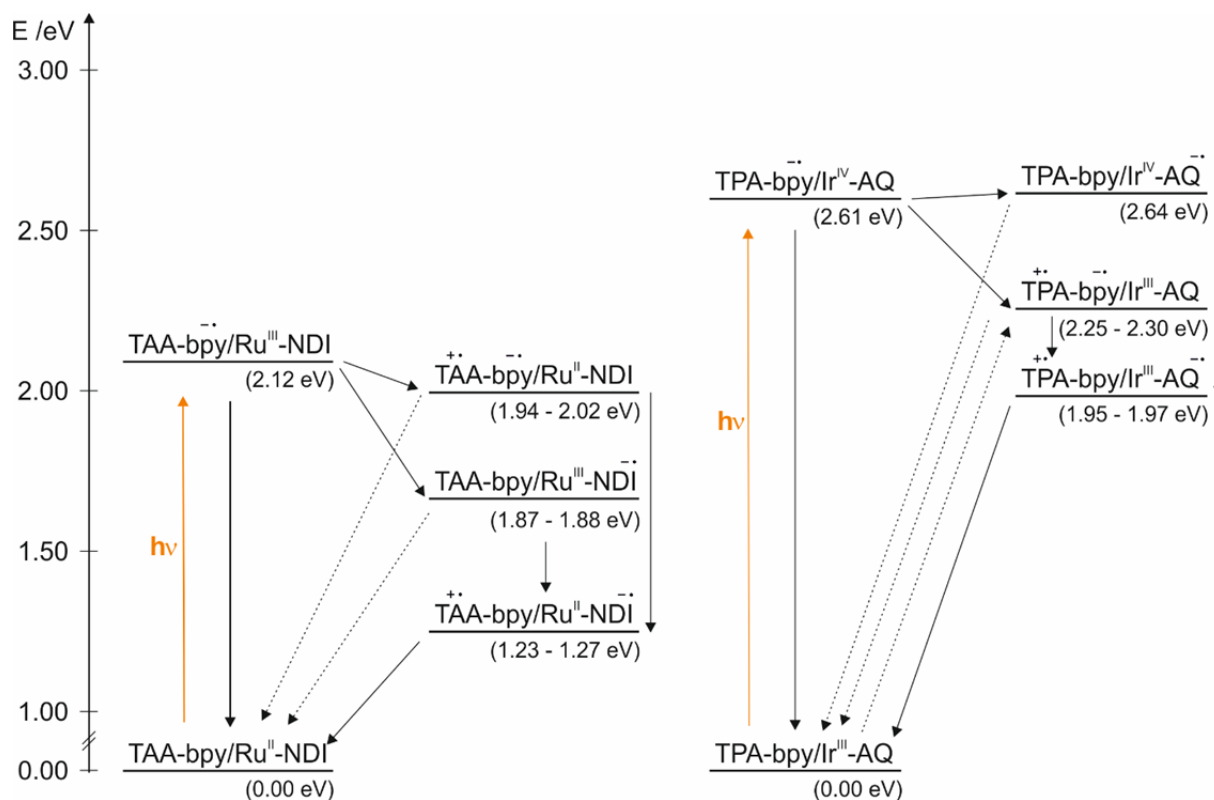
**Figure S10.** Energies of relevant excited states and photoproducts for the Ru-based triads **TAA-ph$_1$-Ru-ph$_1$-NDI** and **TAA-ph$_2$-Ru-ph$_2$-NDI** (left) and the Ir-based triads **TPA-ph$_1$-Ir-ph$_1$-AQ** and **TPA-ph$_2$-Ir-ph$_2$-AQ** (right) in CH$_3$CN. Energies were estimated using equation S1 and the redox potentials from Tables S2 and S3. E$_{00}$ for the Ru(bpy)$_3^{2+}$ unit is 2.12 eV,[16] whilst for the Ir sensitizer unit we found E$_{00}$ = 2.61 eV, see page S34.

Based on the energy-level diagram in the left part of Figure S10, the final charge-separated state in the triads **TAA-ph$_1$-Ru-ph$_1$-NDI** and **TAA-ph$_2$-Ru-ph$_2$-NDI** (Figure S10, left) can be formed in two different ways: i) after excitation of the Ru sensitizer unit, the excited sensitizer can be oxidatively quenched by NDI, followed by an electron transfer from the TAA donor to the now oxidized Ru$^{III}$ photosensitizer, or ii) reductive quenching of the excited Ru(bpy)$_3^{2+}$ sensitizer by TAA, followed by an electron transfer from the reduced photosensitizer to the NDI acceptor.

While the formation of the final charge-separated state in the Ru-based triads proceed over a $^3$MLCT state after initial excitation of the Ru sensitizer, the Ir-based triads **TPA-ph$_1$-Ir-ph$_1$-AQ** and **TPA-ph$_2$-Ir-ph$_2$-AQ** show partly different behavior (Figure S10, right). Excitation of **TPA-ph$_1$-Ir-ph$_1$-AQ** mainly results in an optical charge transfer from the TPA to the bipyridine ligand of the Ir sensitizer since there seems to be a significant oscillator strength for this excitation (see page S32). Electron transfer from the reduced bipyridine to the AQ finally results in the charge-separated state. By contrast, excitation of **TPA-ph$_2$-Ir-ph$_2$-AQ** mainly shows a $^3$MLCT transition comparable to the Ru-based triads. The final charge-separated state can then be generated by i) reductive quenching of the excited Ir sensitizer by TPA, followed by an electron transfer from the reduced Ir sensitizer to the AQ, or ii) oxidative quenching of the excited Ir sensitizer by AQ, followed by an electron transfer from TPA to the Ir$^{IV}$ species.

As is evident from the main paper, our studies focus on the recombination rate of the final charge-separated states of our triads, and it is not particularly relevant whether these states are reached via excitation into MLCT transitions or an optical charge transfer transition.

Transient absorption and spectro-electrochemical studies for TPA-ph$_1$-Ir-ph$_1$-AQ and TPA-ph$_2$-Ir-ph$_2$-AQ



**Figure S11.** (a) Transient UV-Vis absorption spectrum recorded after excitation of 20 μM **TPA-ph$_1$-Ir-ph$_1$-AQ** in dry and de-aerated CH$_3$CN at 20 °C. The sample was excited at 450 nm with laser pulses of ca. 10 ns duration, detection occurred by integration over a period of 200 ns immediately after excitation. (b) Spectro-electrochemical UV-Vis difference spectrum of the TPA unit in **TPA-ph$_1$-Ir-ph$_1$-AQ** in dry and de-aerated CH$_3$CN at 20 °C. The applied oxidation potential was 1.2 V *vs*. SCE, the UV-Vis spectrum recorded prior to application of the potential served as a baseline. (c) Spectro-electrochemical UV-Vis difference spectrum of the AQ unit in **TPA-ph$_1$-Ir-ph$_1$-AQ** in dry and de-aerated CH$_3$CN at 20 °C. The applied reduction potential was -0.9 V *vs*. SCE, the UV-Vis spectrum recorded prior to application of the potential served as a baseline.


The transient absorption spectrum of **TPA-ph$_1$-Ir-ph$_1$-AQ** (Figure S11a), recorded immediately after excitation at 450 nm, clearly shows the spectroscopic signatures of the anticipated charge-separated state, as confirmed by spectro-electrochemical UV-Vis difference spectra for TPA$^+$ (Figure S11b) and AQ$^-$ (Figure S11c). The one-electron oxidized TPA unit exhibits a diagnostic band at 720 nm and a stronger band at 380 nm. The one-electron reduced AQ unit exhibits absorption bands at 385 nm and at 550 nm. In the triad **TPA-ph$_1$-Ir-ph$_1$-AQ**, spectroscopic signatures at 370, 570 and 720 nm are observed which

correspond to a 1:1 combination of the one-electron oxidized TPA unit and the one-electron reduced AQ unit. Small shifts of the band maxima in the transient absorption spectrum compared to the spectro-electrochemical UV-Vis difference spectra are likely due to the used electrolyte in the spectro-electrochemical measurements.
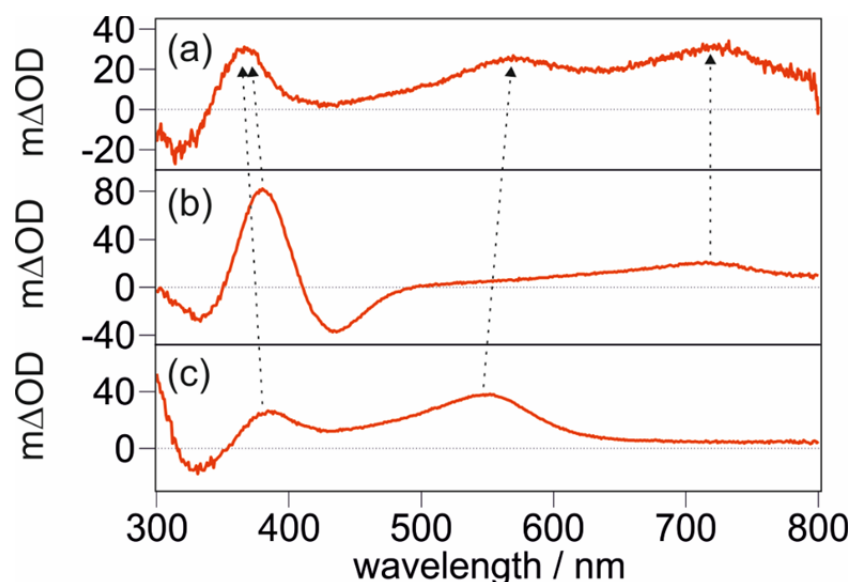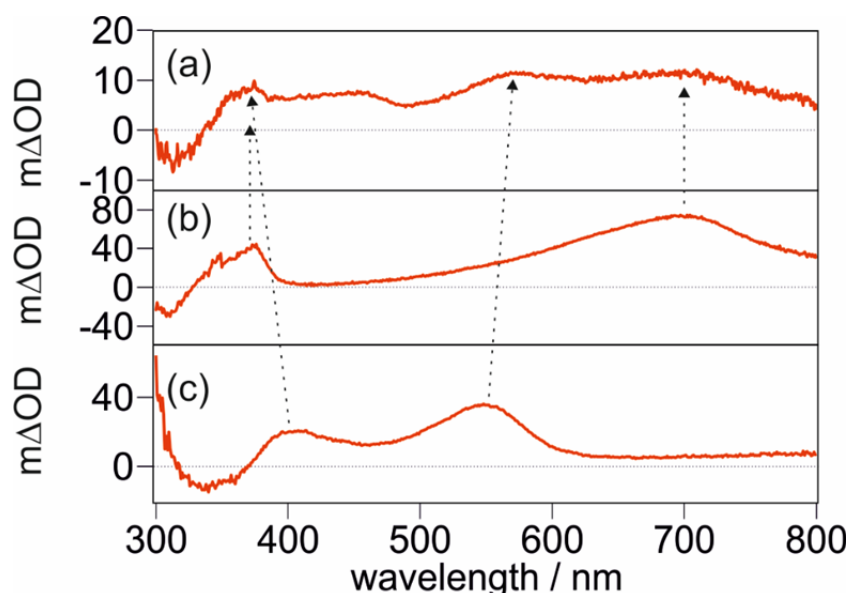


**Figure S12.** (a) Transient UV-Vis absorption spectrum recorded after excitation of 20 µM **TPA-ph$_2$-Ir-ph$_2$-AQ** in dry and de-aerated CH$_3$CN at 20 °C. The sample was excited at 420 nm with laser pulses of ca. 10 ns duration, detection occurred by integration over a period of 200 ns immediately after excitation. (b) Spectro-electrochemical UV-Vis difference spectrum of the TPA unit in **TPA-ph$_2$-Ir-ph$_2$-AQ** in dry and de-aerated CH$_3$CN at 20 °C. The applied oxidation potential was 1.3 V *vs.* SCE, the UV-Vis spectrum recorded prior to application of the potential served as a baseline. (c) Spectro-electrochemical UV-Vis difference spectrum of the AQ unit in **TPA-ph$_2$-Ir-ph$_2$-AQ** in dry and de-aerated CH$_3$CN at 20 °C. The applied reduction potential was -0.9 V *vs.* SCE, the UV-Vis spectrum recorded prior to application of the potential served as a baseline.

The transient absorption spectrum of **TPA-ph$_2$-Ir-ph$_2$-AQ** (Figure S12a) shows the spectroscopic signatures of the anticipated charge-separated state, as confirmed by spectro-electrochemical UV-Vis difference spectra for TPA$^+$ (Figure S12b) and AQ$^-$ (Figure S12c). The one-electron oxidized TPA unit exhibits absorption bands at 700 nm and 370 nm. The one-electron reduced AQ unit shows absorption bands at 405 and 550 nm. In the triad **TPA-**

**ph$_2$-Ir-ph$_2$-AQ**, spectroscopic signatures at 370, 570 and 700 nm are observed which correspond to a 1:1 combination of the one-electron oxidized TPA unit and the one-electron reduced AQ unit. Small shifts of the band maxima in the transient absorption spectrum compared to the spectro-electrochemical UV-Vis difference spectra are likely due to the used electrolyte in the spectro-electrochemical measurements.

Compared to **TPA-ph$_1$-Ir-ph$_1$-AQ**, **TPA-ph$_2$-Ir-ph$_2$-AQ** shows a 20 nm shift of the TPA$^+$ band to higher energies. This shift is probably due to the fact that the interaction of the TPA unit with the bipyridine ligand is somewhat different in the **TPA-ph$_2$-Ir-ph$_2$-AQ** triad (see also page S32) resulting in a shift of the respective TPA$^+$ absorption maximum to higher energies.

Temperature-dependent transient absorption studies and activation free energies for thermal charge recombination
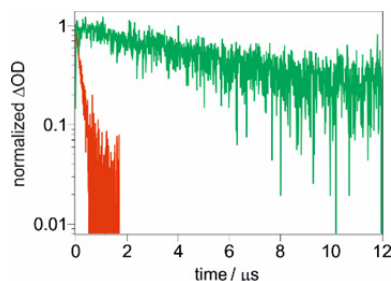


**Figure S13.** (a) Temporal evolution of the transient absorption signals for **TAA-ph$_1$-Ru-ph$_1$-NDI** (red) and **TAA-ph$_2$-Ru-ph$_2$-NDI** (green) in de-aerated CH$_3$CN at 20 °C monitoring the NDI$^-$ absorption band at 607 nm.

The data set in Figure S13 complements the transient absorption decays shown in Figure 1 d/e of the main paper for the **TAA-ph$_1$-Ru-ph$_1$-NDI** and **TAA-ph$_2$-Ru-ph$_2$-NDI** triads. In the main paper, we show the decays of the transient absorption signals at 475 and 770 nm whilst here the transient absorption signal caused by the NDI$^-$ species at 607 nm is shown (Figure S13). Based on the combined kinetic measurements at 475, 607 and 770 nm (Table S7), rate constants ($k_{CR}$) of $(4.8 \pm 0.5) \cdot 10^6$ s$^{-1}$ and $(1.3 \pm 0.1) \cdot 10^5$ s$^{-1}$ were determined for intra-molecular charge recombination between TAA$^+$ and NDI$^-$ in **TAA-ph$_1$-Ru-ph$_1$-NDI** and **TAA-ph$_2$-Ru-ph$_2$-NDI** in de-aerated CH$_3$CN at 20 °C. As noted in the main paper, a decrease of $k_{CR}$ is observed when elongating the donor-acceptor-distance.
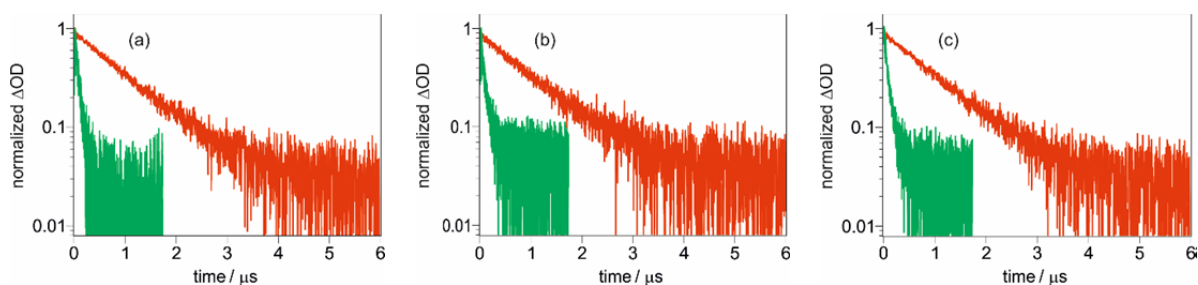


**Figure S14.** Temporal evolution of the transient absorption signals for **TPA-ph$_1$-Ir-ph$_1$-AQ** (red) and **TPA-ph$_2$-Ir-ph$_2$-AQ** (green) in dry and de-aerated CH$_3$CN at 20 °C. (a) Combined

TPA$^+$ and AQ$^-$ absorption at 370 nm. (b) The AQ$^-$ band at 570 nm, and (c) the TPA$^+$ band at 720 nm for **TPA-ph$_1$-Ir-ph$_1$-AQ** and at 700 nm for **TPA-ph$_2$-Ir-ph$_2$-AQ**.

When monitoring the temporal evolution of the AQ$^-$ and TPA$^+$ signals of the triads **TPA-ph$_1$-Ir-ph$_1$-AQ** (red trace) and **TPA-ph$_2$-Ir-ph$_2$-AQ** (green trace) at the relevant wavelengths (Figure S14a-c), one observes instant decays signaling the formation of the AQ$^-$ and TPA$^+$ photoproduct within the duration of the laser pulse (ca. 10 ns). Immediately following excitation, the radical ion pair collapses due to thermal charge recombination via intra-molecular electron transfer. Based on the kinetic measurements in Figure S14 (Table S8), rate constants ($k_{CR}$) of $(1.0 \pm 0.1) \cdot 10^6$ s$^{-1}$ and $(1.2 \pm 0.1) \cdot 10^7$ s$^{-1}$ were determined for **TPA-ph$_1$-Ir-ph$_1$-AQ** and **TPA-ph$_2$-Ir-ph$_2$-AQ** in dry and de-aerated CH$_3$CN at 20 °C. Thus, an increase of $k_{CR}$ is observed when elongating the donor-acceptor-distance.

In the following we present the results from temperature dependent kinetic studies of the **TAA-ph$_n$-Ru-ph$_n$-NDI** and **TPA-ph$_n$-Ir-ph$_n$-AQ** triads, which were performed to estimate the activation free energies for intra-molecular thermal charge recombination in these compounds.

**Table S7.** Time constants ($\tau$) for thermal charge recombination (CR) between NDI$^-$ and TAA$^+$ in the **TAA-ph$_1$-Ru-ph$_1$-NDI** and **TAA-ph$_2$-Ru-ph$_2$-NDI** triads, determined by monitoring the decays of the transient absorption signals at three different wavelengths monitoring NDI$^-$ (475 and 607 nm) and TAA$^+$ (770 nm). Excitation occurred at 532 nm with laser pulses of ca. 10 ns duration. Measured in dry and deoxygenated CH$_3$CN. All time constants are given in nanoseconds.

| T [°C] | TAA-ph$_1$-Ru-ph$_1$-NDI | | | TAA-ph$_2$-Ru-ph$_2$-NDI | | |
| --- | --- | --- | --- | --- | --- | --- |
| | $\tau_{475\,nm}$ | $\tau_{607\,nm}$ | $\tau_{770\,nm}$ | $\tau_{475\,nm}$ | $\tau_{607\,nm}$ | $\tau_{770\,nm}$ |
| 5 | 203 | 197 | 203 | 8290 | 8738 | 8025 |
| 10 | 200 | 200 | 209 | 8023 | 8308 | 8004 |
| 15 | 207 | 201 | 212 | 8031 | 8062 | 7576 |
| 20 | 209 | 199 | 212 | 7413 | 7595 | 7479 |
| 25 | 210 | 194 | 214 | 7702 | 7687 | 7181 |

| 30 | 214 | 214 | 211 | 7622 | 8292 | 7190 |
|----|-----|-----|-----|------|------|------|
| 35 | 217 | 203 | 225 | 7332 | 7922 | 7256 |
| 40 | 220 | 217 | 225 | 7386 | 6513 | 6788 |
| 45 | 222 | 220 | 228 | 6525 | 6462 | 5937 |
| 50 | 222 | 234 | 227 | 5889 | 6880 | 6346 |
| 55 | 225 | 209 | 222 | 6540 | 5613 | 5956 |
| 60 | 228 | 220 | 238 | 5589 | 5412 | 6037 |
| 65 | 231 | 224 | 244 | 7188 | 6549 | 5821 |

**Table S8.** Time constants ($\tau$) for thermal charge recombination (CR) between $AQ^-$ and $TPA^+$ in the **TPA-ph$_1$-Ir-ph$_1$-AQ** and **TPA-ph$_2$-Ir-ph$_2$-AQ** triads, determined by monitoring the temporal evolution of the transient absorption signals at three different wavelengths monitoring $AQ^-$ (370 and 570 nm) and $TPA^+$ (720 nm for **TPA-ph$_1$-Ir-ph$_1$-AQ** and 700 nm for **TPA-ph$_2$-Ir-ph$_2$-AQ**, respectively). Excitation occurred at 450 nm for **TPA-ph$_1$-Ir-ph$_1$-AQ** and at 420 nm for **TPA-ph$_2$-Ir-ph$_2$-AQ** with laser pulses of ca. 10 ns duration. Measured in dry and deoxygenated $CH_3CN$. All time constants are given in nanoseconds.

| | **TPA-ph$_1$-Ir-ph$_1$-AQ** | | | **TPA-ph$_2$-Ir-ph$_2$-AQ** | | |
|---|---|---|---|---|---|---|
| T [°C] | $\tau_{370\,nm}$ | $\tau_{570\,nm}$ | $\tau_{720\,nm}$ | $\tau_{370\,nm}$ | $\tau_{570\,nm}$ | $\tau_{700\,nm}$ |
| 5 | 1059 | 1117 | 1129 | 89 | 86 | 73 |
| 15 | 994 | 1048 | 1060 | 97 | 91 | 76 |
| 20 | 971 | 991 | 982 | 92 | 89 | 76 |
| 25 | 905 | 954 | 976 | 92 | 82 | 76 |
| 35 | 816 | 849 | 853 | 103 | 96 | 80 |
| 45 | 803 | 850 | 841 | 102 | 97 | 78 |
| 55 | 698 | 739 | 744 | 105 | 98 | 77 |
| 65 | 631 | 662 | 665 | 109 | 107 | 80 |
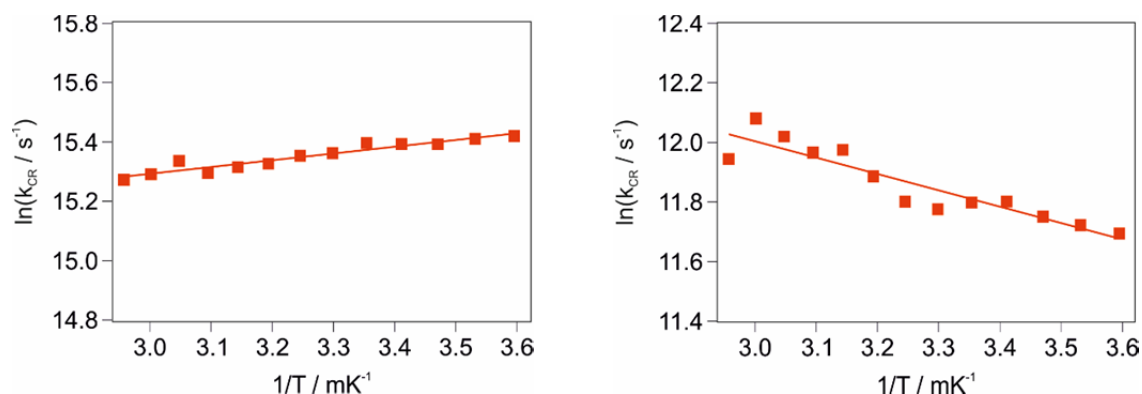
**Figure S15.** Arrhenius plots for thermal electron transfer from NDI⁻ to TAA⁺ in **TAA-ph₁-Ru-ph₁-NDI** and **TAA-ph₂-Ru-ph₂-NDI** in deoxygenated $CH_3CN$. The plots are based on the data in Table S7.
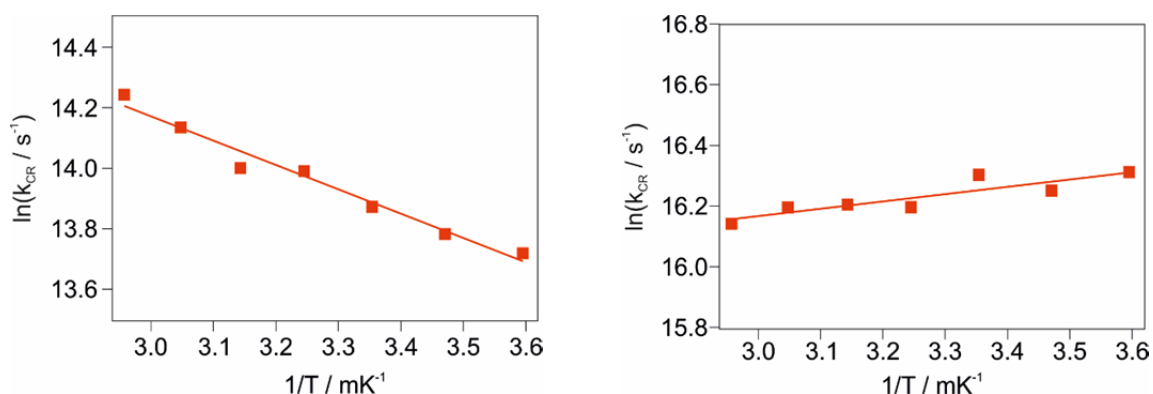


**Figure S16.** Arrhenius plots for thermal electron transfer from AQ⁻ to TPA⁺ in **TPA-ph₁-Ir-ph₁-AQ** and **TPA-ph₂-Ir-ph₂-AQ** in dry and deoxygenated $CH_3CN$. The plots are based on the data in Table S8.

**Table S9.** Apparent activation free energies ($\Delta G_{CR}^{\ddagger}{}_{app.}$) and effective activation free energies ($\Delta G_{CR}^{\ddagger}$) for thermal electron transfer from A⁻ to D⁺ in **TAA-ph₁-Ru-ph₁-NDI**, **TAA-ph₂-Ru-ph₂-NDI**, **TPA-ph₁-Ir-ph₁-AQ** and **TPA-ph₂-Ir-ph₂-AQ** in $CH_3CN$, extracted from the Arrhenius plots in Figures S15 and S16.

| cmpd | $\Delta G_{CR}^{\ddagger}{}_{app.}$ [meV] | $\Delta G_{CR}^{\ddagger}$ [meV] |
|---|---|---|
| **TAA-ph$_1$-Ru-ph$_1$-NDI** | -19.5 ± 1.80 | 0 ± 0.05 |
| **TAA-ph$_2$-Ru-ph$_2$-NDI** | 47.4 ± 6.00 | 47.4 ± 6.00 |
| **TPA-ph$_1$-Ir-ph$_1$-AQ** | 69.3 ± 5.20 | 69.3 ± 5.20 |
| **TPA-ph$_2$-Ir-ph$_2$-AQ** | -20.9 ± 4.80 | 0 ± 0.05 |

For the triads **TAA-ph$_1$-Ru-ph$_1$-NDI** and **TPA-ph$_2$-Ir-ph$_2$-AQ** (small) apparently negative activation free energies are determined from the Arrhenius plots in Figures S15 and S16. This finding is interpreted in terms of electron transfer processes occurring at the activationless point in the respective compounds. As an effective activation free energy we therefore report $\Delta G_{CR}^{\ddagger} = 0$ in Table S9.

To estimate the uncertainties associated with the activation free energies in Table S9, a linear propagation of uncertainty of the activation free energies was performed using the linear regression fits in Figures S15 and S16. In the two cases where charge recombination proceeds in activationless manner, the error was considered equal to the experimental uncertainty associated with the determination of the reaction free energies (± 0.05 eV, see above).

Determination of the reorganization energies ($\lambda$)

The reorganization energies ($\lambda$) for the triads **TAA-ph$_1$-Ru-ph$_1$-NDI**, **TAA-ph$_2$-Ru-ph$_2$-NDI**, **TPA-ph$_1$-Ir-ph$_1$-AQ** and **TPA-ph$_2$-Ir-ph$_2$-AQ** were estimated by solving equation S2 and using the reaction free energies reported in Table S4 and the activation free energies reported in Table S9.

$$\Delta G_{CR}{}^{\ddagger} = \frac{(\lambda + \Delta G_{CR}{}^{0})^2}{4\lambda} \tag{eq S2}$$

For **TAA-ph$_1$-Ru-ph$_1$-NDI** and **TPA-ph$_2$-Ir-ph$_2$-AQ** it was found that electron transfer takes place at the activationless point of the Marcus parabola (see also page S49 and Figure 3 in the main paper). Therefore, application of equation 2 is not necessary in these two cases since $\lambda = -\Delta G_{CR}{}^{0}$ for barrierless reactions. For **TAA-ph$_2$-Ru-ph$_2$-NDI** and **TPA-ph$_1$-Ir-ph$_1$-AQ**, solving the quadratic equation for $\lambda$ yields two mathematically correct solutions. However, since $\lambda$ is expected to increase with increasing $r_{DA}$, only the solutions where an increase in $\lambda$ from the ph$_1$ to the ph$_2$ triad is observable was considered physically meaningful.

**Table S10.** Reorganization energies ($\lambda$) associated with intra-molecular electron transfer from A$^-$ to D$^+$ in the triads **TAA-ph$_1$-Ru-ph$_1$-NDI**, **TAA-ph$_2$-Ru-ph$_2$-NDI**, **TPA-ph$_1$-Ir-ph$_1$-AQ** and **TPA-ph$_2$-Ir-ph$_2$-AQ** in CH$_3$CN.

| cmpd | $\lambda$ [eV] |
|---|---|
| **TAA-ph$_1$-Ru-ph$_1$-NDI** | $1.27 \pm 0.05$ |
| **TAA-ph$_2$-Ru-ph$_2$-NDI** | $1.82 \pm 0.35$ |
| **TPA-ph$_1$-Ir-ph$_1$-AQ** | $1.37 \pm 0.36$ |
| **TPA-ph$_2$-Ir-ph$_2$-AQ** | $1.96 \pm 0.05$ |

The uncertainties associated with the reorganization energies in Table S10 were estimated via error propagation, considering the uncertainties associated with the reaction free energies and the activation free energies.

Determination of electronic coupling matrix elements ($H_{DA}$)

According to semiclassical Marcus theory, electron transfer rates ($k_{ET}$, $k_{CR}$ for charge recombination processes) depend on the reorganization energy ($\lambda$), the reaction free energy ($\Delta G_{ET}^0$, $\Delta G_{CR}^0$ for charge recombination processes) and the electronic coupling matrix element ($H_{DA}$) (equation S3). $k_B$ is the Boltzmann constant.

$$k_{ET} = \sqrt{\frac{\pi}{\hbar^2 \lambda k_B T}} \cdot H_{DA}^2 \cdot \exp\left(-\frac{(\lambda + \Delta G_{ET}^0)^2}{4\lambda k_B T}\right) \qquad \text{(eq S3)}$$

The results from the temperature-dependent kinetic studies in Tables S7 and S8 can be employed to estimate $H_{DA}$.[17] For this purpose, the data from Tables S7 and S8 was re-plotted in the graphs in Figures S17 and S18. Linear regression fits to these data sets with equation S4 (derived from equation S3) then provides estimates for $H_{DA}$. In particular, information about $H_{DA}$ is contained in the intercept (equation S5).

$$\ln\left(k_{CR} \cdot T^{1/2}\right) = \ln\left(\sqrt{\frac{\pi}{\hbar^2 \lambda k_B}} \cdot H_{DA}^2\right) - \left(\frac{(\lambda + \Delta G_{CR}^0)^2}{4\lambda k_B} \cdot \frac{1}{T}\right) \qquad \text{(eq S4)}$$

$$\text{with y-intercept} = \ln\left(\sqrt{\frac{\pi}{\hbar^2 \lambda k_B}} \cdot H_{DA}^2\right) \qquad \text{(eq S5)}$$
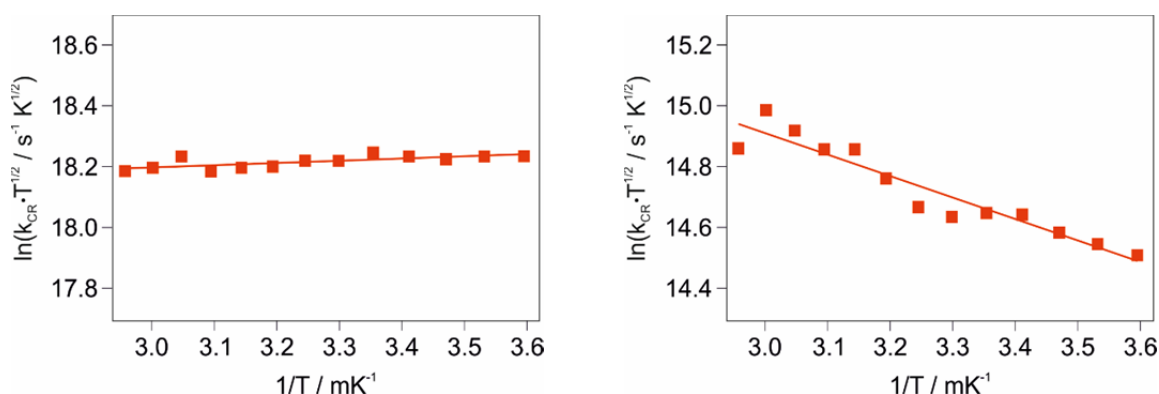


**Figure S17.** Plots of $\ln(k_{CR} \cdot T^{1/2})$ versus $1/T$ for triads **TAA-ph$_1$-Ru-ph$_1$-NDI** and **TAA-ph$_2$-Ru-ph$_2$-NDI** in CH$_3$CN based on the data from Table S7.
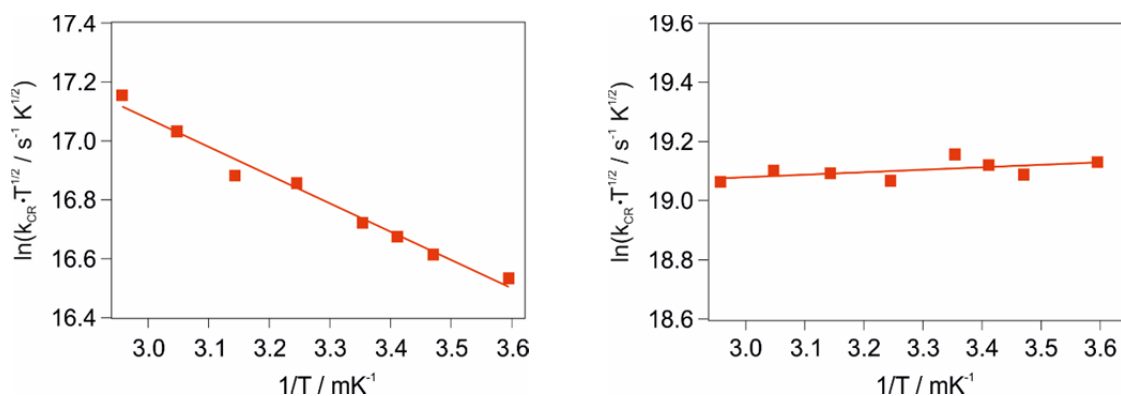
**Figure S18.** Plots of $\ln(k_{CR} \cdot T^{1/2})$ versus $1/T$ for triads **TPA-ph$_1$-Ir-ph$_1$-AQ** and **TPA-ph$_2$-Ir-ph$_2$-AQ** in CH$_3$CN based on the data from Table S8.

**Table S11.** Electronic coupling matrix element ($H_{DA}$) for the triads **TAA-ph$_1$-Ru-ph$_1$-NDI**, **TAA-ph$_2$-Ru-ph$_2$-NDI**, **TPA-ph$_1$-Ir-ph$_1$-AQ** and **TPA-ph$_2$-Ir-ph$_2$-AQ** in CH$_3$CN.

| cmpd | $H_{DA}$ [cm$^{-1}$] |
|---|---|
| **TAA-ph$_1$-Ru-ph$_1$-NDI** | $0.13 \pm 0.02$ |
| **TAA-ph$_2$-Ru-ph$_2$-NDI** | $0.09 \pm 0.02$ |
| **TPA-ph$_1$-Ir-ph$_1$-AQ** | $0.35 \pm 0.06$ |
| **TPA-ph$_2$-Ir-ph$_2$-AQ** | $0.22 \pm 0.04$ |

The uncertainties of the electronic coupling elements $H_{DA}$ were estimated via error propagation considering the uncertainties of the reorganization energy and the uncertainties of the intercept of the linear regression fit. Twice the standard deviations obtained from the linear regression fits in Figures S17 and S18 were used as a basis.

## References

[1]     Bai, X.-L.; Liu, X.-D.; Wang, M.; Kang, C.-Q.; Gao, L.-X., Synthesis of New Bis-BINOLs Linked by a 2,2'-Bipyridine Bridge. *Synthesis* **2005**, 458−464.

[2]     Hankache, J.; Wenger, O. S., Microsecond Charge Recombination in a Linear Triaryl-amine-Ru(bpy)$_3$$^{2+}$-Anthraquinone Triad. *Chem. Commun.* **2011**, *47*, 10145−10147.

[3]     Kuss-Petermann, M.; Wenger, O. S., Increasing Electron-Transfer Rates with Increasing Donor-Acceptor Distance. *Angew. Chem. Int. Ed.* **2016**, *55*, 815−819.

[4]     Orazietti, M.; Kuss-Petermann, M.; Hamm, P.; Wenger, O. S., Light-Driven Electron Accumulation in a Molecular Pentad. *Angew. Chem. Int. Ed.* **2016**, *55*, 9407−9410.

[5]     Mössinger, D.; Jester, S. S.; Sigmund, E.; Müller, U.; Höger, S., Defined Oligo(*p*-phenylene-butadiynylene) Rods. *Macromolecules* **2009**, *42*, 7974−7978.

[6]     Skaisgirski, M.; Guo, X.; Wenger, O. S., Electron Accumulation on Naphthalene Diimide Photosensitized by [Ru(2,2'-Bipyridine)$_3$]$^{2+}$. *Inorg. Chem.* **2017**, *56*, 2432−2439.

[7]     a) Shavaleev, N. M.; Davies, E. S.; Adams, H.; Best, J.; Weinstein, J. A., Platinum(II) Diimine Complexes with Catecholate Ligands Bearing Imide Electron-Acceptor Groups: Synthesis, Crystal Structures, (Spectro)Electrochemical and EPR studies, and Electronic Structure. *Inorg. Chem.* **2008**, *47*, 1532−1547. b) Shavaleev, N. M.; Adams, H.; Best, J.; Weinstein, J. A., Platinum(II) Phosphine Complexes with Acetylene Ligands Containing 1,4,5,8-Naphthalenediimide: Synthesis, Crystal Structure and Electrochemistry. *J. Organomet. Chem.* **2007**, *692*, 921−925.

[8]     Zhu, Q.; Gentry, E. C.; Knowles, R. R., Catalytic Carbocation Generation Enabled by the Mesolytic Cleavage of Alkoxyamine Radical Cations. *Angew. Chem. Int. Ed.* **2016**, *55*, 9969−9973.

[9]     Cai, L.; Qian, X.; Song, W.; Liu, T.; Tao, X.; Li, W.; Xie, X., Effects of Solvent and Base on the Palladium-Catalyzed Amination: PdCl$_2$(Ph$_3$P)$_2$/Ph$_3$P-Catalyzed Selective Arylation of Primary Anilines with Aryl Bromides. *Tetrahedron* **2014**, *70*, 4754−4759.

[10]   a) Lowry, M. S.; Goldsmith, J. I.; Slinker, J. D.; Rohl, R.; Pascal, R. A. Jr.; Malliaras, G. G.; Bernhard, S., Single-Layer Electroluminescent Devices and Photoinduced Hydrogen Production from an Ionic Iridium(III) Complex. *Chem. Mater.* **2005**, *17*,

5712−5719. b) Singh, A.; Teegardin, K.; Kelly, M.; Prasad, K. S.; Krishnan, S.; Weaver, J. D., Facile Synthesis and Complete Characterization of Homoleptic and Heteroleptic Cyclometalated Iridium(III) Complexes for Photocatalysis. *J. Organomet. Chem.* **2015**, *776*, 51−59.

[11]   a) Miller, S. E.; Lukas, A. S.; Marsh, E.; Bushard, P.; Wasielewski, M. R., Photoinduced Charge Separation Involving an Unusual Double Electron Transfer Mechanism in a Donor-Bridge-Acceptor Molecule. *J. Am. Chem. Soc.* **2000**, *122*, 7802−7810. b) Gosztola, D.; Niemczyk, M. P.; Svec, W.; Lukas, A. S.; Wasielewski, M. R., Excited Doublet States of Electrochemically Generated Aromatic Imide and Diimide Radical Anions. *J. Phys. Chem. A* **2000**, *104*, 6545−6551.

[12]   Seo, E. T.; Nelson, R. F.; Fritsch, J. M.; Marcoux, L. S.; Leedy, D. W.; Adams, R. N., Anodic Oxidation Pathways of Aromatic Amines. Electrochemical and Electron Paramagnetic Resonance Studies. *J. Am. Chem. Soc.* **1966**, *88*, 3498−3503.

[13]   Tsai, K. Y.-D.; Chang, I.-J., Oxidation of Bromide to Bromine by Ruthenium(II) Bipyridine-Type Complexes Using the Flash-Quench Technique. *Inorg. Chem.* **2017**, *56*, 8497−8503.

[14]   Weller, A., Photoinduced Electron Transfer in Solution: Exciplex and Radical Ion Pair Formation Free Enthalpies and Their Solvent Dependence. *Z. Phys. Chem.* **1982**, *133*, 93−98.

[15]   Gagliardi, L. G.; Castells, C. B.; Ràfols, C.; Rosés, M.; Bosch, E., Static Dielectric Constants of Acetonitrile/Water Mixtures at Different Temperatures and Debye-Hueckel $A$ and $a_0B$ Parameters for Activity Coefficients. *J. Chem. Eng. Data* **2007**, *52*, 1103−1107.

[16]   Roundhill, D. M., *Photochemistry and Photophysics of Metal Complexes*, Plenum Press: New York, 1994.

[17]   a) Zeng, Y.; Zimmt, M. B., Symmetry Effects on Electron-Transfer Reactions: Temperature Dependence as a Diagnostic Tool. *J. Phys. Chem.* **1992**, *96*, 8395−8403. b) Kumar, K.; Kurnikov, I. V.; Beratan, D. N.; Waldeck, D. H; Zimmt, M. B., Use of Modern Electron Transfer Theories To Determine Electronic Coupling Matrix Elements in Intramolecular Systems. *J. Phys. Chem. A* **1998**, *102*, 5529−5541. c) Wilson, E. K.; Huang, L.; Sutcliffe, M. J.; Mathews, F. S.; Hille, R.; Scrutton, N. S.,

An Exposed Tyrosine on the Surface of Trimethylamine Dehydrogenase Facilitates Electron Transfer to Electron Transferring Flavoprotein: Kinetics of Transfer in Wild-Type and Mutant Complexes. *Biochemistry* **1997**, *36*, 41−48.

# 4 Quantitative Insights into Charge-Separated States Using One- and Two-Pulse Laser Experiments

Charge-separated states (CSSs) are key intermediates in natural photosynthesis (Chapter 2.1) as well as in artificial solar energy conversion[4, 12] and solar fuel production.[5, 7] In particular, photosynthesis-inspired multielectron-transfer reactions to achieve charge accumulation[72, 96–99] are highly dependent on an efficient formation of CSSs. However, the desired reaction steps that bring about charge accumulation compete with light-induced electron-hole recombinations (Scheme 4.1, left part). These recombinations, which are largely unexplored nowadays,[100] are the main deactivation pathway, whose deep understanding is highly desirable to achieve efficient charge accumulation. Moreover, the factors that govern the formation efficiencies of CSSs are still poorly understood[101] since the majority of previous investigations on CSSs only focused on the qualitative CSS formation and its lifetime, after excitation with visible light.[95, 102–106] Systematic quantum yield investigations are rare.[101, 107, 108]
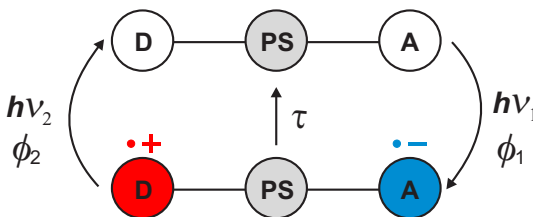


**Scheme 4.1:** Schematic representation of the formation and decay pathways of the CSS in a molecular electron donor-photosensitizer-electron acceptor triad.

The novel approach reported in this chapter is summarized in Scheme 4.1. Formation of the CSS in the schematic donor-photosensitizer-acceptor triad can be achieved by the absorption of a single visible photon (right part of Scheme 4.1). As mentioned above, this charge separation step was mainly studied in a qualitative manner so far.[95] To gain more insights into the factors that govern the CSS formation efficiency, we additionally performed quantitative experiments and determined the quantum yield for charge separation

($\Phi_1$). Charge recombination to the ground-state of the system can occur in two different ways: Well known and studied is the process of thermal charge recombination (central part in Scheme 4.1). However, charge recombination can also be induced by the absorption of a second visible photon (left part in Scheme 4.1).[68] The understanding of this undesired light-induced charge recombination step is crucial for efficient multiphoton processes. If the absorption of a second photon induces charge recombination in the system, efficient accumulation of charges is unlikely. Low quantum yields for charge accumulation, *e.g.* 0.5% in a molecular heptad,[98] can most likely be attributed to light-induced charge recombination after the second photon absorption.

Chapter 3 introduced a set of iridium-based triads that is well suited for the investigations of this chapter (structures of the triads reproduced in Figure 4.1 for clarity). The incorporation of *p*-xylene units (n = 1,2) also allowed us to include distance dependences into our studies. The molecular triads do not permit charge accumulation, which is beneficial for our investigations since the process of light-induced charge recombination can be investigated in isolation. Additionally, the given triads can store roughly 2.0 eV in their CSSs.[95] This amount of stored energy, after absorption of only one visible photon, makes a more detailed investigation of these CSSs worthwhile. For comparison, CSSs that stored energies between 1.7[109] and 1.8 eV[110] were recently declared as highly energetic and the typically stored energy of other triads amounts to about 1.5 eV after single visible light excitation.[47, 94, 108, 111, 112] Highly energetic CSSs are of special interest for driving energy demanding (photo)chemical processes.[109] Another feature that makes the given triads interesting for further investigations is the probability for intraligand charge transfer (CT) after excitation, exclusively in the triad with n = 1. The longer triad (n = 2) exhibits only metal-to-ligand charge transfer (MLCT) after visible light excitation. The presence of different main pathways of CSS formation in the given triads could have an effect on the formation quantum yields.
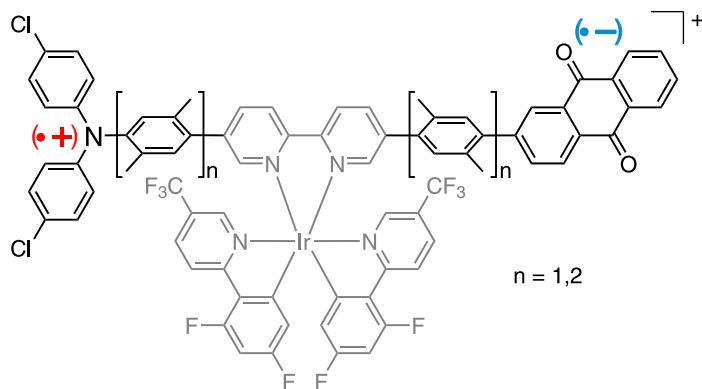


**Figure 4.1:** Molecular structure of the investigated molecular triad including local charges after CSS formation.

The investigations of this study were performed using one- and two-pulse laser experiments (see Chapter 2.4 for details concerning two-pulse experiments). With one-pulse laser flash photolysis, we provide deep insights into the CSS formation quantum yields, which can reach up to 80%. Remarkably, only the triad with n = 1 shows a distinct excitation wavelength dependence of the CSS formation quantum yield, which we explain by intraligand CT competing with more productive MLCT excitation. This intraligand CT is exclusively possible in the shorter triad and reduces the CSS formation quantum yields significantly. Two-pulse laser flash photolysis with a setup developed recently[63] served to elucidate the fate of the CSS upon further (secondary) excitation with green photons. One key finding of our study is that thermal and light-induced charge recombinations show opposite behavior in terms of their distance dependences. Whereas thermal charge recombination in the shorter triad is significantly slower than in the longer triad, light-induced charge recombination shows the exact opposite behavior and is more efficient in the shorter triad, for which we were able to measure a quantum yield of 1.5%. The different efficiencies for light-induced charge recombination in the given systems can be understood in the framework of the MARCUS theory of electron transfer. We propose a key electron-transfer process starting from a highly excited anthraquinone radical anion that follows the conventional distance dependence of the electron-transfer rate, *i.e.* a decrease of the transfer rate with increasing distance, as the most likely explanation for the observed light-induced charge recombination. Thus, light-induced charge recombination is more efficient in the shorter triad. Overall, the findings in this chapter illustrate the importance of quantitative laser experiments and could significantly contribute to the future design and optimization of systems for artificial photosynthesis.

The results of the project that is presented in this chapter were published in Chemical Science[113] during these PhD studies.

- Neumann, S.; Kerzig, C.; Wenger, O. S. Quantitative insights into charge-separated states from one- and two-pulse laser experiments relevant for artificial photosynthesis. *Chem. Sci.* **2019**, *10*, 5624-5633.

## Author Contributions

Svenja Neumann conducted measurements, carried out data analysis and contributed equally to the preparation of the main manuscript and the electronic supporting information.

Christoph Kerzig drafted the main concept of the project. He conducted measurements, carried out data analysis and contributed equally to the preparation of the main manuscript and the electronic supporting information. He also established the setup for

quantitative two-pulse experiments.

Oliver S. Wenger drafted the main concept of the project and contributed equally to data interpretation and the preparation of the main manuscript and the electronic supporting information.

It has to be noted that the synthesis of the triads has already been conducted by Svenja Neumann in an earlier publication presented in Chapter 3.[95]

## EDGE ARTICLE



Check for updates

# Quantitative insights into charge-separated states from one- and two-pulse laser experiments relevant for artificial photosynthesis†

Svenja Neumann, Christoph Kerzig [ID] * and Oliver S. Wenger [ID] *

Charge-separated states (CSSs) are key intermediates in photosynthesis and solar energy conversion. However, the factors governing the formation efficiencies of CSSs are still poorly understood, and light-induced electron–hole recombinations as deactivation pathways competing with desired charge accumulations are largely unexplored. This greatly limits the possibility to perform efficient multi-electron transfer, which is essential for artificial photosynthesis. We present a systematic investigation of two donor–sensitizer–acceptor triads (with different donor–acceptor distances) capable of storing as much as 2.0 eV in their CSSs upon the absorption of a visible photon. Using quantitative one- and two-pulse laser flash photolysis, we provide deep insights into both the CSS formation quantum yield, which can reach up to 80%, and the fate of the CSS upon further (secondary) excitation with green photons. The triad with shorter intramolecular distances shows a remarkable excitation wavelength dependence of the CSS formation quantum yield, and the CSS of this triad undergoes more efficient light-induced charge recombination than the longer equivalent by about one order of magnitude, whilst thermal charge recombination shows the exact opposite behavior. The unexpected results of our detailed photophysical study can be rationalized by detrimental singlet charge transfer states or structural considerations, and could significantly contribute to the future design of CSS precursors for accumulative multi-electron transfer and artificial photosynthesis.

## 1 Introduction

Encouraged by the efficiency of natural photosynthesis,[1] numerous research groups have focused on mimicking its key steps. In particular, a great many studies explored molecular donor–acceptor compounds,[2–27] in which the primary photoinduced charge separation was frequently enabled by a covalently linked photosensitizer.[5,6,10–16,19,24] Optimizing the primary charge separation is without any doubt one basic requirement for the realization of much more complex artificial systems allowing solar fuel production through multiphoton-driven charge accumulation.[28–31] However, the great majority of previous studies on charge-separated states merely investigated their qualitative formation after light absorption and their lifetimes, but systematic quantum yield investigations[12,14,32] are scarce. In direct consequence, the factors governing the charge-separated state (CSS) formation efficiencies are still poorly understood. Even less explored are the processes that occur upon further excitation of CSSs with a second photon, such as

detrimental light-induced charge recombination,[33,34] although their deep understanding is of pivotal importance for the efficient accumulation of redox equivalents.[29,30,35]

The molecular design of our compounds (Scheme 1a) is such that about 2.0 eV are stored (in $CH_3CN$) in the final CSS after absorption of a single visible photon (energies of the photons used for excitation, 2.6 to 3.0 eV). A comparison with CSS energies of other triads revealed that the stored energy typically amounts to about 1.5 eV upon visible light excitation,[9–12,36] and in two recent CSS studies stored energies between 1.7 and 1.8 eV were declared as highly energetic.[4,5] Recently, we reported on the distance dependence of thermal charge recombination in the compounds from Scheme 1a in comparison to two series of other molecular triads.[16] The unusually high CSS energy of the two specific triads in Scheme 1a prompted us to perform a complete quantitative photophysical investigation including new multi-photon excitation studies, geared at understanding light-induced charge recombination. We optimized our laser setup such that it permits one- and two-pulse laser experiments with sensitive and quantitative detection of reaction intermediates, as well as homogeneous excitation in the detection volume (a detailed description of our setup is given in the ESI†). That setup allows us to gain insights that are far beyond those obtained in former investigations of photoinduced electron transfer in donor–acceptor compounds and CSS formation.

*Department of Chemistry, University of Basel, St. Johanns-Ring 19, 4056 Basel, Switzerland. E-mail: christoph.kerzig@unibas.ch; oliver.wenger@unibas.ch*

† Electronic supplementary information (ESI) available: Comprehensive experimental details, further energetic considerations, quantum-mechanical computations and additional laser experiments. See DOI: 10.1039/c9sc01381d
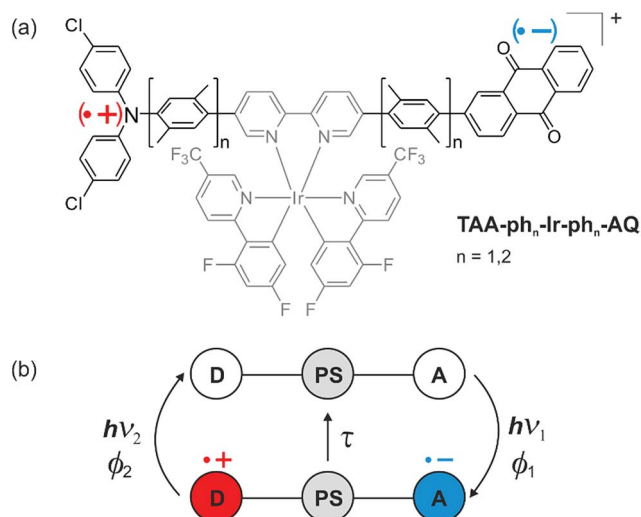
**Scheme 1** (a) Structure of molecular triads. (b) Schematic representation of the mechanism for light-induced ($h\nu_1$) formation of a CSS in a molecular electron donor–photosensitizer–electron acceptor triad together with thermal ($\tau$) and light-induced ($h\nu_2$) charge recombination.

The triads under study contain a triarylamine (TAA) donor and an anthraquinone (AQ) moiety as an acceptor. Symmetrical addition of *p*-xylene units to the central bipyridine moiety enabled us to elongate the triad and to perform distance-dependent studies (Scheme 1a). After visible-light excitation of the iridium photosensitizer, a CSS is formed. As indicated in Scheme 1b, charge recombination between oxidized donor and reduced acceptor can either occur *via* well-known thermal charge recombination with characteristic lifetimes ($\tau$; central part)[16] or through poorly-understood light-induced recombination pathways ($h\nu_2$; left part). Since it is desirable to use high-energy CSSs for demanding (photo)chemical processes,[4] we considered the following aspects in our study: (i) the photoactive system should store as much energy as possible (Section 2.1), (ii) long lifetimes of the CSS are essential for the applicability of the photoactive system for subsequent (photo)reactions (Section 2.2), (iii) high quantum yields for light-induced charge separation are desirable (Section 2.3), (iv) the energy efficiency of photon usage is an important factor, and it is desirable to convert a very large fraction of the photon energy into chemical energy (Sections 2.1 and 2.3), and (v) the absorption of a second visible photon should ideally not induce light-driven charge recombination, which usually represents a detrimental CSS decay pathway (Section 2.4). In particular, that last aspect is underexplored given its importance for accumulative multi-electron transfer,[37–44] and, as noted above, quantitative factors of CSS formation are often neglected in studies of donor–sensitizer–acceptor compounds.[29,30,35]

## 2 Results and discussion

We recently reported the synthesis and characterization of the triads **TAA-ph$_1$-Ir-ph$_1$-AQ** and **TAA-ph$_2$-Ir-ph$_2$-AQ** focusing

exclusively on the influence of driving forces on the distance dependences of thermal charge recombination rates. Our present study substantially extends the earlier investigation of the triads and contains the following new photophysical experiments and insights: (i) excitation wavelength dependent quantum yields for charge separation were measured and insight into the importance of intraligand charge-transfer excitations was obtained; (ii) two-pulse experiments were performed to determine the quantum yield for light-induced charge recombination, to explore whether the distance dependence of that poorly understood side reaction obeys conventional electron transfer theory. The extent of quantitative information gained from these studies is unmatched by earlier investigations of molecular donor–acceptor compounds, and our two-color two-pulse (pump–pump–probe) experiments might inspire new types of photophysical studies.

### 2.1 CSS formation and energetic considerations

Photoexcitation of our Ir-based sensitizer into its metal-to-ligand charge transfer (MLCT) absorption band between 390 and 450 nm produces, after intersystem crossing, its triplet state.[16] However, comparison of the UV-Vis spectrum of **TAA-ph$_1$-Ir-ph$_1$-AQ** (Fig. 1a, green trace) with **TAA-ph$_2$-Ir-ph$_2$-AQ** (Fig. 1a, violet trace) and **Ir-Ref** (Fig. 1a, red trace; see ESI page S8† for molecular structure) shows an unexpectedly high extinction coefficient in the blue for the shorter triad. That observation suggests that this triad exhibits not only an MLCT transition in this spectral range, but there is also an intraligand charge transfer (CT). We postulated earlier that this intraligand CT occurs between the TAA donor and the bipyridine ligand of the photosensitizer and that the increase of the distance between those two moieties in the **TAA-ph$_2$-Ir-ph$_2$-AQ** triad decreases the contribution of the intraligand CT significantly,[16] which is now further substantiated by DFT-calculations (see ESI, page S6†). The population of additional CT transitions is obviously not limited to our system, as the comparison of the UV-Vis absorption spectra within other series of triads suggests, where exclusively the molecules with the shortest distance show additional shoulders in the UV-Vis absorption spectra.[11,45] The same effect can also be observed in dyads with a short TAA-bipyridine distance,[46] while AQ-bipyridine dyads show no differences in the absorption behavior, even with short intramolecular distances.[47]

The amount of stored energy in the CSS ($E_{CSS}$) is equivalent to the driving force ($-\Delta G^0_{CR}$) of the thermal charge recombination process of the photoexcited triads under study. The driving force can be derived from the redox potentials of AQ$^{•-}$ and TAA$^{•+}$ in the respective triad (Fig. 1b and ESI, page S5†), which results in a $-\Delta G^0_{CR}$ value of 1.99 eV for the shorter **TAA-ph$_1$-Ir-ph$_1$-AQ** triad and 1.96 eV for **TAA-ph$_2$-Ir-ph$_2$-AQ**, *i.e.*, both triads can store *ca.* 2.0 eV in their CSSs (in CH$_3$CN). The maximal excitation wavelength for detectable CSS formation in the **TAA-ph$_2$-Ir-ph$_2$-AQ** triad is 450 nm, whereas the CSS of **TAA-ph$_1$-Ir-ph$_1$-AQ** can be generated with wavelengths up to *ca.* 470 nm due to the higher extinction coefficients resulting from the superposition of Ir-based MLCT and intraligand CT transitions (see
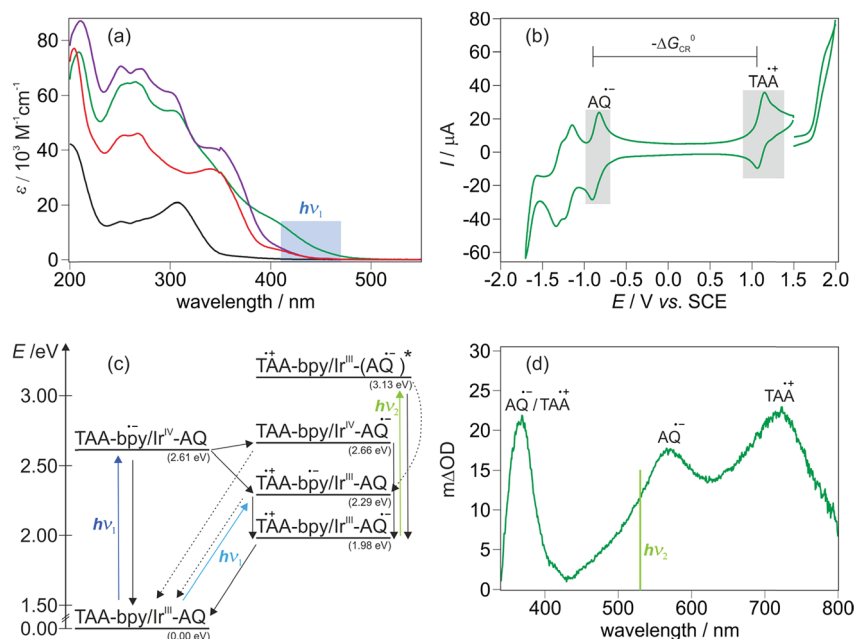
**Fig. 1** (a) UV-Vis absorption spectra of **TAA-ph$_1$-Ir-ph$_1$-AQ** (green), **TAA-ph$_2$-Ir-ph$_2$-AQ** (violet), **Ir-Ref** (red, see Fig. S3† for molecular structure) and the bipyridine-containing free ligand of the longer triad (black) in CH$_3$CN at 293 K. The highlighted region indicates the wavelength range used for photoexcitation. (b) Cyclic voltammogram for **TAA-ph$_1$-Ir-ph$_1$-AQ** in dry and deoxygenated CH$_3$CN. TBAPF$_6$ (0.1 M) was used as an electrolyte and a scan rate of 0.1 V s$^{-1}$ was applied. (c) Averaged energy of relevant excited states and relevant intermediates for **TAA-ph$_1$-Ir-ph$_1$-AQ** and **TAA-ph$_2$-Ir-ph$_2$-AQ** in CH$_3$CN. Energies were estimated using the redox potentials from Table S1 and eqn (S1).† $E_{00}$ for the Ir sensitizer is 2.61 eV (ref. 16) whereas $E_{00}$ for AQ$^{\bullet-}$ was estimated from its long wavelength absorption band.[49] (d) Transient UV-Vis absorption spectrum of **TAA-ph$_1$-Ir-ph$_1$-AQ** in deoxygenated CH$_3$CN at 293 K. A 20 μM solution was excited at 440 nm with laser pulses of *ca.* 10 ns duration; detection occurred by integration over a period of 200 ns immediately afterwards.

Fig. 1a and Section 2.3 for details). Excitation with longer wavelengths is preferred to maximize energy efficiencies ($\eta$), which we define as the ratios of $E_{CSS}$ and the photon energies at the maximum excitation wavelength usable for CSS formation under our conditions. With the photon energies at the above-mentioned limiting wavelengths, energy efficiencies of 71% (longer triad) and 75% (shorter triad) thus result. These values are close to the upper limit of already reported high-energy CSSs where a visible photon was absorbed to form the respective CSS.[4,5,11,48] The energy efficiencies for the triads under study also compare very favorably with a reported two-photon process, which stores the same amount of energy as our triads.[28] Based on the redox potentials from the cyclic voltammograms of the triads (Fig. 1b and ESI, page S5†), an energy level scheme for excited states and relevant intermediates of the triads **TAA-ph$_1$-Ir-ph$_1$-AQ** and **TAA-ph$_2$-Ir-ph$_2$-AQ** was calculated (Fig. 1c). The shown energies are averaged over both triads. Excitation of **TAA-ph$_1$-Ir-ph$_1$-AQ** ($\lambda_1 = 470$ nm) mainly results in an intraligand CT from the TAA unit to the bipyridine ligand of the Ir sensitizer since there is a significant oscillator strength for this excitation (see ESI, page S6†). Electron transfer from the reduced bipyridine to the AQ unit finally gives the long-lived CSS. By contrast, the absorption of a higher energy photon ($\lambda_1 = 450$ nm) by **TAA-ph$_2$-Ir-ph$_2$-AQ** mainly excites an MLCT transition. The final CSS can then be generated by (i) reductive quenching of the excited Ir chromophore by the TAA moiety, followed by an electron transfer from the reduced Ir photosensitizer to the AQ unit, or

(ii) oxidative quenching of the excited Ir sensitizer by the AQ unit, followed by an electron transfer from the TAA moiety to the Ir$^{IV}$ species. The formed final CSS in both triads can then undergo thermal charge recombination into the ground state. In addition, the final CSS can also be selectively photoexcited by absorption of a second visible photon ($\lambda_2 = 532$ nm) inducing rapid reverse electron transfer as discussed in Section 2.4.

The formation of the final CSS was detected immediately after photoexcitation by transient absorption spectroscopy (Fig. 1d and S5 of the ESI†). The transient absorption spectrum of **TAA-ph$_1$-Ir-ph$_1$-AQ** (Fig. 1d) clearly shows the spectroscopic signatures of the anticipated CSS. The one-electron oxidized TAA unit exhibits bands at 370 and 720 nm whereas the AQ$^{\bullet-}$ species is characterized by bands at 370 and 570 nm.[16] For **TAA-ph$_2$-Ir-ph$_2$-AQ**, the same spectroscopic signatures can be observed though the TAA$^{\bullet+}$ signal shifts from 720 to *ca.* 700 nm (see ESI, Fig. S5†).

### 2.2 Lifetimes of charge-separated states

In a recent study we compared the distance dependence of charge recombination rates in **TAA-ph$_1$-Ir-ph$_1$-AQ** and **TAA-ph$_2$-Ir-ph$_2$-AQ** to two other series of triads with Ru-based sensitizers.[16] For **TAA-ph$_1$-Ir-ph$_1$-AQ** and **TAA-ph$_2$-Ir-ph$_2$-AQ** we found that CSS lifetimes decrease with increasing donor–acceptor distance, and this somewhat counter-intuitive behavior is readily understood on the basis of Marcus theory as discussed earlier.[11,16,45,50–52] In the present study, lower excitation densities

were used (see also ESI page S3†) and lifetimes of the CSSs ($\tau_{CSS}$) of *ca.* 1.2 μs for **TAA-ph$_1$-Ir-ph$_1$-AQ** and *ca.* 85 ns for **TAA-ph$_2$-Ir-ph$_2$-AQ** were determined in dry and deoxygenated CH$_3$CN at 293 K. The instantaneous CSS formation within the duration of the exciting laser pulse (*ca.* 10 ns), which is further confirmed by kinetic emission measurements (see ESI page S8†), and thermal charge recombination in both triads are illustrated by Fig. 2.

Consideration of the relationship between a high driving force, *i.e.*, a high $E_{CSS}$, and a long donor–acceptor distance has an important impact on the future design of CSS precursors for artificial photosynthesis and charge accumulation. The capability of high energy storage is desirable, but too long donor–acceptor distances in such systems can counteract a long lifetime of the CSS (see Fig. 2),[11,16,45,52] which is required to exploit the stored energy for subsequent (photo)reactions,[4,53] and are therefore counterproductive for the application in solar energy storage and conversion.

## 2.3 Quantum yields and excitation wavelength dependences of CSS formation

In sophisticated molecular systems designed for multiphoton-driven charge accumulation, the quantum yield for formation of the primary CSS should ideally be close to unity. In this section, we will comprehensibly describe an experimental technique suitable for CSS quantum yield determinations using molecular triads as model compounds to study that process in isolation, and we will provide strategies to understand unexpected results. Our methodology is based on relative actinometry[54] combined with laser flash photolysis (LFP). In principle the actinometry-LFP combo is a rather old approach,[55–57] but many 21st century photochemists do not seem to be familiar with that powerful tool, perhaps due to the lack of tutorial reviews as recently published for other photochemical techniques.[58,59] Fig. 3 enlarges on our quantum yield determination methodology. As reference system suitable for laser flash photolysis actinometry,[60–64] we selected tris(2,2'-bipyridine) ruthenium(ii) [Ru(bpy)$_3$]$^{2+}$ in water (the favorable properties of that system are summarized on page S3 of the ESI†). First, solutions of [Ru(bpy)$_3$]$^{2+}$ and the respective Ir-containing triad
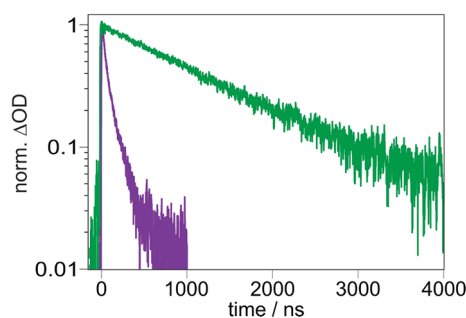


Fig. 3 Raw data used for the quantum yield determination of CSS formation for **TAA-ph$_1$-Ir-ph$_1$-AQ** upon 410 nm laser excitation with 8 mJ laser pulses of about 10 ns duration. (a) UV-Vis absorption spectra of **TAA-ph$_1$-Ir-ph$_1$-AQ** (green, in CH$_3$CN) and [Ru(bpy)$_3$]$^{2+}$ (orange, in water), which was used as reference compound for relative actinometry. (b) Transient absorption traces upon 410 nm excitation of the deoxygenated solutions shown in (a). CSS formation was monitored at 720 nm (green), [Ru(bpy)$_3$]$^{2+}$ ground state bleach at 455 nm (orange). For further explanation, see the main text and Section 1.3 of the ESI.†

were prepared with concentrations ensuring identical absorption values at the desired excitation wavelength. An example for **TAA-ph$_1$-Ir-ph$_1$-AQ** prior to exciting with 410 nm laser pulses is shown in Fig. 3a. Second, employing the very same excitation conditions for the reference system and the triad under study, transient absorption traces at 455 nm (maximum of the [Ru(bpy)$_3$]$^{2+}$ ground state bleach)[63] and the CSS absorption maximum (**TAA-ph$_1$-Ir-ph$_1$-AQ**, 720 nm; **TAA-ph$_2$-Ir-ph$_2$-AQ**, 700 nm) were recorded (Fig. 3b).

Third and finally, the transient absorption traces so obtained were converted into relative intermediate concentrations using the well-established (difference) molar absorption coefficients for the [Ru(bpy)$_3$]$^{2+}$ ground state bleach (together with the quantum yield for the [Ru(bpy)$_3$]$^{2+}$ excitation producing its triplet state, which is unity[65]) and the estimated extinction coefficients at the maximum of the respective CSS (see Section 1.3 of the ESI† for details). Surprisingly, the CSS quantum yields for the two triads differ by almost a factor of 3 under very similar conditions (Fig. 4). Control experiments with 410 nm excitation at significantly reduced laser intensity (to about 50%) gave essentially the same quantum yields for both triads compared to the results at higher intensities (8 mJ, see Fig. 3). We regard these observations as clear evidence for the absence of biphotonic side reactions, such as a two-photon ionization[66] or light-induced charge recombination (compare, Section 2.4), and saturation effects.[67] Moreover, all quantum yield determinations presented in this work were carried out with solutions having absorptions below 0.105 at the excitation wavelengths to avoid filter effects.[68] A simplified procedure frequently used to estimate quantum yields is the analysis of the quenching efficiency of the photosensitizer as CSS precursor employing kinetic measurements.[4,46] This easy-to-obtain quantity, which does not take chemically unproductive deactivation pathways



Fig. 2 Formation and decay of the transient absorption signals for **TAA-ph$_1$-Ir-ph$_1$-AQ** (green) and **TAA-ph$_2$-Ir-ph$_2$-AQ** (violet) in dry and deoxygenated CH$_3$CN at 293 K monitoring the TAA$^{•+}$ band at 720 nm (green) and 700 nm (violet). Excitation of both triads occurred at 433 nm with laser pulses of *ca.* 10 ns duration.
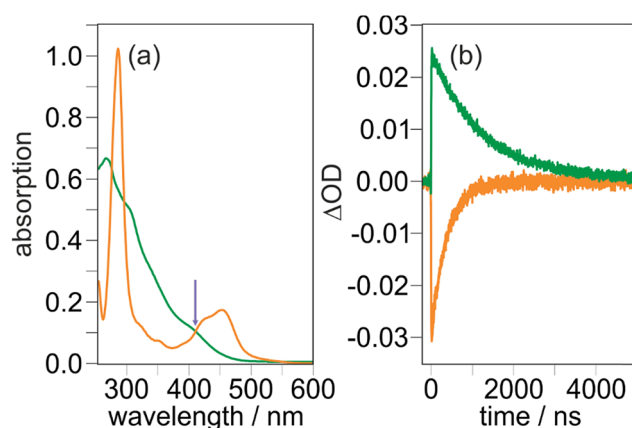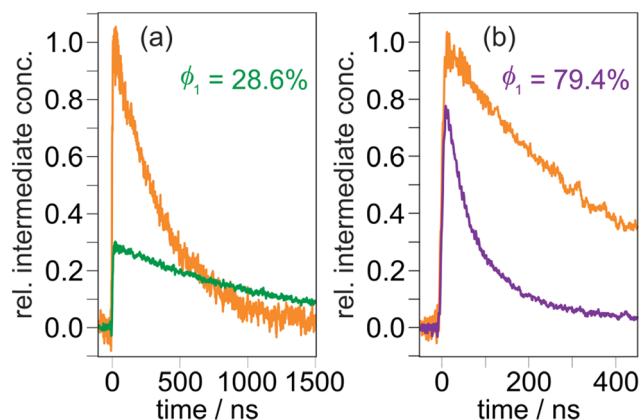
**Fig. 4** CSS formation quantum yields of **TAA-ph$_1$-Ir-ph$_1$-AQ** (a) and **TAA-ph$_2$-Ir-ph$_2$-AQ** (b) upon 410 nm laser excitation (8 mJ pulse energy). The CSS concentrations after the laser pulses were calculated relative to the amounts of absorbed photons as measured by means of relative actinometry with additional experiments on [Ru(bpy)$_3$]$^{2+}$ (orange reference traces) under identical excitation conditions. Further details are given in the main text and Section 1.3 of the ESI.†

**Table 1** Wavelength-dependent quantum yields of CSS formation$^a$

| Excitation wavelength/nm | CSS formation quantum yield$^b$/% | |
| --- | --- | --- |
| | **TAA-ph$_1$-Ir-ph$_1$-AQ** | **TAA-ph$_2$-Ir-ph$_2$-AQ** |
| 410 | 28.6 | 79.4 |
| 425 | 24.4 | 76.6 |
| 433 | 18.9 | 87.4 |
| 440 | 16.1 | 85.4 |
| 450 | 14.4 | 82.0 |
| 460 | 12.8 | —$^c$ |
| 470 | 6.0 | —$^c$ |

$^a$ Measured in deoxygenated CH$_3$CN at 293 K. The maximum relative error is expected to be less than 10%. $^b$ Details concerning the experimental methodology are given in the main text and in Section 1.2 of the ESI. $^c$ Cannot be determined owing to negligible absorption of the triad at the excitation wavelength.

into account, would predict quantitative CSS formation for both **TAA-ph$_1$-Ir-ph$_1$-AQ** and **TAA-ph$_2$-Ir-ph$_2$-AQ** (see Section 4.1 of the ESI†). Therefore, our results highlight the importance of direct quantum yield determinations with relative actinometry.

The widely differing quantum yields obtained upon 410 nm excitation (28.6 vs. 79.4%, Fig. 4) prompted us to explore the influence of the excitation wavelength on CSS formation. Prior to carrying out additional kinetic measurements as in Fig. 4, we recorded transient absorption spectra using at least four different laser wavelengths for exciting our triads. Our experiments demonstrate that the spectral shapes and relative absorption signal intensities do not depend on the excitation wavelength (see Fig. S5 of the ESI†). Hence, in line with Kasha's rule,[69,70] the respective CSS is the only intermediate observable on a nanosecond timescale. Furthermore, more than 500 laser flashes on the very same solution do neither change the CSS absorption spectra nor their intensities, indicating that no photochemical side reactions are taking place. All quantum yield determinations at the excitation wavelengths covering the experimentally accessible range (see Section 2.1) were carried out with the same methodology as at 410 nm (Fig. 3 and 4). To compensate small laser intensity fluctuations and obtain a suitable signal-to-noise ratio, at least 20 kinetic traces were averaged for every quantum yield measurement summarized in Table 1. The results presented in that table reveal a quasi-wavelength independence for the CSS formation quantum yield of **TAA-ph$_2$-Ir-ph$_2$-AQ** with a mean value as high as 82%, whereas for **TAA-ph$_1$-Ir-ph$_1$-AQ**, the CSS formation efficiencies differ by a factor of 5 over the explored excitation wavelength range, decreasing in a systematic manner at longer wavelengths.

A plausible explanation for the markedly different behavior of the quantum yields in Table 1 is provided by different main pathways of CSS formation in the two triads. As discussed in Section 2.1, photoexcitation of **TAA-ph$_1$-Ir-ph$_1$-AQ** mainly occurs

into an intraligand CT transition, whereas in the case of **TAA-ph$_2$-Ir-ph$_2$-AQ**, excitation into MLCT bands of the photo-sensitizer dominates when violet or blue photons are employed. Starting from these charge-transfer states, which are formed in their singlet states due to spin conservation,[71] subsequent intersystem crossing (ISC) to the triplet manifold can occur. Ir-based excited $^1$MLCT states usually undergo very fast (<1 ps) and quantitative ISC,[72,73] but intraligand CT states or CT states in purely organic systems are known for their ultrafast and unproductive (singlet) recombination in polar solvents (the recombination of $^1$TAA$^{•+}$-bpy$^{•−}$/Ir$^{III}$-AQ in this case; see Fig. 1c for details).[74–76] As a direct consequence, the quantum yields for the production of long-lived (triplet) CSSs via $^3$MLCT states can approach values close to unity, while in the intermediate intraligand singlet CT states, ultrafast recombination competes with ISC and productive charge separation. In line with that reasoning, the CSS quantum yields of **TAA-ph$_1$-Ir-ph$_1$-AQ** increase with decreasing excitation wavelengths, i.e., when the admixture of direct MLCT excitation increases relative to intraligand CT excitation (see UV-Vis spectra in Fig. 1a).

## 2.4 Light-induced charge recombination

With the ultimate aim of achieving photoinduced charge accumulation in molecular systems without sacrificial additives, many sophisticated compounds have been prepared, but in the last decade only a handful of investigations succeeded in overcoming the associated difficulties.[31,77–80] Starting from the first CSS, a key problem is the light-induced charge recombination upon excitation of intermediate electrons/holes with a second photon (see Scheme 1b), which is competitive with the desired accumulation of redox equivalents.[29,30] Given that CSSs typically exhibit intense absorptions over a broad wavelength range, selective photosensitizer excitation is even more difficult under conditions of solar (broadband) irradiation than it is under well-defined lab (monochromatic) conditions. However, this is currently a heavily underexplored area given its importance for accumulative multi-electron transfer.[29,33,35,78,81] The molecular triads investigated in this study do not permit charge accumulation, but they are well-suited for studying light-

induced charge recombination processes and for quantum yield determinations of this undesired side reaction, which lay the grounds for structural optimizations to avoid that detrimental process.

Two-pulse two-color laser flash photolysis is the ideal experimental technique to investigate consecutive photoreactions, both for purely intramolecular reactions[34,60,82–84] and reaction sequences with intervening bimolecular processes.[81,85–87] This holds also true for the mechanism shown in Scheme 1b: the first (violet or blue) pulse serves to produce the desired CSS, and the ensuing second (green) pulse[88] investigates the fate of this intermediate upon absorption of another photon. In line with the absorption spectra displayed in Fig. 1a, the latter pulse (532 nm) alone has no effect on the ground states of the triads, which was verified by control experiments. Hence, that pulse selectively excites the CSSs in our systems with $AQ^{\cdot-}$ being the main absorbing species at 532 nm (see Fig. 1d and page S4 of the ESI†). The two-pulse experiments on **TAA-ph$_1$-Ir-ph$_1$-AQ** are summarized in Fig. 5. Initial experiments with an interpulse delay of 240 ns (the pulse sequence is shown at the top of Fig. 5b) and monitoring at the maximum of the CSS, 720 nm, revealed a green-light induced CSS bleach of about 24%, as is evidenced in the main plot of Fig. 5a. The rather long interpulse delay allows sensitive monitoring of the CSS absorption spectrum between the two pulses (200 ns integration time, green spectrum in Fig. 5b), and its comparison with the spectrum observed after the green pulse (gray spectrum in Fig. 5b). Comparing the spectra presented in Fig. 5b, we found that all (positive) absorption peaks in the gray spectrum are less intense by about 39%, and even the ground state bleach at 320 nm recovers accordingly; in other words, the normalized spectra are completely identical (normalization not shown). A correction of the ~39% signal decrease observed in Fig. 5b for the thermal CSS recombination, which also takes place during spectral detection, gave essentially the same result for the light-induced recombination (23%) as extracted from kinetic traces (24%, see above). Moreover, the kinetics of thermal charge recombination are unaffected by the second pulse (Fig. S6 of the

ESI†). Hence, all these two-pulse experiments on **TAA-ph$_1$-Ir-ph$_1$-AQ** unambiguously establish that charge recombination is the only green-light-induced process observable on the nanosecond timescale.

Given the sensitive and isolated detection of light-induced charge recombination, its quantum yield determination became a realistic target. Starting from the experimental conditions presented in Fig. 5a, we analyzed the CSS bleach at six different intensities of the second laser while keeping all other parameters unchanged. The intensity dependent relative recombination yields were extracted by independent fitting of pre- and post-pulse signals and extrapolation to the time of the second laser pulse, i.e., $t = 240$ ns (inset of Fig. 5a, gray data points). For a reliable quantum yield determination, we applied the same method as in a recent investigation on a second-pulse induced photoreaction.[60] Briefly, we again employed $[Ru(bpy)_3]^{2+}$ in water as reference system (compare, Section 2.3) and quantified the relative green-light induced ground state bleach upon excitation with laser pulses spanning a similar intensity range (inset of Fig. 5a, orange data points). To minimize experimental uncertainties associated with single-point actinometry,[61] we fitted both intensity dependencies with a saturation function that is valid for monophotonic photoreactions.[60,89] By analyzing the fit parameters with the extinction coefficients (at 532 nm) of the respective absorbing species (CSS of **TAA-ph$_1$-Ir-ph$_1$-AQ**, 15 500 $M^{-1}$ cm$^{-1}$, see page S4 of the ESI† for details; $[Ru(bpy)_3]^{2+}$, 720 $M^{-1}$ cm$^{-1}$),[62] a quantum yield for the light-induced charge recombination ($\phi_2$) of 1.5% was finally obtained.

Similar two-pulse experiments were carried out with **TAA-ph$_2$-Ir-ph$_2$-AQ** (Section 4.2 of the ESI†). Owing to the shorter CSS lifetime of that triad (Section 2.2), single-wavelength transient absorption kinetic traces are much more sensitive than spectral measurements with (short) detection time windows. However, during kinetic traces recorded at both the $AQ^{\cdot-}$ and the $TAA^{\cdot+}$ absorption maximum with a 45 ns interpulse delay, we did not observe any noticeable second-pulse induced absorption change, although at 532 nm the CSS of **TAA-ph$_2$-Ir-ph$_2$-AQ**
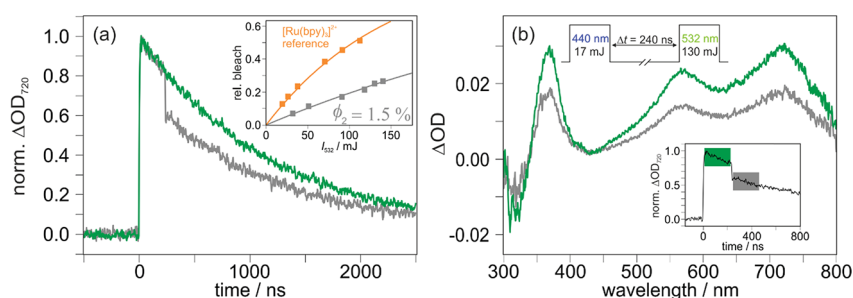


**Fig. 5** Observing and quantifying the light-induced charge recombination in **TAA-ph$_1$-Ir-ph$_1$-AQ** (20 μM in deoxygenated CH$_3$CN) using two-pulse experiments with the general pulse sequence displayed at the top of panel (b). (a) Main plot: kinetic traces for the CSS of the triad at 720 nm with the second laser pulse blocked (green) or unblocked (gray). Inset: relative CSS bleaching at different intensities of the second laser (gray), together with the intensity dependence of the green-light induced $[Ru(bpy)_3]^{2+}$ bleach (orange) used as reference for the charge recombination quantum yield ($\phi_2$) determination. The fit parameters $a$ for the saturation curves $(1 - \exp[-I_{532}/a])$ are 150 mJ (orange) and 463 mJ (gray). (b) Main plot: transient absorption spectrum of **TAA-ph$_1$-Ir-ph$_1$-AQ** before (green) and after (gray) the second laser pulse in a representative two-pulse experiment. The inset shows a kinetic transient absorption measurement under identical conditions (the detection windows used for recording the transient absorption spectra of the main plot have been highlighted). For details, see text.

absorbs slightly more strongly than that of **TAA-ph₁-Ir-ph₁-AQ** (see ESI page S4†). Taking into account the reduced detection sensitivity for these measurements on the short-lived CSS in this triad, we estimate an upper limit of 0.2% for the green-light induced charge recombination of this compound.

Given that the green pulse is mainly absorbed by the anthraquinone radical anion part of the CSS (page S4 of the ESI†), we assume that the following mechanism explains the widely differing quantum yields for light-induced charge recombination in our triads (1.5 *vs.* 0.2%). Excitation of $AQ^{\bullet-}$ at 532 nm (2.33 eV) produces – after ultrafast internal conversion – the lowest excited doublet state $*AQ^{\bullet-}$, whose energy lies ∼1.15 eV above the electronic ground state of $AQ^{\bullet-}$ (estimated from its long wavelength absorption band).[49] Isolated $*AQ^{\bullet-}$ is known to rapidly deactivate back to $AQ^{\bullet-}$: averaging over the available literature values gave a lifetime as short as ∼40 ps,[49,90,91] and we expect a similar natural lifetime of $*AQ^{\bullet-}$ in our triads. Based on structural and energetic considerations, we regard the electron transfer to the bipyridine (bpy) moiety as the most-likely reaction pathway competing with photophysical deactivation. Once the bipyridine radical anion is formed, recombination with the adjacent $TAA^{\bullet+}$ could account for the observed ground-state regeneration through light-induced charge recombination (see also Fig. 1c).

With a driving force of about 0.85 eV for the reaction between $*AQ^{\bullet-}$ and bpy (see energies of the pertinent states in Fig. 1c), a conventional distance dependence of the electron transfer rates is expected, *i.e.*, a rate constant decrease with increasing distances.[9,92,93] With the above-mentioned quantum yields of light-induced charge recombination and a rate of ∼1/40 ps for photophysical deactivation, reasonable rate constants for the intermolecular electron transfer between $*AQ^{\bullet-}$ and bpy on the order of $4 \times 10^8$ s$^{-1}$ (**TAA-ph₁-Ir-ph₁-AQ**) and $<5 \times 10^7$ s$^{-1}$ (**TAA-ph₂-Ir-ph₂-AQ**) can be estimated, if we simply assume that this intramolecular reaction is rate-limiting. The reasoning of the preceding paragraph could thus explain that green-light-induced charge recombination of **TAA-ph₁-Ir-ph₁-AQ** is more efficient than that of **TAA-ph₂-Ir-ph₂-AQ** by about one order of magnitude. Moreover, it is worth emphasizing that a quantum yield of 1.5% for an undesired pathway starting from a CSS is not negligible, since it could clearly outperform the quantum yield of desired charge accumulation (*e.g.*, 0.5% in ref. 77). Although our triads are well-suited test systems to understand (biphotonic) light-induced recombination processes, we consider the probability of a (second) photon absorption by the CSSs of our triads with (sub)microsecond lifetimes as very unlikely under sunlight conditions. This is borne out by previous publications on intensity-dependent photoreactions with intermediates possessing nanosecond[94] to microsecond[60] lifetimes, whose efficient biphotonic ionization was only feasible with pulsed lasers or collimated laser diodes providing light power densities >1 kW cm$^{-2}$.

The experiments of this section illustrate the wealth of information that is accessible by quantitative two-pulse experiments on molecular triads, and that electron transfer rate distance dependencies could also help understand light-induced recombination processes.

**Table 2** Comparative results obtained for the CSSs of the triads under study

| Triad | $E_{CSS}{}^a$/eV | $\tau_{CSS}{}^b$/ns | $\phi_1{}^c$/% | $\phi_2{}^d$/% | $\eta^e$/% |
|---|---|---|---|---|---|
| TAA-ph₁-Ir-ph₁-AQ | 1.99 | 1210 ± 20 | 6.0–28.9$^f$ | 1.5 | 75 |
| TAA-ph₂-Ir-ph₂-AQ | 1.96 | 85 ± 5 | 82.2 ± 4.4 | <0.2 | 71 |

$^a$ Energy of the respective CSS. $^b$ CSS lifetime in deoxygenated CH₃CN at 293 K. $^c$ Quantum yield of CSS formation. $^d$ Quantum yield of light-induced charge recombination upon CSS excitation at 532 nm. $^e$ Upper limit for the efficiency of photon-to-chemical energy conversion. $^f$ Wavelength-dependent, see Table 1 for details.

## 3 Conclusions

The results of our extensive photophysical investigations on two structurally closely related molecular triads clearly demonstrate the difficulty of optimizing all desirable properties for solar energy storage in a single molecular system at once (all pertinent results are summarized in Table 2). After excitation of an Ir-based sensitizer with a single visible photon, both triads are able to form an unusually highly energetic CSS (∼2.0 eV) comprising a triarylamine radical cation and an anthraquinone radical anion. Under optimized excitation conditions, up to 75% of the initial photon energy can be stored in the final CSS. The triad with the short bridge stores the energy 14 times longer than the counterpart with longer intramolecular distances.[16] However, quantitative two-pulse laser experiments revealed that the CSS of the shorter triad (**TAA-ph₁-Ir-ph₁-AQ**) undergoes light-induced charge recombination about ten times more efficiently than that of the longer triad (**TAA-ph₂-Ir-ph₂-AQ**). Thus, the intriguing key finding is that thermal charge recombination is substantially slower in the shorter triad, but at the same time light-induced charge recombination is significantly more efficient in that compound. These observations can be understood in the framework of Marcus theory as pointed out in Sections 2.2 and 2.4. The CSS formation quantum yield of the shorter triad crucially depends on the laser excitation wavelength (anti-Vavilov behavior)[70] and ranges from 6.0 to 28.9%, whereas CSS formation for the longer triad is largely wavelength-independent with a quantum yield as high as 82% under comparable conditions. To our knowledge, these observations have no precedent in the literature on charge-separation in donor-sensitizer-acceptor compounds. The wavelength-dependence and the low quantum yields for CSS formation in the short triad are most likely due to direct excitation into an additional intraligand CT state of singlet parentage (substantiated by DFT calculations), which undergoes ultrafast charge recombination competing with CSS formation. By contrast, the longer triad is predominantly excited into a ¹MLCT excited state, and following rapid intersystem crossing to the ³MLCT state of the Ir sensitizer, productive charge separation outcompetes undesired charge recombination events. This shows that triplet excited states can lead to substantially higher quantum yield for charge separation than singlet excited states.

As has emerged from this work, wavelength-dependent one- and two-pulse laser flash photolysis with quantitative detection

of reaction intermediates is a powerful tool to investigate unexpected or even unexplored effects that are highly relevant for artificial photosynthesis. In particular, quantitative pump–probe and pump–pump–probe spectroscopy combined with electron transfer theory and simple DFT calculations provides a clear picture of important CSS properties. We anticipate that our approach might facilitate both the further optimization of CSS precursors and multi-electron storage in molecular systems.

## Conflicts of interest

There are no conflicts to declare.

## Acknowledgements

## References

1 *Molecular Mechanisms of Photosynthesis*, ed. R. E. Blankenship, Blackwell Science Ltd, Oxford, UK, 2002.

2 M. R. Wasielewski, M. P. Niemczyk, W. A. Svec and E. B. Pewitt, *J. Am. Chem. Soc.*, 1985, **107**, 1080–1082.

3 Y. Luo, M. Wächtler, K. Barthelmes, A. Winter, U. S. Schubert and B. Dietzek, *Chem. Commun.*, 2018, **54**, 2970–2973.

4 G. N. Lim, C. O. Obondi and F. D'Souza, *Angew. Chem., Int. Ed.*, 2016, **55**, 11517–11521.

5 N. Zarrabi, C. Agatemor, G. N. Lim, A. J. Matula, B. J. Bayard, V. S. Batista, F. D'Souza and P. K. Poddutoori, *J. Phys. Chem. C*, 2019, **123**, 131–143.

6 N. Zarrabi, C. O. Obondi, G. N. Lim, S. Seetharaman, B. G. Boe, F. D'Souza and P. K. Poddutoori, *Nanoscale*, 2018, **10**, 20723–20739.

7 R. M. Williams, M. Koeberg, J. M. Lawson, Y.-Z. An, Y. Rubin, M. N. Paddon-Row and J. W. Verhoeven, *J. Org. Chem.*, 1996, **61**, 5055–5062.

8 C. Luo, D. M. Guldi, H. Imahori, K. Tamaki and Y. Sakata, *J. Am. Chem. Soc.*, 2000, **122**, 6535–6551.

9 J. Wiberg, L. Guo, K. Pettersson, D. Nilsson, T. Ljungdahl, J. Mårtensson and B. Albinsson, *J. Am. Chem. Soc.*, 2007, **129**, 155–163.

10 H. Imahori, K. Tamaki, D. M. Guldi, C. Luo, M. Fujitsuka, O. Ito, Y. Sakata and S. Fukuzumi, *J. Am. Chem. Soc.*, 2001, **123**, 2607–2617.

11 M. Kuss-Petermann and O. S. Wenger, *J. Am. Chem. Soc.*, 2016, **138**, 1349–1358.

12 H. Imahori, Y. Sekiguchi, Y. Kashiwagi, T. Sato, Y. Araki, O. Ito, H. Yamada and S. Fukuzumi, *Chem.–Eur. J.*, 2004, **10**, 3184–3196.

13 M. Borgström, N. Shaikh, O. Johansson, M. F. Anderlund, S. Styring, B. Åkermark, A. Magnuson and L. Hammarström, *J. Am. Chem. Soc.*, 2005, **127**, 17504–17515.

14 J. Schäfer, M. Holzapfel, A. Schmiedel, U. E. Steiner and C. Lambert, *Phys. Chem. Chem. Phys.*, 2018, **20**, 27093–27104.

15 L. Sun, L. Hammarström, B. Åkermark and S. Styring, *Chem. Soc. Rev.*, 2001, **30**, 36–49.

16 S. Neumann and O. S. Wenger, *Inorg. Chem.*, 2019, **58**, 855–860.

17 M. M. Waskasi, G. Kodis, A. L. Moore, T. A. Moore, D. Gust and D. V. Matyushov, *J. Am. Chem. Soc.*, 2016, **138**, 9251–9257.

18 J. Sukegawa, C. Schubert, X. Zhu, H. Tsuji, D. M. Guldi and E. Nakamura, *Nat. Chem.*, 2014, **6**, 899–905.

19 K. Hu, A. D. Blair, E. J. Piechota, P. A. Schauer, R. N. Sampaio, F. G. L. Parlane, G. J. Meyer and C. P. Berlinguette, *Nat. Chem.*, 2016, **8**, 853–859.

20 M. Delor, T. Keane, P. A. Scattergood, I. V. Sazanovich, G. M. Greetham, M. Towrie, A. J. H. M. Meijer and J. A. Weinstein, *Nat. Chem.*, 2015, **7**, 689–695.

21 M. Natali, S. Campagna and F. Scandola, *Chem. Soc. Rev.*, 2014, **43**, 4005–4018.

22 M. Krzeszewski, E. M. Espinoza, C. Červinka, J. B. Derr, J. A. Clark, D. Borchardt, G. J. O. Beran, D. T. Gryko and V. I. Vullev, *Angew. Chem., Int. Ed.*, 2018, **57**, 12365–12369.

23 D. S. Tyson, C. R. Luman and F. N. Castellano, *Inorg. Chem.*, 2002, **41**, 3578–3586.

24 M. S. Eberhart, L. M. R. Bowers, B. Shan, L. Troian-Gautier, M. K. Brennaman, J. M. Papanikolas and T. J. Meyer, *J. Am. Chem. Soc.*, 2018, **140**, 9823–9826.

25 J.-J. Shen, J.-Y. Shao, Z.-L. Gong and Y.-W. Zhong, *Inorg. Chem.*, 2015, **54**, 10776–10784.

26 J. Zhou, Y. Wu, I. Roy, A. Samanta, J. F. Stoddart, R. M. Young and M. R. Wasielewski, *Chem. Sci.*, 2019, **10**, 4282–4292.

27 E. Sundin and M. Abrahamsson, *Chem. Commun.*, 2018, **54**, 5289–5298.

28 L. Favereau, A. Makhal, Y. Pellegrin, E. Blart, J. Petersson, E. Göransson, L. Hammarström and F. Odobel, *J. Am. Chem. Soc.*, 2016, **138**, 3752–3760.

29 Y. Pellegrin and F. Odobel, *Coord. Chem. Rev.*, 2011, **255**, 2578–2593.

30 L. Hammarström, *Acc. Chem. Res.*, 2015, **48**, 840–850.

31 M. Orazietti, M. Kuss-Petermann, P. Hamm and O. S. Wenger, *Angew. Chem., Int. Ed.*, 2016, **55**, 9407–9410.

32 T. Higashino, T. Yamada, M. Yamamoto, A. Furube, N. V. Tkachenko, T. Miura, Y. Kobori, R. Jono, K. Yamashita and H. Imahori, *Angew. Chem., Int. Ed.*, 2016, **55**, 629–633.

33 M. Kuss-Petermann and O. S. Wenger, *Helv. Chim. Acta*, 2017, **100**, e1600283.

34 M.-H. Ha-Thi, V.-T. Pham, T. Pino, V. Maslova, A. Quaranta, C. Lefumeux, W. Leibl and A. Aukauloo, *Photochem. Photobiol. Sci.*, 2018, **17**, 903–909.

35 A. Pannwitz and O. S. Wenger, *Chem. Commun.*, 2019, **55**, 4004–4014.
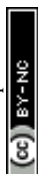
36  M. Lauck, C. Förster, D. Gehrig and K. Heinze, *J. Organomet. Chem.*, 2017, **847**, 33–40.

37  R. Konduri, H. Ye, F. M. MacDonnell, S. Serroni, S. Campagna and K. Rajeshwar, *Angew. Chem., Int. Ed.*, 2002, **41**, 3185–3187.

38  B. Matt, J. Fize, J. Moussa, H. Amouri, A. Pereira, V. Artero, G. Izzet and A. Proust, *Energy Environ. Sci.*, 2013, **6**, 1504–1508.

39  G. Knör, A. Vogler, S. Roffia, F. Paolucci and V. Balzani, *Chem. Commun.*, 1996, 1643–1644.

40  J.-F. Lefebvre, J. Schindler, P. Traber, Y. Zhang, S. Kupfer, S. Gräfe, I. Baussanne, M. Demeunynck, J.-M. Mouesca, S. Gambarelli, V. Artero, B. Dietzek and M. Chavarot-Kerlidou, *Chem. Sci.*, 2018, **9**, 4152–4159.

41  D. Polyansky, D. Cabelli, J. T. Muckerman, E. Fujita, T. Koizumi, T. Fukushima, T. Wada and K. Tanaka, *Angew. Chem., Int. Ed.*, 2007, **46**, 4169–4172.

42  C. N. Valdez, A. M. Schimpf, D. R. Gamelin and J. M. Mayer, *J. Am. Chem. Soc.*, 2016, **138**, 1377–1385.

43  G. F. Manbeck and K. J. Brewer, *Coord. Chem. Rev.*, 2013, **257**, 1660–1675.

44  M. G. Pfeffer, B. Schäfer, G. Smolentsev, J. Uhlig, E. Nazarenko, J. Guthmuller, C. Kuhnt, M. Wächtler, B. Dietzek, V. Sundström and S. Rau, *Angew. Chem., Int. Ed.*, 2015, **54**, 5044–5048.

45  M. Kuss-Petermann and O. S. Wenger, *Angew. Chem., Int. Ed.*, 2016, **55**, 815–819.

46  J. Hankache, M. Niemi, H. Lemmetyinen and O. S. Wenger, *Inorg. Chem.*, 2012, **51**, 6333–6344.

47  J. Hankache, D. Hanss and O. S. Wenger, *J. Phys. Chem. A*, 2012, **116**, 3347–3358.

48  B. Geiß and C. Lambert, *Chem. Commun.*, 2009, 1670–1672.

49  P. Brodard, A. Sarbach, J.-C. Gumy, T. Bally and E. Vauthey, *J. Phys. Chem. A*, 2001, **105**, 6594–6601.

50  B. S. Brunschwig, S. Ehrenson and N. Sutin, *J. Am. Chem. Soc.*, 1984, **106**, 6858–6859.

51  M. Tachiya and S. Murata, *J. Phys. Chem.*, 1992, **96**, 8441–8444.

52  M. Kuss-Petermann and O. S. Wenger, *Phys. Chem. Chem. Phys.*, 2016, **18**, 18657–18664.

53  R. N. Sampaio, L. Troian-Gautier and G. J. Meyer, *Angew. Chem., Int. Ed.*, 2018, **57**, 15390–15394.

54  H. J. Kuhn, S. E. Braslavsky and R. Schmidt, *Pure Appl. Chem.*, 2004, **76**, 2105–2146.

55  R. Bensasson, C. R. Goldschmidt, E. J. Land and T. G. Truscott, *Photochem. Photobiol.*, 1978, **28**, 277–281.

56  I. Carmichael and G. L. Hug, *J. Phys. Chem. Ref. Data*, 1986, **15**, 1–250.

57  J. K. Hurley, H. Linschitz and A. Treinin, *J. Phys. Chem.*, 1988, **92**, 5151–5159.

58  D. M. Arias-Rotondo and J. K. McCusker, *Chem. Soc. Rev.*, 2016, **45**, 5803–5820.

59  L. Buzzetti, G. E. M. Crisenza and P. Melchiorre, *Angew. Chem., Int. Ed.*, 2019, **58**, 3730–3747.

60  C. Kerzig, X. Guo and O. S. Wenger, *J. Am. Chem. Soc.*, 2019, **141**, 2122–2127.

61  M. Brautzsch, C. Kerzig and M. Goez, *Green Chem.*, 2016, **18**, 4761–4771.

62  C. Kerzig and O. S. Wenger, *Chem. Sci.*, 2018, **9**, 6670–6678.

63  M. Goez, C. Kerzig and R. Naumann, *Angew. Chem., Int. Ed.*, 2014, **53**, 9914–9916.

64  P. Müller and K. Brettel, *Photochem. Photobiol. Sci.*, 2012, **11**, 632–636.

65  S. Campagna, F. Puntoriero, F. Nastasi, G. Bergamini and V. Balzani, *Top. Curr. Chem.*, 2007, **280**, 117–214.

66  T. Kohlmann, R. Naumann, C. Kerzig and M. Goez, *Photochem. Photobiol. Sci.*, 2017, **16**, 185–192.

67  C. Kerzig and M. Goez, *Phys. Chem. Chem. Phys.*, 2014, **16**, 25342–25349.

68  M. Montalti, A. Credi, L. Prodi and M. T. Gandolfi, *Handbook of photochemistry*, CRC/Taylor & Francis, Boca Raton, 3rd edn, 2006.

69  A. P. Demchenko, J. Heldt, J. Waluk, P.-T. Chou, P. K. Sengupta, L. Brizhik and J. C. del Valle, *Angew. Chem., Int. Ed.*, 2014, **53**, 14316–14324.

70  A. P. Demchenko, V. I. Tomin and P.-T. Chou, *Chem. Rev.*, 2017, **117**, 13353–13381.

71  G. J. Kavarnos and N. J. Turro, *Chem. Rev.*, 1986, **86**, 401–449.

72  K.-C. Tang, K. L. Liu and I.-C. Chen, *Chem. Phys. Lett.*, 2004, **386**, 437–441.

73  L. Flamigni, A. Barbieri, C. Sabatini, B. Ventura and F. Barigelletti, *Top. Curr. Chem.*, 2007, **281**, 143–203.

74  P. Hazra, D. Chakrabarty and N. Sarkar, *Langmuir*, 2002, **18**, 7872–7879.

75  C. B. Larsen and O. S. Wenger, *Angew. Chem., Int. Ed.*, 2018, **57**, 841–845.

76  N. Banerji, G. Angulo, I. Barabanov and E. Vauthey, *J. Phys. Chem. A*, 2008, **112**, 9665–9674.

77  J. Nomrowski and O. S. Wenger, *J. Am. Chem. Soc.*, 2018, **140**, 5343–5346.

78  S. Karlsson, J. Boixel, Y. Pellegrin, E. Blart, H.-C. Becker, F. Odobel and L. Hammarström, *J. Am. Chem. Soc.*, 2010, **132**, 17977–17979.

79  S. Karlsson, J. Boixel, Y. Pellegrin, E. Blart, H.-C. Becker, F. Odobel and L. Hammarström, *Faraday Discuss.*, 2012, **155**, 233–252.

80  S. Mendes Marinho, M.-H. Ha-Thi, V.-T. Pham, A. Quaranta, T. Pino, C. Lefumeux, T. Chamaillé, W. Leibl and A. Aukauloo, *Angew. Chem., Int. Ed.*, 2017, **56**, 15936–15940.

81  T.-T. Tran, M.-H. Ha-Thi, T. Pino, A. Quaranta, C. Lefumeux, W. Leibl and A. Aukauloo, *J. Phys. Chem. Lett.*, 2018, **9**, 1086–1091.

82  Y. Oseki, M. Fujitsuka, M. Sakamoto and T. Majima, *J. Phys. Chem. A*, 2007, **111**, 9781–9788.

83  M. P. Debreczeny, W. A. Svec, E. M. Marsh and M. R. Wasielewski, *J. Am. Chem. Soc.*, 1996, **118**, 8174–8175.

84  C. Bohne, M. G. Fan, Z. J. Li, Y. C. Liang, J. Lusztyk and J. C. Scaiano, *J. Photochem. Photobiol. Chem.*, 1992, **66**, 79–90.

85  M. Goez and C. Kerzig, *Angew. Chem., Int. Ed.*, 2012, **51**, 12606–12608.

86  R. W. Redmond, J. C. Scaiano and L. J. Johnston, *J. Am. Chem. Soc.*, 1990, **112**, 398–402.

87 M. Sakamoto, X. Cai, S. S. Kim, M. Fujitsuka and T. Majima, *J. Phys. Chem. A*, 2007, **111**, 223–229.

88 For experimental reasons, the only wavelength used for the second laser pulse was 532 nm, because only one of our two Nd:YAG lasers is equipped with an OPO allowing the production of violet or blue photons that are indispensable for the initial CSS production pulse.

89 C. Kerzig and M. Goez, *Chem. Sci.*, 2016, **7**, 3862–3868.

90 J.-C. Gumy and E. Vauthey, *J. Phys. Chem. A*, 1997, **101**, 8575–8580.

91 T. Kumpulainen, B. Lang, A. Rosspeintner and E. Vauthey, *Chem. Rev.*, 2017, **117**, 10826–10939.

92 P. P. Edwards, H. B. Gray, M. T. J. Lodge and R. J. P. Williams, *Angew. Chem., Int. Ed.*, 2008, **47**, 6758–6765.

93 M. Cordes and B. Giese, *Chem. Soc. Rev.*, 2009, **38**, 892–901.

94 T. Kohlmann, R. Naumann, C. Kerzig and M. Goez, *Photochem. Photobiol. Sci.*, 2017, **16**, 1613–1622.

Electronic Supplementary Information (ESI) for

# Quantitative insights into charge-separated states from one- and two-pulse laser experiments relevant for artificial photosynthesis

Svenja Neumann, Christoph Kerzig* and Oliver S. Wenger*

## Contents

## 1 General experimental details

### 1.1 Materials

The compounds under study, except rutheniumtris(bipyridine) dichloride hexahydrate, have been prepared and characterized according to our previously reported procedure.[1] Rutheniumtris(bipyridine) dichloride hexahydrate (99.95%, Aldrich), tetrabutylammonium hexafluorophosphate (TBAPF$_6$, for electrochemical analysis, ≥99.0%, Aldrich) and copper(II) perchlorate hexahydrate (99.999% (metals basis), Alfa Aesar) were purchased from

commercial suppliers and used as received. The solvent for experiments with rutheniumtris(bipyridine) ($[Ru(bpy)_3]^{2+}$) dichloride hexahydrate was ultrapure Millipore MilliQ water (specific resistance, 18.2 MΩ cm), whereas commercially available $CH_3CN$ (anhydrous 99.8 %, Aldrich) was used for optical spectroscopy and irradiation experiments of the compounds under study. Unless stated otherwise, the solutions prepared for laser flash photolysis experiments were deoxygenated with argon (4.8, PanGas) using several cycles of the freeze–pump–thaw technique.

## 1.2 Equipment and methods

All cyclic voltammetry measurements were performed in dry and deoxygenated $CH_3CN$ with $TBAPF_6$ (0.1 M) as electrolyte. A scan rate of 0.1 V/s was applied. An SCE was used as reference, a glassy carbon disk electrode served as working electrode and a silver wire was used as counter electrode. To apply and control the voltage, a Versastat3-200 potentiostat from Princeton Applied Research was used. Steady-state optical absorption spectroscopy was performed on a Cary 5000 instrument from Varian with quartz cuvettes of 1 cm pathlength. If deoxygenated conditions were applied, home-built quartz cuvettes with 1 cm pathlengths were used. UV-Vis transient absorption and emission measurements, together with kinetic studies, were carried out on an LP920-KS instrument from Edinburgh Instruments. A more precise description of the used setup can be found in the next subsection. All spectroscopic experiments of this study were carried out at 293 K.

## 1.3 Laser setup and quantitative laser flash photolysis

An LP920-KS apparatus from Edinburgh Instruments was used to investigate transient species. Excitation of our Ir-containing compounds was carried out by a Quantel Brilliant laser equipped with an OPO from Opotek using excitation wavelengths between 410 und 470 nm. A second Nd:YAG laser (Quantel Brilliant b, *ca.* 10 ns pulse width) operating at 532 nm was used to investigate the photoinduced recombination of the CSSs. All quantitative laser experiments were accompanied by actinometry experiments on the reference compound $[Ru(bpy)_3]^{2+}$ (see next page for details). Synchronization of the two lasers and the detection system was achieved as described previously.[2] The excitation intensities of both lasers were varied by the Q-switch delays and measured with a pyroelectric detector from Ophir immediately before starting the experiments. Control measurements established the laser output stability during each series of experiments.

The beams of both lasers were sent through beam expanders (GBE02-A or GBE05-A, both from Thorlabs) to bring their diameters to either ~1.4 cm (blue laser; maximum laser intensity per area, 13 mJ cm$^{-2}$) or ~1.2 cm (green laser; maximum laser intensity per area, 125 mJ cm$^{-2}$). The beam expansion ensured completely homogeneous laser excitation in the whole detection volume (about 1.2 cm$^3$). The lasers were carefully adjusted before starting the measurements, especially for two-pulse experiments, in which the beam overlap is important. Detection of transient absorption spectra occurred on an iCCD camera from

Andor (with time-integration over 200 ns), while kinetic traces at a single wavelength were recorded using a photomultiplier tube.

We attribute the observed CSS lifetime increase of **TAA-ph$_1$-Ir-ph$_1$-AQ** from ~1.0 μs[1] to ~1.2 μs (this study) to the widely differing local CSS concentrations in the detection volume after the laser pulses. The area-normalized laser intensities in our recent study (~120 mJ cm$^{-2}$, without beam expansion)[1] were about one order of magnitude higher than in the experiments presented in this paper (<13 mJ cm$^{-2}$, with beam expansion). The microsecond CSS lifetime in combination with high local CSS concentrations could enable self-quenching reactions, and thus account for our observations. A kinetic simulation with simultaneous first-order CSS decay (natural lifetime, 1.2 microseconds) and diffusion-controlled[3] CSS self-quenching could indeed reproduce the observed ~17% lifetime reduction, when we assume a CSS concentration as high as ~13 μM in the pump volume right after high-intensity laser excitation. That reasoning is in line with the unchanged lifetime results for **TAA-ph$_2$-Ir-ph$_2$-AQ**, whose short lifetime (<100 ns) does not permit bimolecular reactions between two excited molecules. The slight lifetime increase of **TAA-ph$_1$-Ir-ph$_1$-AQ** does not affect the conclusions drawn in ref. [1].

Using the expanded blue laser beam, we observed a significantly improved photostability of all Ir-containing compounds. Without beam expander, fresh (*i.e.*, unirradiated) solutions were used for every experiment since minor changes in the UV-Vis spectra (indicating photodegradation) were detected after about 200 pulses on the same solution.[1] However, the solutions irradiated with beam expander between laser and cuvettes did not show any detectable changes even after more than 1000 laser flashes.

Quantitative one- and two-pulse laser flash photolysis measurements were carried out using chemical actinometry[4] with the excitation of [Ru(bpy)$_3$]$^{2+}$ into its triplet state (quantum yield, 1.0)[5] as widely accepted reference reaction. Aqueous [Ru(bpy)$_3$]$^{2+}$ solutions were used for the following reasons: (i) The molar absorption coefficient for the [Ru(bpy)$_3$]$^{2+}$ ground state bleach is well-established in water ($\Delta\varepsilon_{455} = -10100$ M$^{-1}$ cm$^{-1}$)[6–9]. (ii) $^3$MLCT formation is the only detectable photochemical process upon visible light absorption by [Ru(bpy)$_3$]$^{2+}$ in water;[6,10] moreover, this actinometry system is even reliable at moderate laser pulse intensities (up to ~30 mJ cm$^{-2}$) under UVA excitation conditions, which in principle allow the biphotonic ionization of [Ru(bpy)$_3$]$^{2+}$.[7,11,12] (iii) Since the refractive indices of water and acetonitrile (solvent for the Ir-containing compounds) differ by less than 1%,[3] corrections of the transient absorption data are unnecessary. (iv) Oxygen removal from the aqueous [Ru(bpy)$_3$]$^{2+}$ solutions is not required, because $^3$[Ru(bpy)$_3$]$^{2+}$ lives long enough in air-saturated water (about 400 ns) for a sensitive detection, and [Ru(bpy)$_3$]$^{2+}$ is not prone to fast photooxidation under these conditions.[8]

The knowledge of the calibrated absorption spectrum of the respective CSS is a basic requirement for all quantitative laser investigations on **TAA-ph$_1$-Ir-ph$_1$-AQ** and **TAA-ph$_2$-Ir-ph$_2$-AQ**. Guided by successful molar absorption coefficient determinations of triarylamines

by chemical oxidation experiments,[13] we first tried to quantitatively oxidize our triads with copper(II) perchlorate, and monitored the spectra of their triarylamine radical cations using steady-state UV-Vis spectroscopy. However, the molar absorption coefficients of TAA$^{\bullet+}$ so obtained depend strongly on the rate of the redox titration and are systematically too low (< 15000 M$^{-1}$ cm$^{-1}$ at the TAA$^{\bullet+}$ absorption maximum in the red), as a comparison with typical literature values shows.[13–15] We attribute these observations to undesired side reactions, which have already been reported for triarylamine radical cations lacking of additional stabilization through methoxy substituents.[16]

Another possibility for calibrating the CSS absorption spectra is provided by the anthraquinone radical anion (AQ$^{\bullet-}$) absorption bands. In contrast to the TAA$^{\bullet+}$ absorptions of the triads in the red region of the visible spectrum, whose maxima differ by about 20 nm, shape and position of the dominant AQ$^{\bullet-}$ absorption at ~560 nm are identical in both triads, as spectroelectrochemical measurements[1] and transient absorption studies (Fig. S5 of the ESI) clearly demonstrate. It seems natural to assume that this species contributes in the same way to the CSSs of the Ir triads under study. Assuming a negligible effect of the adjacent $p$-xylene bridge, we took the mean extinction coefficient at maximum of two previous AQ$^{\bullet-}$ studies in organic solvents, 15100 M$^{-1}$ cm$^{-1}$.[17,18] With that value and the (uncalibrated) spectroelectrochemical signatures of both AQ$^{\bullet-}$ and TAA$^{\bullet+}$ in the CSS of the respective triad (TAA$^{\bullet+}$ still absorbs at the AQ$^{\bullet-}$ maximum, which necessitated a spectral separation),[1] the calibrated CSS absorption spectra were obtained. The molar absorption coefficients at maximum intensity so obtained are 29900 M$^{-1}$ cm$^{-1}$ (720 nm) and 24700 M$^{-1}$ cm$^{-1}$ (700 nm) for **TAA-ph$_1$-Ir-ph$_1$-AQ** and **TAA-ph$_2$-Ir-ph$_2$-AQ**, respectively. These values were used to convert the CSS transient absorption signals into transient CSS concentrations.

The molar absorption coefficients of both CSSs at the wavelength of the second laser, 532 nm, are essential for quantifying the efficiency of second-pulse induced processes. The pertinent coefficients are 15500 M$^{-1}$ cm$^{-1}$ (**TAA-ph$_1$-Ir-ph$_1$-AQ**) and 15800 M$^{-1}$ cm$^{-1}$ (**TAA-ph$_2$-Ir-ph$_2$-AQ**). The anthraquinone radical anion is the dominant absorbing species at this wavelength. The AQ$^{\bullet-}$ contributions to the overall extinction coefficients at 532 nm are 68% (**TAA-ph$_1$-Ir-ph$_1$-AQ**) and 66% (**TAA-ph$_2$-Ir-ph$_2$-AQ**).


## 2 Energies of charge-separated states

The energy of the charge-separated state (CSS) can be derived from the redox potentials of AQ$^{\bullet-}$ and TAA$^{\bullet+}$ in the respective triad since the stored energy ($E_{CSS}$) is equivalent to the driving force ($-\Delta G_{CR}^0$) of the thermal charge recombination process of the photoexcited triad. The redox potentials of the individual components of the triads were determined by cyclic voltammetry (Fig. S1 and Fig. 1b of the main paper). Experimental details are given in Section 1.2 of the ESI as well as in the caption of Fig. S1.
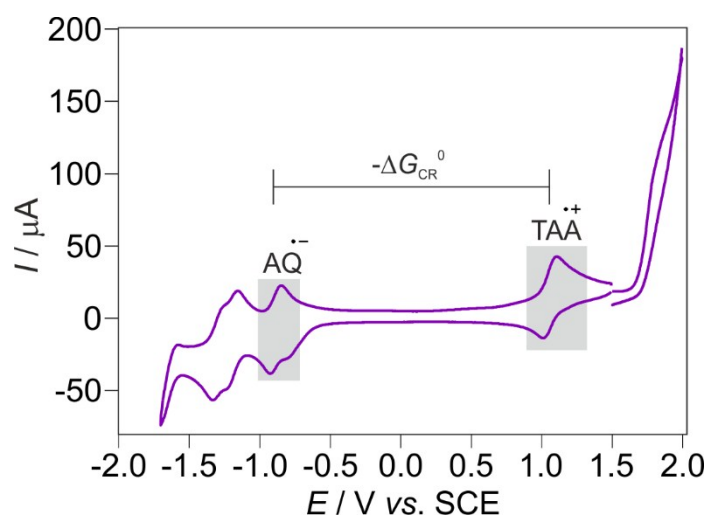
**Fig. S1**: Cyclic voltammogram of **TAA-ph₂-Ir-ph₂-AQ** in deoxygenated CH₃CN with TBAPF₆ (0.1 M) as an electrolyte. A scan rate of 0.1 V/s was applied. For further explanations, see text.

In analogy to the shorter triad **TAA-ph₁-Ir-ph₁-AQ** (main part of the paper, Fig. 1b), the one-electron oxidations of the TAA donor unit and of the iridium moiety are observed when oxidative sweeps are performed with **TAA-ph₂-Ir-ph₂-AQ** (Fig. S1). Likewise, a first (one-electron) reduction of the AQ acceptor, which is followed by the reduction of the bipyridine unit, is observed when performing reductive cyclic voltammetry sweeps. Afterwards, the second reduction of the AQ unit to the quinone dianion occurs before the dF(CF₃)ppy ligands are each reduced by one electron.

**Table S1.** Redox potentials (in V *vs.* SCE) extracted from Fig. 1b of the main part of the paper and Fig. S1.

| Redox potentials | TAA-ph₁-Ir-ph₁-AQ | TAA-ph₂-Ir-ph₂-AQ |
|:---:|:---:|:---:|
| $E^0(dF(CF_3)ppy^{-/2-})$[a] | -1.88 | -1.88 |
| $E^0(dF(CF_3)ppy^{-/2-})$[a] | -1.65 | -1.62 |
| $E^0(AQ^{-/2-})$ | -1.30 | -1.30 |
| $E^0(bpy^{0/-})$ | -1.19 | -1.19 |
| $E^0(AQ^{0/-})$ | -0.86 | -0.89 |
| $E^0(TAA^{+/0})$ | 1.11 | 1.06 |
| $E^0(Ir^{IV/III})$ | 1.78 | 1.75 |

[a] Not shown in Fig. 1b of the main part of the paper and Fig. S1 for clarity of the voltammograms. The values were measured under identical conditions as described above.

The driving force for thermal charge recombination corresponds to the negative reaction free energy ($\Delta G_{CR}^0$) for electron transfer from the reduced acceptor (AQ•−) to the oxidized donor (TAA•+) in the triads under study. Estimations of $\Delta G_{CR}^0$ were performed using equation S1[19] and the reported redox potentials in Table S1. $e$ is the elemental charge, $\varepsilon_0$ is the

vacuum permittivity, and $\varepsilon_S$ is the dielectric constant of the solvent (35.9 for $CH_3CN$)[20]. The used center-to-center distances ($r_{DA}$) are 22.0 Å for **TAA-ph$_1$-Ir-ph$_1$-AQ** and 30.6 Å for **TAA-ph$_2$-Ir-ph$_2$-AQ**.[1] $r_{DA}$ corresponds to the distance between the N-atom of the TAA donor and the centroid of the anthraquinone acceptor unit. Calculated values for the driving force are given in Table S2.

$$\Delta G_{CR}{}^0 = e \cdot \left[ E^0(AQ^{0/-}) - E^0(TAA^{+/0}) \right] - \frac{e^2}{4\pi\varepsilon_0\varepsilon_s r_{DA}}$$ (eq S1)

**Table S2.** Estimated driving forces (-$\Delta G_{CR}{}^0$) for thermal charge recombination on the basis of the redox potentials in Table S1. -$\Delta G_{CR}{}^0$ corresponds to the energy stored in the CSS of the respective triad.

| Triad | -$\Delta G_{CR}{}^0$ [eV] |
|---|---|
| TAA-ph$_1$-Ir-ph$_1$-AQ | 1.99 |
| TAA-ph$_2$-Ir-ph$_2$-AQ | 1.96 |

## 3 Quantum-mechanical calculations

Guided by energetic considerations, we recently explained the additional shoulder in the UV-Vis absorption spectrum of **TAA-ph$_1$-Ir-ph$_1$-AQ** as compared to **TAA-ph$_2$-Ir-ph$_2$-AQ** by an intraligand charge transfer (CT) from the triarylamine donor to the bipyridine moiety.[1] In order to provide further support for that hypothesis, DFT calculations were carried out with the Gaussian 09 package[21] using the B3LYP functional and the 6-31+G(d,p) basis set. Rather than trying to optimize the full heavy-metal containing complexes with a smaller basis set, we performed calculations on the ligands with simplified structures (*i.e.*, without anthraquinone parts and Ir{dF(CF$_3$)ppy}$_2$ fragments).

The optimized geometries of the two model compounds are displayed in Fig. S2. These optimizations were accompanied by frequency analyses, which did not show negative vibrational frequencies indicating convergence on minimum structures. Based on the optimized structures, population analyses were carried out to obtain the orbitals displayed in Fig. S2. The HOMOs of both ligand fragments are TAA-localized, whereas the LUMOs are mainly centered on the bipyridine moiety. Additional time-dependent(TD)-DFT calculations revealed substantially different properties of the lowest energy transition in both structures; for the shorter structure with one *p*-xylene spacer between TAA nitrogen atom and bipyridine, we found a high oscillator strength being in line with the significant overlap integral of the frontier orbitals (Fig. S2, upper row), however, as a result of the additional xylene unit, that transition is completely forbidden in the longer structure (Fig. S2, lower row).

Despite the usage of strongly simplified structures for our calculations, the results summarized in Fig. S2 clearly substantiate the recent explanation of the additional

absorption band in the shorter triad **TAA-ph₁-Ir-ph₁-AQ** by a CT between triarylamine and bipyridine.
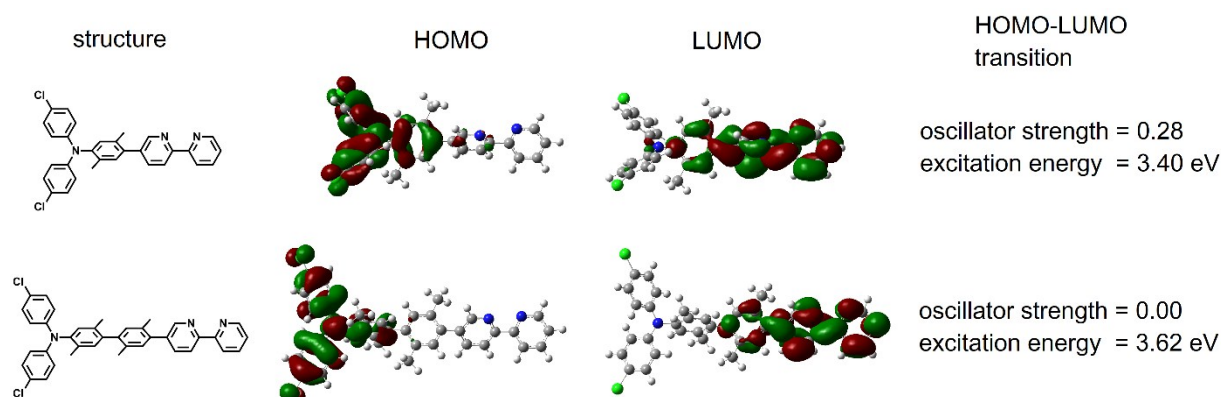


*Fig. S2*: Chemical structure of the two model compounds, their DTF-optimized structures (computed at the B3LYP/6-31+G(d,p) level of theory) together with the corresponding frontier orbitals, and properties of the HOMO-LUMO transitions. For details, see text.

## 4 Additional laser flash photolysis data

### 4.1 Single-pulse experiments

Additional single-pulse experiments on the reference compound **Ir-Ref** are shown in Fig. S3. The transient absorption spectrum following 410 nm laser excitation is practically identical to that presented in our recent study.[1] However, owing to the improved excitation homogeneity in the detection volume when using the beam expander (compare, Section 1.3 of the ESI) and consequently the optimized spatial overlap between pump and probe beams, the signal-to-noise ratio is significantly higher in the present study. Moreover, the emission spectrum of **Ir-Ref** at room temperature (293 K) was measured (upper inset of Fig. S3) to identify the emission maximum, at which additional kinetic emission traces were recorded for **Ir-Ref** and both triads (see, Fig. S4).

As we found by kinetic measurements (lower inset of Fig. S3), both the transient absorption (detection at 570 nm) and emission (detection at 530 nm) signal decays are almost perfectly monoexponential with identical lifetimes, 14.1 μs. It is worth mentioning that the so-obtained excited-state lifetime of **Ir-Ref** is longer by a factor of six compared to those of structurally similar complexes with simple bipyridine or di-*tert*-butyl-bipyridine diimine ligands under identical conditions.[22,23] Given that the latter complex, [Ir{dF(CF₃)ppy}₂(dtbpy)]PF₆, is a commercial and widely-used photoredox catalyst,[24] the much longer lifetime of excited **Ir-Ref** (together with practically identical (photo)redox properties as [Ir{dF(CF₃)ppy}₂(dtbpy)]⁺)[1] might be beneficial for photochemical applications.
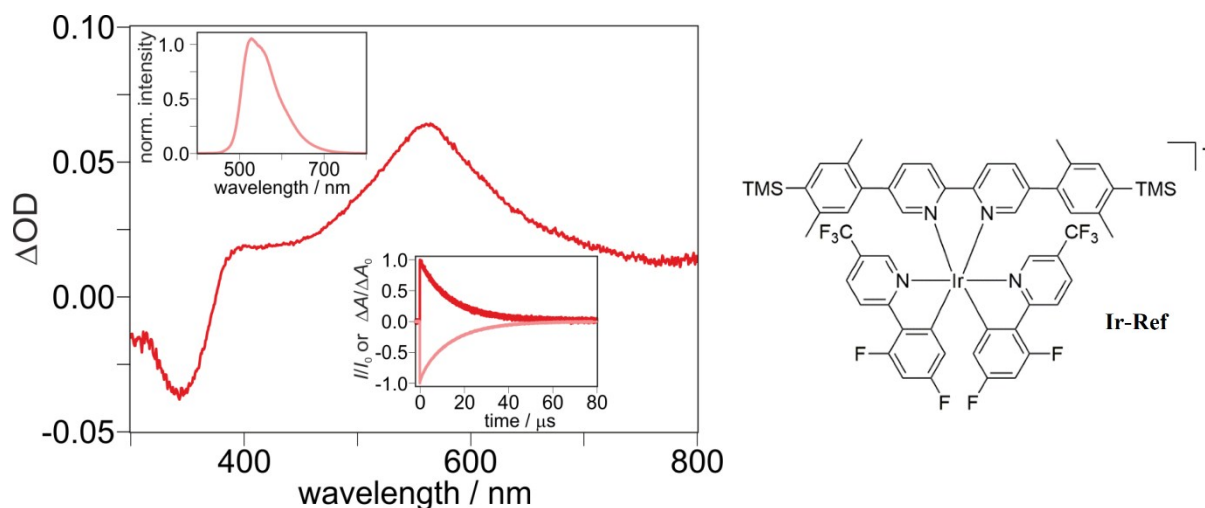
**Fig. S3**: Excited-state properties of **Ir-Ref**, whose structure is shown on the right. Main plot, transient absorption spectrum of **Ir-Ref** (20 μM in dry and deoxygenated $CH_3CN$) following laser excitation at 410 nm (8 mJ). The spectrum was recorded by time-averaging over a period of 200 ns immediately after excitation. Upper inset, emission spectrum of **Ir-Ref** under the conditions as in the main plot, but time-averaged over 10 μs. Lower inset, kinetic absorption and emission data with the same color code as in the corresponding spectra.

Comparative kinetic emission traces for the three Ir-containing compounds under identical excitation and detection conditions are shown in Fig. S4. The MLCT emission of the triads is almost instantaneously quenched indicating that the MLCT lifetime is significantly shorter than the laser pulse duration (~10 ns). A more detailed discussion of these measurements can be found in Section 2.3 of the main paper.
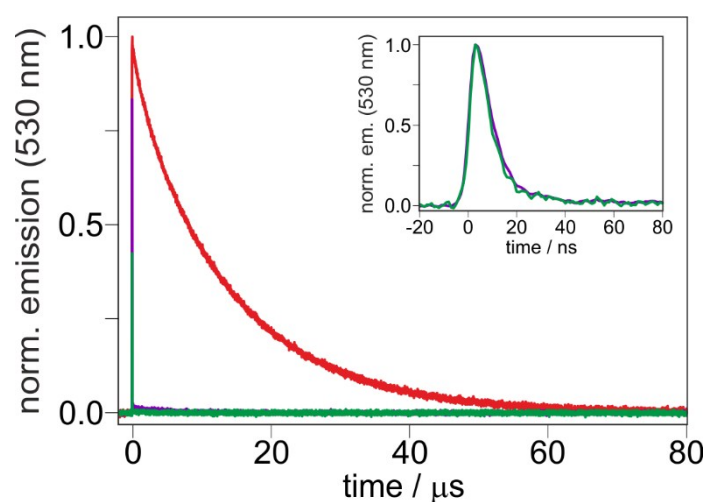


**Fig. S4**: Kinetic emission traces of **TAA-ph₁-Ir-ph₁-AQ** (green), **TAA-ph₂-Ir-ph₂-AQ** (violet) and **Ir-Ref** (red) after 410 nm excitation (8 mJ laser pulses of ~10 ns duration) of Ar-saturated $CH_3CN$ solutions with an OD of ~0.1 at the excitation wavelength recorded at the maximum of the **Ir-Ref** MLCT emission (530 nm). The inset shows the emission traces of the triads on a nanosecond timescale. For further explanation see text and main part of the paper.

The excitation wavelength dependent transient absorption spectra collected in Fig. S5 prove that the CSSs are the only detectable intermediates upon visible light excitation of our triads (see also Section 2.3 of the main paper; for clarity, only three spectra for each triad are shown).
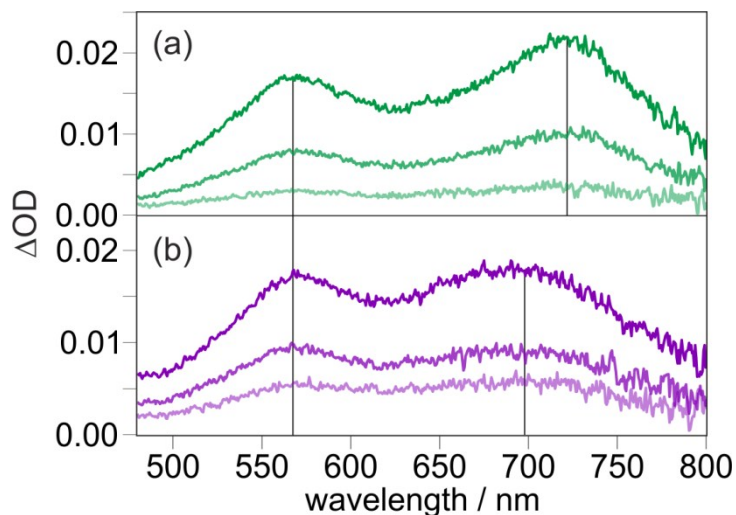


**Fig. S5**: Transient absorption spectra (time-integrated over 200 ns immediately following excitation) of **TAA-ph$_1$-Ir-ph$_1$-AQ** (a) and **TAA-ph$_2$-Ir-ph$_2$-AQ** (b) recorded at different excitation wavelengths (**TAA-ph$_1$-Ir-ph$_1$-AQ**: 410 nm, 440 nm and 470 nm; **TAA-ph$_2$-Ir-ph$_2$-AQ**: 410 nm, 433 nm and 450 nm) in deoxygenated CH$_3$CN at 293 K. Spectral range chosen such that the dominant AQ$^{\bullet-}$ (~570 nm) and TAA$^{\bullet+}$ (red edge of the visible spectrum) absorption bands are displayed.

## 4.2 Two-pulse experiments

The same data set as in Fig. 5a of the main paper is displayed in Fig. S6. The logarithmic representation used in Fig. S6, however, facilitates illustrating the first-order recombination kinetics of the **TAA-ph$_1$-Ir-ph$_1$-AQ** CSS.
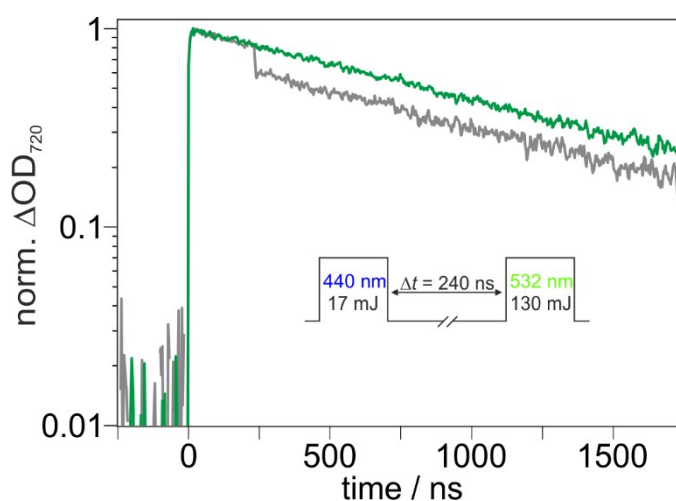


**Fig. S6**: Two-pulse experiment presented in Fig. 5a of the main paper with logarithmic y-axis to illustrate that the second pulse does not affect the kinetics for thermal charge recombination.

Two-pulse experiments on **TAA-ph₂-Ir-ph₂-AQ** are shown in Fig. S7. Transient absorption kinetics were detected at the spectral maximum of $AQ^{\bullet-}$ (panel a) and $TAA^{\bullet+}$ (panel b).
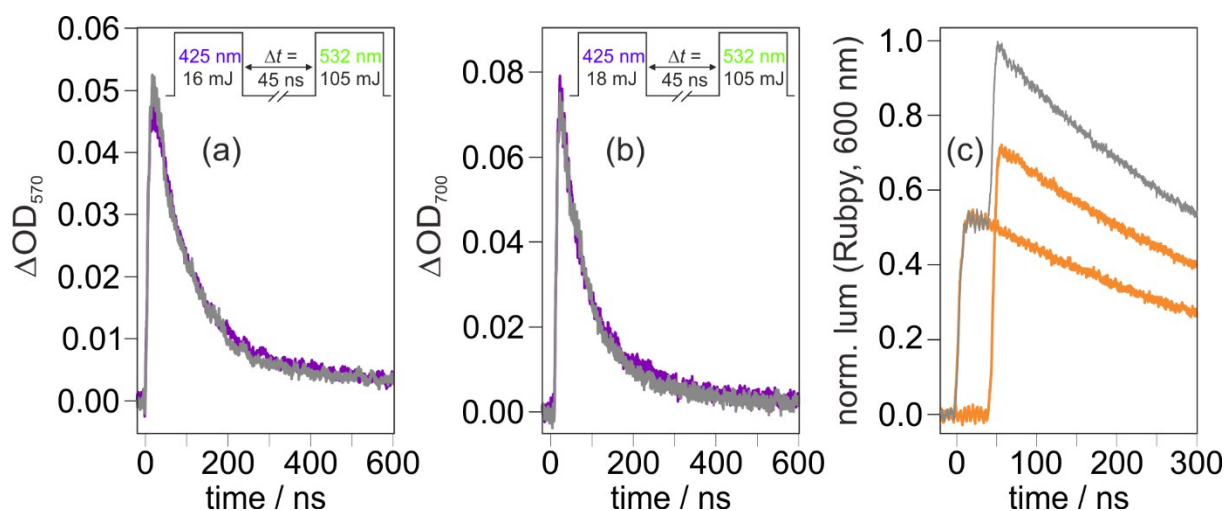


*Fig. S7*: Two-pulse experiments (pulse schemes are given above traces) on solutions of 40 µM **TAA-ph₂-Ir-ph₂-AQ** (panels a and b; in deoxygenated CH₃CN) and 10 µM [Ru(bpy)₃]²⁺ (panel c, in air-saturated water). Kinetic traces for the triad were monitored at 570 nm (a) and 700 nm (b) with the second laser pulse blocked (violet) or unblocked (gray). The control experiments on the kinetic [Ru(bpy)₃]²⁺ emission (panel c) serve to visualize the pulse scheme (same as in panel b). For details, see text.

The negligible second pulse induced absorption change during the experiments displayed in Fig. S7 (panels a and b) prompted us to visualize the pulse scheme with a control measurement on [Ru(bpy)₃]²⁺ (panel c, very same laser settings as in panel b). The kinetic [Ru(bpy)₃]²⁺ emission traces with just one laser (orange traces in panel c, the other pulse was selectively blocked) and both laser pulses (gray trace in Fig. S7c) clearly indicate that the desired pulse scheme has also been applied to **TAA-ph₂-Ir-ph₂-AQ**.

A comparative discussion of the two-pulse experiments on both triads is given in Section 2.4 of the main paper.


## 5 Supplementary references

1      S. Neumann and O. S. Wenger, *Inorg. Chem.*, 2019, **58**, 855–860.
2      M. Kuss-Petermann and O. S. Wenger, *Helv. Chim. Acta*, 2017, **100**, e1600283.
3      M. Montalti, A. Credi, L. Prodi and M. T. Gandolfi, *Handbook of photochemistry*, CRC/Taylor & Francis, Boca Raton, 3rd ed., 2006.
4      H. J. Kuhn, S. E. Braslavsky and R. Schmidt, *Pure Appl. Chem.*, 2004, **76**, 2105–2146.
5      S. Campagna, F. Puntoriero, F. Nastasi, G. Bergamini and V. Balzani, *Top. Curr. Chem.*, 2007, **280**, 117–214.
6      M. Goez, C. Kerzig and R. Naumann, *Angew. Chem. Int. Ed.*, 2014, **53**, 9914–9916.
7      P. Müller and K. Brettel, *Photochem. Photobiol. Sci.*, 2012, **11**, 632–636.
8      C. Kerzig and M. Goez, *Chem. Sci.*, 2016, **7**, 3862–3868.

9       C. Kerzig and O. S. Wenger, *Chem. Sci.*, 2018, **9**, 6670–6678.

10      C. Kerzig, X. Guo and O. S. Wenger, *J. Am. Chem. Soc.*, 2019, **141**, 2122–2127.

11      C. Kerzig and M. Goez, *Phys. Chem. Chem. Phys.*, 2014, **16**, 25342–25349.

12      M. Goez, D. von Ramin-Marro, M. H. Othman Musa and M. Schiewek, *J. Phys. Chem. A*, 2004, **108**, 1090–1100.

13      K. Sreenath, T. G. Thomas and K. R. Gopidas, *Org. Lett.*, 2011, **13**, 1134–1137.

14      R. F. Nelson and R. H. Philp, *J. Phys. Chem.*, 1979, **83**, 713–716.

15      J. L. Baptista and H. D. Burrows, *J. Chem. Soc. Faraday Trans. 1*, 1974, **70**, 2066–2079.

16      J. F. Ambrose, L. L. Carpenter and R. F. Nelson, *J. Electrochem. Soc.*, 1975, **122**, 876–894.

17      M. Büschel, C. Stadler, C. Lambert, M. Beck and J. Daub, *J. Electroanal. Chem.*, 2000, **484**, 24–32.

18      S. U. Pedersen, T. Bo Christensen, T. Thomasen and K. Daasbjerg, *J. Electroanal. Chem.*, 1998, **454**, 123–143.

19      A. Weller, *Z. Phys. Chem.*, 1982, **133**, 93–98.

20      L. G. Gagliardi, C. B. Castells, C. Ràfols, M. Rosés and E. Bosch, *J. Chem. Eng. Data*, 2007, **52**, 1103–1107.

21      M. J. Frisch, G. W. Trucks, H. B. Schlegel, G. E. Scuseria, M. A. Robb, J. R. Cheeseman, G. Scalmani, V. Barone, B. Mennucci, G. A. Petersson, H. Nakatsuji, M. Caricato, X. Li, H. P. Hratchian, A. F. Izmaylov, J. Bloino, G. Zheng, J. L. Sonnenberg, M. Hada, M. Ehara, K. Toyota, R. Fukuda, J. Hasegawa, M. Ishida, T. Nakajima, Y. Honda, O. Kitao, H. Nakai, T. Vreven, J. A. Montgomery, J. E. Peralta, F. Ogliaro, M. Bearpark, J. J. Heyd, E. Brothers, K. N. Kudin, V. N. Staroverov, R. Kobayashi, J. Normand, K. Raghavachari, A. Rendell, J. C. Burant, S. S. Iyengar, J. Tomasi, M. Cossi, N. Rega, J. M. Millam, M. Klene, J. E. Knox, J. B. Cross, V. Bakken, C. Adamo, J. Jaramillo, R. Gomperts, R. E. Stratmann, O. Yazyev, A. J. Austin, R. Cammi, C. Pomelli, J. W. Ochterski, R. L. Martin, K. Morokuma, V. G. Zakrzewski, G. A. Voth, P. Salvador, J. J. Dannenberg, S. Dapprich, A. D. Daniels, Farkas, J. B. Foresman, J. V. Ortiz, J. Cioslowski, and D. J. Fox. Gaussian 09 Revision B.01, 2010.

22      M. S. Lowry, J. I. Goldsmith, J. D. Slinker, R. Rohl, R. A. Pascal, G. G. Malliaras and S. Bernhard, *Chem. Mater.*, 2005, **17**, 5712–5719.

23      D. Hanss, J. C. Freys, G. Bernardinelli and O. S. Wenger, *Eur. J. Inorg. Chem.*, 2009, **2009**, 4850–4859.

24      C. K. Prier, D. A. Rankic and D. W. C. MacMillan, *Chem. Rev.*, 2013, **113**, 5322–5363.

# 5 A Molecular Mimic of the Photosynthetic Z-Scheme

The so-called photosynthetic Z-scheme is a multifunctional molecular machine embedded in the thylakoid membrane of chloroplasts and can be seen as the 'heart' of light-dependent natural photosynthesis. Detailed information concerning the structure of this molecular machinery and the processes that take place was already presented in Chapter 2.1. In the Z-scheme, two photosystems (PS I and PS II) work in series to achieve the formation of a highly energetic charge-separated state (CSS) with a long lifetime, which cannot be formed by use of only one photosystem. This CSS is characterized by a strong oxidant in PS II, which can drive water oxidation, and a strong reductant in PS I, which can be used for reduction of $NADP^+$ to NADPH. For the formation of the highly energetic CSS, each photosystem is independently excited by absorption of a single visible photon of relatively low energy, which is why the Z-scheme can also be seen as an upconversion system for light energy. Since two photosystems are involved, a wider range of visible light can be exploited, which is another advantage of the Z-scheme.[4, 7, 9, 12]

Despite the importance of the Z-scheme in nature and the benefits that result from this two-step excitation process, artificial Z-schemes using visible light excitation are rare. It was reported that water splitting can be achieved by two-step photoexcitation with visible light when either two isolated semiconductor types are connected by a reversible donor/acceptor pair as a redox mediator[114–117] or when two semiconductors are linked *via* a metal junction.[118, 119] Visible light driven water splitting could also be observed in a photoelectrochemical cell[120] comprised of semiconductors and an attached organic dye and in a photobioelectrochemical cell[121] which used quantum dots and the integration of PS II, as reported recently. The principle of two-step excitation with visible light was also successfully applied for $CO_2$ reduction. Here, reduction was achieved by use of two semiconductors[122, 123] or by one semiconductor directly linked to a molecular dyad.[124–126] However, none of those reported artificial Z-schemes is purely molecular like the components in the Z-scheme in natural photosynthesis and their performances are mainly based on semiconductors. To the best of the author's knowledge, only two purely molecular artificial Z-schemes have been reported so far. The first system is a

supramolecular tetrad consisting of two linked dyads that showed reversible formation of a long-lived CSS only when two excitation pulses were applied to it.[67] However, the tetrad did not aim for an increase of the charge separation energy since the CSSs of the respective dyads, each generated by the uptake of a single visible photon, are higher in energy than the CSS of the tetrad. In contrast, the energy upconversion principle of the Z-scheme, as well as a significant increase in the lifetime of the final CSS, was successfully demonstrated in a different tetrad (Figure 5.1) that also consists of two linked dyads (Bodipy-NDI and TAPD-Ru).[53] This artificial Z-scheme stored 2 eV in the CSS (in toluene) after two consecutive photon absorptions, which is more than the respective dyads could store after single excitation.
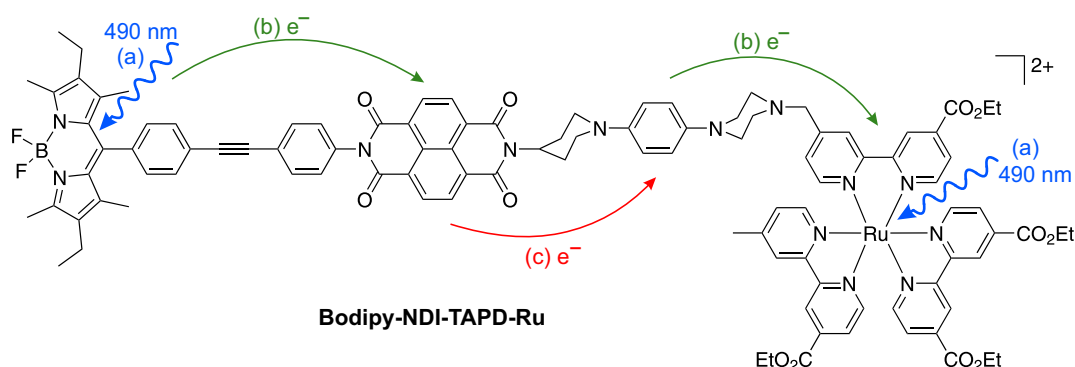


**Figure 5.1:** Molecular structure of Bodipy-NDI-TAPD-Ru and schematic representation of the light-induced formation of the final CSS Bodipy$^{\cdot+}$-NMI-TAPD-Ru$^{\cdot-}$. (a) Excitation of the photosensitizers at 490 nm within the duration of the same laser pulse; (b) electron-transfer step induced by excitation of the photosensitizer; (c) thermal charge recombination step in the central unit of the tetrad to form the final CSS.

The tetrad shown in Figure 5.1 consists of a 4,4-difluoro-1,3,5,7-tetramethyl-2,6-diethyl-4-bora-3a,4a-diaza-*s*-indacene (Bodipy) photosensitizer, a naphthalene diimide (NDI) electron acceptor, a tetraalkylphenyldiamine (TAPD) electron donor and a Ru(II)(bipyridine)$_3$ (Ru) photosensitizer. The two photosensitizers can be excited with equal probability at 490 nm, which leads to a cooperative formation of a highly energetic CSS in the system. After visible light excitation, an electron is transferred from the excited Bodipy unit to the NDI moiety and the excited Ru unit is reductively quenched by electron transfer from the TAPD moiety. A twofold CSS Bodipy$^{\cdot+}$-NMI$^{\cdot-}$-TAPD$^{\cdot+}$-Ru$^{\cdot-}$ results, in which the central electron-hole pair (marked in red) undergoes thermal charge recombination to form the final CSS. The energy efficiency of the tetrad lies at 47% (of the sum of the photon threshold energies) and the overall quantum yield of the final CSS was estimated at 24%.

Here, a study regarding a new artificial molecular Z-scheme is presented. With this system, we anticipate to store significantly more than 2 eV in the final CSS after two-step

photoexcitation with visible light. The generation of highly energetic CSSs is especially desired for driving energy demanding (photo)chemical processes.[109] Furthermore, the carefully designed system is purely organic, which is a conceptually new approach for an artificial Z-scheme (see Chapter 5.1).

## 5.1 Considerations for the Structural Design of the New Molecular Z-Scheme Approach

Our new approach for a molecular Z-scheme is a tetrad (Figure 5.2) that consists of a naphthalene monoimide (NMI) electron acceptor, a tetraphenyl-diaminobenzol (TPDB) electron donor, a pyrene-4,5,9,10-tetraone (PT) electron acceptor and a triarylamine (TAA) electron donor unit.
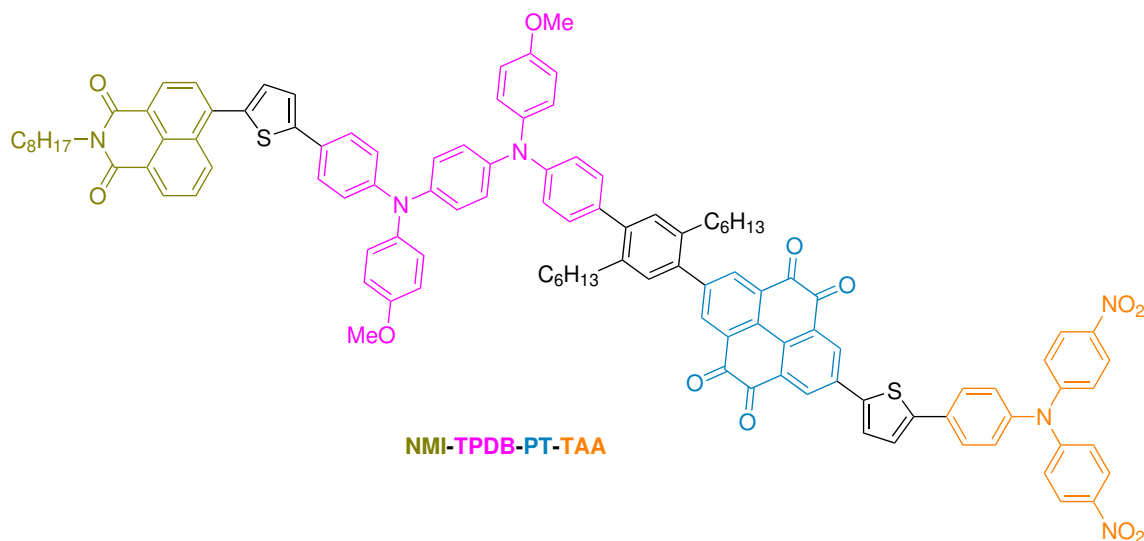


**Figure 5.2:** Molecular structure of the NMI-TPDB-PT-TAA tetrad.

The NMI-TPDB-PT-TAA tetrad can be divided into two dyads (NMI-TPDB and PT-TAA), whereby each dyad represents a single photosystem, unlike the artificial Z-scheme presented in Figure 5.1. Photoexcitation of the respective dyads is designed to be into intramolecular charge transfer (CT) transitions. This behavior is an advantage of the purely organic approach, since CT transitions directly separate charge, which negates additional decay pathways present in metal-based photosensitizer systems.[127–129] However, these emissive CSSs are known to be highly solvatochromic[130] and obey the energy gap law.[131, 132] It is therefore necessary to work in low polarity solvents to avoid fast and unproductive recombination.[133–135] Furthermore, a thiophene (th) spacer was introduced as a linker between the donor and acceptor of each dyad. Thiophene spacers were found to facilitate CT transitions in donor-acceptor compounds since a more planar conformation of the donor to the acceptor is induced.[136, 137] The conformation change enhances the electronic coupling between donor and acceptor, which also results in higher extinction coefficients concerning the CT absorption band. An increase in the extinction coefficient is favorable concerning the probability for (efficient) photon absorption by the photosystem. Additionally, thiophene incorporation produces a red-shift of the absorption of the dyad,
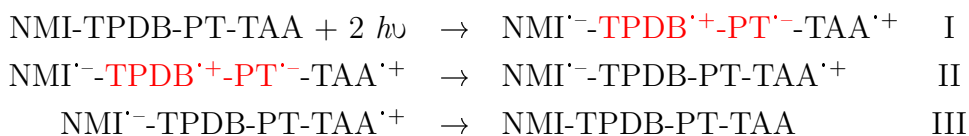
which facilitates excitation with visible light. As mentioned above, to further stabilize the CSSs of the dyads and the tetrad, nonpolar solvents like toluene should be considered for measurements. It also needs to be considered that the central TPDB-PT unit of the given tetrad could behave as a donor-acceptor dyad, too. To suppress this possibility, a $p$-(di-$n$-hexyl)phenyl (hxy) spacer was introduced to link the two dyads. Besides the positive effect on the solubility of the overall tetrad, a hxy spacer should also reduce the electronic coupling between TPDB and PT, due to a larger torsion angle, which hampers direct excitation with visible light absorption.

An important factor concerning the planning of the molecular design were also the reported (first) oxidation and reduction potentials (*vs.* SCE), respectively, of the single moieties (Table 5.1), which play a key role concerning the directionality of CT transitions in the anticipated tetrad. The single units of the tetrad were chosen in a way that a weak electron acceptor (wA; NMI) and a weak electron donor (wD; TAA) are at the ends of the tetrad (see Figure 5.3). The middle part of the tetrad contains a strong electron donor (sD; TPDB) and a strong electron acceptor (sA, PT). The given directionality should permit the formation of the highly energetic CSS. For clarity, further discussion of these potentials is included in the explanation for the anticipated behavior after two-step photoexcitation (see below).

**Table 5.1:** First oxidation or reduction potential of the electron donor and electron acceptor units used in the NMI-TPDB-PT-TAA tetrad.

|  | Potential (V *vs.* SCE) | Remarks |
|---|---|---|
| $E^0(\text{NMI}^{0/-})$ | -1.40 | benzonitrile; ref[138] |
| $E^0(\text{TPDB}^{+/0})$ | ca. 0.40 | CH$_3$CN; estimated on ref[139, 140] |
| $E^0(\text{PT}^{0/-})$ | -0.41 | DMF; ref[141] |
| $E^0(\text{TAA}^{+/0})$ | 1.35 | CH$_3$CN; ref[142] |

Due to the expected short lifetimes of the organic dyad CSSs, it would be favorable to excite both dyads within the duration of the same laser pulse (instead of a more complicated two-pulse experiment), presuming that there is a wavelength at which both dyads will be excited with equal probability. The reaction Equations I-III summarize the expected behavior of the tetrad after absorption of two photons. Additionally, electron pathways for Equations I-III are visualized in Figure 5.3.
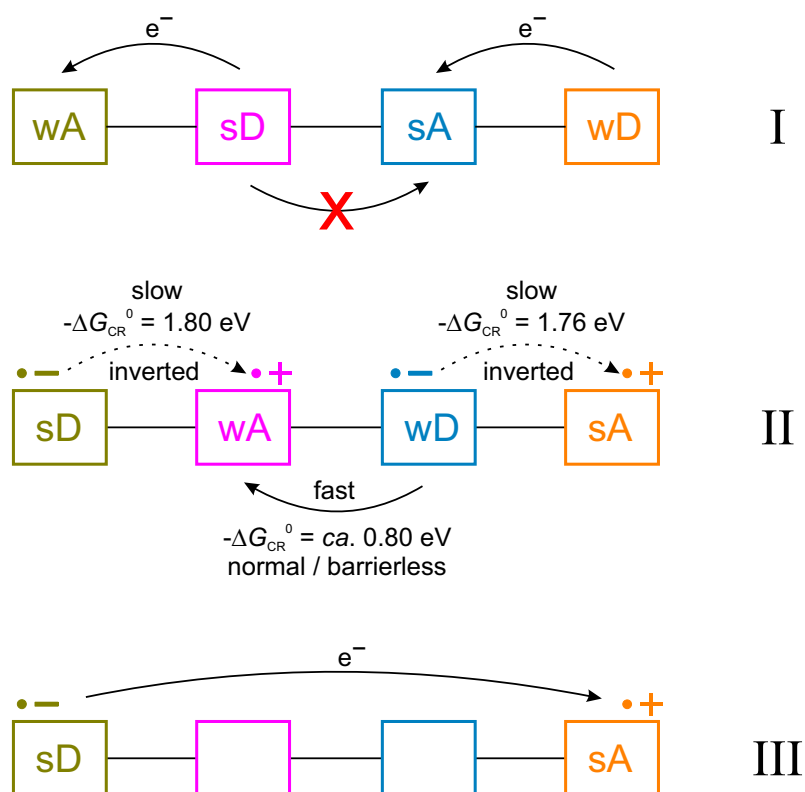
$$\text{NMI-TPDB-PT-TAA} + 2\,h\upsilon \quad \rightarrow \quad \text{NMI}^{\cdot-}\text{-TPDB}^{\cdot+}\text{-PT}^{\cdot-}\text{-TAA}^{\cdot+} \qquad \text{I}$$
$$\text{NMI}^{\cdot-}\text{-TPDB}^{\cdot+}\text{-PT}^{\cdot-}\text{-TAA}^{\cdot+} \quad \rightarrow \quad \text{NMI}^{\cdot-}\text{-TPDB-PT-TAA}^{\cdot+} \qquad\qquad \text{II}$$
$$\text{NMI}^{\cdot-}\text{-TPDB-PT-TAA}^{\cdot+} \quad \rightarrow \quad \text{NMI-TPDB-PT-TAA} \qquad\qquad\qquad \text{III}$$

**Figure 5.3:** Schematic representation of electron pathways in the tetrad NMI-TPDB-PT-TAA after double excitation with visible light. The shown reaction sequences correspond to Equations I-III of the main text.

Efficient double photoexcitation of the tetrad should result in the (short-living) twofold CSS shown in Equation I. Direct CT transitions should therefore only occur in the excited photosystems NMI-TPDB and PT-TAA and not in the TPDB-PT dyad. As a consequence of the direct CT excitation, oxidized donor moieties of the ground-state of the tetrad now act as acceptor units in the twofold CSS and reduced acceptor moieties become donor units. The central part of the twofold CSS is labeled as weak donor and acceptor in Figure 5.3 in comparison to the donor and acceptor units at the end of the tetrad, since they differ by roughly 1.0 eV. The central hole-electron pair (marked in red) is expected to collapse rapidly to form the final CSS as indicated in Equation II since the driving force for charge recombination in the dyads (*ca.* 1.8 eV) is highly inverted, whereas the driving force for recombination of the central hole-electron pair lies at *ca.* 0.8 eV (see Appendix for calculations). In the final CSS, a state comprised of a strong reductant and a strong oxidant, nearly 2.8 eV should be stored based on the reported redox potentials (Table 5.1). This CSS is also expected to show a significantly longer lifetime than in the isolated CSSs of the dyads.[53, 67] In the final step III, thermal charge recombination to the ground-state of the tetrad should occur.

Because the synthesis of the anticipated tetrad is rather ambitious and time-consuming,

it was decided to begin the investigations concerning our new molecular Z-scheme with the synthesis and study of reference dyads (Figure 5.4) to gain more knowledge if our approach for the tetrad is promising enough to pursue. With these reference compounds on hand, we want to evaluate if the expected CT transitions in the NMI-TPDB and PT-TAA references occur and if the hxy spacer between the TPDB and PT units inhibits an undesired direct CT excitation.

Furthermore, emission lifetimes should clarify if the CSSs of the dyads are sufficiently long-living for the applicability in our tetrad. Also, redox potentials for our actual systems need to be measured.
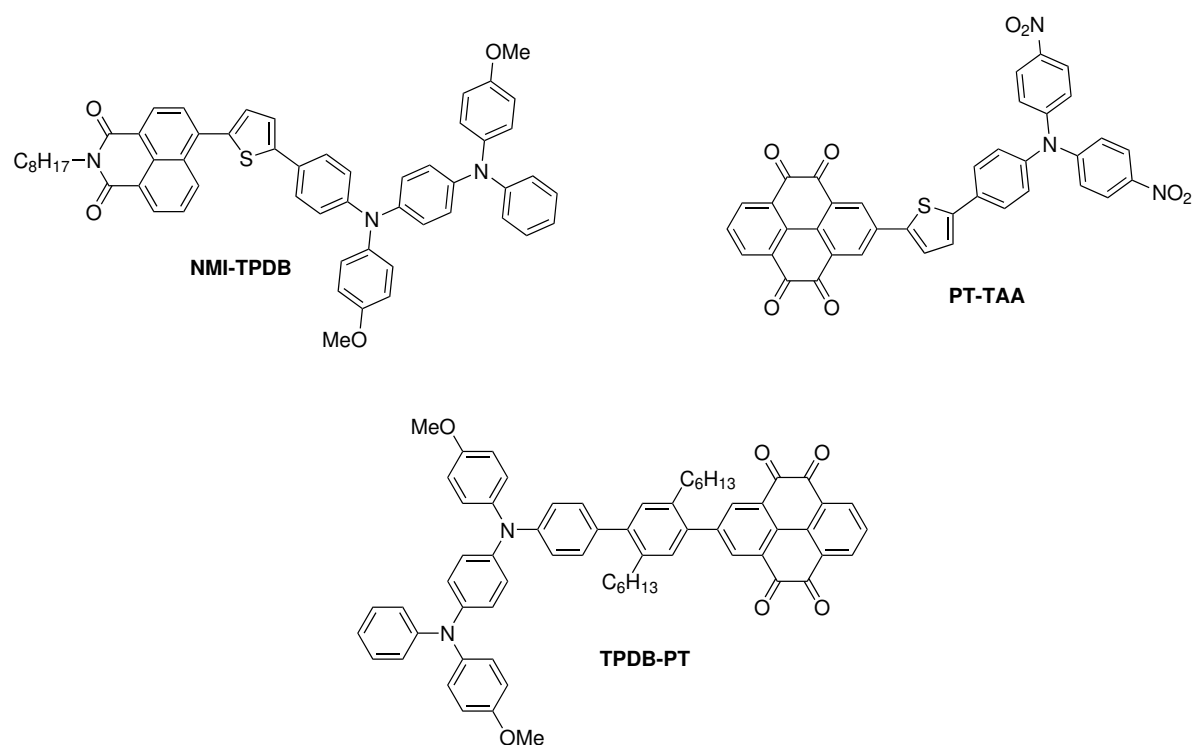


**Figure 5.4:** Molecular structures of the reference dyads NMI-TPDB, TPDB-PT and PT-TAA.

## 5.2 NMI-TPDB Reference

The NMI-TPDB reference plays the role of one of the two photosystems needed for photo-excitation *via* a Z-scheme approach. To characterize the properties of the given dyad, a variety of studies were performed in up to 4 different solvents, ranging from nonpolar toluene to more polar benzonitrile. Electronic absorption spectroscopy was performed to confirm the possibility of a CT excitation in the dyad, which was substantiated by DFT calculations. By measuring cyclic voltammograms, reduction and oxidation potentials for our specific system could be obtained and can be used to estimate the energy of the CSS and the driving force for thermal charge recombination. Spectro-electrochemical measurements gave insights into the expected spectroscopic signatures of the oxidized TPDB and the reduced NMI moieties. Additional, steady-state and time-resolved emission spectroscopies were performed to investigate emission behavior and lifetime of NMI-TPDB.

### 5.2.1 Synthesis of NMI-TPDB

The reference compound NMI-TPDB was successfully synthesized following the synthetic route summarized in Scheme 5.1.

In a first step, the NMI moiety was generated by a condensation reaction between 4-bromo-1,8-naphthalic anhydride and $n$-octylamine in 86% yield. Suzuki coupling with thiophene-2-boronic acid pinacol ester, followed by a selective bromination in the $\alpha$-position of the thiophene with $Br_2$ in $CHCl_3$, yielded NMI-th-Br (**3**). The coupling substrate TMS-ph-B(OH)$_2$ (**5**) was synthesized in two steps from 1,4-dibromobenzene: *ipso* exchange of one bromo by trimethylsilyl (TMS) followed by conversion of the second bromo to a boronic acid. Suzuki coupling of compound **3** and compound **5** afforded NMI-th-ph-TMS (**6**) in 95% yield. After deprotection of the TMS-protecting group with ICl in DCM and a Buchwald-Hartwig amination with $p$-anisidine, the secondary amine **8** was obtained. Compound **8** was then coupled *via* Buchwald-Hartwig amination with the iodinated triarylamine **11**, which afforded the reference compound NMI-TPDB in 47% yield. To synthesize compound **11**, a Chan-Lam coupling of phenylboronic acid with $p$-anisidine, using copper(II) acetate and NEt$_3$ in DCM at room temperature, was performed to yield compound **9** in 56%. Then, a Buchwald-Hartwig amination, followed by a TMS deprotection was performed.
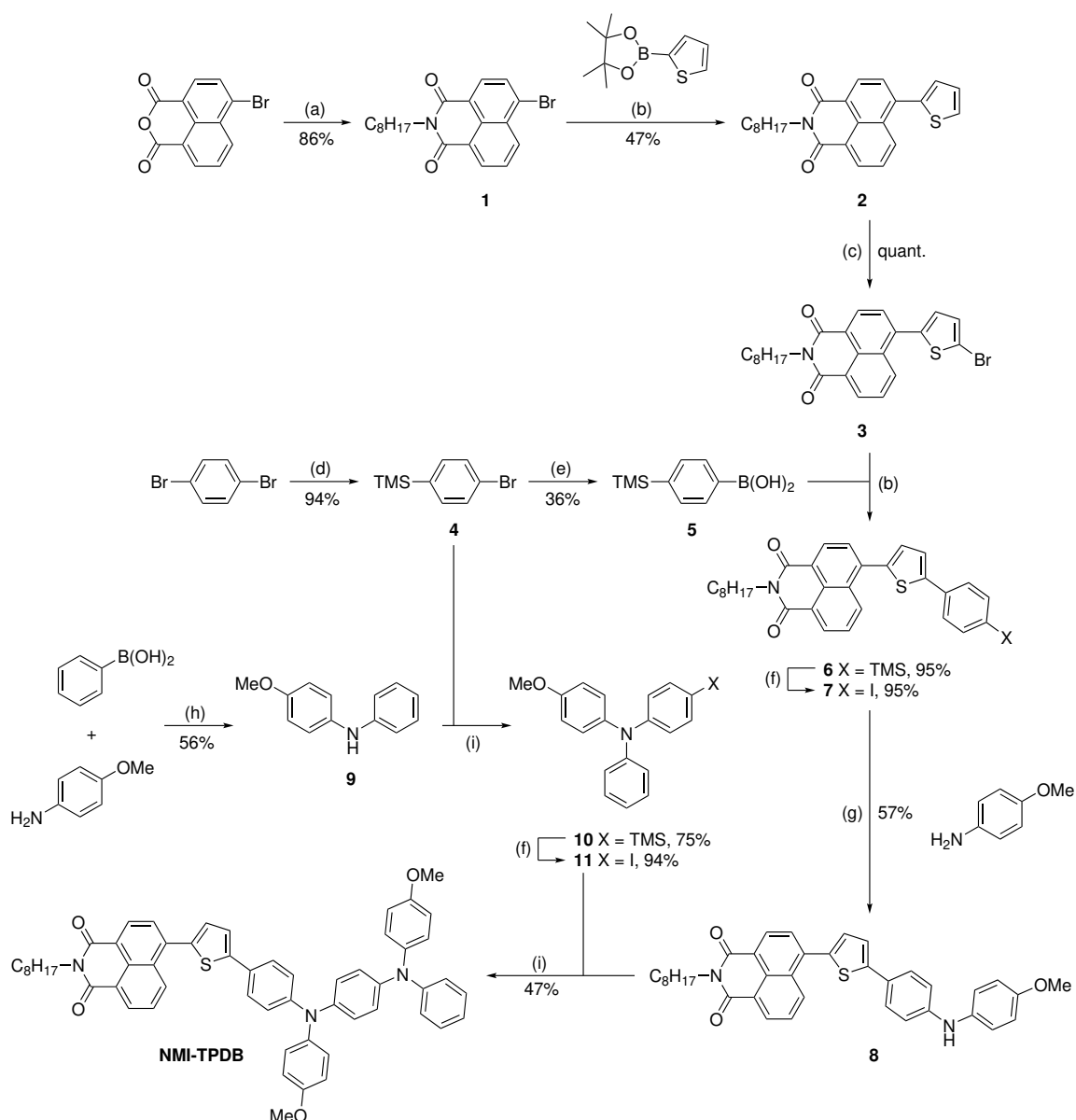
**Scheme 5.1:** Reaction scheme for the synthesis of the NMI-TPDB reference. (a) *n*-Octylamine, ethanol, reflux, 18 h; (b) Pd(PPh$_3$)$_4$, Na$_2$CO$_3$, toluene/water/ethanol, 90 °C, overnight; (c) Br$_2$, acetic acid, CHCl$_3$, rt, 20 min; (d) *n*-BuLi, Et$_2$O, −78 °C, 15 min, TMSCl, −78 °C → rt, 45 min; (e) *n*-BuLi, THF, −78 °C, 1.5 h, trimethyl borate, −78 °C, 30 min, −78 °C → rt, overnight, HCl; (f) ICl, DCM, −78 °C, 1 h; (g) Pd(dba)$_2$, (HP$^t$Bu$_3$)BF$_4$, KO$^t$Bu, toluene, 90 °C, 19 h; (h) Cu(OAc)$_2$, NEt$_3$, DCM, rt, 19 h; (i) Pd(dba)$_2$, (HP$^t$Bu$_3$)BF$_4$, KO$^t$Bu, toluene, 100 °C, overnight.

## 5.2.2 Electronic Absorption Spectroscopy

Electronic absorption spectroscopy (see Figure 5.5) was performed at 293 K with 20 μM solutions of NMI-TPDB in toluene (red trace), THF (black trace), DCM (blue trace) and benzonitrile (green trace).
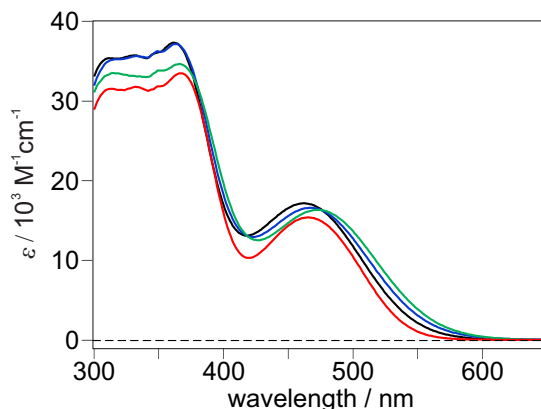
**Figure 5.5:** UV-Vis absorption spectra of NMI-TPDB (20 μM) at 293 K in the following solvents: toluene (red), THF (black), DCM (blue) and benzonitrile (green).

The spectra of the reference compound NMI-TPDB exhibit $\pi$-$\pi^*$ absorption bands in the UV region from about 310 to 380 nm. More interesting for our anticipated artificial Z-scheme is the observable broad CT absorption band in the visible region of roughly 420 to 560 nm. The absorption maximum of this band shifts only slightly when the solvent polarity is changed (Table 5.2), which is congruent with literature observations.[130, 133] To substantiate the CT character of the broad absorption band in the visible region, simple DFT calculations were performed. Based on the optimized structure of (simplified) NMI-TPDB, HOMO and LUMO frontier molecular orbitals were calculated (Figure 5.6). During the electronic transition from the HOMO to the LUMO, an electron is transferred from the TPDB unit to the NMI unit of the dyad. This is in agreement with a CT character of the first excited state of the compound, consisting of an NMI radical anion and a TPDB radical cation. Time-dependent DFT calculations confirmed that the lowest energy transition is indeed HOMO-LUMO. Additionally, the experimental extinction coefficients and the presence of a CT absorption band are comparable with reported values for similar NMI-TAA compounds.[143, 144]

**Table 5.2:** Maxima of the CT absorption bands for NMI-TPDB in the investigated solvents.

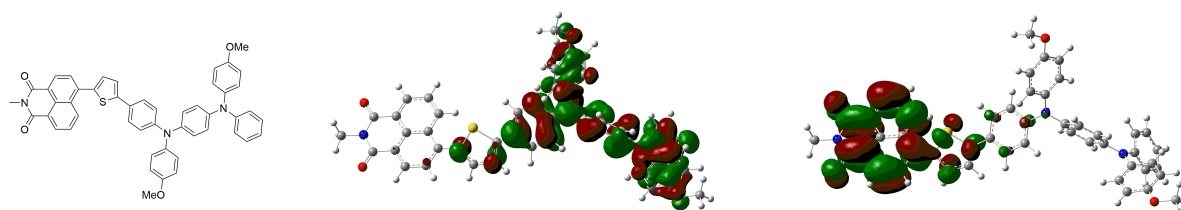|  | $\lambda_{\text{max, CT}}$ / nm |
| --- | --- |
| toluene | 465 |
| THF | 462 |
| DCM | 467 |
| benzonitrile | 473 |

**Figure 5.6:** Simplified chemical structure of NMI-TPDB (left), its DFT-optimized structure (computed with B3LYP functional and the 3-21G basis set) together with the corresponding HOMO (middle) and LUMO (right) frontier molecular orbitals.

## 5.2.3 Electrochemistry and Driving Forces

Cyclic voltammograms of NMI-TPDB were measured in THF (Figure 5.7, left), DCM (Figure 5.7, middle) and benzonitrile (Figure 5.7, right). Experimental details can be found in Chapter 7.2.
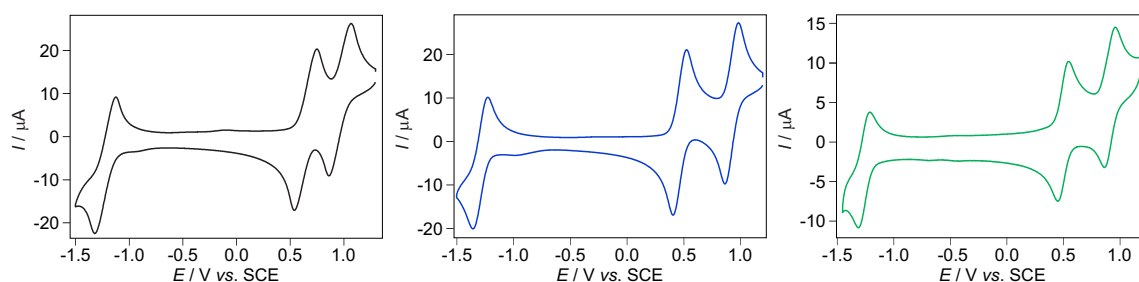


**Figure 5.7:** Cyclic voltammograms of 1 mM solutions of NMI-TPDB measured in dry and deoxygenated THF (black), DCM (blue) and benzonitrile (green). TBAPF$_6$ (0.1 M) was used as an electrolyte and a scan rate of 0.1 V/s was applied.

In all investigated solvents, oxidative cyclic voltammetry results in the reversible first and second oxidation of the TPDB donor whereas the NMI acceptor reversible reduction is observed when performing reductive sweeps. Based on the first oxidation and reduction potentials of the NMI acceptor and the TPDB donor, the driving force (-$\Delta G_{CR}^0$) for thermal charge recombination, which equals the amount of stored energy in the CSS of the dyad, can be derived. The calculated driving forces are summarized in Table 5.3. Corresponding calculations can be found in the Appendix.

**Table 5.3:** Redox potentials (in V *vs.* SCE) extracted from Figure 5.7.

|  | THF / V | DCM / V | benzonitrile / V |
|---|---|---|---|
| $E^0(\text{NMI}^{0/-})$ | -1.21 | -1.29 | -1.26 |
| $E^0(\text{TPDB}^{+/0})$ | 0.64 | 0.47 | 0.50 |
| $E^0(\text{TPDB}^{2+/+})$ | 0.96 | 0.92 | 0.91 |
| $-\Delta G_{\text{CR}}^0/\text{eV}$ | 1.85 | 1.76 | 1.76 |

## 5.2.4 Spectro-Electrochemistry

Spectro-electrochemical measurements of the NMI-TPDB reference were performed to identify the spectroscopic signatures of the oxidized TPDB and the reduced NMI moieties. In case of the reduced NMI species, the spectroscopic signatures are anticipated to be seen in the transient absorption spectrum of the final CSS (NMI˙⁻-TPDB-PT-TAA˙⁺) of the overall tetrad. Measurements were performed in THF (black traces), DCM (blue traces) and benzonitrile (green traces).

Formation of the one-electron oxidized TPDB species (Figure 5.8) was achieved by application of 0.82 (THF) and 0.70 V *vs.* SCE (DCM and benzonitrile). Diagnostic bands are observed at 415 and 574 nm. Additionally, a third band develops at $\lambda > 800$ nm. The observations are consistent in the different solvents and are in agreement with comparable compounds reported in the literature.[140, 145, 146]
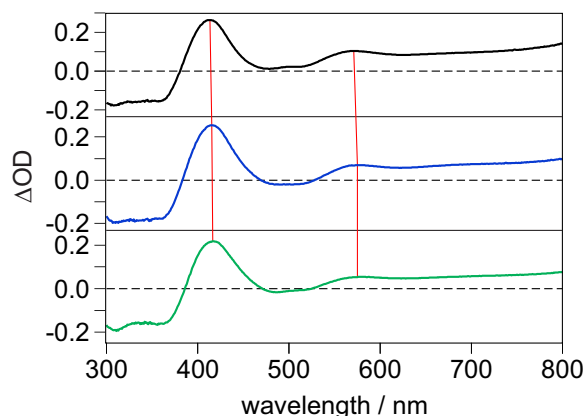


**Figure 5.8:** Spectro-electrochemical UV-Vis difference spectra of the TPDB unit in NMI-TPDB (0.2 mM) in THF (black), DCM (blue) and benzonitrile (green) at 293 K. The applied oxidation potentials were 0.82 V *vs.* SCE in THF and 0.70 V *vs.* SCE in DCM and benzonitrile. The UV-Vis spectum recorded prior to application of the potential served as baseline.

Application of -1.40 (THF and benzonitrile) and -1.45 V *vs.* SCE (DCM), to achieve the one-electron reduced NMI species, resulted in the spectro-electrochemical UV-Vis

difference spectra shown in Figure 5.9. The obtained spectra vary with solvent and show a band with maxima in the region of ca. 400 to 420 nm. A further band that occurs at 545 and 550 nm in DCM and benzonitrile, respectively, is not clearly visible in THF.
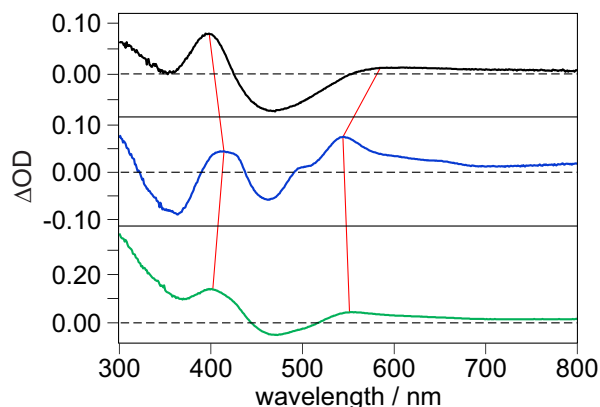


**Figure 5.9:** Spectro-electrochemical UV-Vis difference spectra of the NMI unit in NMI-TPDB (0.2 mM) in THF (black), DCM (blue) and benzonitrile (green) at 293 K. The applied reduction potentials were -1.40 V *vs.* SCE in THF and benzonitrile and -1.45 V *vs.* SCE in DCM. The UV-Vis spectum recorded prior to application of the potential served as baseline.

## 5.2.5 Steady-State Emission Spectroscopy

Steady-state emission spectroscopy of a 10 μM solution of NMI-TPDB was performed in toluene, THF and benzonitrile. However, owing to the low emission quantum yield in polar solvents, suitable emission spectra could only be obtained in toluene (Figure 5.10). A broad and intense emission band with a maximum centered around 650 nm was observed. The strong emission in toluene is consistent with the CT character of NMI-TPDB observed in the UV-Vis spectrum (Figure 5.5).
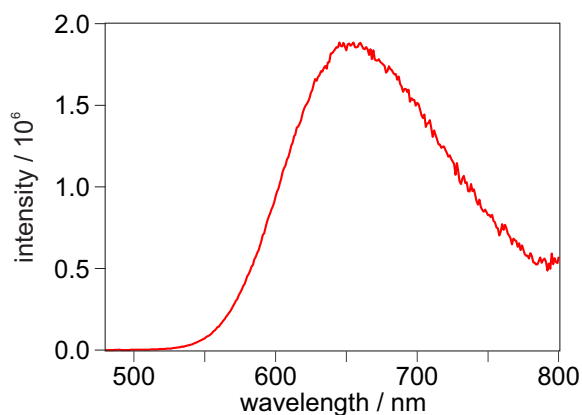


**Figure 5.10:** Steady-state emission spectrum of NMI-TPDB (10 μM) in dry and deoxygenated toluene following excitation at 465 nm.

### 5.2.6 Time-Resolved Emission Spectroscopy

Despite very weak emissions in THF and benzonitrile, time-correlated single photon countings (TCSPCs) were measured. Measurements were performed in 20 µM solutions of NMI-TPDB in toluene, THF and benzonitrile, monitoring the band at 650 nm. Excitation was carried out at 473 nm.

In toluene (Figure 5.11), an emission lifetime of 1.74 ns was determined, which is slightly shorter than in a comparable dyad.[144] However, the lifetime is promising enough for applicability in the anticipated tetrad.
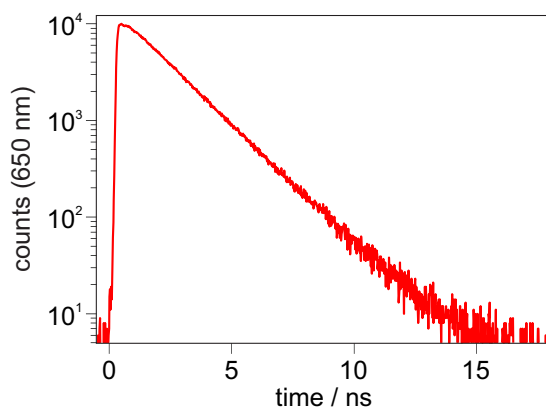


**Figure 5.11:** Formation and decay of the luminescence signal for the reference NMI-TPDB (20 µM) in toluene at 293 K monitoring, the band at 650 nm. Excitation occured at 473 nm.

As expected, measurements in THF and benzonitrile were nearly impossible to perform. From the obtained data, an upper limit lifetime of 30 ps in THF was extrapolated. The quality of the data in benzonitrile was even worse than in THF, which is why an emission lifetime of $< 30$ ps was stated in Table 5.4.

**Table 5.4:** Time constants ($\tau$) for the emission of NMI-TPDB (20 µM) in toluene, THF and benzonitrile, monitoring the decay of the emission signal at 650 nm.

|  | $\tau_{650\ nm}$ |
| --- | --- |
| toluene | 1.74 ns |
| THF | $30 \pm 5$ ps |
| benzonitrile | $< 30$ ps |

### 5.2.7 Summary

The investigations on the reference dyad NMI-TPDB indicate the applicability of the dyad in the overall tetrad. A broad and intense absorption band in the UV-Vis spectrum

(Figure 5.5) indicated direct CT transitions. After visible light excitation, NMI-TPDB indeed formed a CSS with a lifetime of 1.74 ns in toluene. However, excitation studies are limited to toluene as a solvent since no efficient lifetime was observable in more polar solvents, as expected. Investigations were also performed to determine the redox potentials and the driving forces (1.76 V in DCM and benzonitrile, 1.85 V in THF) in different solvents.

## 5.3 PT-TAA Reference

The PT-TAA reference represents the second photosystem required for photoexcitation *via* a Z-scheme approach in our anticipated tetrad. Therefore, analogous investigations to those presented in Chapter 5.2 were planned. However, the PT-TAA reference could not be obtained to date.

### 5.3.1 Synthesis of PT-TAA

The most promising reaction sequence for the synthesis of the reference PT-TAA is illustrated in Scheme 5.2.
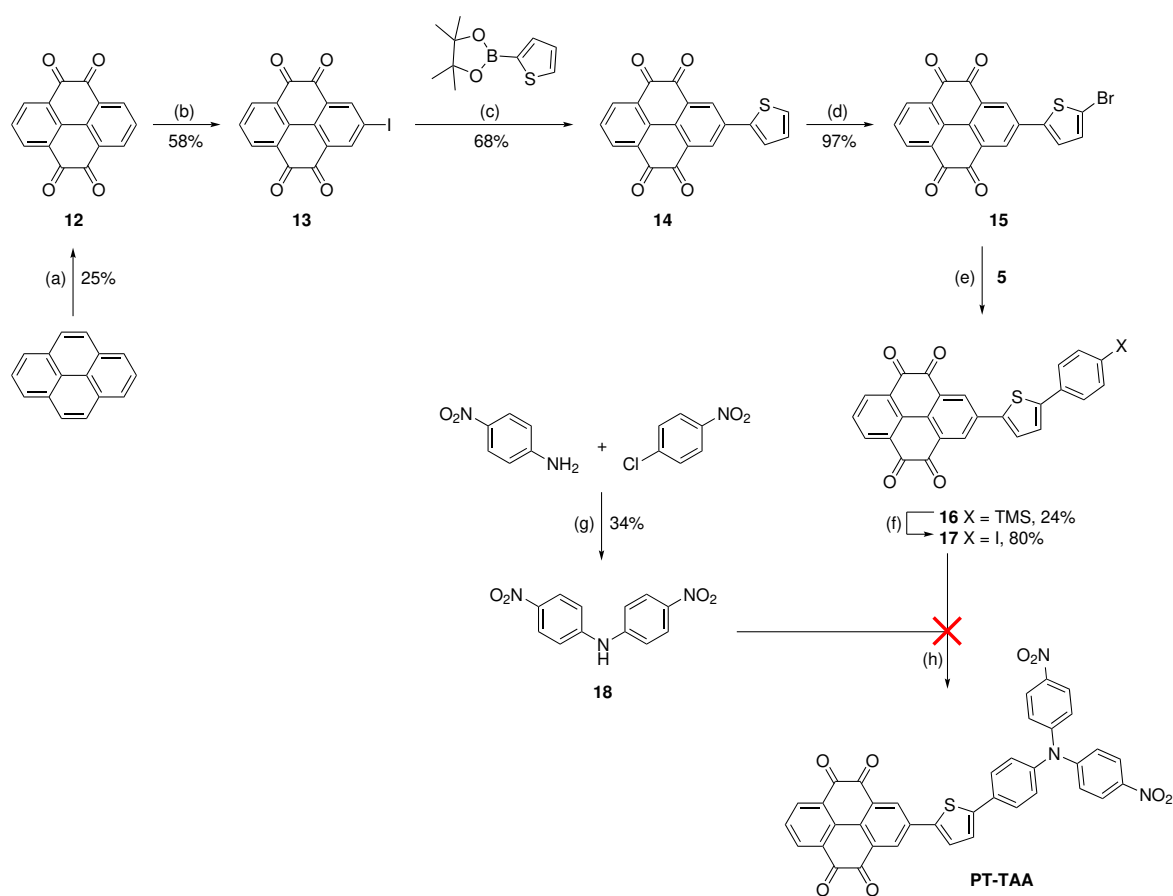


**Scheme 5.2:** Reaction scheme for the synthesis of the PT-TAA reference. (a) RuCl$_3$ · x H$_2$O, NaIO$_4$, DCM/CH$_3$CN/water, 40 °C, 23 h; (b) *N*-iodosuccinimide, H$_2$SO$_4$, 40 °C, 1 h; (c) Pd(PPh$_3$)$_4$, Na$_2$CO$_3$, toluene/water/ethanol, 90 °C, 22 h; (d) *N*-bromosuccinimide, DMF, 65 °C, 17 h; (e) Pd(PPh$_3$)$_4$, Na$_2$CO$_3$, toluene/water/ethanol, 90 °C, 39 h; (f) ICl, DCM, rt, 3 h; (g) K$_2$CO$_3$, DMSO, 150 °C, 5 h; (h) Pd(dba)$_2$, (HP$^t$Bu$_3$)BF$_4$, KO$^t$Bu, DMF, 90 °C, 42 h.

In a first step, pyrene was oxidized to PT (**12**), which was then mono-iodinated to PT-I (**13**) by stirring with *N*-iodosuccinimide in H$_2$SO$_4$ at 40 °C for 1 h. Formation of the

bis-iodinated species of compound **13** could not be avoided. However, multiple chromatography attempts on silica gel columns afforded isolated PT-I. Suzuki coupling of compound **13** with thiophene-2-boronic acid pinacol ester yielded PT-th (**14**) in 68%. Selective bromination in the α-position of the thiophene using *N*-bromosuccinimide in DMF at 65 °C and subsequent Suzuki coupling with TMS-ph-B(OH)$_2$ (**5**) afforded PT-th-ph-TMS (**16**). Deprotection of the TMS-protecting group was achieved with ICl in DCM in 80% yield. However, the solubility of the synthesized compounds worsen throughout the reaction sequence. The deprotected compound **17** was only soluble in DMF and DMSO. The final Buchwald-Hartwig amination of compound **17** with the secondary amine **18**, synthesized *via* uncatalyzed amination, was performed in dry and degassed DMF under an N$_2$ atmosphere. Under the chosen reaction conditions ((h) in Scheme 5.2), no indication for successful formation of the reference PT-TAA could be found. Due to a lack of substance of compound **17**, the final coupling could only be tested once and no modifications concerning the reaction conditions could be undertaken.

Alternative synthetic routes to PT-TAA were also unsuccessful. Direct coupling of PT-th-Br (**15**) with the desired TAA unit, containing a boronic acid pinacol ester, failed as well as building up the reference from the TAA-thiophene moiety. Since solubility became a growing problem in the reaction sequence in Scheme 5.2, it could be a solution to modify the design of the PT-TAA reference slightly as discussed in Chapter 5.5.
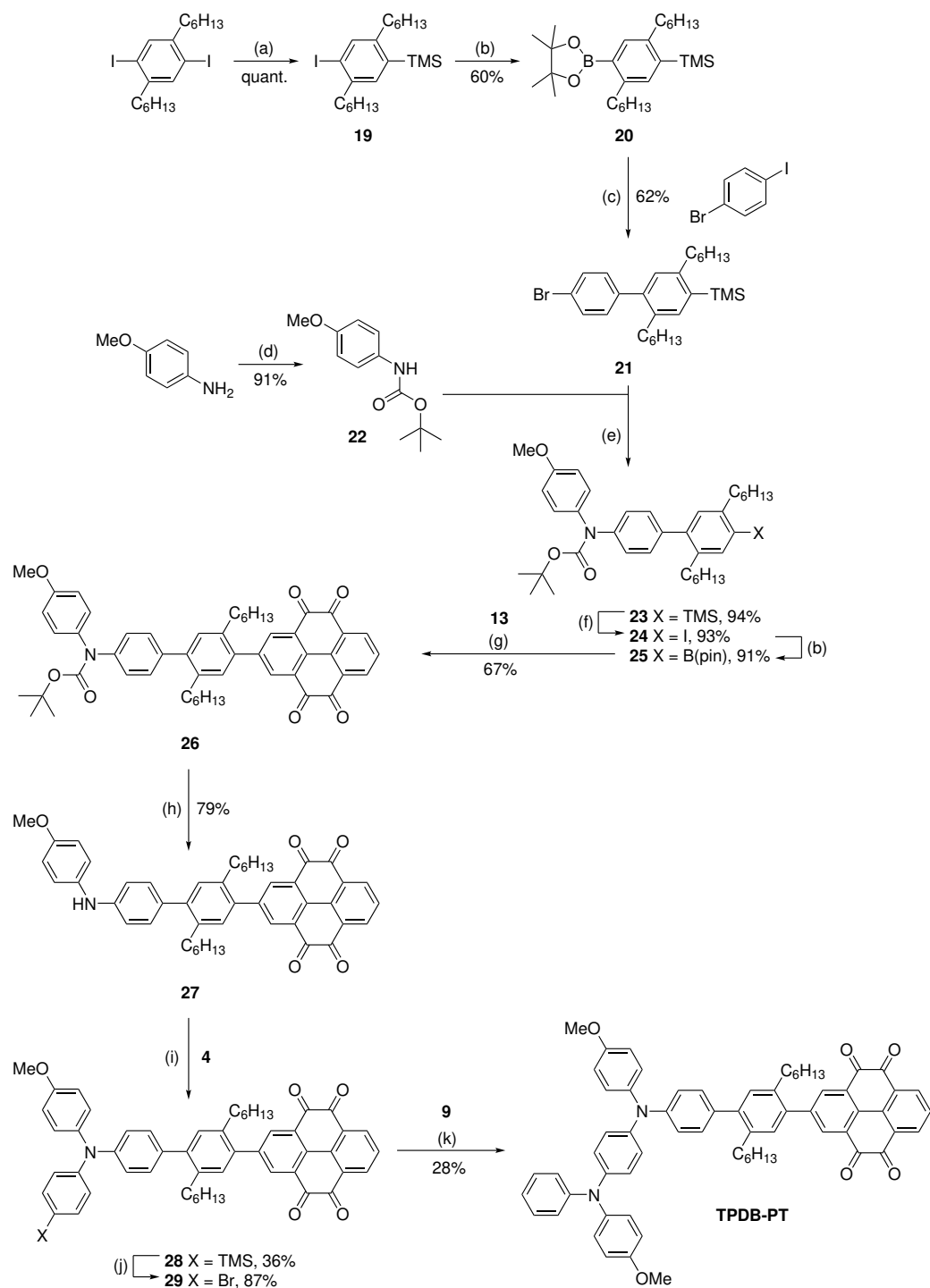
## 5.4 TPDB-PT Reference

In the TPDB-PT reference, direct CT transitions between the donor and acceptor unit are supposed to be inhibited by the hxy spacer. To support this assumption, electronic absorption and steady-state emission spectroscopies were performed. Time-resolved emission spectroscopy was excluded from the investigations of TPDB-PT since no emission could be observed during the steady-state measurements. As the proposed final CSS state in the tetrad consists of a reduced NMI and an oxidized TAA, neither of which are incorporated in the TPDB-PT reference, spectro-electrochemical measurements were also excluded from the investigations. However, characteristic signatures for the oxidized TPDB species were presented in Chapter 5.2.4 and characteristic signatures for the reduced PT species can be included in the studies of the PT-TAA reference. Electrochemical measurements were performed to determine the oxidation and reduction potentials of the TPDB-PT dyad. Based on these values, the energy of the CSS of the dyad and the driving force for thermal charge recombination can be estimated. The investigations were performed in up to four solvents, ranging from nonpolar toluene to more polar benzonitrile.

### 5.4.1 Synthesis of TPDB-PT

The reference compound TPDB-PT was successfully synthesized following the synthetic route summarized in Scheme 5.3.

In a first reaction sequence, the hxy spacer was modified in a way that allowed successful coupling with PT-I (**13**) and the first building block for the TPDB unit. First, one of the iodo groups of I-hxy-I was converted into a TMS-protecting group in quantitative yield. Following this, a Miyaura borylation was performed to introduce a boronic acid pinacol ester which allowed Suzuki coupling with 1-bromo-4-iodobenzene to form Br-ph-hxy-TMS (**21**) in 62% yield. During the synthetic route for TPDB-PT, it was proven unfavorable to use primary amines for Buchwald-Hartwig aminations. Therefore, a *tert*-butoxycarbonyl (Boc) protecting group was introduced by stirring *p*-anisidine with (Boc)$_2$O in glycerol at room temperature. Subsequent Buchwald-Hartwig amination of the Boc-protected amine **22** with compound **21** afforded DPNBoc-hxy-TMS (**23**) in 94% yield. After deprotection of the TMS group with ICl in DCM, a boronic acid pinacol ester was introduced by Miyaura borylation to yield DPNBoc-hxy-B(pin) (**25**) in 91%. Suzuki coupling of compound **25** with compound **13** yielded DPNBoc-hxy-PT (**26**) in 67%. Addition of TFA to a solution of **26** in DCM afforded the deprotected compound **27**, which was then coupled *via* Buchwald-Hartwig amination with TMS-ph-Br (**4**) to yield the triarylamine containing compound (OMe)(TMS)TAA-hxy-PT (**28**). After deprotection of the TMS unit with Br$_2$ and NaOAc in THF, the reference compound TPDB-PT could be obtained

*via* Buchwald-Hartwig amination of compound **29** with DPNH (**9**). In contrast to the synthesis of the reference compound NMI-TPDB, the reaction path for the sythesis of the TPDB unit in TPDB-PT needed to be modified, since Buchwald-Hartwig amination of the secondary amine **27** with (OMe)TAA-I (**11**) did not result in any TPDB-PT formation.

**Scheme 5.3:** Reaction scheme for the synthesis of the TPDB-PT reference. (a) *n*-BuLi, Et$_2$O, 0 °C, 1 h, TMSCl, 0 °C → rt, overnight; (b) bis(pinacolato)diboron, Pd(PPh$_3$)Cl$_2$, KOAc, DMSO, 90 °C, overnight; (c) Pd(PPh$_3$)$_4$, Na$_2$CO$_3$, THF/water, 85 °C, 41 h; (d) di-*tert*-butyl dicarbonate, glycerol, rt, 25 min; (e) Pd(dba)$_2$, *S*-Phos, Cs$_2$CO$_3$, toluene, 90 °C, 63 h; (f) ICl, DCM, −78 °C, 1 h; (g) Pd(PPh$_3$)$_4$, Na$_2$CO$_3$, THF/water, 85 °C, 19 h; (h) TFA, DCM, rt, 3 h; (i) Pd(dba)$_2$, (HP$^t$Bu$_3$)BF$_4$, NaO$^t$Bu, 1,4-dioxane, 95 °C, 47 h; (j) Br$_2$, NaOAc, THF, 0 °C, 10 min, 0 °C → rt, 3 h; (k) Pd(dba)$_2$, (HP$^t$Bu$_3$)BF$_4$, NaO$^t$Bu, toluene, 90 °C, 44 h.

## 5.4.2 Electronic Absorption Spectroscopy

Electronic absorption spectroscopy (see Figure 5.12) was performed at 293 K with 20 μM solutions of TPDB-PT in toluene (red trace), THF (black trace), DCM (blue trace) and benzonitrile (green trace).
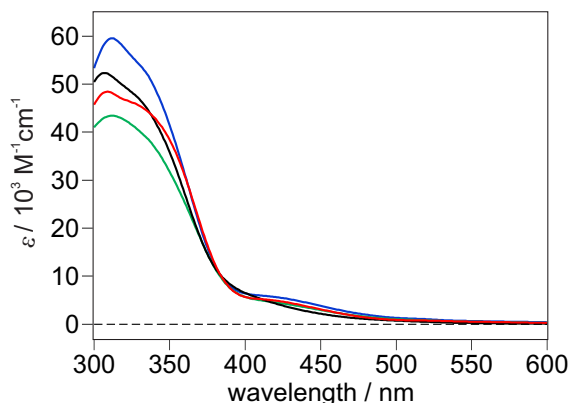


**Figure 5.12:** UV-Vis absorption spectra of TPDB-PT (20 μM) at 293 K in toluene (red), THF (black), DCM (blue) and benzonitrile (green).

In the region of *ca.* 310 to 380 nm, π-π* absorption bands are observed. However, a pronounced CT absorption band such as observed for the NMI-TPDB reference (Figure 5.5) cannot be observed for TPDB-PT. It was shown in Chapter 5.2 and in the literature[147] that donor-acceptor compounds containing TPDB or PT units do exhibit CT absorptions. The incorporation of the hxy spacer therefore weakens the donor-acceptor interaction, due to a larger torsion angle, minimizing these absorptions. The CT absorptions are observable as broad bands covering the region from *ca.* 400 to 500 nm with extinction coefficients under 6000 $M^{-1}$ $cm^{-1}$. However, direct CT excitation can be minimized by choosing $\lambda > 470$ nm for excitation.

At first glance, one could expect to observe a red-shift of the CT absorption band in TPDB-PT compared to NMI-TPDB (see Figure 5.5). However, the phenyl and thiophene spacers have a non neglectable influence on the position of those bands. It is known that thiophene spacers induce a more planar geometry in donor-acceptor compounds than phenyl spacers.[137, 148] As a result, a greater delocalization of the electrons, *i.e.* a stronger electronic coupling between the donor and acceptor units, is evoked. Thus, the electronic coupling in the TPDB-PT dyad is expected to be weaker than in the NMI-TPDB reference dyad, which should result in a blue-shift of the CT absorption band as shown in the literature.[137, 148, 149] This qualitative view is in very good agreement with the observed data for TPDB-PT in Figure 5.12. The very weak CT absorption bands are blue-shifted compared to the CT absorption band maxima in NMI-TPDB (462-473 nm, dependent on the solvent).

### 5.4.3 Electrochemistry and Driving Forces

Cyclic voltammograms of NMI-TPDB were measured in THF (Figure 5.13, left), DCM (Figure 5.13, middle) and benzonitrile (Figure 5.13, right). Experimental details can be found in Chapter 7.2.
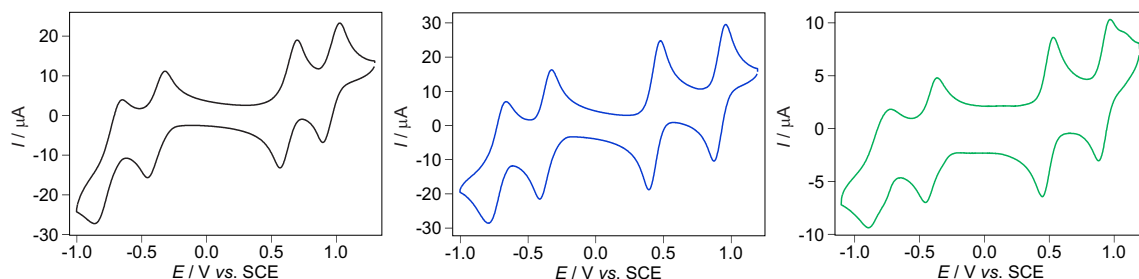


**Figure 5.13:** Cyclic voltammograms of 1 mM solutions of TPDB-PT measured in THF (black), DCM (blue) and benzonitrile (green). TBAPF$_6$ (0.1 M) was used as an electrolyte and a scan rate of 0.1 V/s was applied.

The one- and two-electron oxidations of the TPDB unit, observed when oxidative sweeps are performed, are in very good agreement with the potentials found in the NMI-TPDB reference (Table 5.3). Reductive cyclic voltammetry in the scanned regions shows two reversible reduction waves which are consistent with the literature.[141, 147, 150] These waves are assigned to the first and second one-electron reductions of the PT unit. In theory, PT can be reduced four times. However, the first two reductions should be easier to achieve and should also result in reversible waves like the ones shown in Figure 5.13. Acceptance of a third or even a fourth electron by the PT unit should go in hand with electrostatic repulsion, which leads to higher reduction potentials and more likely to irreversible waves.[150] The extracted redox potentials (Table 5.5) can be used for determination of the driving force for thermal charge recombination in the given system. Corresponding calculations can be found in the Appendix.

**Table 5.5:** Redox potentials (in V *vs.* SCE) extracted from Figure 5.13.

|  | THF / V | DCM / V | benzonitrile / V |
|---|---|---|---|
| $E^0(\text{PT}^{-/2-})$ | -0.76 | -0.73 | -0.79 |
| $E^0(\text{PT}^{0/-})$ | -0.38 | -0.37 | -0.41 |
| $E^0(\text{TPDB}^{+/0})$ | 0.63 | 0.44 | 0.49 |
| $E^0(\text{TPDB}^{2+/+})$ | 0.96 | 0.92 | 0.92 |
| $-\Delta G_{\text{CR}}{}^0$ / eV | 1.01 | 0.81 | 0.90 |

## 5.4.4 Steady-State Emission Spectroscopy

Steady-state emission spectra were recorded with 20 μM solutions of TPDB-PT in toluene and THF. However, no suitable emission spectra could be obtained upon excitation into the weak CT absorption band ($\Delta$OD $\approx$ 0.1 at excitation wavelength of 420 nm). This observation is in very good agreement with the expected behavior of this reference dyad. The UV-Vis spectra in Figure 5.12 suggest that an excitation with 420 nm is indeed possible, even if the extinction coefficient is low. However, since no CT emission can be observed, it appears that thermal charge recombination back to the ground-state of TPDB-PT is very fast. Thus, the CT emission is too short-lived in the given dyad to be observable.

## 5.4.5 Summary

The investigations on the reference dyad TPDB-PT indicate the applicability of the hxy spacer in the overall tetrad. Excitation into the weak CT absorption band at 420 nm suggests that thermal charge recombination appears to be rapid, since no emission could be observed. Due to the introduction of a hxy spacer, minimization of direct (optical) CT transition was achieved, which is a necessary requirement for efficient formation of the final CSS in the tetrad. Direct CT excitation can be minimized further by choosing $\lambda > 470$ nm for excitation. Additionally, driving forces for thermal charge recombination of the CSS of TPDB-PT were calculated based on measured redox potentials (1.01 eV in THF, 0.81 eV in DCM, 0.90 eV in benzonitrile).

## 5.5 Overall Summary and Outlook

In summary, investigations on the reference dyad NMI-TPDB indicate its applicability concerning our molecular Z-scheme approach. The presented experiments for TPDB-PT suggest that thermal charge recombination in this building block appears to be rapid, since no emission could be observed after excitation into the weak CT absorption bands ($\varepsilon$ < 5000 M$^{-1}$ cm$^{-1}$, OD $\approx$ 0.1). The design principle of the overall tetrad appears to be promising. However, it is not foreseeable yet, if the hxy spacer will allow rapid thermal charge recombination between the oxidized TPDB and the reduced PT units in the twofold excited state NMI$^{\cdot-}$-TPDB$^{\cdot+}$-PT$^{\cdot-}$-TAA$^{\cdot+}$. Experiments on the reference dyads are promising since thermal charge recombination in TPDB-PT was found to be significantly more rapid than in NMI-TPDB. However, it is not appreciable if the charge recombination rate of TPDB-PT will also outcompete thermal charge recombination in PT-TAA. In general, a driving force for thermal charge recombination between the oxidized TPDB and the reduced PT units of about 0.80 to 1.00 eV (depending on the solvent) is expected to drive the reaction, but this charge recombination step remains a risk.

To date, the synthesis of the second photosystem reference PT-TAA was unsuccessful. It was found during the synthesis attempts that the solubility decreases drastically on the way to the final reference dyad. A possible way to solve this impediment could be to slightly modify the design of the reference. Addition of a hxy unit next to the PT unit should increase the solubility of the system significantly while it should not have an influence on the properties of the PT-TAA part. Instead of PT-TAA, it should be aimed for hxy-PT-TAA as a reference. A proposed synthetic route for the synthesis of hxy-PT-TAA is summarized in Scheme 5.4. In principle, other solubility groups like 1,2,3-tris(hexyloxy)-benzene could also be used, but the reference dyad is aimed to be as similar to the overall tetrad as possible.

In the proposed synthetic route, the terminal hxy unit is synthesized by mono-dehalogenation of I-hxy-I to afford hxy-I (**30**). After Miyaura borylation, the resulting compound **31** should undergo Suzuki coupling with I-PT-I (**32**), obtained *via* double iodination of PT (**12**), to give hxy-PT-I (**33**). Another Suzuki coupling, followed by selective α-bromination of the thiophene unit should form hxy-PT-th-Br (**35**). Suzuki coupling with TMS-ph-B(OH)$_2$ (**5**) and deprotection of the TMS group should yield compound **37**. In the final step, Buchwald-Hartwig amination should afford the anticipated hxy-PT-TAA reference.
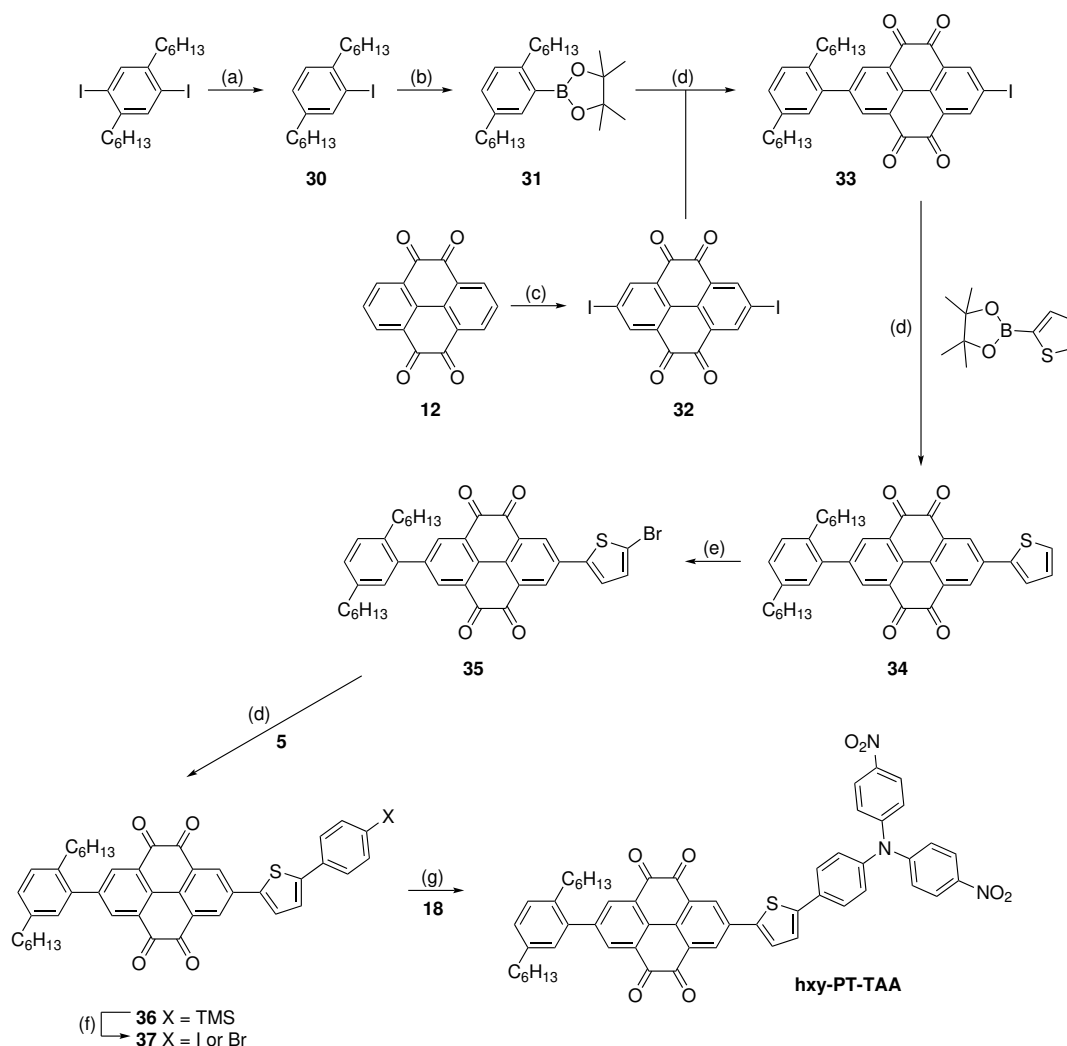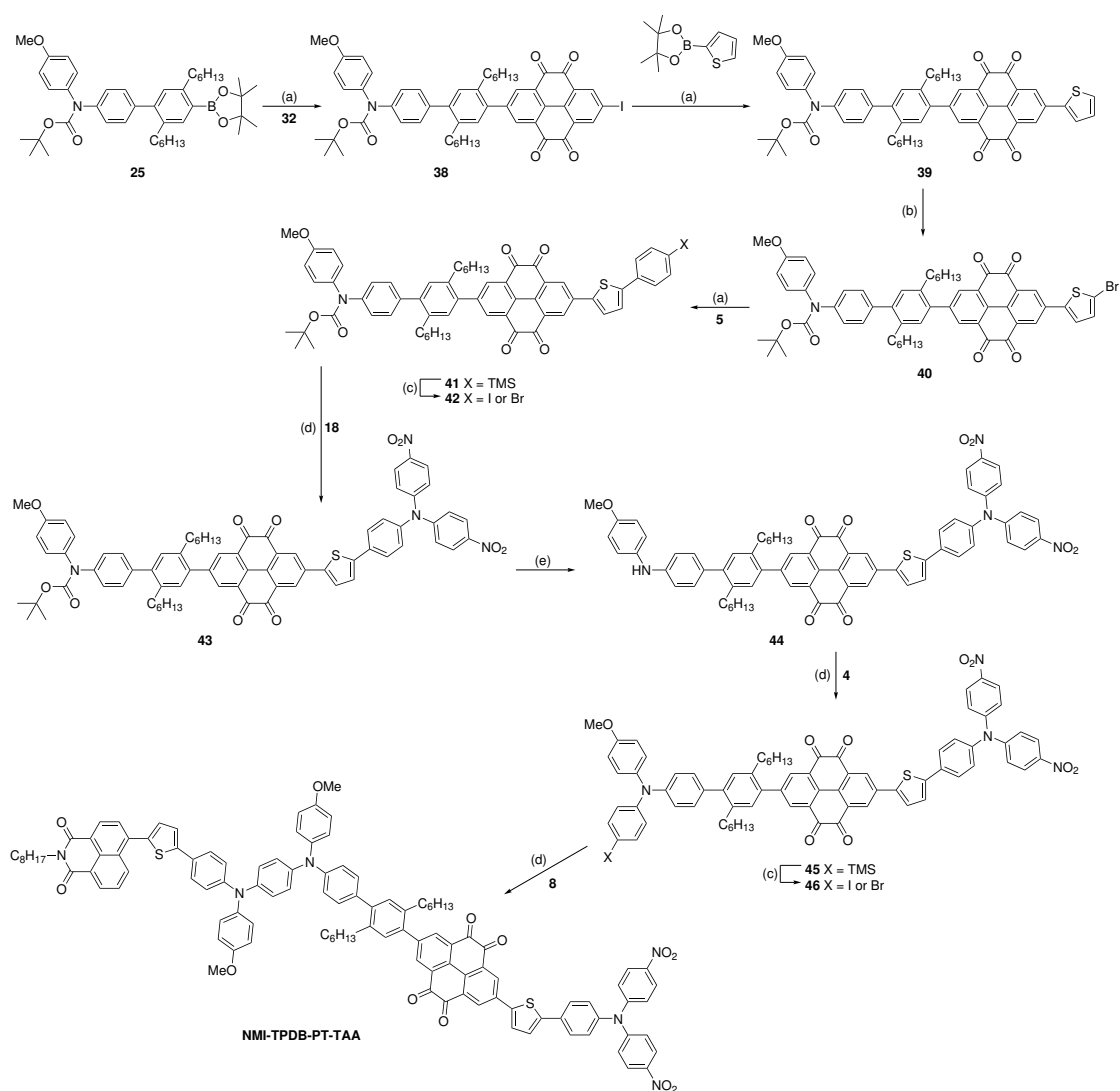
**Scheme 5.4:** Proposed synthetic route for the synthesis of the hxy-PT-TAA reference. (a) Dehalogenation; (b) Miyaura borylation; (c) iodination; (d) Suzuki coupling; (e) selective bromination in α-position; (f) TMS-protecting group deprotection; (g) Buchwald-Hartwig amination.

Assuming that the hxy-PT-TAA dyad shows favorable properties concerning the applicability to act as the second photosystem in the overall molecular Z-scheme tetrad NMI-TPDB-PT-TAA, a synthetic route for the synthesis of the tetrad was developed (Scheme 5.5). The proposed route, 28 steps in total, is based on synthetic experiences acquired during the synthesis of the reference compounds. For reasons of clarity, only new synthetic steps are shown.

DPNBoc-hxy-B(pin) (**25**) is supposed to perform Suzuki coupling with I-PT-I (**32**) to afford DPNBoc-hxy-PT-I (**38**). This reaction needs to be performed with a large excess of compound **32** to prevent twofold Suzuki coupling. In a next step, Suzuki coupling with thiophene-2-boronic acid pinacol ester, followed by selective α-bromination of the thiophene unit, should result in the formation of DPNBoc-hxy-PT-th-Br (**40**). A reaction

sequence of Suzuki coupling of compound **40** with TMS-ph-B(OH)$_2$ (**5**), TMS deprotection and Buchwald-Hartwig amination with (NO$_2$)DPNH (**18**) is supposed to yield DPNBoc-hxy-PT-th-TAA (**43**). At this stage, one of the photosystems is successfully incorporated into the compound. To implement the second photosystem, the *N*-Boc protecting group needs to be deprotected under acidic conditions before a TAA unit can be synthesized *via* Buchwald-Hartwig amination with TMS-ph-Br (**4**). TMS-protecting group deprotection and Buchwald-Hartwig amination of compound **46** with NMI-th-DPNH (**8**) should finally result in the formation of the desired tetrad NMI-TPDB-PT-TAA.



**Scheme 5.5:** Proposed synthetic route for the synthesis of the molecular Z-scheme tetrad NMI-TPDB-PT-TAA. (a) Suzuki coupling; (b) selective bromination in α-position; (c) TMS-protecting group deprotection; (d) Buchwald-Hartwig amination; (e) *N*-Boc deprotection.

After successful synthesis of the molecular tetrad NMI-TPDB-PT-TAA, the artificial Z-

scheme should be tested for its spectroscopic, redox and photophysical properties. It would be desirable if the tetrad could store more than 2.5 eV in its final CSS (NMI$^{\cdot-}$-TPDB-PT-TAA$^{\cdot+}$) after absorption of two single visible photons by the two photosystems. To date, the maximum energy stored in an artifical molecular Z-scheme is 2.0 eV.[53] The formation of such a highly energetic CSS can be seen as direct proof of the light upconversion principle of the photosynthetic Z-scheme, which generated a strong oxidant and a strong reductant in the overall system. The formation of such a strong oxidant and reductant could not be achieved by only one photosystem. Furthermore, it will be interesting to see if the lifetime of the final CSS in the tetrad, compared to the reference dyads, also increases by multiple orders of magnitude due to the Z-scheme approach as it is reported for other molecular Z-schemes.[53, 67] With the formation of a highly energetic CSS and an increase in the lifetime of this state, tetrad NMI-TPDB-PT-TAA would be the first purely organic and molecular artificial Z-scheme. This would show that the Z-scheme approach is not limited to metal-containing compounds.

# 6 General Summary and Conclusion

In this thesis, processes relevant for artificial photosynthesis were investigated to gain more knowledge about (fundamental) aspects of electron-transfer reactions initiated by visible light. Improved understanding of the distance dependence of electron transfer, the properties of charge-separated states and the photosynthetic Z-scheme can help to develop novel systems to perform more efficient artificial photosynthesis and solar energy conversion.

In the first project (Chapter 3), the distance dependence of electron-transfer rates in donor-photosensitizer-acceptor triads was studied in a systematic manner with a focus on the influence of the driving force. Against the background of recent findings in our group,[93, 94] two sets of molecular triads with either a low (*ca.* 1.2 eV in TAA-ph$_n$-Ru-ph$_n$-NDI) or a high (*ca.* 2.0 eV in TPA-ph$_n$-Ir-ph$_n$-AQ) driving force for thermal charge recombination were synthesized. Symmetrical addition of phenyl spacers allowed the elongation of the donor-acceptor distances (n = 1,2). With these triads in hand, we wanted to distinguish a counterintuitive effect, namely an increase in the electron-transfer rate for thermal charge recombination after an increase of the donor-acceptor distance, observed earlier. Taken as a basis was a reported triad by WENGER and KUSS-PETERMANN with a driving force of *ca.* 1.6 eV. Theoretical considerations suggested that a further increase of the driving force should result in a more pronounced counterintuitive effect when elongating the donor-acceptor distance, whereas a significantly lower driving force should shift the electron-transfer behavior back to a typical constant decrease of the electron-transfer rate. Indeed, our investigations confirmed that highly exergonic electron-transfer reactions can exhibit fundamentally different distance dependences than the more commonly investigated weakly exergonic electron transfers (Figure 6.1).
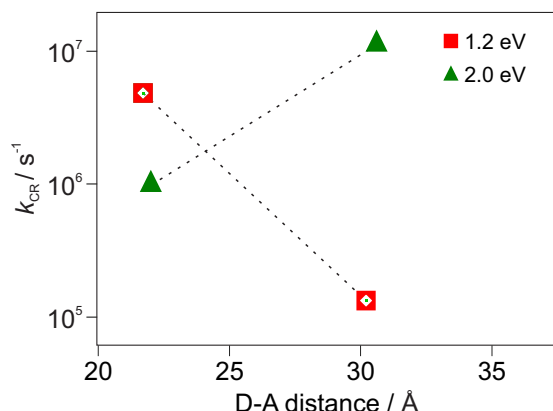
**Figure 6.1:** Distance dependences of the electron-transfer rates of the investigated molecular triads.

For the triads with a low driving force, elongation of the donor-acceptor distance resulted in a decrease of the electron-transfer rate for thermal charge recombination. Elongation of the distance in the triads with a high driving force showed opposite behavior. An increase of the electron-transfer rate was observed. This can be explained by a changeover from activationless electron transfer to the normal region of the MARCUS model in the case of the triads with a low driving force. In the triads with a high driving force, electron transfer occurs in the inverted regime for the shorter triad and proceeds in an activationless manner for the longer compound. These observations are of high relevance in the context of artificial photosynthesis and solar energy conversion. The energies that are stored in the charge-separated states (CSSs) of the investigated triads could theoretically be used for driving other reactions. It would therefore be desirable to have long lifetimes of the CSSs to facilitate subsequent reactions to occur. Additionally, it would be desirable to store high amounts of energy to drive energetically demanding reactions. However, our studies showed that the distance between two reactants is especially crucial in highly energetic states, in our case storage of 2.0 eV, since too long distances could have a counterproductive effect and decrease the lifetime significantly.

As mentioned above, highly energetic CSSs are desirable for artificial photosynthesis and solar energy conversion. The project presented in Chapter 4 therefore studied the iridium-based triads from Chapter 3, which store 2.0 eV in their CSSs, in more detail. Whereas previous investigations of the triads focused exclusively on the qualitative formation of the CSSs and the distance dependences of thermal charge recombination, this study extended the earlier investigations by adding quantitative aspects, *i.e.* quantum yields, and studies concerning light-induced charge recombination. Both CSS quantum yields and light-induced charge recombinations are largely unexplored nowadays. Using one- and two-pulse laser flash photolysis, we were able to obtain insights into the CSS formation quantum yields and the behavior of the CSSs after absorption of a second photon. The

formation quantum yields reached up to 80%. However, the formation efficiency is highly dependent on the main formation pathway in the given system. High quantum yields were only observed if the formation of the CSS proceeded exclusively *via* an MLCT transition. In the shorter triad, intraligand charge transfer was possible, which decreased the quantum yield drastically. Additionally, only the shorter triad showed a wavelength dependence of the formation quantum yield due to the admixture of MLCT transitions, depending on the chosen excitation wavelength. Interestingly, two-pulse experiments revealed that light-induced charge recombination shows opposite behavior compared to thermal charge recombination in terms of their distance dependences. Light-induced charge recombination in the shorter triad was significantly more efficient than in the longer triad, but thermal charge recombination was slower. The findings of this project illustrate the importance of quantitative laser experiments and the results can be used for the optimization of future systems for artificial photosynthesis, *e.g.* for systems capable of performing charge accumulation.

In the third project (Chapter 5), the synthesis and investigation of a purely organic and molecular Z-scheme mimic was anticipated. This project combines the processes of electron transfer over large distances, the formation of a highly energetic CSS and multiple photon absorption. For the study, a molecular tetrad (NMI-TPDB-PT-TAA) was designed to utilize the upconversion principle of the photosynthetic Z-scheme. Since the synthesis of the anticipated tetrad is rather ambitious and time-consuming, three reference dyads (NMI-TPDB, TPDB-PT and PT-TAA) were developed to gain more knowledge if the approach for the tetrad is promising enough to pursue. While the successful synthesis of the PT-TAA reference is still pending due to synthetic difficulties, the dyads NMI-TPDB and TPDB-PT were examined and their applicability for the tetrad was verified. The NMI-TPDB dyad represents one of the photosystems needed for a Z-scheme approach and formed a CSS after visible light excitation into a direct charge transfer (CT) absorption band. The lifetime was determined to be 1.74 ns in toluene, which is expected to be long-living enough to facilitate thermal charge recombination in the central unit of the tetrad (TPDB-PT), after absorption of two photons by the tetrad, instead of direct charge recombination back to the ground-state. It is a necessary requirement for the tetrad that the central unit of the molecule cannot efficiently form a CSS. Therefore, a hxy linker was introduced between the TPDB and PT units. The investigations showed that TPDB-PT can indeed only exhibit weak CT absorptions. Excitation into the CT absorption band confirmed that TPDB-PT cannot efficiently undergo charge separation since thermal charge recombination to the ground-state occurs to rapid. The results obtained to date are very promising. However, no conclusion for the overall tetrad can be stated yet. If the anticipated tetrad can successfully mimic the photosynthetic Z-scheme, it would be

demonstrated that the molecular Z-scheme approach is not limited to metal-containing artificial systems.[53]

In summary, the results obtained in this thesis significantly contribute to an improved understanding of processes relevant for artificial photosynthesis and might facilitate the development of novel and more efficient systems for artificial solar energy storage and solar energy conversion.

# 7 Experimental Section

## 7.1 General Methods

The synthesis of air and water sensitive compounds was performed under inert conditions ($N_2$) using the Schlenk line technique. All commercially available chemicals used for synthesis were purchased from commercial sources (ABCR, Alfa Aesar, Acros Organics, Combi-Blocks, Fluka, Fluorochem, Sigma-Aldrich) and used as received. Dry THF, DCM and $Et_2O$ (HPLC grade) were obtained from a solvent purification system from Innovative Technology. Additional dry solvents were purchased from Sigma-Aldrich or from Acros Organics. For spectroscopic measurements, dry solvents from Sigma-Aldrich were used. Deuterated solvents for NMR spectroscopy were purchased from Cambridge Isotope Laboratories. Column chromatography was performed on silica gel (40-63 µm, Silicycle) and silica plates for thin layer chromatography were obtained from Merck (60 F254). Samples for spectroscopic methods were deoxygenated by purging the samples with argon for several minutes.

## 7.2 Analytical Methods

The analytical methods employed for the studies in Chapter 5 are described below. The methods relevant for the studies in Chapter 3 and Chapter 4 are described separately in the supporting information of the respective publications.

### NMR Spectroscopy

$^1$H NMR spectroscopy was performed on a Bruker Avance III instrument operating at 400 MHz proton frequency. All chemical shifts ($\delta$) reported in this thesis are given in ppm. The proton residue signal of the deuterated solvents[151] DMSO-$d_6$ ($\delta$ = 2.50 ppm), $CD_2Cl_2$ ($\delta$ = 5.32 ppm) and $CDCl_3$ ($\delta$ = 7.26 ppm) was used as the respective reference. Coupling constants ($J$) are given in Hz and the multiplicity is listed as follows: singlet (s), broad singlet (broad s), doublet (d), doublet of doublets (dd), triplet (t), triplet of triplets (tt), multiplet (m).

## Mass Spectrometry

High-resolution mass spectra were measured on a Bruker maXis 4G QTOF ESI spectrometer by Dr. Heinz Nadig and Dr. Michael Pfeffer in the Department of Chemistry at University of Basel.

## Elemental Analysis

Elemental analyses were performed by Ms. Sylvie Mittelheisser on a Vario Micro Cube instrument in the Department of Chemistry at University of Basel.

## UV-Vis Spectroscopy

Optical absorption spectroscopy was performed on a Cary 5000 UV-Vis-NIR instrument from Varian.

## Cyclic Voltammetry

A Versastat3-200 potentiostat from Princeton Applied Research was used to perform cyclic voltammetric measurements. The setup was comprised of an SCE reference electrode, a silver wire serving as counter electrode and a glassy carbon disk as working electrode. Measurements were performed in dry and Ar-purged THF, DCM and benzonitrile with tetrabutylammonium hexafluorophosphate (TBAPF$_6$, 0.1 M) as an electrolyte. For all measurements, a potential scan rate of 0.1 V/s was applied. The UV-Vis-NIR spectrometer was used in combination with the Versastat3-200 potentiostat to perform spectroelectrochemical measurements. Here, a quartz cuvette was equipped with a platinum grid as working electrode, a platinum wire as counter electrode and an SCE reference electrode.

## Steady-State Luminescence

Steady-state luminescence measurements were performed in dry and Ar-purged THF and toluene. A Fluorolog-322 instrument from Horiba Jobin-Yvon was used.

## Time-Resolved Luminescence

Time-resolved luminescence measurements were performed in dry and Ar-purged toluene, THF and benzonitrile. A LifeSpec II TCSPC spectrometer from Edinburgh Instruments using a picosecond pulsed diode laser (75.5 ps pulse width) for excitation at 473 nm was used.

## DFT Calculations

All DFT calculations were performed by Dr. Christoph Kerzig (group of Prof. Dr. Oliver S. Wenger, University of Basel) who kindly provided the following paragraph.

All calculations were performed with the Gaussian 09 package[152]. DFT calculations with the B3LYP functional and the 3-21G basis set were carried out to optimize the geometry of the model compound ($CH_3$ instead of $C_8H_{17}$). The geometry optimization was accompanied by a frequency analysis; the absence of negative vibrational frequencies indicated convergence on a minimum energy structure. Based on the optimized structure, TD-DFT (Time-Dependent Density Functional Theory) calculation were employed to obtain the vertical excitation energies of the model compound as well as the corresponding oscillator strengths.

## 7.3  Synthesis

Full experimental details for the synthesis of the triads TAA-ph$_n$-Ru-ph$_n$-NDI and TPA-ph$_n$-Ir-ph$_n$-AQ (named TAA-ph$_n$-Ir-ph$_n$-AQ in Chapter 4) can be found in the supporting information of the published paper presented in Chapter 3.

### 7.3.1  Synthesis of the NMI-TPDB Reference

#### NMI-Br (1)
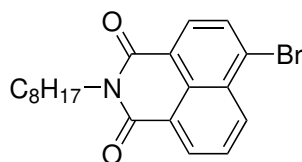


The following procedure was adapted from literature.[153, 154] 4-Bromo-1,8-naphthalic anhydride (2.50 g, 9.03 mmol, 1.00 eq.) was suspended in ethanol (50 mL) under $N_2$ atmosphere. The mixture was degassed for 15 min before $n$-octylamine (3.00 mL, 18.1 mmol, 2.00 eq.) was added and the mixture was heated at reflux for 18 h. After cooling to room temperature, the precipitate was collected by filtration and washed with water (300 mL). The product was purified by chromatography on a silica gel column with 1:1 (v:v) $n$-pentane/DCM as an eluent. The product was obtained as a yellow solid (3.00 g, 7.73 mmol, 86%). $^1$H NMR (400 MHz, CDCl$_3$): δ [ppm] = 8.62 (dd, $J$ = 7.3, 1.1 Hz, 1 H), 8.52 (dd, $J$ = 8.5, 1.1 Hz, 1 H), 8.38 (d, $J$ = 7.9 Hz, 1 H), 8.00 (d, $J$ = 7.9 Hz, 1 H), 7.82 (dd, $J$ = 8.5, 7.3 Hz, 1 H), 4.18−4.11 (m, 2 H), 1.78−1.65 (m, 2 H), 1.46−1.19 (m, 10 H), 0.93−0.82 (m, 3 H).

#### NMI-th (2)
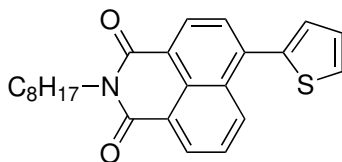


NMI-Br (**1**, 1.00 g, 2.58 mmol, 1.00 eq.), thiophene-2-boronic acid pinacol ester (651 mg, 3.10 mmol, 1.20 eq.) and Na$_2$CO$_3$ (820 mg, 7.74 mmol, 3.00 eq.) were suspended in a mixture of toluene (20 mL), water (10 mL) and ethanol (5 mL). The mixture was degassed for 15 min, Pd(PPh$_3$)$_4$ (150 mg, 0.13 mmol, 0.05 eq.) was added and the mixture was degassed for additional 10 min. The mixture was stirred at 90 °C under $N_2$ atmosphere for 20 h and then cooled to room temperature. Water (10 mL) was added and the aqueous

phase was extracted with DCM (3 × 30 mL). The combined organic phases were dried over anhydrous $Na_2SO_4$ and the solvents were removed under reduced pressure. The product was purified by chromatography on two silica gel columns. First, a chromatography with 1:1 (v:v) $n$-pentane/DCM as an eluent was performed. Further purification was possible on a second column with 7:1 (v:v) $n$-pentane/EtOAc as an eluent. The product was obtained as a yellow solid (476 mg, 1.22 mmol, 47%). $^1$H NMR (400 MHz, $CDCl_3$): δ [ppm] = 8.59−8.53 (m, 2 H), 8.52 (d, $J$ = 7.6 Hz, 1 H), 7.74 (d, $J$ = 7.6 Hz, 1 H), 7.69 (t, $J$ = 7.9, 7.9 Hz, 1 H), 7.54−7.51 (m, 1 H), 7.32−7.29 (m, 1 H), 7.24−7.20 (m, 1 H), 4.18−4.12 (m, 2 H), 1.77−1.67 (m, 2 H), 1.47−1.17 (m, 10 H), 0.92−0.80 (m, 3 H).

## NMI-th-Br (3)
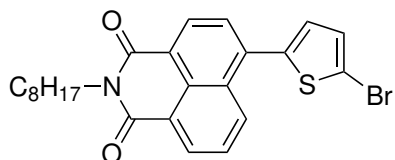


Following a published protocol,[154] a mixture of $Br_2$ (70 μL, 1.37 mmol, 1.26 eq.) in $CHCl_3$ (3 mL) was added dropwise over 20 min to a solution of NMI-th (**2**, 427 mg, 1.09 mmol, 1.00 eq.) in acetic acid (13 mL). The mixture was stirred at room temperature for 20 min before sat. aq. $Na_2S_2O_3$ (5 mL) and sat. aq. $NaHCO_3$ solutions (20 mL) were added. The aqueous phase was extracted with DCM (3 × 15 mL) and the combined organic phases were dried over anhydrous $Na_2SO_4$. Removal of the solvents under reduced pressure yielded the product as a yellow solid (quant. yield). $^1$H NMR (400 MHz, $CDCl_3$): δ [ppm] = 8.63 (dd, $J$ = 7.3, 1.0 Hz, 1 H), 8.58 (d, $J$ = 7.6 Hz, 1 H), 8.57 (dd, $J$ = 8.5, 1.0 Hz, 1 H), 7.79−7.73 (m, 2 H), 7.20 (d, $J$ = 3.8 Hz, 1 H), 7.09 (d, $J$ = 3.8 Hz, 1 H), 4.20−4.14 (m, 2 H), 1.78−1.68 (m, 2 H), 1.47−1.20 (m, 10 H), 0.90−0.84 (m, 3 H).
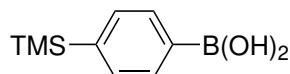
## TMS-ph-Br (4)
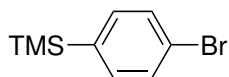


The following procedure was adapted from literature.[155] 1,4-Dibromobenzene (2.50 g, 10.6 mmol, 1.00 eq.) was dissolved in dry $Et_2O$ (20 mL) and cooled to −78 °C under $N_2$ atmosphere. $n$-BuLi (2.5 M in hexanes, 5.00 mL, 12.5 mmol, 1.18 eq.) was added dropwise and the mixture was stirred for 15 min at −78 °C. Chlorotrimethylsilane (1.70 mL, 13.4 mmol, 1.26 eq.) was slowly added while cooling at −78 °C was maintained. The mixture was allowed to warm to room temperature and stirred for 45 min. Water (40 mL) was added and the aqueous phase was extracted with $Et_2O$ (2 × 20 mL). The combined

organic phases were dried over anhydrous $Na_2SO_4$ and the solvents were removed under reduced pressure. The product was obtained as a colorless oil (2.30 g, 10.0 mmol, 94%). $^1$H NMR (400 MHz, CDCl$_3$): δ [ppm] = 7.52–7.48 (m, 2 H), 7.41–7.38 (m, 2 H), 0.28 (s, 9 H).

## TMS-ph-B(OH)$_2$ (5)



Following a published protocol,[156] TMS-ph-Br (**4**, 6.06 g, 26.3 mmol, 1.00 eq.) was dissolved in dry THF (130 mL) and the solution was cooled to −78 °C under $N_2$ atmosphere. $n$-BuLi (2.5 M in hexanes, 10.6 mL, 26.5 mmol, 1.00 eq.) was added dropwise and the mixture was stirred for 1.5 h at −78 °C. Afterwards, trimethyl borate (3.29 mL, 29.0 mmol, 1.10 eq.) was added over a period of 10 min while cooling at −78 °C was maintained. The mixture was stirred at −78 °C for additional 30 min and was then allowed to warm to room temperature and stirred overnight. Aq. HCl solution (1 M, 85 mL) and EtOAc (40 mL) were added and the phases were separated. The aqueous phase was extracted with EtOAc (3 × 40 mL), the combined organic phases were dried over anhydrous $Na_2SO_4$ and the solvents were removed under reduced pressure. The residue was recrystallized from $n$-pentane to afford TMS-ph-B(OH)$_2$ as a white solid (1.82 g, 9.38 mmol, 36%). $^1$H NMR (400 MHz, CDCl$_3$): δ [ppm] = 8.22–8.18 (m, 2 H), 7.70–7.66 (m, 2 H), 0.33 (s, 9 H).
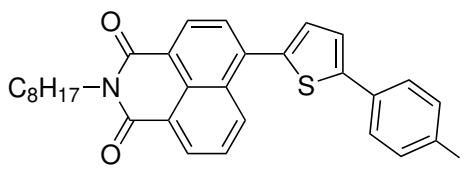
## NMI-th-ph-TMS (6)
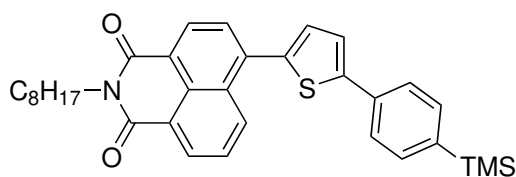


A mixture of NMI-th-Br (**3**, 496 mg, 1.05 mmol, 1.00 eq.), TMS-ph-B(OH)$_2$ (**5**, 245 mg, 1.26 mmol, 1.20 eq.) and $Na_2CO_3$ (334 mg, 3.15 mmol, 3.00 eq.) in a mixture of toluene (10 mL), water (5 mL) and ethanol (2.5 mL) was degassed for 20 min before Pd(PPh$_3$)$_4$ (61.0 mg, 0.05 mmol, 0.05 eq.) was added. The mixture was degassed for additional 10 min and stirred at 90 °C under $N_2$ atmosphere for 24 h. Once the reaction mixture had nearly reached room temperature, water was added and the aqueous phase was extracted with DCM (3 × 30 mL). The combined organic phases were dried over anhydrous $Na_2SO_4$ and the solvents were removed under reduced pressure. After purification of the product by chromatography on a silica gel column with 20:1 (v:v) $n$-pentane/EtOAc as an eluent,

the product was obtained as a yellow solid (541 mg, 1.00 mmol, 95%). $^1$H NMR (400 MHz, CDCl$_3$): δ [ppm] = 8.73 (dd, $J$ = 8.5, 1.1 Hz, 1 H), 8.66 (dd, $J$ = 7.3, 1.1 Hz, 1 H), 8.62 (d, $J$ = 7.6 Hz, 1 H), 7.87 (d, $J$ = 7.6 Hz, 1 H), 7.79 (dd, $J$ = 8.5, 7.3 Hz, 1 H), 7.69−7.65 (m, 2 H), 7.61−7.57 (m, 2 H), 7.47 (d, $J$ = 3.7 Hz, 1 H), 7.34 (d, $J$ = 3.7 Hz, 1 H), 4.23−4.17 (m, 2 H), 1.81−1.71 (m, 2 H), 1.48−1.22 (m, 10 H), 0.90−0.85 (m, 3 H), 0.31 (s, 9 H).

## NMI-th-ph-I (7)



NMI-th-ph-TMS (**6**, 30.0 mg, 55.6 µmol, 1.00 eq.) was dissolved in dry DCM (2 mL) and cooled to −78 °C under N$_2$ atmosphere. Iodine monochloride (4 µL, 78.4 µmol, 1.41 eq.) in dry DCM (0.5 mL) was added dropwise and the mixture was stirred for 1 h before sat. aq. Na$_2$S$_2$O$_3$ solution (5 mL) was added. The mixture was allowed to warm to room temperature and the aqueous phase was extracted with DCM (3 × 10 mL). The combined organic phases were dried over anhydrous Na$_2$SO$_4$ and the solvent was removed under reduced pressure. The product was purified by chromatography on a silica gel column with 1:1 (v:v) $n$-pentane/DCM as an eluent. The product was obtained as a yellow solid (31.2 mg, 53.0 µmol, 95%). $^1$H NMR (400 MHz, CD$_2$Cl$_2$): δ [ppm] = 8.71 (dd, $J$ = 8.5, 1.0 Hz, 1 H), 8.63 (dd, $J$ = 7.3, 1.0 Hz, 1 H), 8.58 (d, $J$ = 7.6 Hz, 1 H), 7.87 (d, $J$ = 7.6 Hz, 1 H), 7.83−7.76 (m, 3 H), 7.49 (d, $J$ = 3.8 Hz, 1 H), 7.48−7.44 (m, 2 H), 7.37 (d, $J$ = 3.8 Hz, 1 H), 4.18−4.13 (m, 2 H), 1.77−1.67 (m, 2 H), 1.46−1.23 (m, 10 H), 0.91−0.85 (m, 3 H).

## NMI-th-DPNH (8)
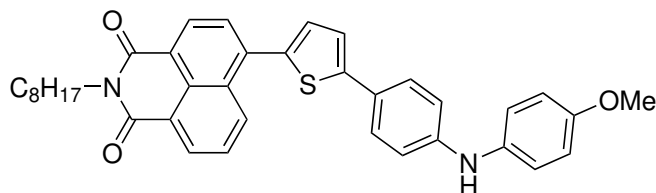


Dry and degassed toluene (3 mL) was added to a mixture of NMI-th-ph-I (**7**, 30.0 mg, 50.5 µmol, 1.00 eq.), $p$-anisidine (35.7 mg, 290 µmol, 5.74 eq.), Pd(dba)$_2$ (1.50 mg, 2.61 µmol, 0.05 eq.), tri-$tert$-butylphosphonium tetrafluoroborate (0.90 mg, 3.10 µmol, 0.06 eq.), and potassium $tert$-butoxide (16.8 mg, 150 µmol, 2.97 eq.) under N$_2$ atmos-
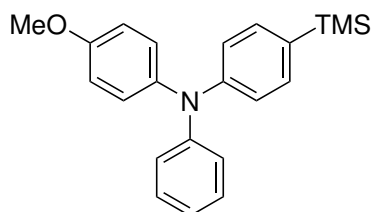
phere. The mixture was stirred at 90 °C for 19 h, cooled to room temperature and diluted with water (10 mL). The aqueous phase was extracted with DCM (3 × 10 mL) and the combined organic phases were dried over anhydrous $Na_2SO_4$. After removal of the solvents under reduced pressure, the product was purified by chromatography on a silica gel column with 3:1 (v:v) $n$-pentane/EtOAc as an eluent. The product was obtained as a red solid (17.0 mg, 28.9 μmol, 57%). $^1$H NMR (400 MHz, $CD_2Cl_2$): δ [ppm] = 8.77 (dd, $J$ = 8.5, 1.1 Hz, 1 H), 8.62 (dd, $J$ = 7.3, 1.1 Hz, 1 H), 8.57 (d, $J$ = 7.6 Hz, 1 H), 7.87 (d, $J$ = 7.6 Hz, 1 H), 7.79 (dd, $J$ = 8.5, 7.3 Hz, 1 H), 7.57−7.53 (m, 2 H), 7.34 (s, 2 H), 7.16−7.11 (m, 2 H), 6.97−6.93 (m, 2 H), 6.92−6.87 (m, 2 H), 5.78 (s, 1 H), 4.18−4.12 (m, 2 H), 3.80 (s, 3 H), 1.77−1.67 (m, 2 H), 1.47−1.24 (m, 10 H), 0.91−0.85 (m, 3 H).

## DPNH (9)
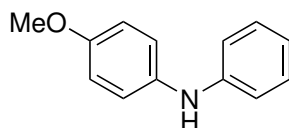


The following procedure was adapted from literature.[157] $p$-Anisidine (1.00 g, 8.10 mmol, 1.00 eq.), phenylboronic acid (1.19 g, 9.74 mmol, 1.20 eq.) and copper(II) acetate (1.77 g, 9.74 mmol, 1.20 eq.) were suspended in DCM (160 mL). After addition of $NEt_3$ (2.26 mL, 16.2 mmol, 2.00 eq.), the mixture was stirred at room temperature for 19 h. The solvent was removed under reduced pressure and the product was purified by chromatography on a silica gel column with DCM as an eluent. The product was obtained as a yellow solid (906 mg, 4.55 mmol, 56%). $^1$H NMR (400 MHz, $CD_2Cl_2$): δ [ppm] = 7.23−7.16 (m, 2 H), 7.10−7.04 (m, 2 H), 6.93−6.88 (m, 2 H), 6.88−6.83 (m, 2 H), 6.81 (tt, $J$ = 7.4, 1.0 Hz, 1 H), 5.59 (broad s, 1 H), 3.78 (s, 3 H).
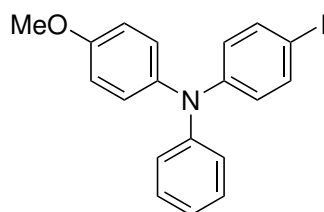
## (OMe)TAA-TMS (10)



A mixture of DPNH (**9**, 200 mg, 1.00 mmol, 1.00 eq.), TMS-ph-Br (**4**, 280 mg, 1.22 mmol, 1.22 eq.), $Pd(dba)_2$ (28.8 mg, 50.1 μmol, 0.05 eq.), tri-*tert*-butylphosphonium tetrafluoroborate (15.1 mg, 52.0 μmol, 0.05 eq.) and potassium *tert*-butoxide (341 mg, 3.04 mmol, 3.04 eq.) was suspended in dry and degassed toluene (5 mL) under $N_2$ atmosphere. The mixture was stirred at 100 °C for 17 h, cooled to room temperature and diluted with
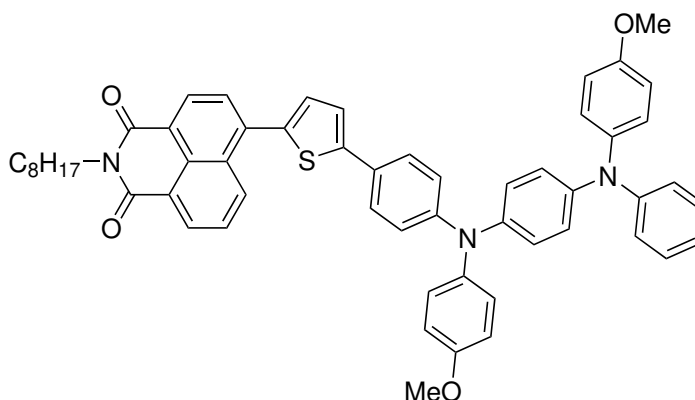
water (10 mL). The aqueous phase was extracted with DCM (3 × 15 mL), the combined organic phases were dried over anhydrous $Na_2SO_4$ and the solvents were removed under reduced pressure. The product was purified by chromatography on a silica gel column with 2:1 (v:v) $n$-pentane/DCM as an eluent. The product was obtained as a colorless oil (260 mg, 0.75 mmol, 75%). ^{1}H NMR (400 MHz, $CD_2Cl_2$): δ [ppm] = 7.36−7.32 (m, 2 H), 7.25−7.19 (m, 2 H), 7.08−7.00 (m, 4 H), 6.98−6.93 (m, 3 H), 6.88−6.83 (m, 2 H), 3.79 (s, 3 H), 0.23 (s, 9 H).

## (OMe)TAA-I (11)



(OMe)TAA-TMS (**10**, 53.6 mg, 154 μmol, 1.00 eq.) was dissolved in dry DCM (2 mL) and cooled to −78 °C under $N_2$ atmosphere. Iodine monochloride (20 μL, 392 μmol, 2.55 eq.) in dry DCM (0.5 mL) was added dropwise and the mixture was stirred for 1 h before sat. aq. $Na_2S_2O_3$ solution (5 mL) was added. The mixture was allowed to warm to room temperature and the aqueous phase was extracted with DCM (3 × 10 mL). The combined organic phases were dried over anhydrous $Na_2SO_4$ and the solvent was removed under reduced pressure. After purification of the product by chromatography on a silica gel column with 3:1 (v:v) $n$-pentane/DCM as an eluent, the product was obtained as a colorless oil (58.0 mg, 145 μmol, 94%). ^{1}H NMR (400 MHz, $CD_2Cl_2$): δ [ppm] = 7.50−7.44 (m, 2 H), 7.28−7.20 (m, 2 H), 7.08−6.97 (m, 5 H), 6.89−6.83 (m, 2 H), 6.79−6.73 (m, 2 H), 3.79 (s, 3 H).

## NMI-TPDB

NMI-th-DPNH (**8**, 15.0 mg, 25.0 µmol, 1.00 eq.), (OMe)TAA-I (**11**, 13.4 mg, 33.0 µmol, 1.32 eq.), Pd(dba)$_2$ (0.80 mg, 1.35 µmol, 0.05 eq.), tri-*tert*-butylphosphonium tetrafluoro-borate (0.50 mg, 1.72 µmol, 0.07 eq.) and potassium *tert*-butoxide (9.10 mg, 81.0 µmol, 3.24 eq.) were suspended in dry and degassed toluene (2 mL) under N$_2$ atmosphere. The mixture was stirred at 100 °C for 18 h, cooled to room temperature and diluted with water (5 mL). The aqueous phase was extracted with DCM (3 × 15 mL), the combined organic phases were dried over anhydrous Na$_2$SO$_4$ and the solvents were removed under reduced pressure. The product was purified by chromatography on a silica gel column with 4:1 (v:v) *n*-pentane/EtOAc as an eluent. The product was obtained as a red solid (10.1 mg, 12.0 µmol, 47%). $^1$H NMR (400 MHz, CD$_2$Cl$_2$): δ [ppm] = 8.66 (dd, $J$ = 8.5, 1.1 Hz, 1 H), 8.52 (dd, $J$ = 7.3, 1.1 Hz, 1 H), 8.46 (d, $J$ = 7.6 Hz, 1 H), 7.76 (d, $J$ = 7.6 Hz, 1 H), 7.68 (dd, $J$ = 8.5, 7.3 Hz, 1 H), 7.48−6.72 (m, 23 H), 4.09−4.03 (m, 2 H), 3.71 (s, 3 H), 3.70 (s, 3 H), 1.68−1.58 (m, 2 H), 1.39−1.16 (m, 10 H), 0.83−0.75 (m, 3 H). ESI-HRMS ($m/z$) calcd. for C$_{56}$H$_{51}$N$_3$O$_4$S, [M]$^+$: 861.3595; found: 861.3600. Anal. calcd. for C$_{56}$H$_{51}$N$_3$O$_4$S · H$_2$O: C, 76.42; H, 6.07; N, 4.77; found: C, 76.77; H, 6.31; N, 4.38.

## 7.3.2 Synthesis of the PT-TAA Reference

### PT (12)
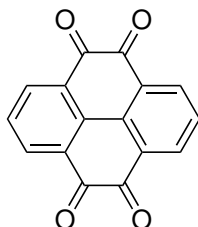


The following procedure was adapted from literature.[158] Pyrene (4.04 g, 20.0 mmol, 1.00 eq.) was dissolved in a mixture of DCM (80 mL) and $CH_3CN$ (80 mL). Then, $NaIO_4$ (35.0 g, 164 mmol, 8.20 eq.), water (100 mL) and $RuCl_3 \cdot x\ H_2O$ (500 mg, 2.40 mmol, 0.12 eq.) were added. The suspension was heated at 40 °C under $N_2$ atmosphere for 23 h and poured into water (600 mL). DCM (400 mL) was added and the organic phase was separated. The aqueous phase was extracted with DCM ($3 \times 300$ mL) and the combined organic phases were dried over anhydrous $Na_2SO_4$. After removal of the solvents under reduced pressure, the product was purified by gradient chromatography on a silica gel column with pure DCM to 9:1 (v:v) DCM/EtOAc as an eluent. The product was obtained as a brown solid (1.33 g, 5.07 mmol, 25%). $^1H$ NMR (400 MHz, DMSO-$d_6$): δ [ppm] = 8.33 (d, $J$ = 7.7 Hz, 4 H), 7.74 (t, $J$ = 7.7 Hz, 2 H).

### PT-I (13)
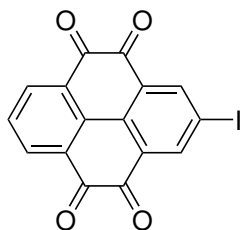


The following procedure was adapted from literature.[141] A mixture of PT (**12**, 200 mg, 0.76 mmol, 1.00 eq.) and $N$-iodosuccinimide (687 mg, 3.05 mmol, 4.02 eq.) in $H_2SO_4$ (3 mL) was stirred at 40 °C for 1 h and poured into water (100 mL). The resulting precipitate was collected by filtration and washed with water and ethanol. After purification of the product by chromatography on multiple silica gel columns with 9:1 (v:v) DCM/EtOAc as an eluent, the product was obtained as an orange solid (171 mg, 0.44 mmol, 58%). $^1H$ NMR (400 MHz, CDCl$_3$): δ [ppm] = 8.79 (s, 2 H), 8.51 (d, $J$ = 7.8 Hz, 2 H), 7.75 (t, $J$ = 7.8 Hz, 1 H).

## PT-th (14)
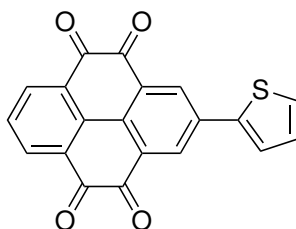


PT-I (**13**, 70.0 mg, 180 µmol, 1.00 eq.), thiophene-2-boronic acid pinacol ester (287 mg, 1.37 mmol, 7.59 eq.), $Na_2CO_3$ (172 mg, 1.62 mmol, 9.00 eq.) and $Pd(PPh_3)_4$ (32.6 mg, 28.2 µmol, 0.16 eq.) were suspended in a mixture of degassed toluene (5 mL), degassed water (2.5 mL) and degassed ethanol (1.25 mL) under $N_2$ atmosphere. The mixture was stirred at 90 °C for 22 h and then cooled to room temperature. The mixture was diluted with water (25 mL) and the aqueous phase was extracted with DCM (6 × 50 mL). The combined organic phases were dried over anhydrous $Na_2SO_4$ and the solvents were removed under reduced pressure. The product was purified by chromatography on a silica gel column with 30:1 (v:v) DCM/EtOAc as an eluent. The product was obtained as a red solid (42.1 mg, 122 µmol, 68%). $^1$H NMR (400 MHz, DMSO-$d_6$): δ [ppm] = 8.47 (s, 2 H), 8.33 (d, $J$ = 7.7 Hz, 2 H), 7.92 (dd, $J$ = 3.7, 1.0 Hz, 1 H), 7.77 (dd, $J$ = 5.0, 1.0 Hz, 1 H), 7.73 (t, $J$ = 7.7 Hz, 1 H), 7.26 (dd, $J$ = 5.0, 3.7 Hz, 1 H).

## PT-th-Br (15)
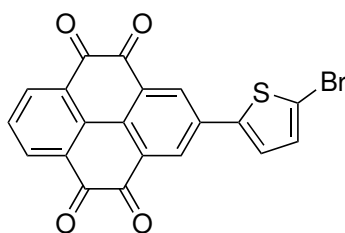


A mixture of PT-th (**14**, 20.0 mg, 58.0 µmol, 1.00 eq.) and *N*-bromosuccinimide (52.0 mg, 290 µmol, 5.00 eq.) in DMF (3 mL) was stirred at 65 °C for 17 h and then water was added. The precipitate was collected by filtration, washed with water and $Et_2O$ and dried under air. The product was obtained as a red solid (23.5 mg, 56.0 µmol, 97%). $^1$H NMR (400 MHz, DMSO-$d_6$): δ [ppm] = 8.40 (s, 2 H), 8.34 (d, $J$ = 7.7 Hz, 2 H), 7.80 (d, $J$ = 3.9 Hz, 1 H), 7.74 (t, $J$ = 7.7 Hz, 1 H), 7.39 (d, $J$ = 3.9 Hz, 1 H).

## PT-th-ph-TMS (16)
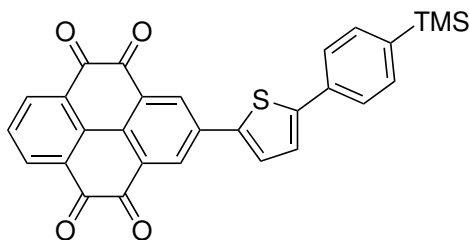


PT-th-Br (**15**, 24.7 mg, 58.4 μmol, 1.00 eq.), TMS-ph-B(OH)$_2$ (**5**, 56.6 mg, 292 μmol, 5.00 eq.), Na$_2$CO$_3$ (18.6 mg, 175 μmol, 3.00 eq.) and Pd(PPh$_3$)$_4$ (6.70 mg, 5.84 μmol, 0.10 eq.) were suspended in a mixture of degassed toluene (10 mL), degassed water (5 mL) and degassed ethanol (2.5 mL) under N$_2$ atmosphere. The mixture was stirred at 90 °C for 39 h and cooled to room temperature. Water (5 mL) was added and the aqueous phase was extracted with DCM (3 × 15 mL). The combined organic phases were dried over anhydrous Na$_2$SO$_4$ and the solvents were removed under reduced pressure. Purification of the product by chromatography on a silica gel column with 50:1 (v:v) DCM/EtOAc as an eluent yielded the product as a red solid (6.90 mg, 14.0 μmol, 24%). $^1$H NMR (400 MHz, CD$_2$Cl$_2$): δ [ppm] = 8.65 (s, 2 H), 8.46 (d, $J$ = 7.7 Hz, 2 H), 7.72−7.64 (m, 4 H), 7.63−7.58 (m, 2 H), 7.45 (d, $J$ = 3.9 Hz, 1 H), 0.31 (s, 9 H).

## PT-th-ph-I (17)
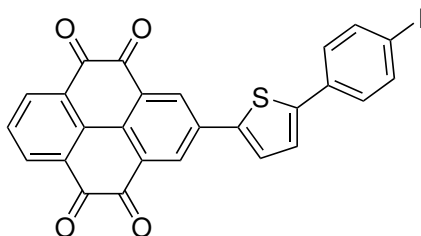


PT-th-ph-TMS (**16**, 12.6 mg, 25.6 μmol, 1.00 eq.) was dissolved in dry DCM (25 mL) under N$_2$ atmosphere. Iodine monochloride (0.1 M in dry DCM, 50.0 μL, 51.2 μmol, 2.00 eq.) was added dropwise and the mixture was stirred at room temperature for 3 h. The precipitate was collected by filtration and washed with DCM and Et$_2$O. The product was obtained as a red solid (11.2 mg, 20.5 μmol, 80%). $^1$H NMR (400 MHz, DMSO-$d_6$): δ [ppm] = 8.50 (s, 2 H), 8.34 (d, $J$ = 7.7 Hz, 2 H), 7.99−7.96 (m, 1 H), 7.84−7.80 (m, 2 H), 7.76−7.70 (m, 2 H), 7.63−7.59 (m, 2 H).

## (NO$_2$)DPNH (18)
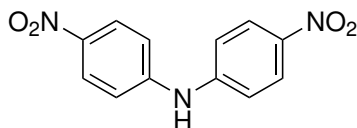


Following a published protocol,[159] dry DMSO (15 mL) was added to a mixture of *p*-nitrochlorobenzene (1.58 g, 10.0 mmol, 1.00 eq.), *p*-nitroaniline (3.45 g, 25.0 mmol, 2.50 eq.) and K$_2$CO$_3$ (5.52 mg, 39.9 mmol, 1.60 eq.) under N$_2$ atmosphere. The mixture was degassed for 10 min, stirred at 150 °C for 5 h and poured into cold water (200 mL). The precipitate was collected by filtration, washed with aq. HCl solution (12 M, 50 mL), water (500 mL) and Et$_2$O (20 mL). The residue was recrystallized from toluene and the product was obtained as an orange solid (869 mg, 3.35 mmol, 34%). $^1$H NMR (400 MHz, DMSO-$d_6$): δ [ppm] = 9.97 (s, 1 H), 8.23−8.18 (m, 4 H), 7.39−7.34 (m, 4 H).

### 7.3.3 Synthesis of the TPDB-PT Reference

### I-hxy-TMS (19)
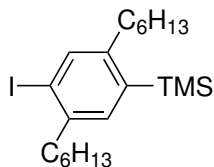


Following a published protocol,[160] I-hxy-I (5.00 g, 10.0 mmol, 1.00 eq.) was dissolved in dry $Et_2O$ (50 mL) under $N_2$ atmosphere. The mixture was cooled to 0 °C and $n$-BuLi (2.5 M in hexanes, 4.80 mL, 12.0 mmol, 1.20 eq.) was slowly added while cooling at 0 °C was maintained. The mixture was stirred at 0 °C for 1 h before chlorotrimethylsilane (1.60 mL, 12.6 mmol, 1.26 eq.) was added dropwise. The mixture was allowed to warm to room temperature and stirred overnight, water (50 mL) was added and the aqueous phase was extracted with DCM (3 × 50 mL). The combined organic phases were washed with $Na_2S_2O_3$ (50 mL) and dried over anhydrous $Na_2SO_4$. Removal of the solvents under reduced pressure gave a yellow oil (quant. yield) which was used without further purification in the next step.

### B(pin)-hxy-TMS (20)
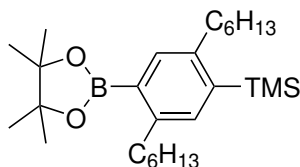


Dry and degassed DMSO (10 mL) was added to a mixture of I-hxy-TMS (**19**, 1.64 g, 3.69 mmol, 1.00 eq.), bis(pinacolato)diboron (1.41 g, 5.54 mmol, 1.50 eq.), KOAc (1.45 g, 14.8 mmol, 4.00 eq.) and $Pd(PPh_3)_2Cl_2$ (130 mg, 0.18 mmol, 0.05 eq.) under $N_2$ atmosphere. The mixture was stirred at 90 °C for 21 h, cooled to room temperature and filtered over celite. The residue was washed with $Et_2O$ (4 × 50 mL) before the combined organic filtrates were washed with water (3 × 30 mL). The combined aqueous phases were extracted with $Et_2O$ (3 × 50 mL) and the combined organic phases were then dried over anhydrous $Na_2SO_4$. After removal of the solvent under reduced pressure, the product was purified by chromatography on a silica gel column with 9:1 (v:v) $n$-pentane/DCM as an eluent. The product was obtained as a yellow oil (989 mg, 2.22 mmol, 60%). $^1$H NMR (400 MHz, $CDCl_3$): δ [ppm] = 7.57 (s, 1 H), 7.24 (s, 1 H), 2.84−2.78 (m, 2 H), 2.68−2.62 (m, 2 H), 1.64−1.26 (m, 28 H), 0.93−0.86 (m, 6 H), 0.31 (s, 9 H).

## Br-ph-hxy-TMS (21)
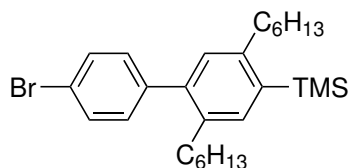


A mixture of B(pin)-hxy-TMS (**20**, 2.48 g, 5.58 mmol, 1.00 eq.), 1-bromo-4-iodobenzene (3.16 g, 11.2 mmol, 2.00 eq.) and $Na_2CO_3$ (1.77 g, 16.7 mmol, 3.00 eq.) was suspended in a mixture of THF (100 mL) and water (20 mL) under $N_2$ atmosphere. The mixture was degassed for 25 min and $Pd(PPh_3)_4$ (324 mg, 280 μmol, 0.05 eq.) was added. The mixture was degassed for additional 15 min and was then stirred at 85 °C for 41 h. Once the mixture had nearly reached room temperature, water (30 mL) was added and the aqueous phase was extracted with DCM (3 × 100 mL). The combined organic phases were dried over anhydrous $Na_2SO_4$ and the solvents were removed under reduced pressure. Purification of the product by chromatography on a silica gel column with *n*-pentane as an eluent gave the product as a colorless oil (1.64 g, 3.46 mmol, 62%). $^1H$ NMR (400 MHz, $CD_2Cl_2$): δ [ppm] = 7.47−7.43 (m, 2 H), 7.26 (s, 1 H), 7.13−7.08 (m, 2 H), 6.91 (s, 1 H), 2.63−2.57 (m, 2 H), 2.46−2.40 (m, 2 H), 1.54−1.45 (m, 2 H), 1.37−1.05 (m, 14 H), 0.83−0.78 (m, 3 H), 0.77−0.72 (m, 3 H), 0.26 (s, 9 H).

## PNHBoc (22)
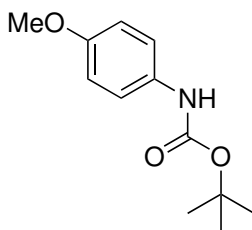


Following a published protocol,[161] *p*-anisidine (124 mg, 1.00 mmol, 1.00 eq.) and di-*tert*-butyl dicarbonate (219 mg, 1.00 mmol, 1.00 eq) were stirred in glycerol (2 mL) at room temperature for 25 min. Water (10 mL) was added and the mixture was extracted with 9:1 (v:v) petroleum ether/EtOAc (3 × 20 mL). The combined organic phases were dried over anhydrous $Na_2SO_4$ and the solvents were removed under reduced pressure. Chromatography on a silica gel column with DCM as an eluent yielded the product as a white solid (204 mg, 0.91 mmol, 91%). $^1H$ NMR (400 MHz, $CD_2Cl_2$): δ [ppm] = 7.29−7.22 (m, 2 H), 6.86−6.80 (m, 2 H), 6.41 (broad s, 1 H), 3.76 (s, 3 H), 1.49 (s, 9 H).

## DPNBoc-hxy-TMS (23)
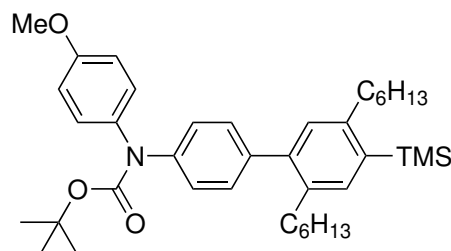


Br-ph-hxy-TMS (**21**, 1.11 g, 2.34 mmol, 1.00 eq.), PNHBoc (**22**, 784 mg, 3.51 mmol, 1.50 eq.), Pd(dba)$_2$ (132 mg, 230 µmol, 0.10 eq.), *S*-Phos (94.8 mg, 231 µmol, 0.10 eq.) and Cs$_2$CO$_3$ (2.29 g, 7.02 mmol, 3.00 eq.) were suspended in dry and degassed toluene (11.7 mL) under N$_2$ atmosphere. The mixture was stirred at 90 °C for 63 h, cooled to room temperature and diluted with water (20 mL). After extraction of the aqueous phase with DCM (3 × 50 mL), the combined organic phases were dried over anhydrous Na$_2$SO$_4$ and the solvents were removed under reduced pressure. The product was purified by chromatography on a silica gel column with DCM as an eluent and the product was obtained as a yellow solid (1.36 g, 2.21 mmol, 94%). $^1$H NMR (400 MHz, CD$_2$Cl$_2$): δ [ppm] = 7.33 (s, 1 H), 7.23 (s, 4 H), 7.20−7.15 (m, 2 H), 7.03 (s, 1 H), 6.90−6.85 (m, 2 H), 3.80 (s, 3 H), 2.71−2.65 (m, 2 H), 2.57−2.51 (m, 2 H), 1.64−1.53 (m, 2 H), 1.45 (s, 9 H), 1.43−1.15 (m, 14 H), 0.91−0.86 (m, 3 H), 0.85−0.81 (m, 3 H), 0.34 (s, 9 H).

## DPNBoc-hxy-I (24)
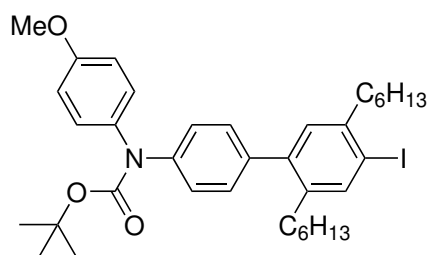


DPNBoc-hxy-TMS (**23**, 149 mg, 242 µmol, 1.00 eq.) was dissolved in dry DCM (7 mL) and cooled to −78 °C under N$_2$ atmosphere. Iodine monochloride (24.5 µL, 480 µmol, 2.00 eq.) in dry DCM (1.5 mL) was added dropwise and the mixture was stirred for 1 h before sat. aq. Na$_2$S$_2$O$_3$ solution (10 mL) was added. The mixture was allowed to warm to room temperature and the aqueous phase was extracted with DCM (3 × 15 mL). The combined organic phases were dried over anhydrous Na$_2$SO$_4$ and the solvent was removed under reduced pressure. The product was purified by chromatography on a silica gel column with DCM as an eluent. The product was obtained as a colorless oil (151 mg, 225 µmol, 93%). $^1$H NMR (400 MHz, CD$_2$Cl$_2$): δ [ppm] = 7.71 (s, 1 H), 7.26−7.14 (m,

6 H), 7.02 (s, 1 H), 6.90−6.85 (m, 2 H), 3.80 (s, 3 H), 2.70−2.64 (m, 2 H), 2.51−2.46 (m, 2 H), 1.62−1.55 (m, 2 H), 1.45 (s, 9 H), 1.43−1.14 (m, 14 H), 0.92−0.86 (m, 3 H), 0.86−0.80 (m, 3 H).

## DPNBoc-hxy-B(pin) (25)
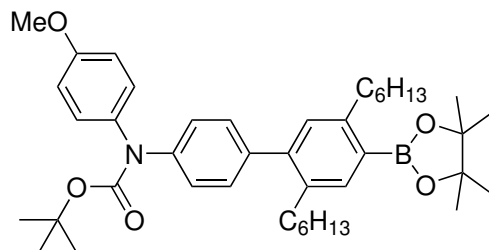


Dry and degassed DMSO (6 mL) was added to a mixture of DPNBoc-hxy-I (**24**, 271 mg, 405 mmol, 1.00 eq.), bis(pinacolato)diboron (154 mg, 606 µmol, 1.50 eq.), KOAc (157 mg, 1.60 mmol, 3.95 eq.) and Pd(PPh$_3$)$_2$Cl$_2$ (14.6 mg, 20.8 µmol, 0.05 eq.) under N$_2$ atmosphere. The mixture was stirred at 90 °C for 14 h and cooled to room temperature. Water (10 mL) was added and the aqueous phase was extracted with Et$_2$O (4 × 25 mL). The combined organic phases were dried over anhydrous Na$_2$SO$_4$. After removal of the solvent under reduced pressure, the product was purified by chromatography on a silica gel column with 9:1 (v:v) $n$-pentane/EtOAc as an eluent. The product was obtained as a white solid (248 mg, 370 µmol, 91%). $^1$H NMR (400 MHz, CD$_2$Cl$_2$): δ [ppm] = 7.61 (s, 1 H), 7.23 (s, 4 H), 7.20−7.15 (m, 2 H), 7.00 (s, 1 H), 6.90−6.85 (m, 2 H), 3.80 (s, 3 H), 2.86−2.80 (m, 2 H), 2.58−2.52 (m, 2 H), 1.58−1.14 (m, 37 H), 0.91−0.86 (m, 3 H), 0.85−0.81 (m, 3 H).

## DPNBoc-hxy-PT (26)
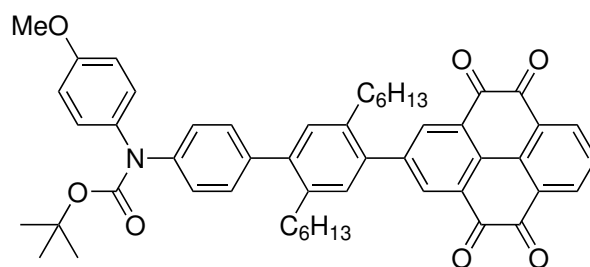


DPNBoc-hxy-B(pin) (**25**, 248 mg, 370 µmol, 1.00 eq.), PT-I (**13**, 172 mg, 443 µmol, 1.20 eq.), Na$_2$CO$_3$ (118 mg, 1.11 mmol, 3.00 eq.) and Pd(PPh$_3$)$_4$ (42.8 mg, 37.0 mmol, 0.10 eq.) were suspended in a mixture of degassed THF (30 mL) and degassed water (6 mL) under N$_2$ atmosphere. The mixture was stirred at 85 °C for 19 h, cooled to room temperature and filtered over celite. The residue was washed with DCM (3 × 20 mL) and water (10 mL) was added to the collected filtrate. The aqueous phase was then extracted

with DCM (3 × 25 mL). The combined organic phases were dried over anhydrous $Na_2SO_4$ and the solvents were removed under reduced pressure. The product was purified by chromatography on a silica gel column with 20:1 (v:v) DCM/EtOAc as an eluent and the titel compound was obtained as a red solid (200 mg, 249 µmol, 67%). $^1$H NMR (400 MHz, $CD_2Cl_2$): δ [ppm] = 8.48 (d, $J$ = 7.8 Hz, 2 H), 8.46 (s, 2 H), 7.72 (t, $J$ = 7.8 Hz, 1 H), 7.30 (s, 4 H), 7.22−7.17 (m, 4 H), 6.92−6.87 (m, 2 H), 3.81 (s, 3 H), 2.66−2.57 (m, 4 H), 1.56−1.48 (m, 2 H), 1.47 (s, 9 H), 1.28−1.13 (m, 14 H), 0.85−0.76 (m, 6 H).
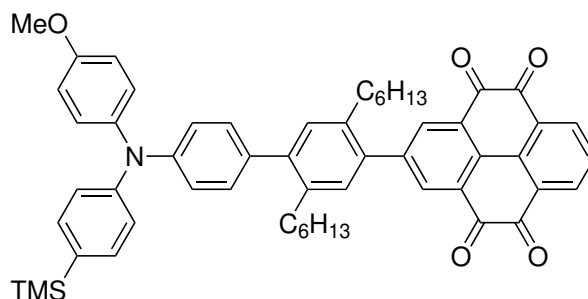
## DPNH-hxy-PT (27)
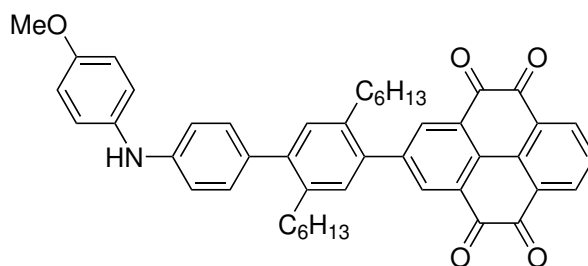


DPNBoc-hxy-PT (**26**, 200 mg, 249 µmol, 1.00 eq.) was dissolved in dry DCM (8.3 mL) under $N_2$ atmosphere. TFA (0.95 mL, 12.4 mmol, 50.0 eq.) was added and the mixture was stirred at room temperature for 3 h. After removal of the solvents under reduced pressure, the product was purified by chromatography on a silica gel column with 2:1 (v:v) $n$-pentane/EtOAc as an eluent. The product was obtained as a green solid (138 mg, 196 µmol, 79%). $^1$H NMR (400 MHz, $CD_2Cl_2$): δ [ppm] = 8.49 (d, $J$ = 7.8 Hz, 2 H), 8.46 (s, 2 H), 7.73 (t, $J$ = 7.8 Hz, 1 H), 7.23−7.17 (m, 4 H), 7.16−7.11 (m, 2 H), 7.01−6.96 (m, 2 H), 6.91−6.86 (m, 2 H), 5.70 (broad s, 1 H), 3.80 (s, 3 H), 2.67−2.57 (m, 4 H), 1.57−1.15 (m, 16 H), 0.86−0.76 (m, 6 H).
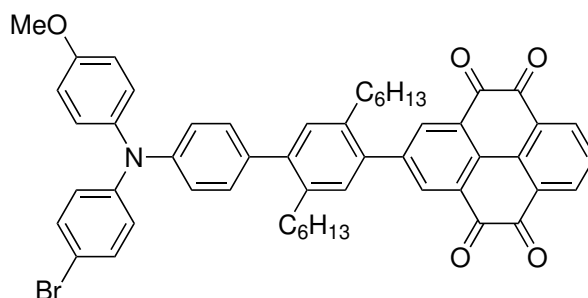
## (OMe)(TMS)TAA-hxy-PT (28)



Dry and degassed 1,4-dioxane (0.3 mL) was added to a mixture of DPNH-hxy-PT (**27**, 30.0 mg, 42.6 µmol, 1.00 eq.), TMS-ph-Br (**4**, 96.6 mg, 422 µmol, 9.89 eq.), Pd(dba)$_2$ (2.45 mg, 4.30 µmol, 0.10 eq.), tri-*tert*-butylphosphonium tetrafluoroborate (1.85 mg,

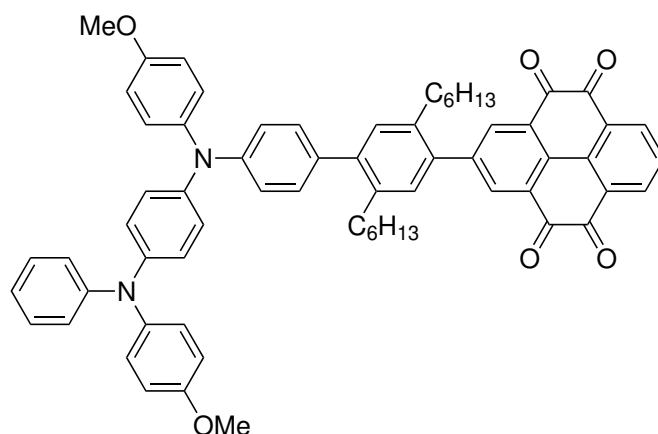6.40 µmol, 0.15 eq.) and sodium *tert*-butoxide (12.3 mg, 128 µmol, 3.00 eq.) under $N_2$ atmosphere. The mixture was stirred at 95 °C for 47 h, cooled to room temperature and diluted with water (5 mL). Then, the aqueous phase was extracted with DCM (3 × 15 mL) and the combined organic phases were dried over anhydrous $Na_2SO_4$. After removal of the solvents under reduced pressure, the product was purified by chromatography on a silica gel column with 3:1 (v:v) *n*-pentane/EtOAc as an eluent. The product was obtained as a brown solid (13.0 mg, 15.0 µmol, 36%). $^1$H NMR (400 MHz, $CD_2Cl_2$): δ [ppm] = 8.49 (d, $J$ = 7.8 Hz, 2 H), 8.47 (s, 2 H), 7.73 (t, $J$ = 7.8 Hz, 1 H), 7.42−7.37 (m, 2 H), 7.25−7.21 (m, 3 H), 7.19 (s, 1 H), 7.16−7.08 (m, 4 H), 7.07−7.03 (m, 2 H), 6.92−6.87 (m, 2 H), 3.81 (s, 3 H), 2.69−2.63 (m, 2 H), 2.63−2.57 (m, 2 H), 1.58−1.15 (m, 16 H), 0.88 −0.83 (m, 3 H), 0.82−0.77 (m, 3 H), 0.26 (s, 9 H).

## (OMe)(Br)TAA-hxy-PT (29)



(OMe)(TMS)TAA-hxy-PT (**28**, 40.8 mg, 47.9 µmol, 1.00 eq.) and NaOAc (7.90 mg, 96.3 µmol, 2.01 eq.) were suspended in dry THF (2 mL) under $N_2$ atmosphere. The mixture was cooled to 0 °C and protected from light. $Br_2$ (4.90 µL, 95.8 µmol, 2.00 eq.) in dry THF (0.5 mL) was added dropwise while cooling at 0 °C was maintained. The mixture was stirred at 0 °C for 10 min and was then allowed to warm to room temperature while stirring for another 3 h. Then, $NEt_3$ (30.0 µL, 215 µmol, 4.49 eq.) and sat. aq. $Na_2S_2O_3$ solution (5 mL) were added and the phases were separated. The aqueous phase was extracted with DCM (3 × 10 mL) and the combined organic phases were dried over anhydrous $Na_2SO_4$. After removal of the solvents under reduced pressure, the product was purified by chromatography on a silica gel column with 3:1 (v:v) *n*-pentane/EtOAc as an eluent. The product was obtained as a brown solid (35.9 mg, 41.8 µmol, 87%). $^1$H NMR (400 MHz, $CD_2Cl_2$): δ [ppm] = 8.49 (d, $J$ = 7.8 Hz, 2 H), 8.46 (s, 2 H), 7.73 (t, $J$ = 7.8 Hz, 1 H), 7.35−7.31 (m, 2 H), 7.26−7.21 (m, 3 H), 7.19 (s, 1 H), 7.15−7.07 (m, 4 H), 6.98−6.94 (m, 2 H), 6.92−6.87 (m, 2 H), 3.81 (s, 3 H), 2.69−2.63 (m, 2 H), 2.63−2.58 (m, 2 H), 1.58−1.15 (m, 16 H), 0.88−0.82 (m, 3 H), 0.82−0.77 (m, 3 H).

## TPDB-PT



(OMe)(Br)TAA-hxy-PT (**29**, 14.3 mg, 16.7 µmol, 1.00 eq.), DPNH (**9**, 5.00 mg, 25.1 µmol, 1.50 eq.), Pd(dba)$_2$ (1.00 mg, 1.73 µmol, 0.10 eq.), tri-*tert*-butylphosphonium tetrafluoroborate (0.70 mg, 2.41 µmol, 0.14 eq.) and sodium *tert*-butoxide (4.80 mg, 50.0 µmol, 3.00 eq.) were suspended in dry and degassed toluene (0.3 mL) under N$_2$ atmosphere. The mixture was stirred at 90 °C for 44 h, cooled to room temperature and diluted with water (5 mL). The aqueous phase was extracted with DCM (3 × 15 mL), the combined organic phases were dried over anhydrous Na$_2$SO$_4$ and the solvents were removed under reduced pressure. The product was purified by chromatography on a silica gel column with 3:1 (v:v) *n*-pentane/EtOAc as an eluent. The product was obtained as a brown solid (4.60 mg, 4.70 µmol, 28%). $^1$H NMR (400 MHz, CD$_2$Cl$_2$): δ [ppm] = 8.49 (d, $J$ = 7.8 Hz, 2 H), 8.46 (s, 2 H), 7.73 (t, $J$ = 7.8 Hz, 1 H), 7.27−6.83 (m, 23 H), 3.81 (s, 3 H), 3.79 (s, 3 H), 2.68−2.63 (m, 2 H), 2.62−2.57 (m, 2 H), 1.56−1.13 (m, 16 H), 0.86−0.75 (m, 6 H). ESI-HRMS (*m/z*) calcd. for C$_{66}$H$_{60}$N$_2$O$_6$, [M]$^+$: 976.4446; found: 976.4441. Anal. calcd. for C$_{66}$H$_{60}$N$_2$O$_6$ · 3H$_2$O: C, 76.87; H, 6.45; N, 2.72; found: C, 77.03; H, 6.32; N, 2.34.

# 8 Appendix

## Estimated Energies of the Individual States of the Triads

The energies ($E$) of the individual states presented in Figure S10 in the supporting information of Chapter 3 were estimated using the following equation:

$$E = e \cdot (E_{Ox}{}^0 \text{ - } E_{Red}{}^0)$$

$E_{Ox}{}^0$ and $E_{Red}{}^0$ represent the oxidation and reduction potential, respectively, for the involved electron-transfer step. For calculations, experimental potentials presented in Tables S2 and S3 of the supporting information were used. For the final charge-separated states TAA$^{\cdot+}$-bpy/Ru$^{II}$-NDI$^{\cdot-}$ and TPA$^{\cdot+}$-bpy/Ir$^{III}$-AQ$^{\cdot-}$, calculations can be found on page S38 of the supporting information.

The values of the lowest $^3$MLCT excited state of [Ru(bpy)$_3$]$^{2+}$ (2.12 eV) was taken from the literature,[32] whilst the value for the iridium sensitizer was determined experimentally to 2.61 eV. The ground-states of the triads, prior to excitation, were set to 0.00 eV.

### Estimations of the Individual States in TAA-ph$_1$-Ru-ph$_1$-NDI

- TAA$^{\cdot+}$-bpy$^{\cdot-}$/Ru$^{II}$-NDI
  $E = e \cdot (E^0(\text{TAA}^{+/0}) \text{ - } E^0(\text{bpy}^{0/-})) = e \cdot (0.69 \text{ V - (-1.33 V)}) = 2.02 \text{ eV}$
- TAA-bpy/Ru$^{III}$-NDI$^{\cdot-}$
  $E = e \cdot (E^0(\text{Ru}^{III/II}) \text{ - } E^0(\text{NDI}^{0/-})) = e \cdot (1.31 \text{ V - (-0.56 V)}) = 1.87 \text{ eV}$

### Estimations of the Individual States in TAA-ph$_2$-Ru-ph$_2$-NDI

- TAA$^{\cdot+}$-bpy$^{\cdot-}$/Ru$^{II}$-NDI
  $E = e \cdot (E^0(\text{TAA}^{+/0}) \text{ - } E^0(\text{bpy}^{0/-})) = e \cdot (0.64 \text{ V - (-1.30 V)}) = 1.94 \text{ eV}$
- TAA-bpy/Ru$^{III}$-NDI$^{\cdot-}$
  $E = e \cdot (E^0(\text{Ru}^{III/II}) \text{ - } E^0(\text{NDI}^{0/-})) = e \cdot (1.30 \text{ V - (-0.58 V)}) = 1.88 \text{ eV}$

### Estimations of the Individual States in TPA-ph$_1$-Ir-ph$_1$-AQ

- TPA-bpy/Ir$^{IV}$-AQ$^{\cdot-}$
  $E = e \cdot (E^0(\text{Ir}^{IV/III}) - E^0(\text{AQ}^{0/-})) = e \cdot (1.78 \text{ V} - (-0.86 \text{ V})) = 2.64 \text{ eV}$
- TPA$^{\cdot+}$-bpy$^{\cdot-}$/Ir$^{III}$-AQ
  $E = e \cdot (E^0(\text{TPA}^{+/0}) - E^0(\text{bpy}^{0/-})) = e \cdot (1.11 \text{ V} - (-1.19 \text{ V})) = 2.30 \text{ eV}$

### Estimations of the Individual States in TPA-ph$_2$-Ir-ph$_2$-AQ

- TPA-bpy/Ir$^{IV}$-AQ$^{\cdot-}$
  $E = e \cdot (E^0(\text{Ir}^{IV/III}) - E^0(\text{AQ}^{0/-})) = e \cdot (1.75 \text{ V} - (-0.89 \text{ V})) = 2.64 \text{ eV}$
- TPA$^{\cdot+}$-bpy$^{\cdot-}$/Ir$^{III}$-AQ
  $E = e \cdot (E^0(\text{TPA}^{+/0}) - E^0(\text{bpy}^{0/-})) = e \cdot (1.06 \text{ V} - (-1.19 \text{ V})) = 2.25 \text{ eV}$

# Estimated Energies of the Different Species Involved in the Tetrad and Dyads

The driving forces $(-\Delta G_{\text{CR}}{}^0)$ for thermal charge recombination presented in Chapter 5 were estimated using the following equation:

$$-\Delta G_{\text{CR}}{}^0 = -e \cdot (E_{\text{Red}}{}^0 - E_{\text{Ox}}{}^0)$$

$E_{\text{Red}}{}^0$ and $E_{\text{Ox}}{}^0$ represent the reduction and oxidation potential, respectively, for the involved electron-transfer step. Potentials for the theoretical calculations regarding the NMI-TPDB-PT-TAA tetrad were taken from the literature (see Table 5.1).[138–142] For calculations concerning the reference dyads NMI-TPDB and TPDB-PT, experimental potentials presented in Tables 5.3 and 5.5 were used. The driving force for thermal charge recombination equals the energy of the CSS.

### Theoretical Estimations of the Isolated States of the Tetrad

- NMI$^{\cdot-}$-TPDB$^{\cdot+}$-PT-TAA
  $-\Delta G_{\text{CR}}{}^0 = -e \cdot (E^0(\text{NMI}^{0/-}) - E^0(\text{TPDB}^{+/0})) = -e \cdot (-1.40 \text{ V} - 0.40 \text{ V}) = 1.80 \text{ eV}$
- NMI-TPDB-PT$^{\cdot-}$-TAA$^{\cdot+}$
  $-\Delta G_{\text{CR}}{}^0 = -e \cdot (E^0(\text{PT}^{0/-}) - E^0(\text{TAA}^{+/0})) = -e \cdot (-0.41 \text{ V} - 1.35 \text{ V}) = 1.76 \text{ eV}$
- NMI-TPDB$^{\cdot+}$-PT$^{\cdot-}$-TAA
  $-\Delta G_{\text{CR}}{}^0 = -e \cdot (E^0(\text{PT}^{0/-}) - E^0(\text{TPDB}^{+/0})) = -e \cdot (-0.41 \text{ V} - 0.40 \text{ V}) = 0.81 \text{ eV}$

- NMI$^{\cdot-}$-TPDB-PT-TAA$^{\cdot+}$
  $-\Delta G_{\mathrm{CR}}{}^0 = -e \cdot (E^0(\mathrm{NMI}^{0/-}) - E^0(\mathrm{TAA}^{+/0})) = -e \cdot (-1.40\text{ V} - 1.35\text{ V}) = 2.75$ eV

## Estimations for the NMI-TPDB Dyad in Different Solvents

- NMI$^{\cdot-}$-TPDB$^{\cdot+}$ (THF)
  $-\Delta G_{\mathrm{CR}}{}^0 = -e \cdot (E^0(\mathrm{NMI}^{0/-}) - E^0(\mathrm{TPDB}^{+/0})) = -e \cdot (-1.21\text{ V} - 0.64\text{ V}) = 1.85$ eV
- NMI$^{\cdot-}$-TPDB$^{\cdot+}$(DCM)
  $-\Delta G_{\mathrm{CR}}{}^0 = -e \cdot (E^0(\mathrm{NMI}^{0/-}) - E^0(\mathrm{TPDB}^{+/0})) = -e \cdot (-1.29\text{ V} - 0.47\text{ V}) = 1.76$ eV
- NMI$^{\cdot-}$-TPDB$^{\cdot+}$(benzonitrile)
  $-\Delta G_{\mathrm{CR}}{}^0 = -e \cdot (E^0(\mathrm{NMI}^{0/-}) - E^0(\mathrm{TPDB}^{+/0})) = -e \cdot (-1.26\text{ V} - 0.50\text{ V}) = 1.76$ eV

## Estimations for the TPDB-PT Dyad in Different Solvents

- TPDB$^{\cdot+}$-PT$^{\cdot-}$ (THF)
  $-\Delta G_{\mathrm{CR}}{}^0 = -e \cdot (E^0(\mathrm{PT}^{0/-}) - E^0(\mathrm{TPDB}^{+/0})) = -e \cdot (-0.38\text{ V} - 0.63\text{ V}) = 1.01$ eV
- TPDB$^{\cdot+}$-PT$^{\cdot-}$ (DCM)
  $-\Delta G_{\mathrm{CR}}{}^0 = -e \cdot (E^0(\mathrm{PT}^{0/-}) - E^0(\mathrm{TPDB}^{+/0})) = -e \cdot (-0.37\text{ V} - 0.44\text{ V}) = 0.81$ eV
- TPDB$^{\cdot+}$-PT$^{\cdot-}$ (benzonitrile)
  $-\Delta G_{\mathrm{CR}}{}^0 = -e \cdot (E^0(\mathrm{PT}^{0/-}) - E^0(\mathrm{TPDB}^{+/0})) = -e \cdot (-0.41\text{ V} - 0.49\text{ V}) = 0.90$ eV

# Bibliography

[1] International Energy Agengy, *Key World Energy Statistics*; 2018.

[2] Steinmann, Z. J. N.; Schipper, A. M.; Hauck, M.; Giljum, S.; Wernet, G.; Huijbregts, M. A. J. *Environ. Sci. Technol.* **2017**, *51*, 6360–6366.

[3] Al-Ghussain, L. *Environ. Prog. Sustain. Energy* **2019**, *38*, 13–21.

[4] Balzani, V.; Credi, A.; Venturi, M. *ChemSusChem* **2008**, *1*, 26–58.

[5] Gust, D.; Moore, T. A.; Moore, A. L. *Acc. Chem. Res.* **2009**, *42*, 1890–1898.

[6] Derks, A.; Schaven, K.; Bruce, D. *Biochim. Biophys. Acta - Bioenerg.* **2015**, *1847*, 468–485.

[7] Whang, D. R.; Apaydin, D. H. *ChemPhotoChem* **2018**, *2*, 148–160.

[8] Beyer, I.; Bickel, H.; Gropengießer, H.; Kluge, S.; Knauer, B.; Kronberg, I.; Krull, H.-P.; Lichtner, H.-D.; Schneeweiß, H.; Ströhla, G.; Tischer, W. *Natura Biologie für Gymnasien*; Klett Schulbuchverlag: Stuttgart, 2005.

[9] Barber, J. *Chem. Soc. Rev.* **2009**, *38*, 185–196.

[10] Bar-Even, A. *Plant Sci.* **2018**, *273*, 71–83.

[11] Pettersson, G.; Ryde-Pettersson, U. *Eur. J. Biochem.* **1988**, *175*, 661–672.

[12] McConnell, I.; Li, G.; Brudvig, G. W. *Chem. Biol.* **2010**, *17*, 434–447.

[13] Tachibana, Y.; Vayssieres, L.; Durrant, J. R. *Nat. Photonics* **2012**, *6*, 511–518.

[14] Ferreira, K. N.; Iverson, T. M.; Maghlaoui, K.; Barber, J.; Iwata, S. *Science* **2004**, *303*, 1831–1838.

[15] Umena, Y.; Kawakami, K.; Shen, J.-R.; Kamiya, N. *Nature* **2011**, *473*, 55–61.

[16] Kok, B.; Forbush, B.; McGloin, M. *Photochem. Photobiol.* **1970**, *11*, 457–475.

[17] Dau, H.; Haumann, M. *Biochim. Biophys. Acta - Bioenerg.* **2007**, *1767*, 472–483.

[18] Haumann, M.; Liebisch, P.; Müller, C.; Barra, M.; Grabolle, M.; Dau, H. *Science* **2005**, *310*, 1019–1021.

[19] Atkins, P. W.; de Paula, J. *Physikalische Chemie*; WILEY-VHC: Weinheim, 2006.

[20] Gade, L. H. *Koordinationschemie*; WILEY-VHC: Weinheim, 1998.

[21] Seybold, P. G.; Kier, L. B.; Cheng, C.-K. *J. Phys. Chem. A* **1998**, *102*, 886–891.

[22] Ma, H.; Peng, Q.; An, Z.; Huang, W.; Shuai, Z. *J. Am. Chem. Soc.* **2019**, *141*, 1010–1015.

[23] Kavarnos, G. J.; Turro, N. J. *Chem. Rev.* **1986**, *86*, 401–449.

[24] Ma, Y.; Zhang, H.; Shen, J.; Che, C. *Synth. Met.* **1998**, *94*, 245–248.

[25] Calcaterra, L. T.; Schuster, D. I. *J. Am. Chem. Soc.* **1981**, *103*, 2460–2461.

[26] Miskoski, S.; Soltermann, A. T.; Molina, P. G.; Günther, G.; Zanocco, A. L.; Garcia, N. A. *Photochem. Photobiol.* **2005**, *81*, 325–332.

[27] Kasha, M. *Discuss. Faraday Soc.* **1950**, *9*, 14–19.

[28] Prier, C. K.; Rankic, D. A.; MacMillan, D. W. C. *Chem. Rev.* **2013**, *113*, 5322–5363.

[29] Tang, K.-C.; Liu, K. L.; Chen, I.-C. *Chem. Phys. Lett.* **2004**, *386*, 437–441.

[30] Ward, M. D. *Chem. Soc. Rev.* **1997**, *26*, 365–375.

[31] Hanss, D.; Freys, J. C.; Bernardinelli, G.; Wenger, O. S. *Eur. J. Inorg. Chem.* **2009**, 4850–4859.

[32] Roundhill, D. M. *Photochemistry and Photophysics of Metal Complexes*; Plenum Press: New York, 1994.

[33] Marcus, R. A.; Sutin, N. *Biochim. Biophys. Acta* **1985**, *811*, 265–322.

[34] Marcus, R. A. *J. Chem. Phys.* **1956**, *24*, 966–978.

[35] Marcus, R. A. *J. Chem. Phys.* **1956**, *24*, 979–989.

[36] Marcus, R. A. *J. Chem. Phys.* **1957**, *26*, 867–871.

[37] Marcus, R. A. *J. Chem. Phys.* **1957**, *26*, 872–877.

[38] Hush, N. S. *Trans. Faraday Soc.* **1961**, *57*, 557–580.

[39] Hush, N. S. *Prog. Inorg. Chem.* **1967**, *8*, 391–444.

[40] Kuss-Petermann, M.; Wenger, O. S. *Phys. Chem. Chem. Phys.* **2016**, *18*, 18657–18664.

[41] Marcus, R. A. *Discuss. Faraday Soc.* **1960**, *29*, 21–31.

[42] Sutin, N. *Prog. Inorg. Chem.* **1983**, *30*, 441–498.

[43] Barbara, P. F.; Meyer, T. J.; Ratner, M. A. *J. Phys. Chem.* **1996**, *100*, 13148–13168.

[44] Kuss-Petermann, M.; Wenger, O. S. *Chimia* **2016**, *70*, 177–181.

[45] McConnell, H. M. *J. Chem. Phys.* **1961**, *35*, 508–515.

[46] Edwards, P. P.; Gray, H. B.; Lodge, M. T. J.; Williams, R. J. P. *Angew. Chem. Int. Ed.* **2008**, *47*, 6758–6765.

[47] Wiberg, J.; Guo, L.; Pettersson, K.; Nilsson, D.; Ljungdahl, T.; Mårtensson, J.; Albinsson, B. *J. Am. Chem. Soc.* **2007**, *129*, 155–163.

[48] Goez, M.; Zubarev, V.; Eckert, G. *J. Am. Chem. Soc.* **1998**, *120*, 5347–5348.

[49] Lambert, C. R.; Kochevar, I. E.; Redmond, R. W. *J. Phys. Chem. B* **1999**, *103*, 3737–3741.

[50] Scaiano, J. C.; Johnston, L. J.; McGimpsey, W. G.; Weir, D. *Acc. Chem. Res.* **1988**, *21*, 22–29.

[51] Fujitsuka, M.; Kim, S. S.; Lu, C.; Tojo, S.; Majima, T. *J. Phys. Chem. B* **2015**, *119*, 7275–7282.

[52] Debreczeny, M. P.; Svec, W. A.; Marsh, E. M.; Wasielewski, M. R. *J. Am. Chem. Soc.* **1996**, *118*, 8174–8175.

[53] Favereau, L.; Makhal, A.; Pellegrin, Y.; Blart, E.; Petersson, J.; Göransson, E.; Hammarström, L.; Odobel, F. *J. Am. Chem. Soc.* **2016**, *138*, 3752–3760.

[54] Cai, X.; Sakamoto, M.; Hara, M.; Sugimoto, A.; Tojo, S.; Kawai, K.; Endo, M.; Fujitsuka, M.; Majima, T. *Photochem. Photobiol. Sci.* **2003**, *2*, 1209–1214.

[55] Tran, T.-T.; Ha-Thi, M.-H.; Pino, T.; Quaranta, A.; Lefumeux, C.; Leibl, W.; Aukauloo, A. *J. Phys. Chem. Lett.* **2018**, *9*, 1086–1091.

[56] Sakamoto, M.; Cai, X.; Hara, M.; Fujitsuka, M.; Majima, T. *J. Am. Chem. Soc.* **2004**, *126*, 9709–9714.

[57] Sakamoto, M.; Cai, X.; Fujitsuka, M.; Majima, T. *J. Phys. Chem. A* **2006**, *110*, 11800–11808.

[58] Pagès, S.; Lang, B.; Vauthey, E. *J. Phys. Chem. A* **2006**, *110*, 7547–7553.

[59] Redmond, R. W.; Scaiano, J. C.; Johnston, L. J. *J. Am. Chem. Soc.* **1990**, *112*, 398–402.

[60] Johnston, L. J.; Lougnot, D. J.; Wintgens, V.; Scaiano, J. C. *J. Am. Chem. Soc.* **1988**, *110*, 518–524.

[61] Faria, J. L.; Steenken, S. *J. Am. Chem. Soc.* **1990**, *112*, 1277–1279.

[62] Kerzig, C.; Goez, M. *Chem. Sci.* **2016**, *7*, 3862–3868.

[63] Kerzig, C.; Guo, X.; Wenger, O. S. *J. Am. Chem. Soc.* **2019**, *141*, 2122–2127.

[64] Goez, M.; Kerzig, C. *Angew. Chem. Int. Ed.* **2012**, *51*, 12606–12608.

[65] Yamaji, M.; Cai, X.; Sakamoto, M.; Fujitsuka, M.; Majima, T. *J. Phys. Chem. A* **2009**, *113*, 1696–1703.

[66] Goez, M.; Kerzig, C.; Naumann, R. *Angew. Chem. Int. Ed.* **2014**, *53*, 9914–9916.

[67] Andersson, M.; Sinks, L. E.; Hayes, R. T.; Zhao, Y.; Wasielewski, M. R. *Angew. Chem. Int. Ed.* **2003**, *42*, 3139–3143.

[68] Kuss-Petermann, M.; Wenger, O. S. *Helv. Chim. Acta* **2017**, *100*, e1600283.

[69] Ha-Thi, M.-H.; Pham, V.-T.; Pino, T.; Maslova, V.; Quaranta, A.; Lefumeux, C.; Leibl, W.; Aukauloo, A. *Photochem. Photobiol. Sci.* **2018**, *17*, 903–909.

[70] Oseki, Y.; Fujitsuka, M.; Sakamoto, M.; Majima, T. *J. Phys. Chem. A* **2007**, *111*, 9781–9788.

[71] Hayes, R. T.; Walsh, C. J.; Wasielewski, M. R. *J. Phys. Chem. A* **2004**, *108*, 3253–3260.

[72] Orazietti, M.; Kuss-Petermann, M.; Hamm, P.; Wenger, O. S. *Angew. Chem. Int. Ed.* **2016**, *55*, 9407–9410.

[73] Fujita, M.; Ishida, A.; Majima, T.; Takamuku, S. *J. Phys. Chem.* **1996**, *100*, 5382–5387.

[74] Majima, T.; Fukui, M.; Ishida, A.; Takamuku, S. *J. Phys. Chem.* **1996**, *100*, 8913–8919.

[75] Gosztola, D.; Niemczyk, M. P.; Svec, W.; Lukas, A. S.; Wasielewski, M. R. *J. Phys. Chem. A* **2000**, *104*, 6545–6551.

[76] Beckwith, J. S.; Lang, B.; Grilj, J.; Vauthey, E. *J. Phys. Chem. Lett.* **2019**, *10*, 3688–3693.

[77] Gray, H. B.; Winkler, J. R. *J. Electroanal. Chem.* **1997**, *438*, 43–47.

[78] Antolovich, M.; Keyte, P. J.; Oliver, A. M.; Paddon-Row, M. N.; Kroon, J.; Verhoeven, J. W.; Jonker, S. A.; Warman, J. M. *J. Phys. Chem.* **1991**, *95*, 1933–1941.

[79] Pannwitz, A.; Wenger, O. S. *J. Am. Chem. Soc.* **2017**, *139*, 13308–13311.

[80] Cordes, M.; Giese, B. *Chem. Soc. Rev.* **2009**, *38*, 892–901.

[81] Montes, V. A.; Pérez-Bolívar, C.; Agarwal, N.; Shinar, J.; Anzenbacher Jr., P. *J. Am. Chem. Soc.* **2006**, *128*, 12436–12438.

[82] Hanss, D.; Wenger, O. S. *Inorg. Chem.* **2009**, *48*, 671–680.

[83] Welter, S.; Lafolet, F.; Cecchetto, E.; Vergeer, F.; De Cola, L. *ChemPhysChem* **2005**, *6*, 2417–2427.

[84] Tachiya, M.; Murata, S. *J. Phys. Chem.* **1992**, *96*, 8441–8444.

[85] Brunschwig, B. S.; Ehrenson, S.; Sutin, N. *J. Am. Chem. Soc.* **1984**, *106*, 6858–6859.

[86] Wasielewski, M. R.; Niemczyk, M. P.; Svec, W. A.; Pewitt, E. B. *J. Am. Chem. Soc.* **1985**, *107*, 1080–1082.

[87] Closs, G. L.; Miller, J. R. *Science* **1988**, *240*, 440–447.

[88] Fox, L. S.; Kozik, M.; Winkler, J. R.; Gray, H. B. *Science* **1990**, *247*, 1069–1071.

[89] Marcus, R. A. *Rev. Mod. Phys.* **1993**, *65*, 599–610.

[90] Miller, J. R.; Peeples, J. A.; Schmitt, M. J.; Closs, G. L. *J. Am. Chem. Soc.* **1982**, *104*, 6488–6493.

[91] Newton, M. D. *Chem. Rev.* **1991**, *91*, 767–792.

[92] Marcus, R. A. *J. Chem. Phys.* **1965**, *43*, 679–701.

[93] Kuss-Petermann, M.; Wenger, O. S. *Angew. Chem. Int. Ed.* **2016**, *55*, 815–819.

[94] Kuss-Petermann, M.; Wenger, O. S. *J. Am. Chem. Soc.* **2016**, *138*, 1349–1358.

[95] Neumann, S.; Wenger, O. S. *Inorg. Chem.* **2019**, *58*, 855–860.

[96] Hammarström, L. *Acc. Chem. Res.* **2015**, *48*, 840–850.

[97] Karlsson, S.; Boixel, J.; Pellegrin, Y.; Blart, E.; Becker, H.-C.; Odobel, F.; Hammarström, L. *J. Am. Chem. Soc.* **2010**, *132*, 17977–17979.

[98] Nomrowski, J.; Wenger, O. S. *J. Am. Chem. Soc.* **2018**, *140*, 5343–5346.

[99] O'Neil, M. P.; Niemczyk, M. P.; Svec, W. A.; Gosztola, D.; Gaines, G. L. I.; Wasielewski, M. R. *Science* **1992**, *257*, 63–65.

[100] Pannwitz, A.; Wenger, O. S. *Chem. Commun.* **2019**, *55*, 4004–4014.

[101] Higashino, T.; Yamada, T.; Yamamoto, M.; Furube, A.; Tkachenko, N. V.; Miura, T.; Kobori, Y.; Jono, R.; Yamashita, K.; Imahori, H. *Angew. Chem. Int. Ed.* **2016**, *55*, 629–633.

[102] Céspedes-Guirao, F. J.; Ohkubo, K.; Fukuzumi, S.; Fernández-Lázaro, F.; Sastre-Santos, Á. *Chem. Asian. J.* **2011**, *6*, 3110–3121.

[103] Supur, M.; El-Khouly, M. E.; Seok, J. H.; Kay, K.-Y.; Fukuzumi, S. *J. Phys. Chem. A* **2011**, *115*, 14430–14437.

[104] Lebedeva, M. A.; Chamberlain, T. W.; Scattergood, P. A.; Delor, M.; Sazanovich, I. V.; Davies, E. S.; Suyetin, M.; Besley, E.; Schröder, M.; Weinstein, J. A.; Khlobystov, A. N. *Chem. Sci.* **2016**, *7*, 5908–5921.

[105] Hankache, J.; Niemi, M.; Lemmetyinen, H.; Wenger, O. S. *J. Phys. Chem. A* **2012**, *116*, 8159–8168.

[106] King, A. J.; Zatsikha, Y. V.; Blessener, T.; Dalbec, F.; Goff, P. C.; Kayser, M.; Blank, D. A.; Kovtun, Y. P.; Nemykin, V. N. *J. Organomet. Chem.* **2019**, *887*, 86–97.

[107] Schäfer, J.; Holzapfel, M.; Schmiedel, A.; Steiner, U. E.; Lambert, C. *Phys. Chem. Chem. Phys.* **2018**, *20*, 27093–27104.

[108] Imahori, H.; Sekiguchi, Y.; Kashiwagi, Y.; Sato, T.; Araki, Y.; Ito, O.; Yamada, H.; Fukuzumi, S. *Chem. Eur. J.* **2004**, *10*, 3184–3196.

[109] Lim, G. N.; Obondi, C. O.; D'Souza, F. *Angew. Chem. Int. Ed.* **2016**, *55*, 11517–11521.

[110] Zarrabi, N.; Agatemor, C.; Lim, G. N.; Matula, A. J.; Bayard, B. J.; Batista, V. S.; D'Souza, F.; Poddutoori, P. K. *J. Phys. Chem. C* **2019**, *123*, 131–143.

[111] Lauck, M.; Förster, C.; Gehrig, D.; Heinze, K. *J. Organomet. Chem.* **2017**, *847*, 33–40.

[112] Imahori, H.; Tamaki, K.; Guldi, D. M.; Luo, C.; Fujitsuka, M.; Ito, O.; Sakata, Y.; Fukuzumi, S. *J. Am. Chem. Soc.* **2001**, *123*, 2607–2617.

[113] Neumann, S.; Kerzig, C.; Wenger, O. S. *Chem. Sci.* **2019**, *10*, 5624–5633.

[114] Abe, R.; Takata, T.; Sugihara, H.; Domen, K. *Chem. Commun.* **2005**, 3829–3831.

[115] Sasaki, Y.; Kato, H.; Kudo, A. *J. Am. Chem. Soc.* **2013**, *135*, 5441–5449.

[116] Maeda, K.; Higashi, M.; Lu, D.; Abe, R.; Domen, K. *J. Am. Chem. Soc.* **2010**, *132*, 5858–5868.

[117] Sayama, K.; Mukasa, K.; Abe, R.; Abe, Y.; Arakawa, H. *J. Photochem. Photobiol. A* **2002**, *148*, 71–77.

[118] Sasaki, Y.; Nemoto, H.; Saito, K.; Kudo, A. *J. Phys. Chem. C* **2009**, *113*, 17536–17542.

[119] Kobayashi, R.; Tanigawa, S.; Takashima, T.; Ohtani, B.; Irie, H. *J. Phys. Chem. C* **2014**, *118*, 22450–22456.

[120] Windle, C. D.; Kumagai, H.; Higashi, M.; Brisse, R.; Bold, S.; Jousselme, B.; Chavarot-Kerlidou, M.; Maeda, K.; Abe, R.; Ishitani, O.; Artero, V. *J. Am. Chem. Soc.* **2019**, *141*, 9593–9602.

[121] Riedel, M.; Wersig, J.; Ruff, A.; Schuhmann, W.; Zouni, A.; Lisdat, F. *Angew. Chem. Int. Ed.* **2019**, *58*, 801–805.

[122] Bhosale, R.; Jain, S.; Vinod, C. P.; Kumar, S.; Ogale, S. *ACS Appl. Mater. Interfaces* **2019**, *11*, 6174–6183.

[123] Xiong, W.; Dai, W.; Hu, X.; Yang, L.; Wang, T.; Qin, Y.; Luo, X.; Zou, J. *Mater. Lett.* **2018**, *232*, 36–39.

[124] Muraoka, K.; Kumagai, H.; Eguchi, M.; Ishitani, O.; Maeda, K. *Chem. Commun.* **2016**, *52*, 7886–7889.

[125] Nakada, A.; Kuriki, R.; Sekizawa, K.; Nishioka, S.; Vequizo, J. J. M.; Uchiyama, T.; Kawakami, N.; Lu, D.; Yamakata, A.; Uchimoto, Y.; Ishitani, O.; Maeda, K. *ACS Catal.* **2018**, *8*, 9744–9754.

[126] Sekizawa, K.; Maeda, K.; Domen, K.; Koike, K.; Ishitani, O. *J. Am. Chem. Soc.* **2013**, *135*, 4596–4599.

[127] Hankache, J.; Niemi, M.; Lemmetyinen, H.; Wenger, O. S. *Inorg. Chem.* **2012**, *51*, 6333–6344.

[128] Borgström, M.; Shaikh, N.; Johansson, O.; Anderlund, M. F.; Styring, S.; Åker-

mark, B.; Magnuson, A.; Hammarström, L. *J. Am. Chem. Soc.* **2005**, *127*, 17504–17515.

[129] Johansson, O.; Borgström, M.; Lomoth, R.; Palmblad, M.; Bergquist, J.; Hammarström, L.; Sun, L.; Åkermark, B. *Inorg. Chem.* **2003**, *42*, 2908–2918.

[130] Larsen, C. B.; van der Salm, H.; Clark, C. A.; Elliott, A. B. S.; Fraser, M. G.; Horvath, R.; Lucas, N. T.; Sun, X.-Z.; George, M. W.; Gordon, K. C. *Inorg. Chem.* **2014**, *53*, 1339–1354.

[131] Caspar, J. V.; Kober, E. M.; Sullivan, B. P.; Meyer, T. J. *J. Am. Chem. Soc.* **1982**, *104*, 630–632.

[132] Caspar, J. V.; Meyer, T. J. *J. Phys. Chem.* **1983**, *87*, 952–957.

[133] Larsen, C. B.; Wenger, O. S. *Angew. Chem. Int. Ed.* **2018**, *57*, 841–845.

[134] Banerji, N.; Angulo, G.; Barabanov, I.; Vauthey, E. *J. Phys. Chem. A* **2008**, *112*, 9665–9674.

[135] Hazra, P.; Chakrabarty, D.; Sarkar, N. *Langmuir* **2002**, *18*, 7872–7879.

[136] Kim, B.-G.; Chung, K.; Kim, J. *Chem. Eur. J.* **2013**, *19*, 5220–5230.

[137] Kathiravan, A.; Srinivasan, V.; Khamrang, T.; Velusamy, M.; Jaccob, M.; Pavithra, N.; Anandan, S.; Velappan, K. *Phys. Chem. Chem. Phys.* **2017**, *19*, 3125–3135.

[138] Bullock, J. E.; Vagnini, M. T.; Ramanan, C.; Co, D. T.; Wilson, T. M.; Dicke, J. W.; Marks, T. J.; Wasielewski, M. R. *J. Phys. Chem. B* **2010**, *114*, 1794–1802.

[139] Lauw, S. J. L.; Xu, X.; Webster, R. D. *ChemPlusChem* **2015**, *80*, 1288–1297.

[140] Lambert, C.; Nöll, G. *J. Am. Chem. Soc.* **1999**, *121*, 8434–8442.

[141] Kawano, S.-I.; Baumgarten, M.; Chercka, D.; Enkelmann, V.; Müllen, K. *Chem. Commun.* **2013**, *49*, 5058–5060.

[142] Sreenath, K.; Suneesh, C. V.; Ratheesh Kumar, V. K.; Gopidas, K. R. *J. Org. Chem.* **2008**, *73*, 3245–3251.

[143] Li, L.-B.; Ji, S.-J.; Liu, Y. *Chinese J. Chem.* **2008**, *26*, 595–598.

[144] Inari, T.; Yamano, M.; Hirano, A.; Sugawa, K.; Otsuki, J. *J. Phys. Chem. A* **2014**, *118*, 5178–5188.

[145] Cheng, H.-C.; Chiu, K. Y.; Lu, S. H.; Chen, C.-C.; Lee, Y. W.; Yang, T.-F.; Kuo, M. Y.; Chen, P. P.-Y.; Su, Y. O. *J. Phys. Chem. A* **2015**, *119*, 1933–1942.

[146] Wu, J.-T.; Hsiang, T.-L.; Liou, G.-S. *J. Mater. Chem. C* **2018**, *6*, 13345–13351.

[147] Keller, S. N.; Bromby, A. D.; Sutherland, T. C. *Eur. J. Org. Chem.* **2017**, 3980–3985.

[148] Barnsley, J. E.; Shillito, G. E.; Mapley, J. I.; Larsen, C. B.; Lucas, N. T.; Gordon, K. C. *J. Phys. Chem. A* **2018**, *122*, 7991–8006.

[149] Barnsley, J. E.; Shillito, G. E.; Larsen, C. B.; van der Salm, H.; Horvath, R.; Sun, X. Z.; Wu, X.; George, M. W.; Lucas, N. T.; Gordon, K. C. *Inorg. Chem.* **2019**, *58*, 9785–9795.

[150] Albold, U.; Hoyer, C.; Neuman, N. I.; Sobottka, S.; Hazari, A. S.; Lahiri, G. K.; Sarkar, B. *Inorg. Chem.* **2019**, *58*, 3754–3763.

[151] Fulmer, G. R.; Miller, A. J. M.; Sherden, N. H.; Gottlieb, H. E.; Nudelman, A.; Stoltz, B. M.; Bercaw, J. E.; Goldberg, K. I. *Organometallics* **2010**, *29*, 2176–2179.

[152] Frisch, M. J. et al. Gaussian 09 Revision B.01. 2010.

[153] Sample, C. S.; Goto, E.; Handa, N. V.; Page, Z. A.; Luo, Y.; Hawker, C. J. *J. Mater. Chem. C* **2017**, *5*, 1052–1056.

[154] Li, Y.; Li, H.; He, J.; Xu, Q.; Li, N.; Chen, D.; Lu, J. *Chem. Asian. J.* **2016**, *11*, 906–914.

[155] Delor, M.; Keane, T.; Scattergood, P. A.; Sazanovich, I. V.; Greetham, G. M.; Towrie, M.; Meijer, A. J. H. M.; Weinstein, J. A. *Nat. Chem.* **2015**, *7*, 689–695.

[156] Grüning, W. R.; Rossini, A. J.; Zagdoun, A.; Gajan, D.; Lesage, A.; Emsley, L.; Copéret, C. *Phys. Chem. Chem. Phys.* **2013**, *15*, 13270–13274.

[157] Wang, J.; Zhao, Y.; Gao, H.; Gao, G.-L.; Yang, C.; Xia, W. *Asian J. Org. Chem.* **2017**, *6*, 1402–1407.

[158] Hu, J.; Zhang, D.; Harris, F. W. *J. Org. Chem.* **2005**, *70*, 707–708.

[159] Zhang, X.; Jin, Y.-H.; Diao, H.-X.; Du, F.-S.; Li, Z.-C.; Li, F.-M. *Macromolecules* **2003**, *36*, 3115–3127.

[160] Skaisgirski, M.; Larsen, C. B.; Kerzig, C.; Wenger, O. S. *Eur. J. Inorg. Chem.* **2019**, DOI: 10.1002/ejic.201900453.

[161] Ingale, A. P.; More, V. K.; Gangarde, U. S.; Shinde, S. V. *New J. Chem.* **2018**, *42*, 10142–10147.